CRYSTAL NUCLEATION AND GROWTH IN SODA-LIME-SILICA GLASSES

A Thesis Presented

by

CARLOS JULIAN ROSENDO GONZALEZ OLIVER

For the Degree

of

Doctor of Philosophy

of

The University of Sheffield

Department of Ceramics, Glasses and Polymers,
The University of Sheffield

February, 1979

ACKNOWLEDGEMENTS

I would like to express my sincere thanks to my supervisor, Dr P.F. James, for his constant interest in the project, for many helpful discussions and for the suggestions which he has made throughout the course of the work.

I am also sincerely grateful to Professor J.P. Roberts and Professor H. Rawson for providing the opportunity to carry out this research in the Department of Ceramics, Glasses and Polymers.

Thanks are due to the members of the Academic Staff and Technical Staff of the Department for their help and advice. Thanks are also due to Mrs M. Hodgins for her help in preparing the thesis.

Finally, I am indebted to the British Council for financial support and to the University of Cordoba for leave of absence.

TO ADELA, CELINA AND CARLOS ARMANDO

SUMMARY

The kinetics of crystal nucleation and growth were studied in glasses near the $Na_2O.2CaO.3SiO_2$ (NC_2S_3) composition in the soda-lime-silica system. The effects of systematic changes in composition and of various additions to the NC_2S_3 glass were investigated and related to detailed viscosity measurements. Optical and electron microscopy, differential thermal analysis and X-ray diffraction were the main techniques used.

For the exact NC_2S_3 composition the internal nucleation rates of the NC_2S_3 crystal phase showed non-steady state behaviour at low temperatures, the incubation times decreasing with rise in temperature. The crystal-liquid interfacial free energy was obtained from theoretical analysis of the steady state rates using the heat of fusion determined by DTA. Electron microscopy revealed imperfections in the crystals at an early stage of growth.

On varying the base composition, the increases in nucleation for glasses containing less than 50 mole% SiO_2 could be correlated with reductions in viscosity. Large increases in nucleation and decreases in viscosity occurred for small additions of H_2O and NaF to the NC_2S_3 base glass, indicating a decrease in the kinetic barrier to nucleation ΔG_D. Increases in the crystal growth rates for these additions closely corresponded to reductions in viscosity. Additions of ZrO_2 decreased the nucleation and growth rates and increased the viscosity. Additions of P_2O_5, TiO_2 and MoO_3 decreased nucleation.

In glasses containing precipitated platinum there was evidence for heterogeneous nucleation both from kinetic studies and from electron microscopy.

For glasses heat treated isothermally intercepts with the time axis were observed in plots of crystal size against time. The origin of these intercepts is discussed.

Various physical chemical properties of glass ceramics with NC_2S_3 as the major crystalline phase were investigated, including mechanical strength, thermal expansion and chemical durability. The results indicate that the materials may have certain practical applications.

CHAPTER 1 - INTRODUCTION AND SURVEY OF THE RELEVANT LITERATURE

CHAPTER 2 - EXPERIMENTAL TECHNIQUES

CHAPTER 2 - continued

CHAPTER 3 - EXPERIMENTAL RESULTS $Na_2O.2CaO.3SiO_2$ GLASS COMPOSITION AND GLASSES CLOSE TO THIS COMPOSITION

CHAPTER 3 - continued

CHAPTER 4 - EXPERIMENTAL RESULTS. GLASSES WITH H_2O, NaF, ZrO_2 P_2O_5, TiO_2, MoO_3 and Pt ADDITIONS

CHAPTER 5 - DISCUSSION AND ANALYSIS OF THE EXPERIMENTAL RESULTS. PROPERTIES OF SOME GLASS CERAMICS IN THE SODA-LIME-SILICA SYSTEM

APPENDICES

CHAPTER 1

INTRODUCTION AND SURVEY OF THE RELEVANT LITERATURE

Phase transformations in glass forming systems constitute a very active field in both science and technology.

The phenomenon of liquid-liquid immiscibility or 'glass in glass' phase separation has been known for many years (1.1). A number of glasses exhibit 'immiscibility gaps' and under certain conditions will separate into glassy phases of different compositions. The study of this transformation is important in glass technology because of the different physical and chemical properties generally exhibited by phase separated glasses. There has been considerable scientific study of the kinetics of this process.

Uncontrolled crystallization of glasses initiated either from the surface or from internal inclusions is usually termed 'devitrification'. A great deal of attention has been given to developing glass compositions which will not undergo devitrification during the shaping processes of glass articles. Also, fundamental studies have been made of the devitrification process and its relation to certain glass properties such as viscosity.

The discovery of controlled internal crystallization of glasses (1.2) gave rise to a new class of materials, namely glass ceramics. Glass ceramics are obtained by a controlled heat treatment schedule, of specially prepared glasses, which results in the nucleation and growth of crystal phases within the glass. It is possible to prepare very fine grain polycrystalline bodies which possess, in general, certain improved properties when compared either with the related glass or ceramic (1.3). For example, the complete absence of porosity in glass ceramics (if prepared from bubble-free glasses)

contrasts with the situation in 'normal' ceramics which are very rarely free from closed pores. Also the fine grain glass ceramic can be more resistant than the original glass to the propagation of cracks initiated in either the surface or the interior of the body. These factors contribute to the often high mechanical strengths of glass ceramic materials.

Some of the earliest glass ceramics were prepared by precipitating metallic particles in the glass, these acting as sites where the main crystalline phase could nucleate and grow. This process is known as heterogeneous nucleation. However certain glasses will crystallize internally without adding any type of nucleation catalyst to the glass batch. For this reason they are believed to undergo homogeneous nucleation. The term 'nucleating agent' is given to those materials, added to the glass batch, that will promote internal crystallization of the final glass. For example a nucleating agent could enhance phase separation of the glass upon heating. After further heating the main crystalline phases could nucleate homogeneously in one of the glassy phases. Whatever the details of the process, the final stages in making a glass ceramic will involve the nucleation and growth of the main crystalline phases. A nucleation heat treatment in which a large number of small crystals are formed is followed by heat treatment at higher temperatures where the crystals are grown to produce the desired degree of crystallinity.

Studies of crystal nucleation and growth in glasses are very relevant to glass and glass ceramic technology. Also, due to the relatively slow molecular rearrangements and diffusion these processes

can be conveniently studied in glasses.

The main objectives of this investigation were to carry out fundamental studies of crystal nucleation (including heterogeneous nucleation) and crystal growth in soda-lime-silica glasses. A further objective was to investigate the possibilities of making practical glass ceramics from this system which, from the point of view of raw materials, is one of the cheapest glass forming systems. The effects of different nucleating agents on the nucleation and growth of $Na_2O.2CaO.3SiO_2$ (NC_2S_3) crystals were analysed for glass compositions close to the NC_2S_3 composition. The properties of the glasses and final glass ceramics were studied as well as the effect of the base composition on the NC_2S_3 crystal nucleation.

1.1 The kinetics of nucleation

1.1a Homogeneous Nucleation Theory

Let us consider one mole of a one component system at a constant external pressure. The thermodynamic condition for equilibrium (1.4) is that the Gibbs Free Energy of the system $G = H - TS$, where H and S are respectively the enthalpy and entropy per mole of the substance at absolute temperature T(°K), is a minimum. At the melting point of the substance, characterized by a temperature T_m, the liquid (ℓ) and the solid (s) phases coexist, both having the same free energy, i.e. $G^{\ell} = G^{s}$. At $T < T_m$ the solid phase is stable whereas at $T > T_m$ the liquid is the stable phase. At any temperature the value $-\Delta G = -(G^{s} - G^{\ell})$ is called the 'driving

force' of the transformation liquid → solid. Let us assume that the liquid can be supercooled to $T < T_m$ without the occurrence of crystallization. We wish to analyse the 'supercooled liquid to solid' transformation using nucleation theory. This was originally developed for liquid condensation from the vapour (1.5). Nucleation theory, in Volmer's sense (1.6), assumes the existence of heterophase fluctuations by which embryos of the solid phase can be formed inside the liquid. This involves the formation of an interface between the solid and liquid characterized by an interfacial free energy per unit area σ. The total free energy change in forming a spherical embryo of radius r is given by

$$W = W(r) = \frac{4}{3}\pi r^3 \frac{\Delta G}{V_m} + 4\pi r^2 \sigma \qquad (1.1)$$

where V_m is the molar volume of the crystallizing phase. This is shown schematically in Figure 1.1. For $T > T_m$ ($\Delta G > 0$) W increases very rapidly with embryo size, whereas for $T < T_m$ ($\Delta G < 0$) W increases initially with r but reaches a maximum W* at a critical radius r* and then decreases. The value of r* can be calculated from equation (1.1) by solving $\frac{dW(r)}{dr} = 0$ and W* can be obtained by substituting back into equation (1.1). Thus

$$W^* = \frac{16}{3}\pi \sigma^3 \frac{V_m^2}{\Delta G^2} \qquad (1.2a)$$

$$r^* = -\frac{2\sigma}{\Delta G} V_m \qquad (1.2b)$$

Embryos of $r > r^*$ are called nuclei. By calculating $\left(\frac{d^2W}{dr^2}\right)_{r=r^*}$ it can be observed that the system is in an unstable state at $r = r^*$. Those embryos with $r < r^*$ will tend to dissolve and the

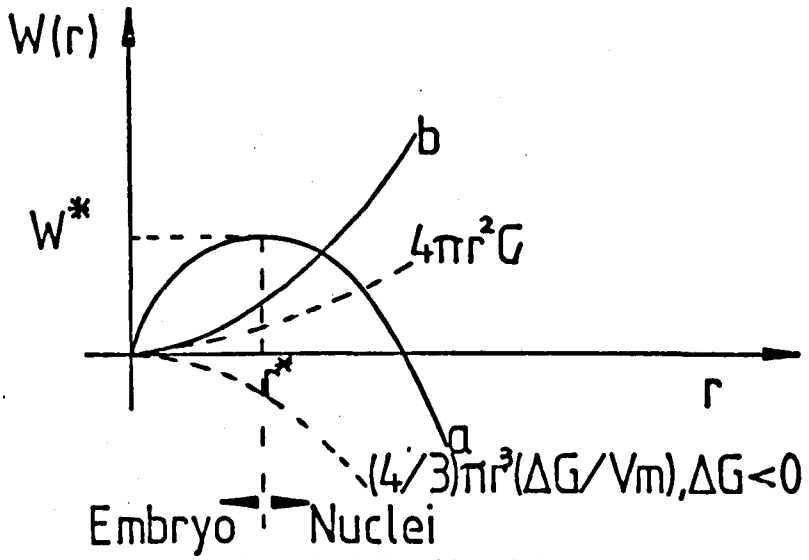

a: $\Delta G<0$ ($T<Tm$), metastable liquid compared to the solid

b: $\Delta G>0$ ($T>Tm$), stable " " " " "

FIGURE 1.1 Work W required to form an embryo/nucleus of radius r.

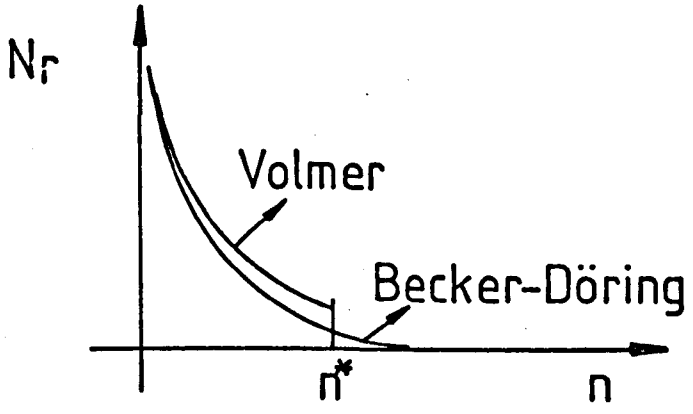

FIGURE 1.2 Distribution Functions.

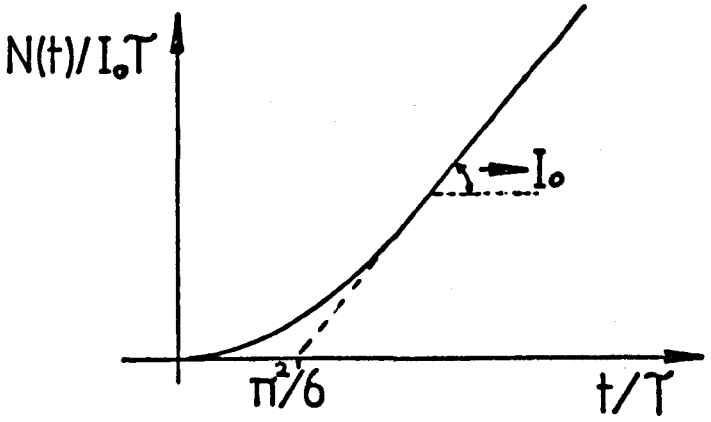

FIGURE 1.3

nuclei with $r > r^*$ will tend to grow. For the initial stages of the transformation it is assumed that embryos grow or shrink by the addition or removal of individual atoms or 'formula units'. W^* is often called the thermodynamic barrier to nucleation.

The distribution of embryos (valid for $r < r^*$) is given by

$$N_r = N_v \exp\left(-\frac{W(r)}{kT}\right) \tag{1.3a}$$

where N_r is the number of embryos of radius r, N_v is the number of atoms of liquid per unit volume and the exponential term is the usual Boltzmann's factor for the probability of finding an embryo of radius r. Also the probability for an embryo of radius $r = r^*$ to grow is given by

$$s^* \nu \exp\left(-\frac{\Delta G_D}{kT}\right) \tag{1.3b}$$

where ΔG_D is the activation energy for an atom to cross the liquid-solid interface, ν is the atomic vibration frequency ($\simeq \frac{kT}{h}$; k is Boltzmann's constant and h is Planck's constant) and s^* is the number of atoms facing the solid critical size embryo. ΔG_D is usually called the 'kinetic barrier for nucleation'. Finally the nucleation rate or the number of nuclei of solid produced per unit time can be written as

$$I = N_v s^* \frac{kT}{h} \exp\left(-\frac{(W^* + \Delta G_D)}{kT}\right) \tag{1.4a}$$

In this derivation it is assumed that a steady state distribution of embryos of critical size has been attained. Also equation (1.4a)

is valid for the initial stages of the transformation where the untransformed volume is essentially the starting volume of liquid. The embryo distribution assumed by Volmer, for the case of condensation from the vapour, was such that it vanished for embryos of $r > r^*$. However Becker and Döring considered a distribution such that at the critical radius the number of embryos was lower, whereas for very small r the distribution was essentially the same as Volmer's. This is shown schematically in Figure 1.2. When all these refinements are applied to the liquid-solid transformation the pre-exponential factor is given by

$$N_v \frac{kT}{h} s^* \left(\frac{W^*}{3\pi kT}\right)^{\frac{1}{2}}$$

However steady state nucleation rates may be represented to a good approximation by

$$I = A \exp\left| - \frac{(W^* + \Delta G_D)}{kT} \right| \qquad (1.4b)$$

where A is essentially independent of temperature when compared to the exponential term.

Finally it should be noticed that for precipitation of crystals the equilibrium shape of the crystal need not be spherical. The crystal will tend to adopt that shape which minimizes the surface free energy. This shape can be calculated from Wulff's construction (1.6). Hence the previous equations have to be modified by replacing σ by $\bar{\sigma} = \frac{\Sigma A_i \sigma_i}{\Sigma A_i}$ where the σ_i and A_i are respectively the free energy per unit area and area of crystal face i. Also

the appropriate shape factors (1.7) have to be included. However the general form of equations (1.2a,b) do not change where now a typical 'critical dimension' plays the role of the previous critical radius.

1.1b Non-steady state homogeneous nucleation

The creation of a stationary size distribution of embryos of the stable phase may take a definite time interval in condensed systems, this time being governed by the atomic transport in the liquid and by the inherent instabilities of the embryos. The non-stationary nucleation rates for small t (1.6) can be written as

$$I = I_o \, e^{-\tau/t} \tag{1.5a}$$

where τ (originally calculated by Zeldovich (1.6)) is given by

$$\tau \simeq \frac{n^{*2}}{4D^*} \tag{1.5b}$$

were n^* is the number of atoms in the central nucleus ($r=r^*$). Also $D^* \simeq \frac{kT}{h} s^* \, e^{-\Delta G_0/kT}$, i.e. $\tau = \tau_0 \exp\left(\frac{\Delta G_D}{kT}\right)$ where $\tau_0 = \frac{n^{*2}h}{4kTs^*}$. Russel (1.6) found $\tau \simeq \frac{n^{*2}}{10D^*}$ for precipitation reactions involving long range diffusion. Hillig (1.8) found that the time to form a nucleus was

$$\bar{t} \simeq \frac{\pi}{4D} \left(\frac{V_L}{V_M}\right)^2 \left(\frac{r^*}{X}\right)^2 \tag{1.6}$$

where V_L, V_M are the molar volume of liquid and solid phases, D refers to the solute diffusion coefficient and X is the mole fraction of solid. Hillig emphasized that "this time is expected to be much shorter than the actual time to achieve steady-state conditions

because the inherent instability of a subcritical nucleus has not been taken into account".

Finally Kashchiev (1.9) found

$$I = I_o \left[1 + 2 \sum_{j=1}^{\infty} (-1)^j \exp(-j^2 t/\tau) \right] \qquad (1.7a)$$

and

$$\tau = \frac{8kT}{\pi D \left(\frac{d^2W}{dn^2}\right)_{n=n^*}} = \frac{8\ kT}{\pi s^* Z \left(\frac{d^2W}{dn^2}\right)_{n=n^*}} \qquad (1.7b)$$

where Z is the number of atoms attached to the critical nucleus per unit time per unit area. For comparison with experiment it is better to obtain an expression for N(t), the number of nuclei per unit time per unit volume;

$$\frac{N(t)}{I_o \tau} = \frac{t}{\tau} - \frac{\pi^2}{6} - 2 \sum_{j=1}^{\infty} \frac{(-1)^j}{j^2} \exp(-j^2 t/\tau) \qquad (1.8a)$$

where for $t > 5\ \tau$

$$N(t) \simeq I_o\ t - \frac{I_o \pi^2}{6} \tau \qquad (1.8b)$$

This last expression means that the steady state nucleation rate (I_o) and τ value can be calculated (1.10) from the linear part of the N(t) versus t plot (Figure 1.3) if the experimental results obey equation (1.8a).

1.1c Heterogeneous Nucleation Rates

In homogeneous nucleation the probability of nucleation at any site is identical to that at any other site. In heterogeneous

nucleation the probability of nucleation at certain preferred sites in the assembly is much greater than at other sites. Nucleation can occur on inclusions or solid impurity particles, on the surface of the supercooled liquid or on uniformly distributed particles of metals or other substances precipitated by homogeneous nucleation in the liquid. In principle the interfaces produced in a liquid-liquid phase separation process could also offer preferred sites for nucleation. In order to reduce the complexity, in the following derivation, let us assume the same general conditions stated in section 1.1a plus the existence of M flat rigid substrates per unit volume in the supercooled liquid. Let us consider the formation of a spherical cap (Figure 1.4) of radius r of the solid (s) on the substrate (f). At equilibrium the contact angle satisfies

$$\cos\theta = q = \frac{\sigma_{\ell f} - \sigma_{sf}}{\sigma_{\ell s}} \tag{1.9}$$

where $\sigma_{\ell f}$, σ_{sf} and $\sigma_{\ell s}$ are the interfacial free energies per unit area between liquid-substrate, solid-substrate and liquid-solid. The free energy involved in forming such a cap can be written as:

$$W_f(r) = W_f = V_{\ell s}\frac{\Delta G}{V_m} + A_{\ell s}\,\sigma_{\ell s} + A_{sf}\,\sigma_{sf} - A_{sf}\,\sigma_{\ell f} \tag{1.10}$$

where

$$V_{\ell s} = \pi r^3\left(\frac{2 - 3q + q^3}{3}\right),\ A_{\ell s} = 2\pi r^2(1 - q) \text{ and } A_{sf} = \pi r^2(1 - q^2)$$

The free energy of formation of the critical size nucleus can be calculated by solving $\left(\frac{dW_f(r)}{dr}\right)_{r=r^*} \equiv 0$. The critical radius

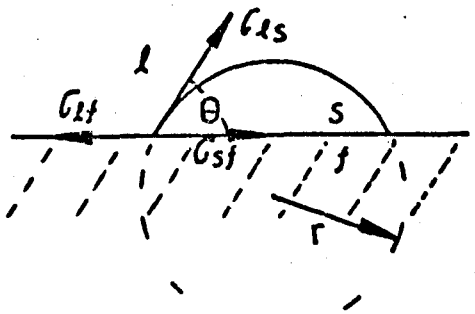

FIGURE 1.4 Formation of a solid(s) cluster on a solid substrate(f) from the supercooled liquid (l).

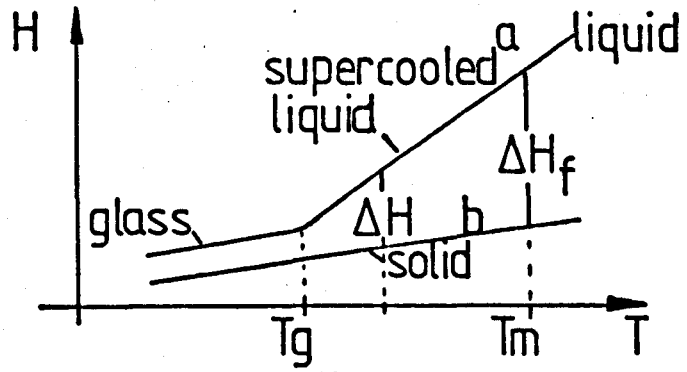

FIGURE 1.5 Enthalpy of the liquid and solid as a function of temperature.

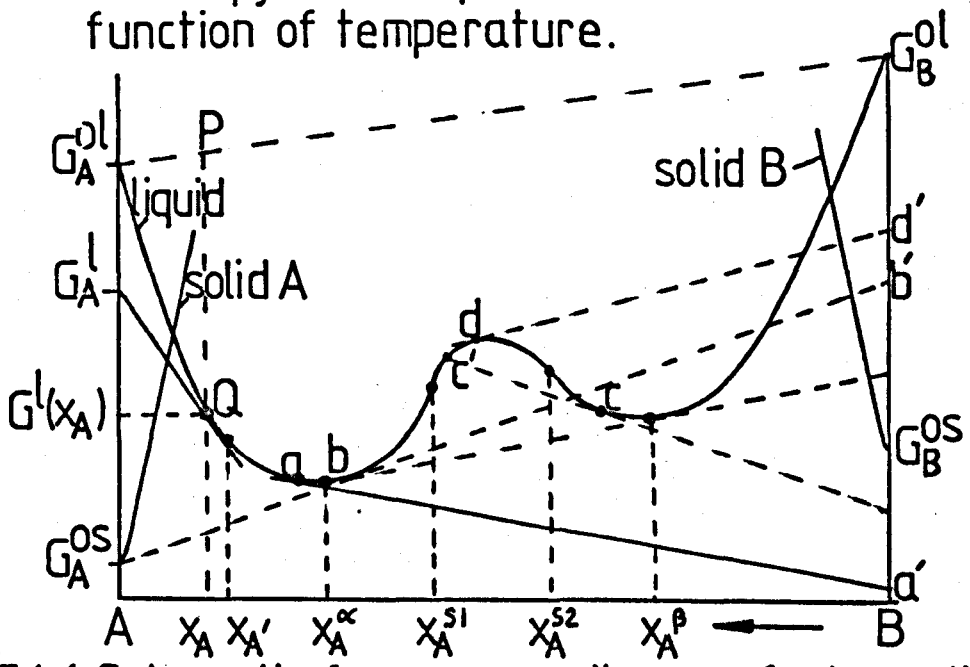

FIGURE 1.6 Schematic free energy diagram for two solids and a liquid as a function of composition and at constant T.

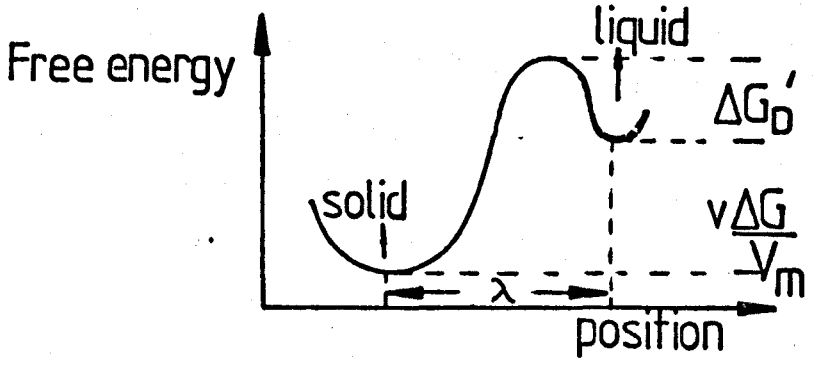

FIGURE 1.7 Free energy vs.position for a atom to cross the solid–liquid interface.

obtained is:

$$r^* = - \frac{2\sigma_{\ell s} V_m}{\Delta G} \tag{1.11}$$

and the work W_f^* is:

$$W_f^* = \frac{16}{3} \pi \frac{\sigma_{\ell s}^3 V_m^2}{\Delta G^2} f(\theta) = W^* f(\theta) \tag{1.12}$$

where $f(\theta) = \frac{2-3\cos\theta + \cos^3\theta}{4}$. The function $f(\theta)$ varies from 0 to 1 when θ varies from 0 to π. Thus, although the critical radius is the same as in the case of homogeneous nucleation, the thermodynamic barrier for nucleation can be much smaller in the heterogeneous case. For example, for $\theta = \frac{\pi}{2}$, $W_f^* = \frac{W^*}{2}$. For $\theta = 0$ complete wetting of the substrate by the solid in the presence of the liquid occurs and $W_f^* = 0$ i.e. there is no thermodynamic barrier to nucleation. The interfacial energy between s and f will in general depend on the kind of interface between them. σ_{sf} can be approximately (1.11) described as $\sigma_{sf} = \sigma_{sf}^{q} + \sigma_{sf}^{st}$ where σ_{sf}^{q} arises from the chemical interaction between s and f molecules across the interface. σ_{sf}^{st} corresponds to the elastic strains in s and f and the dislocations at the interface necessary to accommodate the mismatch δi between them. The 'ideal disregistry' is defined as $\delta i = \frac{a_f^\circ - a_s^\circ}{a_s^\circ}$ where a_f° and a_s° are the equilibrium atomic spacings of free substrate (f) and free solid (s) respectively.

Now the equilibrium number of embryos of radius r is given by

$$Nr = N^f \exp\left(- \frac{W_f(I)}{kT}\right) \tag{1.13}$$

where N^f is the total number of atoms of liquid in contact with substrate particles. The number of nuclei produced per unit time (1.6) is

$$N^f \frac{kT}{h} \exp\left[- \left(\frac{W_f^* + \Delta G_D}{kT} \right) \right] \qquad (1.14)$$

where A^f is the total surface area of substrate particles. Finally, the nucleation rate per unit volume of liquid is

$$V_I^f = V_N^f \frac{kT}{h} \exp\left[- \left(\frac{W_f^* + \Delta G_D}{kT} \right) \right] \qquad (1.15)$$

where V_N^f is tht total number of atoms of liquid in contact with the substrate particles per unit volume of liquid. Also this number is given by

$$V_N^f = Mn^f \qquad (1.16)$$

where n^f is the number of atoms of liquid in contact with one substrate particle.

1.2 The thermodynamic driving force of phase transformations

As we have seen in the previous section the 'driving force' is an important quantity in nucleation theory. It also occurs in the theories of crystal growth. We will now show how it may be calculated for both single and multicomponent systems.

1.2a Single component systems

Let us consider a single component glass forming liquid. On cooling the enthalpy function will in general follow curve a in Figure 1.5. On reaching Tm, for kinetic reasons the stable liquid passes to the metastable supercooled liquid state without crystallization. At T ~ Tg a 'bend' in the H^{ℓ} vs T curve is observed. This corresponds to the

glass transformation temperature range where the supercooled liquid state of the system changes gradually (depending on the cooling rate) to a 'solid like' state (1.12). The corresponding crystalline material (curve b, Figure 1.5) will have lower enthalpy in the same temperature range.

At a temperature $T < Tm$ the change in free energy per mole is given by:

$$\Delta G = -\frac{\Delta H_f}{Tm}(Tm - T) - \int_T^{Tm} \Delta Cp\, dT' + T\int_T^{Tm} \Delta Cp \frac{dT'}{T'} \qquad (1.17)$$

where $\Delta G = \Delta H - T\Delta S = G^s - G^\ell$, $\Delta H_f = H^\ell - H^s > 0$ and $\Delta Cp = Cp^s - Cp^\ell < 0$ where Cp^s, Cp^ℓ are the specific heats (cal $mole^{-1}$ $°K^{-1}$) at constant pressure for the solid and liquid respectively. If $\Delta Cp = 0$ we obtain

$$\Delta G = -\frac{\Delta H_f}{Tm}(Tm - T) \qquad (1.18)$$

In general ΔCp is a function of temperature. However if ΔCp = constant from Tm to the temperature of interest equation (1.17) can be integrated to give:

$$\Delta G = -\frac{\Delta H_f}{Tm}(Tm - T) - \Delta Cp\,(Tm - T) + \Delta Cp\, T \ln\left(\frac{Tm}{T}\right) \qquad (1.19)$$

Now neglecting terms of the order $\left(\frac{Tm-T}{Tm+T}\right)^3$ and higher in $\ln\left(\frac{Tm}{T}\right)$ we obtain:

$$\Delta G = -\frac{\Delta H_f}{Tm}(Tm - T)\left[1 + \frac{\Delta Cp}{\Delta H_f}\frac{Tm-T}{Tm+T}Tm\right] \qquad (1.20)$$

For those cases where ΔCp is an unknown constant Hoffman (1.13) found (see also (1.14))

$$\Delta G = -\frac{\Delta H_f}{Tm}(Tm - T)\frac{T}{Tm} \qquad (1.21)$$

It is interesting to compare the different values obtained from equations (1.18) to (1.21) for a given compound. Let us assume a material where $\Delta Cp = -38$ cal mole^{-1} °K^{-1}, $\Delta H_f = 21000$ cal mole^{-1} and $Tm = 1562$ °K (1289°C). The results at T = 893°K (620°C), T = 993 °K (720°C) and T = 1423°K (1150°C) are listed in Table 1.1.

TABLE 1.1 ΔG RESULTS FROM EQUATIONS 1.18 TO 1.21

T(°K) \ ΔG (cal mole^{-1})	(1.18)	(1.19)	(1.20)	(1.21)
893	-8994.2	-2545.9	-2066.6	-5142.0
993	-7649.8	-3121.0	-2834.6	-4863.2
1423	-1868.8	-1626.5	-1622.8	-1702.5

It can be seen that at high temperatures the four different equations give almost the same ΔG irrespective of whether ΔCp is constant or not. But at much lower temperatures the difference between the cases $\Delta Cp = 0$ and $\Delta Cp = -38$ cal mole^{-1}°K^{-1} is very significant. For example at 893°K equation (1.20) gives -2066.6 cal mole^{-1} which is 77% lower than from equation (1.18). Finally it is interesting to examine the validity of the approximation involved in the derivation of equation (1.20). The value from equation (1.20) is approximately 9% lower than that from the more accurate equation (1.19) at 993°K.

1.2b Binary Systems

Let us consider the G^{ℓ} vs. X_A free energy diagram of Figure 1.6 where three phases can be observed i.e. A(s), liquid and B(s). At the moment let us concentrate on the precipitation of pure solid A from compositions X_A between X_A^{α} and 1. $G_A^{o\ell}$, G_A^{os} are the molar free energies of pure liquid and solid at the temperature of interest. The molar free energy change in precipitating N_A moles of pure A (G_A^{os}) and $N_{x'}$ moles of liquid of composition $X_{A'}$ ($G^{\ell}(X_{A'})$) from Nx moles of solution of composition X_A ($G^{\ell}(X_A)$) (neglecting interfacial effects) is

$$\Delta G = \frac{\Delta G'}{N_A} = \frac{1}{N_A}[N_{x'}\, G^{\ell}(X_{A'}) + N_A\, G_A^{os} - Nx\, G^{\ell}(X_A)]$$

where $Nx = N_A + N_{x'}$ and $N_A << N_{x'}$. It can be shown (1.11) that

$$\Delta G = [G_A^{os} - G^{\ell}(X_A)] + (1 - X_A)\frac{dG^{\ell}}{dX_A} = G_A^{os'} - G_A^{\ell} \qquad (1.22)$$

Hence ΔG is the vertical distance from the intersection of the tangent line at $G^{\ell}(X_A)$ with the pure A axis to G_A^{os}. Equation (1.22) is of fundamental importance in phase transformations in glasses (References 1.15 to 1.20). For example a supercooled liquid of composition a (Figure 1.6) cannot precipitate solid B initially since the value of $G_B^{os} - a'$ is positive (a' is the intersection of the tangent at a with the pure B axis). However solid A can precipitate and the remaining liquid will change composition until B formation is possible thermodynamically (tangent bb').

Let us assume that for kinetic reasons neither solid A nor solid B can precipitate for liquid compositions between X_A^{α} and X_A^{β}. Then

the initial liquid will separate into two liquids of compositions X_A^{α} and X_A^{β}. For compositions between the inflection point X_A^{s2} $\left(\frac{d^2G^{\ell}}{dX_A^2} = 0\right)$ and X_A^{β} the system is metastable towards infinitesimal compositional fluctuations $\left(\frac{d^2G^{\ell}}{dX_A^2} > 0\right)$. Thus for a liquid of composition c phase separation can only take place if a fluctuation exceeding the composition c' occurs. In this case the kinetics of the process are governed by nucleation and growth, as already discussed. For compositions between the inflection points the liquid is unstable towards infinitesimal compositional fluctuations $\left(\frac{d^2G^{\ell}}{dX_A^2} < 0\right)$ and the kinetics of phase separation for the initial stages are governed by an 'uphill' diffusion process ('spinodal decomposition') where the interfaces between the initial liquids are diffuse rather than sharp as in the nucleation case. Whether phase separation occurs by a nucleation or spinodal mechanism, the final stages are governed by a coarsening process which is driven by a lowering of the interfacial energy between the phases.

Let us now assume that for liquid compositions between the spinodal compositions (X_A^{s1}, X_A^{s2} in Figure 1.6) solid A cannot precipitate for kinetic reasons. There are two cases to consider. The first case is typified by a liquid of composition c. For this composition solid B cannot precipitate unless phase separation (by a nucleation mechanism) occurs first. The second case applies to compositions where the driving force for B precipitation is positive, for example composition d. Thermodynamically B could precipitate from the beginning. However B formation will involve a large change in composition requiring long range diffusion, whereas the liquid is in an unstable state and will tend to quickly phase separate into two liquids. Although by this

process the thermodynamic barrier to nucleation of B is increased at the same time the kinetic barrier to nucleation may be considerably decreased.

Now the activity of A (referred to the pure liquid state) in the liquid of composition X_A is given by (1.4):

$$G_A^{\ell} = G_A^{o\ell} + RT \ln a_A^{\ell} \tag{1.23}$$

where R is the gas constant. From equations (1.18), (1.22) and (1.23) we obtain:

$$\Delta G = - \frac{\Delta H_f}{Tm} (Tm - T) - RT \ln a_A^{\ell} \tag{1.24}$$

The activity is given by $a_A^{\ell} = X_A \gamma_A^{\ell}$, where γ_A^{ℓ} is the activity coefficient for component A which is in general a function of temperature and composition. Then

$$\Delta G = - \frac{\Delta H_f}{Tm} (Tm - T) - RT \ln X_A - RT \ln \gamma_A^{\ell} \tag{1.25}$$

At the liquidus temperature (T_L) of the system, $\Delta G = 0$ and from equation (1.24) it is found

$$- \frac{\Delta H_f}{Tm} (Tm - T) = RT_L \ln a_A^{\ell} \tag{1.26}$$

For an Ideal solution $\gamma_A^{\ell} = 1$ (i.e. a_A^{ℓ} is independent of temperature) we find

$$\Delta G = - \frac{\Delta H_f}{T_L} (T_L - T) \tag{1.27}$$

where the relationship between T_L and X_A is given by

$$- \frac{\Delta H_f}{R \, Tm \, T_L} (Tm - T_L) = \ln X_A \tag{1.28}$$

In order to introduce the regular solution model it is convenient to reformulate the problem in terms of the free energy of mixing ΔG_m^{ℓ} at the composition X_A (distance PQ in Figure 1.6). This is carried out in Appendix AO. ΔG is now given by equation (AO8) and the relationship between X_A and TL is expressed in equation (AO10). Note that a knowledge of $\Delta H_m^{\ell}(A)$ is required to calculate the liquidus curve. Further discussion of this model is given in the Appendix. Finally for systems of more than two components the free energy change $G_i^{os} - G_i^{\ell}$ for any component i can be calculated from an equation similar to equation (1.24) where again activity data is required.

1.3 Crystal Growth Rates

Once a stable nucleus has formed the growth of the crystal proceeds by incorporating atomic species from the supercooled liquid. Again the free energy difference between liquid and crystal drives the transformations. Also an activation energy $\Delta G'_D$ (in general different from that for nucleation) for an atom or growth unit to cross the liquid-solid interface has to be considered.

Normal Growth

In the following discussion, for simplicity the growth units will be referred to as "atoms" although a better term would be 'formula units'.

Let us assume that the probability of atomic attachment is unity at the interface. The transfer of atoms in either direction across the interface will be equal to the number of atoms at the interface s times the frequency of attempted jumps ν times the fraction of atoms which acquire enough thermal energy to jump. The fraction of atoms to

jump across the interface (Figure 1.7) from the solid side is given by $\exp\left[\left(\frac{\Delta G'_D + \frac{V|\Delta G|}{Vm}}{kT}\right)\right]$ where V is the atomic volume. The fraction of atoms for the reverse direction is given by $\exp\left(-\frac{\Delta G'_D}{kT}\right)$. The growth rate will be proportional to the net transfer of atoms from the liquid to the solid. That is

$$u \propto s\nu \exp(-\Delta G'_D/kT) - s\,\nu \exp\left(-\frac{\Delta G'_D + \frac{V|\Delta G|}{Vm}}{kT}\right)$$

If s atoms are transferred growth of one layer occurs, i.e:

$$u = \lambda\,\nu \exp(-\Delta G'_D/kT)\left[1 - \exp -\frac{V|\Delta G|}{VmkT}\right] \qquad (1.29)$$

It can be seen that u vanishes at $T = Tm$ and that u has a maximum at lower temperatures. Two limiting cases can be obtained from equation (1.29). For

$$\frac{V|\Delta G|}{Vm} \ll kT \text{ (small supercooling)}$$

$$u \simeq \lambda\,\nu\,\frac{V|\Delta G|}{Vm}\exp\left(-\frac{\Delta G'_D}{kT}\right) \qquad (1.30)$$

As we have shown in section 1.2a, equation (1.18) is a very good approximation for $\Delta T = Tm - T$ small. So equation (1.30) becomes

$$u \simeq \lambda\,\nu\,\frac{V}{Vm}\,\frac{\Delta H_f}{Tm}\,\Delta T \exp\left(-\frac{\Delta G'_D}{kT}\right) \qquad (1.31)$$

i.e. u is proportional to ΔT

For $\frac{V|\Delta G|}{Vm} \gg kT$ (large supercooling)

$$u \simeq \lambda\,\nu \exp\left(-\frac{\Delta G'_D}{kT}\right) \qquad (1.32)$$

It should be noticed that $\Delta G'_D = \Delta H'_D - T\Delta S'_D$ where $\Delta H'_D$, $\Delta S'_D$ are the

enthalpy and entropy of activation. Then

$$\ln u = \ln (\lambda\nu) + \frac{\Delta S'_D}{k} - \frac{\Delta H'_D}{kT} \tag{1.33}$$

In other words the slope of a ln u vs $\frac{1}{T}$ plot gives the activation enthalpy rather than $\Delta G'_D$.

Surface nucleation model for crystal growth

By defining the diffusion coefficient for growth as

$$D = D_o \exp\left(-\frac{\Delta G'_D}{kT}\right) \tag{1.34}$$

where $D_o = \nu \lambda^2$ and including the fraction of crystal sites f on the surface of the solid to which atoms can be attached ($0 \leq f \leq 1$) the growth rate becomes

$$u = \frac{D f}{\lambda}\left[1 - \exp\left(-\frac{V|\Delta G|}{VmkT}\right)\right] \tag{1.35}$$

Let us examine closely the significance of equation (1.35). Rough interfaces on an atomic scale provide many sites for growth, so that the factor f should approach unity and the growth rate should be isotropic. However for very smooth interfaces growth occurs with greater difficulty and f should be less than 1. Furthermore if a crystal has both kind of surfaces in general the growth rate will be anisotropic, the layers growing rapidly on the rough surfaces and slowly on the smooth surfaces. For materials (1.23) characterized by low entropies of fusion $\Delta S_f < 2R$ even the closely packed surfaces should be smooth on an atomic scale and the growth rate should be highly anisotropic showing a definite faceted morphology. Two models have been put forward to estimate the factor f (1.24). Both assume that growth occurs only

at steps on a smooth surface.

For an atomically smooth surface (without intersecting dislocations) crystal growth may occur by first forming a two dimensional nucleus (1.25). Let us consider the formation of a "pill-box" nucleus of radius r and height a_o. The work to form such a nucleus is given by

$$W_A(r) = \pi r^2 a_o \frac{\Delta G}{Vm} + 2\pi r a_o \gamma \tag{1.36}$$

where γ is the interfacial free energy per unit area at the edge of the nucleus. By a similar procedure to that used in section 1.1a the thermodynamic barrier to nucleation and the critical radius are

$$W_A^* = -\pi a_o \gamma^2 \frac{Vm}{\Delta G} \qquad (\Delta G < 0) \tag{1.37}$$

$$r^* = -\gamma \frac{Vm}{\Delta G}$$

The nucleation rate of monolayer islands is given by

$$I^A = N^A \nu \exp\left(-\frac{W^*}{kT}\right) \frac{2\pi r^*}{a_o} \tag{1.38}$$

where N^A is the number of possible nucleation sites, $2\pi r^*/a_o$ is the number of edge sites where an atom can be attached and ν is a frequency for atomic transfer from the liquid to the nucleus. If ΔG is given by equation (1.18) we obtain

$$I^A = N^A \nu \frac{2\pi r^*}{a_o} \exp\left(-\frac{\pi a_o \gamma^2 Vm\, Tm}{kT\, \Delta H_f (Tm-T)}\right) \tag{1.39}$$

For small ΔT a single nucleation event will result in an island spreading across the interface to form a new layer. Hence the growth

rate depends on the frequency of nucleus formation i.e. $u = I\, a_o$ and

$$u \propto \exp(-B/T\Delta T) \tag{1.40}$$

where $B = \dfrac{\pi\, a_o\, \gamma^2 Vm\, Tm}{k\Delta H_f}$. It can be seen from equation (1.40) that the growth rate according to this model will be unobservably low for ΔT small.

For very large supercoolings the growth rate is controlled by the rate of attachment of atoms rather than by the nucleation of new layers and the growth mechanism will be similar to normal growth.

Screw dislocation model for crystal growth

The screw dislocation mechanism assumes step formation by screw dislocations intersecting the interface. The dislocation provides a perpetual ledge where atoms can be attached to the crystal. The tighter the spiral ledge the higher will be the growth rate of the whole surface. The equation of the spiral is $r = b\theta$ where r is the radius, b the separation of the turns of the spiral and θ the angular coordinate. Setting the radius of the central island of the spiral equal to r^* ($r^* = \frac{b}{2}$) it is found that $r = 2\theta r^*$. From equations (1.37) and (1.18) the spacing b is inversely proportional to ΔT. Hence the total length of spiral is directly proportional to ΔT. The factor f is given by (1.25):

$$f = \frac{a_o\, \Delta H_f\, \Delta T}{2\pi\, \gamma\, Vm\, Tm} \tag{1.41}$$

Thus for small ΔT, equation (1.35) approaches

$$u \simeq \frac{D}{\lambda}\, f\, \frac{V}{Vm}\, \frac{\Delta H_f}{Tm}\, \frac{\Delta T}{kT} = \frac{a_o\, D\, v}{2\pi\lambda\, V^2 m\gamma} \left(\frac{\Delta H_f}{Tm}\right)^2 \left(\frac{\Delta T}{kT}\right)^2 \tag{1.42}$$

If the diffusion coefficient is given by the Stokes Einstein equation

$$D = \frac{kT}{3\pi\lambda\eta} \tag{1.43}$$

where η is the viscosity and λ the atomic diameter, an inverse dependence of growth rate on viscosity should be observed. It is convenient to define the reduced growth rate u_R as

$$u_R = \frac{u\eta}{\left[1 - \exp\left(-\frac{v\Delta G}{VmkT}\right)\right]} \tag{1.44}$$

Thus the temperature dependence of f can be obtained from the temperature dependence of U_R. For normal growth a horizontal line of U_R versus T should be obtained. For screw dislocation growth (ΔT small) a straight line passing through the origin should be found. Finally for surface nucleation growth a curve (positive curvature) passing through the origin should be obtained for small ΔT.

1.4 Literature Review

Na_2O-CaO-SiO_2 System

The Na_2O-CaO-SiO_2 phase diagram determined by Morey and Bowen (1.26) was revised by Shahid and Glasser (1.27). Shahid and Glasser found two 'new' eutectics inside the $Na_2C.2SiO_2$ (NS_2) field as originally delineated by Morey and Bowen. Shahid and Glasser also showed the existence of two 'new' phase fields, namely N_3S_8 and NCS_5, inside the 'old' NS_2 field. The revised equilibrium diagram from 50 wt.% SiO_2 to

100 wt.% SiO_2 is shown in Figure 1.8. Segnit (1.28) found two compounds to the left of the NS-CS join. These were NC_2S_2 (40 mole% SiO_2) and $N_4C_3S_5$ (41.6 mole% SiO_2). Also the stability field of the NC_2S_3 phase was considerably enlarged from that given by Morey and Bowen. Thus the liquidus surface of NC_2S_3 extended nearly to the $N_4C_3S_5$ composition. The binary NS-CS was carefully examined by Moir and Glasser (1.29). This section is shown in Figure 1.9. The NC_2S_3 phase (33.3 mole% $Na_2O.SiO_2$) shows an extensive solid solution range whereas the N_2CS_3 phase (66.6 mole% NS) shows, comparatively, a much smaller range of solid solution. This phase diagram can be used to obtain information on the thermodynamic behaviour of the composition NC_2S_3. Mole fractions in the binary system CS-NS (from the NC_2S_3 composition to NS) were transformed to mole fractions in the binary NC_2S_3-NS system. A plot of $\ln X_R$ vs $1/T_L$ is given in Figure 1.10, where X_R is the mole fraction of NC_2S_3, for the range $1 \leq X_R \leq 0.525$, i.e. from 33.3 to 65 mole% NS in Figure 1.9.

This plot is linear in the composition range considered. The slope and intercept with the $\ln X_R$ axis were -13578.26 and 8.596. Assuming ideal behaviour, from equation (1.28) we obtain a heat of fusion of 27 kcal $mole^{-1}$ (from either the slope or the intercept of the $\ln X_R$ vs $\frac{1}{T_L}$ plot). This value is about 5 kcal $mole^{-1}$ greater than the known value for the heat of fusion of the NC_2S_3 compound (1.33).

Moir and Glasser (1.30) also studied the soda-lime-silica system for 5, 10 and 15 wt.% Al_2O_3 additions and found that the NC_2S_3 field extended up to 67, 63 and 61 mole% SiO_2 respectively.

The NC_2S_3 crystalline compound exhibits (1.29) a high to low polymorphic transformation at 485°C. The low form (1.31) is hexagonal

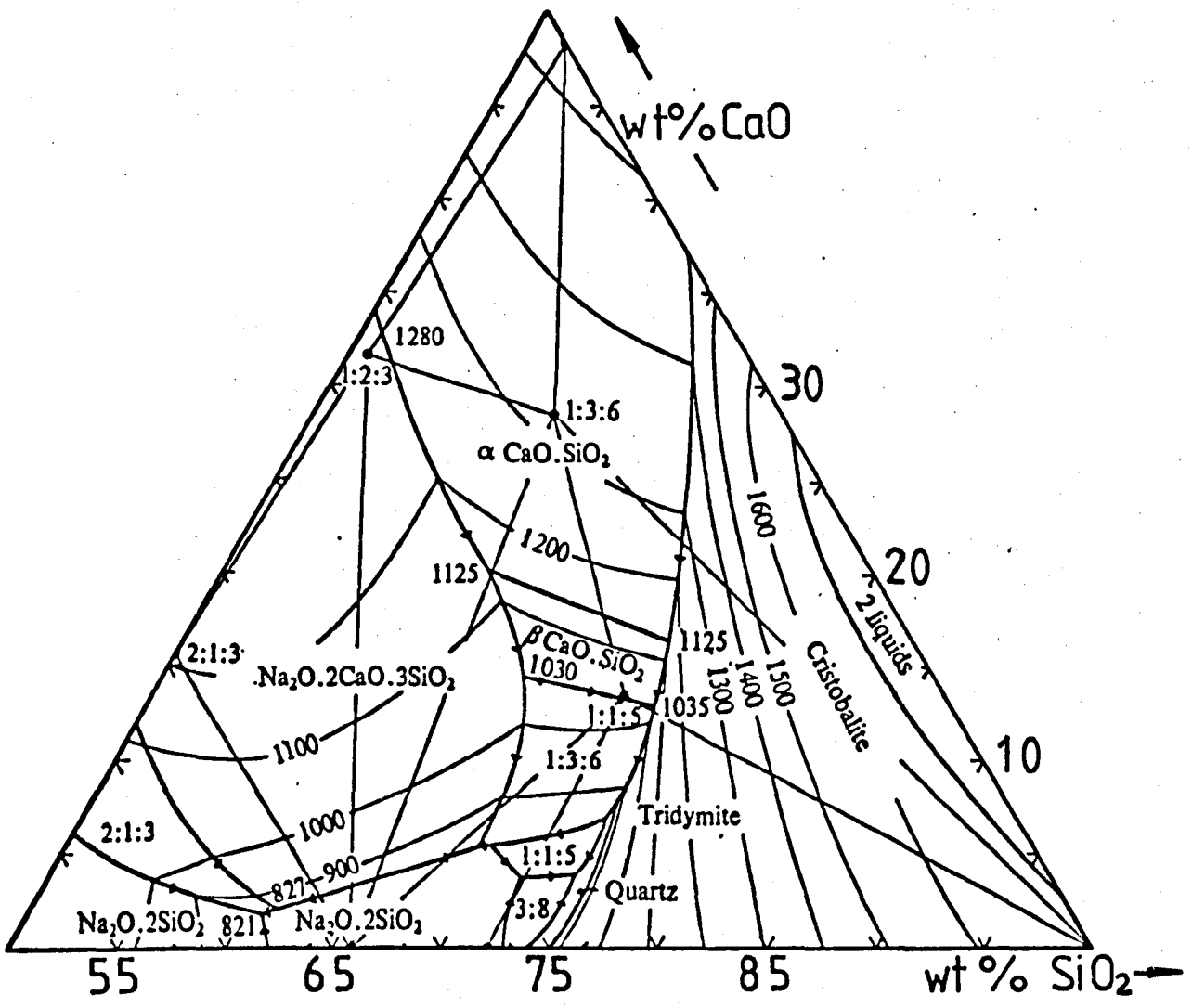

FIGURE 1.8 Equilibrium diagram acc.to Shahid and Glasser.(127)

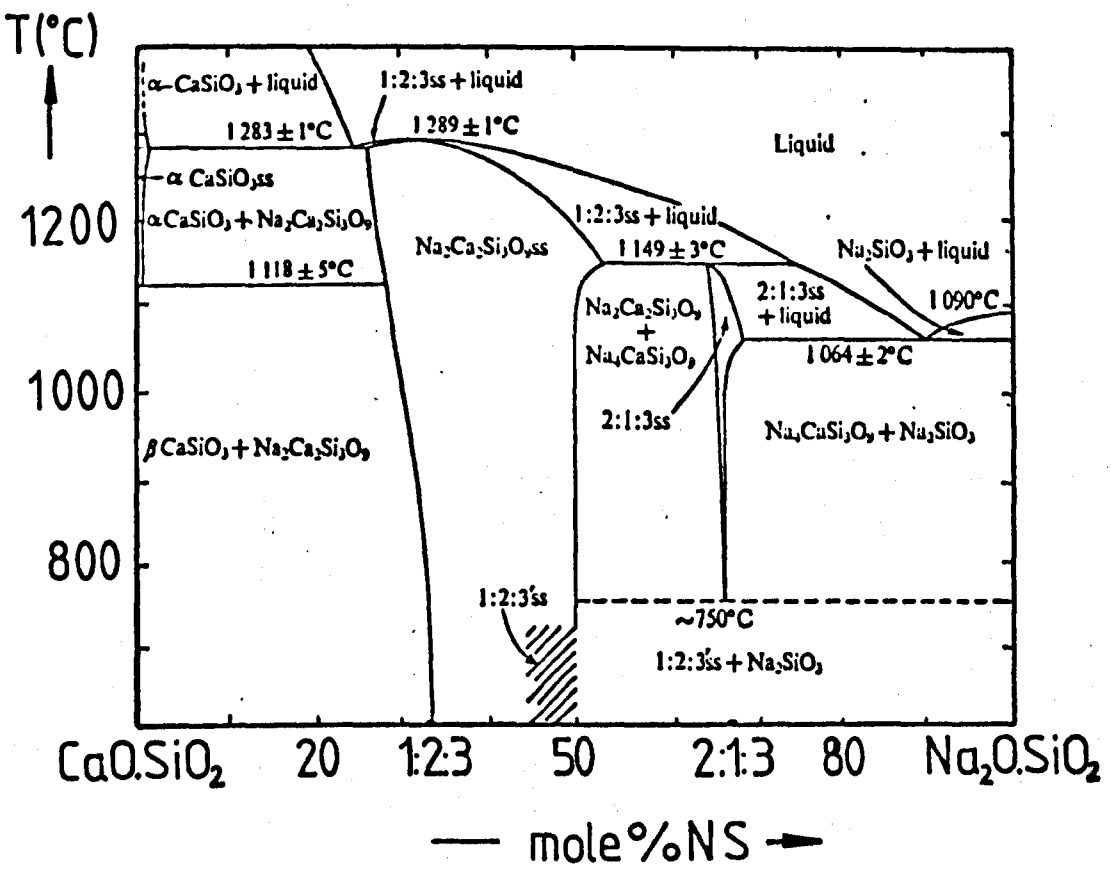

FIGURE 1.9 Section NS-CS of the N-C-S system acc. to Moir and Glasser.(1.29)

FIGURE 1.10 $\ln X_R$ AS A FUNCTION OF $\frac{1}{T_L}$ FROM DATA ACCORDING TO REFERENCE (1.29)

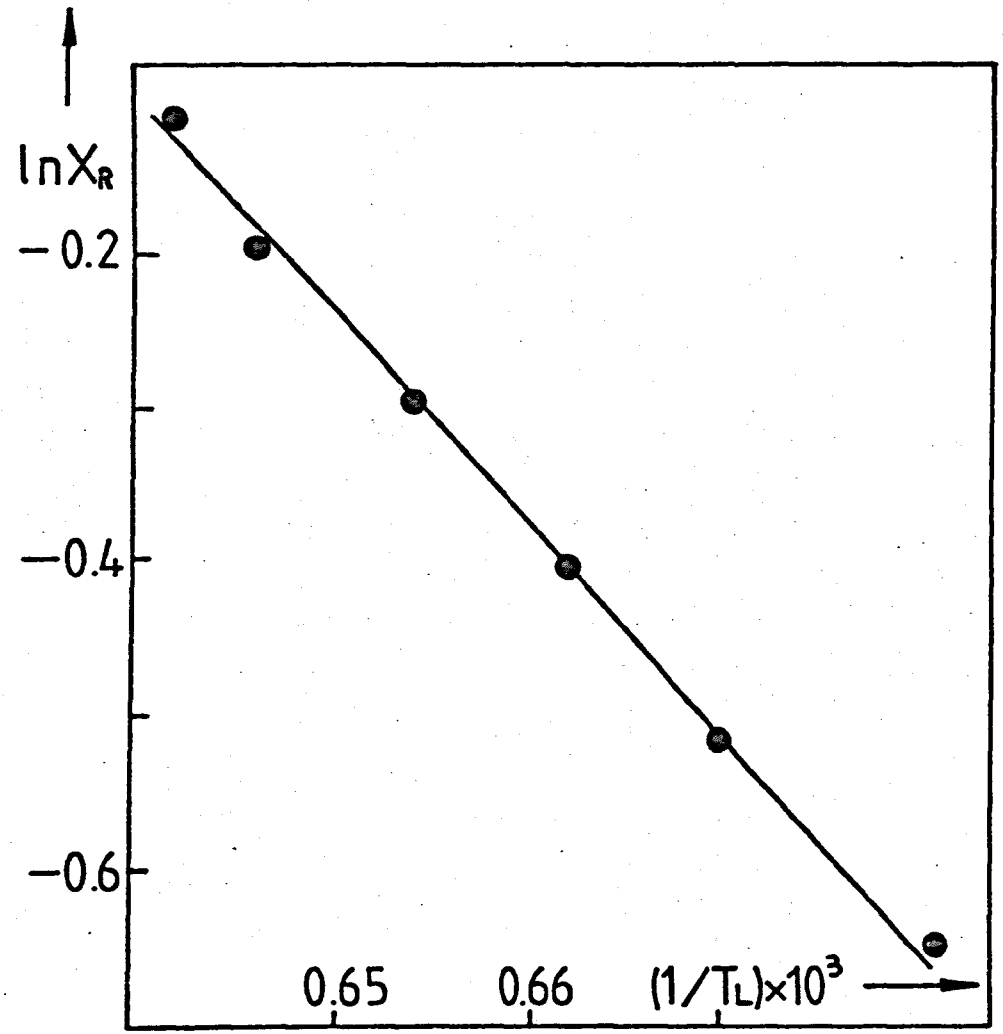

DATA FROM THE JOIN CS-NS ACCORDING TO REFERENCE (1.29)

$\frac{1}{T_L} \times 10^3$	X(mole% NS)	X_R	$\ln X_R$
0.640	33.3	1	0
0.642	40.	0.90	-0.1054
0.646	45.	0.825	-0.1924
0.654	50.	0.75	-0.2877
0.662	55.	0.675	-0.3930
0.670	60.	0.600	-0.5108
0.681	65.	0.525	-0.6444

Least squares slope = -13578.26

Least squares origen ordinate = 8.596

T_m = (1289°C) = 1562°C

X refers to mole fraction of NS in CS-NS system

X_R refers to mole fraction of $\frac{1}{3}(NC_2S_3)$ in $\frac{1}{3}(NC_2S_3)$-NS system

whereas the high form is rhombohedral (1.32). There is no data available on the heat of this transformation, however it will be shown later that it is much smaller than the heat of crystallization. The heat of fusion was found to be 21.8 kcal $mole^{-1}$ from solution calorimetry (1.33). Taylor and Hill (1.34) studied the NC_2S_3 crystals obtained as devitrification products from soda-lime glasses with a higher percentage of silica. The crystals were approximately cubic, gave refractive indices between 1.596 and 1.599 and were uniaxial positive with some lamellar twinning.

Frischat and Oel (1.35) studied the NC_2S_3 composition in both the glassy and crystalline states. For the glass they obtained a DTA Tg of 575°C and a density of 2.75 g cm^{-3}. For the crystal the density was 2.80 g cm^{-3}. The polymorphic transformation was at approximately 470°C. They studied Na^+ and Ca^{2+} self diffusion in the glass and crystalline materials as well as the specific electrical conductivity for both states. For example the activation energies for electrical conductivity were 25.9 kcal $mole^{-1}$ (250 - 600°C) for the glass and 26.2 kcal $mole^{-1}$ (470 - 900°C) for the crystal. The activation energies for self diffusion of ^{22}Na were 27.5 kcal $mole^{-1}$ (200 - 600°C) for the glass and 29.9 kcal $mole^{-1}$ (470 - 900°C) for the crystal. The results for ^{45}Ca self diffusion were 56.1 kcal $mole^{-1}$ (460 - 600°C) for the glass and 34.5 kcal $mole^{-1}$ (390 - 920°C) for the crystalline compound. Application of the Nerst-Einstein equation gave correlation factors f between 0.4 and 0.5 for the glass and the crystal which indicated an interstitialcy mechanism for ion movement.

Hammel (1.36) studied the kinetics of phase separation for a

glass of 13 Na_2O, 11 CaO and 76 SiO_2 (mole%). The nucleation induction for the process agreed well with the values calculated from equation (1.6). The agreement between theory and experiment for the homogeneous nucleation rates was initially considered to be excellent. However, (see Russell (1.37)) it was later noted that the theoretical nucleation rates were calculated with a diffusion coefficient 10^8 times smaller than the true value. Burnett and Douglas (1.38) studied the kinetics of liquid-liquid phase separation for 'glass 80' (80 SiO_2, 10 CaO and 10 Na_2O (mole%)) and 'glass 75' (75 SiO_2, 12.5 CaO and 12.5 Na_2O (mole%)). For glass 75 the initial stages could be described by a nucleation and growth mechanism. The maximum temperature at which nucleation could be detected was 660°C whereas the miscibility temperature was 687°C. The later stages could be described by a coarsening process. For glass 80 the initial separation process was much faster and only the coarsening stage was detected. It is interesting to note that on heating at temperatures between 690°C and the miscibility temperature (890°C) phase separation occurred as droplets whereas for lower temperatures an interconnected microstructure was detected. The highly interconnected microstructure broke up to form spherical particles for the longer heat treatments.

Strnad and Douglas (1.39) found that internal nucleation of NC_2S_3 and N_2CS_3 crystals occurs for compositions near the NS-CS join. They analysed the internal and surface crystal nucleation for glasses along the join S-NC. It was shown that surface nucleation occurred at smaller supercoolings than internal nucleation. Also they found non-steady state internal nucleation for the glass with 57.5 mole% SiO_2.

Finally they showed that the growth rates determined for internal crystals and for surface crystals were the same. Mukherjee and Rogers (1.40) studied the effect of CaF_2 on nucleation for two series of glasses in the CS field of the N-C-S system. One series also had Al_2O_3 as a component. It was found that the glasses tended to liquid-liquid phase separate before the crystallization. They found no correlation between the density of droplets and the density of crystals. The nucleation rates for the glasses containing Al_2O_3 had a maximum at 662°C irrespectively of the F content. Also the curves of nucleation rate vs temperature became increasingly broader for increasing F content. The nucleation rates for the glasses without Al_2O_3 were much lower than for the Al_2O_3 containing glasses. Kalinina and Filipovich (1.41) studied the nucleation of N_2CS_3 crystals in a glass of 50 SiO_2, 10.7 CaO and 38.9 Na_2O (mole%). The N_2CS_3 crystals were spherical. For this glass the dilatometric glass transition temperature was 460°C and the maximum steady state nucleation rate of 10^5 mm^{-3} min^{-1} was found at 485°C at which temperature the nucleation induction time was zero. They also quoted the crystal growth rate at 550°C as 0.13 μm min^{-1}. The higher value for the temperature of the maximum nucleation rate as compared with Tg was explained in terms of the large increase of the activation energy for diffusion (across the crystal-liquid interface) for temperatures approaching Tg. Dietzel (1.42a) studied growth rates in soda-lime-silica glasses for different primary phase fields. For example, in the tridymite field the lines of constant growth rate vs composition were almost parallel to the liquidus temperature (T_L) contours where it was observed that

for T_L increasing the growth rates also increased. Swift (1.42b) studied the effect on growth rates of different additions of MgO and Al_2O_3. For example for no MgO addition the devitrite (NC_3S_6) maximum growth rate was 0.31 mm hr^{-1} whereas for 2% MgO addition the maximum growth rate was decreased to approximately 0.11 mm hr^{-1}. Sadeghi (1.43) studied growth rates for compositions lying along the NC_2S_3-NS_2 join. The activation energies for growth, obtained in the low temperature range below the maximum rate, decreased on moving away from the NC_2S_3 composition. These values were 104, 90, 81 and 70 kcal $mole^{-1}$ for glasses with compositions of NC_2S_3, $N_7C_{10}S_{19}$, $N_2C_2S_5$ and $N_3C_2S_7$ respectively.

Other work relevant to the thesis

Maurer (1.44) studied the effect of gold catalyst particle size on the heterogeneous nucleation of lithium metasilicate from a glass of 81 SiO_2, 10 Li_2O, 5 K_2O, 4 Al_2O_3, 0.02 CeO_2, 0.15 Sb_2O_3 and 0.005 Au (wt.%). It was found that the Au particles had to reach a diameter of about 80 Å before the main crystalline phase could nucleate. It was suggested that nucleation was inhibited by strain between the crystalline embryo and the underlying gold substrate particles. Maurer also studied (1.45) crystal nucleation in a glass of 56 SiO_2, 20 Al_2O_3, 15 MgO and 9 TiO_2 (wt.%) using light scattering and X-ray diffraction. It was found that the initial isotropic regions (presumably formed by liquid phase separation) transformed to crystalline magnesium dititanate after heat treatments in the range 742 to 791°C.

Gutzow and Toschev (1.46) analysed the catalysing effect of Au,

Ag, Rh, Pt and Ir in a $NaPO_3$ glass. They observed induction times in the N_v vs time plots. Also they found that the catalytic power increased with increasing difference in thermal expansivities between glass and metal. It is interesting to note that when Pt was used as a catalyst the main crystalline phase ($Na_3P_3O_9$) tended to grow at the tip of the rod shaped Pt particles. Rindone (1.47) showed that Pt addition to a $Li_2O.4SiO_2$ glass increased the rate of $Li_2O.2SiO_2$ crystallization. Ohlberg et al (1.48) observed that in a SiO_2, TiO_2, Al_2O_3 and MgO containing glass 'magnesium dititanate' precipitated first from a previously phase separated glass and then catalysed the crystallization of silica O, the main crystalline phase. Neilson (1.49) found no evidence of phase separation prior to crystallization of ZrO_2 containing glasses in the SiO_2-Al_2O_3-MgO system. He concluded that the initial stages of crystallization, at high temperatures, may involve the homogeneous nucleation and growth of uniform crystallites of ZrO_2.

McMillan ((1.50) see also (1.51)) studied crystal nucleation in Li_2O-SiO_2 glasses containing P_2O_5. It was found that crystal nucleation was enhanced with P_2O_5 addition whereas the growth rates were decreased with P_2O_5 addition. Matusita and Tashiro (1.52) studied the effect of added oxides on the crystallization of $Li_2O.2SiO_2$ (LS_2). A constant heating rate was used up to a series of different temperatures. The total number of particles, thus produced, was inversely proportional to the increased glass viscosity at 485°C for Al_2O_3 and TiO_2 additions of 3 mole%. Ito et al (1.53) studied the crystallization process in LS_2. In the context of the present work it is parti-

cularly interesting to note that, when they plotted the length of the long axis of LS_2 crystals against time a considerable intercept with the time axis was found for measurements at lower temperatures. Filipovich and Kalimina (1.54) also found intercepts with the time axis when plotting the maximum size of LS_2 crystals against time. For example at 600°C the intercept was approximately 25 min., whereas at the same growth temperature the glass preheated at 450°C for 100 hr showed an intercept of 2 min. Matusita and Tashiro (1.55) measured nucleation rates in $Li_2O.2SiO_2$ glass. By identifying the activation energy for nucleation with that for viscosity, equation (1.4b) can be written as

$$I = \frac{A'}{\eta} \exp\left[- \frac{16\pi}{3} \frac{\sigma^3}{\Delta G^2} \frac{Vm^2}{kT} \right] \qquad (1.45)$$

where A' can be taken as a smooth function of temperature. From plots of $\ln(I\eta)$ against $\frac{1}{\Delta G^2 T}$, σ was found to be 196 erg cm^{-2}. Although they could not detect homogeneous nucleation for the $Na_2O.2SiO_2$ (NS_2) and $K_2O.2SiO_2$ (SK_2) glasses, they estimated σ for the latter glasses through a comparison with the LS_2 results. They found that $\sigma(LS_2) > \sigma(NS_2) > \sigma(KS_2)$ and concluded, from nucleation theory, that the negligible nucleation of NS_2 and KS_2 was due to the much smaller driving force ΔG for these glasses as compared with ΔG for LS_2. James (1.10) studied the kinetics of internal crystal nucleation in two Li_2O-SiO_2 glasses, the LS_2 and a glass containing 35.5 mole% LiO_2. Pronounced non-steady state behaviour was observed at lower temperatures. Also the nucleation induction time increased rapidly with decreasing temperature. Rowlands (1.7) studied the crystallization process in Li_2O-BaO-SiO_2

glasses along the $Li_2O.2SiO_2$-$BaO.2SiO_2$ (LS_2-BS_2) join. A much larger nucleation rate was found for a glass of composition BS_2 than for a LS_2 glass. The lower value of σ for BS_2 was the main reason for the observed behaviour. Ramsden (1.56) showed that for BaO-SiO_2 glasses in the range 25 to 35 mole% BaO, liquid-liquid immiscibility had a considerable effect on $BaO.2SiO_2$ crystal nucleation. The composition change, due to phase separation, altered both the thermodynamic driving force and the kinetic barrier for nucleation.

Boulos and Kreidl (1.57) reviewed the effect of H_2O on the properties of glasses. The viscosity of glass was reduced with increasing OH content, the effect being more pronounced in the transformation range than at the softening point. Also H_2O additions have been found to enhance liquid phase separation in sodium silicate glasses. Other literature on the effect of water additions will be fully discussed in a later chapter.

CHAPTER 2

EXPERIMENTAL TECHNIQUES

A variety of experimental techniques have been used during this work. Although a complete explanation of the principles of each technique employed would be outside the scope of this thesis, it was considered necessary to describe most of the techniques in reasonable detail.

2.1 Preparation of glasses

Glass homogeneity is very important in the fabrication of glass ceramics both industrially and on a laboratory scale. It may be assumed that reasonable homogeneity has been achieved when a uniform density of crystals and a uniform crystal size distribution are observed throughout the volume of the nucleated glass. Furthermore for the glasses studied in this work we have observed that crystal shape is dependent on changes in composition (see Chapter 3) and so changes in shape might indicate the presence of inhomogeneity.

In this thesis a fairly wide area of the soda-lime-silica system has been covered. A large portion of the work was concentrated on glasses around the NC_2S_3 composition. Compositions of higher silica content (up to 80 mole% SiO_2) were also studied. The nominal compositions of the glasses are listed in Table 2.1.

The glasses were prepared with the following analytical grade reagents:

Na_2CO_3, $CaCO_3$, NaF, CaF_2, $Na_2S.9H_2O$, P_2O_5, TiO_2, MoO_3, ZrO_2, Cr_2O_3, TiO_2, $AgNO_3$, CeO_2, Sb_2O_3, $PtCl_4$.

Glass G16 was prepared with Silquartz (SiO_2AR). The rest of

TABLE 2.1 NOMINAL COMPOSITIONS OF GLASSES MELTED

Glass Code	Nominal Compositions				
G1	$NC_2S_3 \equiv (Na_2O.2CaO.3SiO_2) \equiv N2C3S$				
G2	NC_2S_3				12.97 at% Na
G3	$97(NC_2S_3).3NaF$	,3 mol% NaF,0.36 wt% NaF,0.16 wt% F,13.10 at% Na			
G4	$94(NC_2S_3).6NaF$	,6 mol% NaF,0.73 wt% NaF,0.33 wt% F,13.29 at% Na			
G5	$82(NC_2S_3).18NaF$	,18 mol% NaF,2.53 wt% NaF,1.15 wt% F,14.05 at% Na			
G6	$45(NC_2S_3).55NaF$	,55 mol% NaF,12.66 wt% NaF,5.73 wt% F,18.28 at% Na			
G7	$97(C_2S_3).95.5Na_2O..3NaF$	,	0.36 wt% NaF,0.16 wt% F,12.98 at% Na		
G8	$97(NC_2S_3).3P_2O_5$	,3 mol% P_2O_5,1.2 wt% P_2O_5,			,12.83 at% Na
G9	$97(NC_2S_3).3TiO_2$	,3 mol% TiO_2,0.69 wt% TiO_2,			,12.90 at% Na
G10	$97(NC_2S_3).3MoO_3$	,3 mol% MoO_3,1.2 wt% MoO_3,			,12.83 at% Na
G11	$94(NC_2S_3).6MoO_3$	,6 mol% MoO_3,2.53 wt% MoO_3,			,12.66 at% Na
G12	$97(NC_2S_3).3ZrO_2$	,3 mol% ZrO_2,1.06 wt% ZrO_2,			,12.85 at% Na
G13	$94(NC_2S_3).6ZrO_2$	,6 mol% ZrO_2,2.2 wt% ZrO_2,			,12.71 at% Na
G14	$NC_2S_3 + H_2O$	,	,0.0404 wt% H_2O,		,
G15	$1.47Na_2O.0.319CaO.5.34SiO_2$	,		,	,
G16	NC_2S_3,(SiO_2 AR)	,		,	,
G17	NC_2S_3 Exact 1:2:3 ratio	,16.66 m% Na_2O,33.33 m% CaO,50.00 m% SiO_2	17.49 m% " ,31.65 wt% " ,50.86 wt% "		
G18	0.928N.2C.3S (+0.41 wt% Na_2O,0.28 wt% CaO)	15.65 m% Na_2O,33.74 m% CaO,50.61 m% SiO_2	16.44 wt% " 32.05 wt% " ,51.52 wt% "		
G19	1.072N.2C.3S (+0.41 wt% Na_2O,0.28 wt% CaO)	17.65 m% Na_2O,32.93 m% CaO, 49.41 m% SiO_2	18.52 wt% " ,31.25 wt% " , 50.23 wt% "		
G20	1N.1.911C.3S (+0.41 wt% Na_2O,0.28 wt% CaO)	16.92 m% Na_2O,32.33 m% CaO,50.75 m% SiO_2	17.74 wt% " ,30.67 wt% " ,51.59 wt% "		
G21	1N.2.091C.3S (+0.41 wt% Na_2O,0.28 wt% CaO)	16.42 m% Na_2O,34.33 m% CaO, 49.25 m% SiO_2	17.24 wt% " ,32.61 wt% " , 50.14 wt% "		
G22	1N.2C.2.882S (+0.41 wt% Na_2O,0.28 wt% CaO)	17.00 m% Na_2O,34.00 m% CaO,49.00 m% SiO_2	17.85 wt% " ,32.29 wt% " ,49.86 wt% "		
G23	1N.2C.3.122S (+0.41 wt% Na_2O,0.28 wt% CaO)	16.33 m% Na_2O,32.67 m% CaO,51.00 m% SiO_2	17.13 wt% " ,31.00 wt% " ,51.86 wt% "		
G24	NC_2S_3 + 0.2 wt% Pt				
G25	NC_2S_3 + 0.46 wt% Pt				
G26	NC_2S_3 + 0.50 wt% Ag_2O + 0.50 wt% Sb_2O_3 + 0.20 wt% CeO_2				
G27	NC_2S_3 + 1.12 wt% Al_2O_3 (+0.41 wt% Na_2O,0.28 wt% CaO)				
G28	NC_2S_3 + 2.00 wt% Al_2O_3 (")				
G29	NC_2S_3 + 2.0 wt% NaF + 3.5 wt% Al_2O_3 (+0.41 wt% Na_2O,0.28 wt% CaO)				
G30	NC_2S_3 + 4.0 wt% Al_2O_3 (+0.41 wt% Na_2O,0.28 wt% CaO)				
G31	1.70N.2.90C.5.4S	17.00 m% Na_2O,29.00 m% CaO,54.00 m% SiO_2	17.79 wt% " ,27.45 wt% " ,54.76 wt% "		
G32	G31 + 2.17 wt% ZrO_2				
G33	G31 + 2.8 wt% NaF				
G34	1.74N.2.46C.58S	17.40 m% Na_2O,24.60 m% CaO,58.00 m% SiO_2	18.14 wt% " ,23.21 wt% " ,58.64 wt% "		
G35	G34 + 2.17 wt% ZrO_2				
G36	G34 + 2.54 wt% NaF				

TABLE 2.1 (continued)

Glass Code	Nominal Compositions	
G37	1.78N.2.02C.6.2S	17.78 m% Na_2O,20.22 m% CaO,62.00 m% SiO_2 18.48 wt% " ,19.02 wt% " ,62.49 wt% "
G38	G37 + 6.5 wt% ZrO_2	
G39	G37 + 12.9 wt% ZrO_2	
G40	G37 + 6.0 wt% TiO_2	
G41	G37 + 12.9 wt% TiO_2	
G42	G37 + 9 wt% NaF	
G43	G37 + 9 wt% CaF_2	
G44	G37 + 9 wt% Na_2S	
G45	G37 + 6 wt% Cr_2O_3	
G46	G37 + 6 wt% Fe_2O_3	
G47	0.87N.2.93C.6.2S	8.70 m% Na_2O,29.30 m% CaO,62.00 m% SiO_2 9.13 wt% " ,27.82 wt% " ,63.06 wt% "
G48	G47 + 6 wt% ZrO_2	
G49	G47 + 12 wt% ZrO_2	
G50	G47 + 6 wt% TiO_2	
G51	G47 + 12 wt% TiO_2	
G52	G47 + 16.14 wt% TiO_2	
G53	G47 + 9 wt% NaF	
G54	G47 + 9 wt% CaF_2	
G55	G47 + 8.81 wt% Na_2S	
G56	G47 + 6 wt% Cr_2O_3	
G57	G47 + 6 wt% Fe_2O_3	
G58	0.93N.3.67C.5.4S	9.30 m% Na_2O,36.70 m% CaO,54.00 m% SiO_2 9.80 wt% " ,35.01 wt% " ,55.19 wt% "
G59	G58 + 6 wt% ZrO_2	
G60	G58 + 12 wt% ZrO_2	
G61	G58 + 6 wt% TiO_2	
G62	G58 + 12 wt% TiO_2	
G63	G58 + 9 wt% NaF	
G64	G58 + 9 wt% CaF_2	
G65	G58 + 9 wt% Na_2S	
G66	G58 + 6 wt% Cr_2O_3	
G67	G58 + 6 wt% Fe_2O_3	
G68	0.93N.3.67C.5.4S + 0.3 wt% Ag_2O + 0.3 wt% Sb_2O_3 + 0.1 wt% CeO_2	
G69	1.78N.2.02C.6.2S + 0.29 " + 0.29 " + 0.14 "	
G70	1.78N.2.02C.6.2S + 1.2 " + 1.0 " + 0.40 "	
G71	0.87N.2.93C.6.2S + 0.3 " + 0.3 " + 0.10 "	
G72	0.87N.2.93C.6.2S + 1.2 " + 1.0 " + 0.40 "	
G73	N.C.8S + 0.3 " + 0.3 " + 0.10 "	
G74	N.C.8S + 0.5 " + 0.5 " + 0.10 "	
G75	N.C.8S + 1.2 " + 1.0 " + 0.40 "	
G76	N.C.8S + 0.3 wt% Pt	

the glasses were prepared with Belgian sand (total Fe < 0.009 wt.%, total Al_2O_3 < 0.05 wt.%). This sand was first passed through a 60 B.S. mesh size; second, the sand was acid washed at 80°C with HNO_3 (25 vol.% in distilled H_2O) for a total time of three hours to reduce the levels of impurities. For the glasses G24, G25 and G76 Pt was added as $PtCl_4$ as follows: the required amount of AR $PtCl_4$ was first dissolved in 10 ml of AR HCl. The solution was poured uniformly onto the sand, previously weighed in a porcelain dish. Finally, the mixture was dried at 100°C.

The batches were dry mixed either in a rotating machine or by hand. The size of the batches ranged from 300 g to 700 g. Also, some of the batches were sintered to avoid losses (e.g. the glass with P_2O_5).

The glasses were melted in Pt 2% Rh crucibles with the exception of the glasses with Na_2S. The latter glasses were melted in Al_2O_3 crucibles. Electric furnaces were used throughout (SiC heating elements). All glasses were melted for approximately five hours with two hours total stirring time. The stirrers were made of Pt except when melting glasses with Na_2S where they were made of re-crystallized Al_2O_3. The melting temperature for glasses near the NC_2S_3 composition was 1380°C. Glasses with higher SiO_2 (and/or CaO) content needed higher melting temperatures. (For example for glasses G73 - 76 the temperature used was 1500°C). To avoid either surface crystallization or metallic precipitation the glasses were given a fast quench. This was achieved by pressing the molten glass either between two steel plates joined by a longitudinal hinge (glasses around the NC_2S_3 composition) or onto a

grooved steel block. Usually the glass plates broke into small pieces due to residual thermal stresses. However these pieces were large enough for further experiments. The quenching was needed to avoid nuclei formation during cooling from the melt.

The glasses were homogeneous and bubble free. Some samples of the glasses were also cast into a cylindrical shape. These were annealed by a standard procedure.

2.2 Nucleation and Growth Measurements

A good estimation of the number of crystal nuclei per unit volume produced at a given temperature and time of nucleation can be obtained (2.1) by giving the glass an additional growth treatment, and then analyzing the numbers of crystals present on a random cross-sectional plane through it. Crystal growth rates can be determined by analyzing the sizes of crystals on a random plane through the glass after isothermal growth treatment, as will be explained below.

2.2.1 Heat treatments

Kanthal or Platinum wound horizontal tube furnaces, controlled by either Eurotherm (type 072), Sirect or Ether controllers, were used. With the Eurotherm and Sirect controllers the temperature could be maintained constant to within $\pm\frac{1}{2}^{\circ}C$. The Ether controller was particularly useful to obtain finely controlled heating or cooling rates. The sample temperature was measured by placing a Pt/Pt:13Rh thermocouple over the sample. The specimens were contained in either platinum or ceramic boats.

For glasses around the NC_2S_3 composition a two stage heat treatment schedule was used. All the samples were heat treated in the temperature range 550°C - 700°C for a given time. The nucleated samples which consisted of approximately 5 mm x 3 mm x 3 mm pieces, were subsequently heat treated at a higher temperature to grow the nucleated crystals to observable dimensions. The growth temperature chosen was in the range 725°C - 740°C. The growth treatment time was approximately three minutes. The growth temperature was chosen with the requirement that the nucleation rate at this temperature was negligible. Also, the duration of the growth treatment was chosen to avoid overlapping of the particles after growth.

2.2.2 Optical microscope technique

The glass samples were cemented to glass slides with either pitch or Canada Balsam and ground with silicon carbide down to 1000 grade size. Sometimes 1000 grade alumina was used in the final grinding stage. They were then polished either with ceri-rouge or diamond paste (down to 0.1 μm grain size). After a good washing with hot water the samples were etched in a 0.001 vol.% HF 0.0004 vol.% HCl distilled water solution for 120 s. During this operation the solution was continuously stirred. Next the samples were cleaned in a ultrasonic machine using a dilute detergent solution. Finally they were given a rinse in distilled water and dried with a hair drier.

For glasses other than those near the NC_2S_3 composition solutions ten times stronger were required for the same etching time, to achieve sufficient contrast between crystals and glass in the optical microscope.

The samples were examined in a Leitz microscope at magnifications up to 500 times, using the eyepiece or up to 160 times on the photographic film. Photomicrographs were taken on FP4 film which was developed with a ultra fine grain developer. The negatives were printed following a standard technique. The crystal cross-section sizes were analysed from the prints with a graticule specially made by a photographic reduction process consisting of 35 circles covering the range 0.30 mm to 6.15 mm.

2.2.3 Method of analysis of micrographs

Nucleation densities were determined by estimating the number of particles per unit volume from the optical micrographs of the polished and etched surfaces of the samples given either the two stage nucleation and growth treatment or a single nucleation treatment. The following expression was used.

$$N_V = \frac{2}{\pi} N_A \left\langle \frac{1}{b} \right\rangle \qquad (2.1)$$

where : N_V = number of particles per unit volume, N_A = number of particle intersections per unit area, $\left\langle \frac{1}{b} \right\rangle$ = mean value of the reciprocals of the measured diameters for all circular intersections. This relation was developed by De Hoff and Rhines (2.2) for spherical particles. Also on certain occasions the simpler formula:

$$N_V = \frac{N_A}{b'} \qquad (2.2)$$

valid for constant particle size was used where N_V and N_A are as above and b' is the largest cross-section diameter. This latter approach was particularly useful for determining nucleation densities in systems where the particle shape was polyhedral (for

example cubic). In these cases b´ was a characteristic distance across the largest particle cross-section. For example for cubic crystals b´ was the side of the largest square cross-section.

Also, for samples where a distribution of particle sizes was expected a more laborious method developed by Saltykow (2.3) was used. With this method it is possible to estimate the particle densities in each size group as well as the total nucleation density (see Chapter 3).

Finally the optimum measuring conditions were established. These were a large number of particle intersections (typically 300) as large a maximum intersection diameter as possible and a reasonably large total area. This can be seen by considering the source of errors in the simple equation (2.2) using $N_A = \frac{N}{A}$ and $A = xy$ where N is the total number of intersections, A the plate area and x,y typical linear dimensions, it is found:

$$\frac{\Delta N_V}{N_V} \approx \frac{\Delta N}{N} + \frac{\Delta x}{x} + \frac{\Delta y}{y} + \frac{\Delta b'}{b'}$$

For example for $N = 300$, $\Delta N = 2$

$x \approx y = 150$ mm

$\Delta x = 1$ mm $= \Delta y$

$b' \approx 5$ mm

$\Delta b' \approx 0.1$ mm

$$\frac{\Delta N_V}{N_V} \approx 0.6\% + 0.6\% + 2\% = 3.2\%.$$

So the main conclusion is that for a large number of particles (N) and large total area (A) the particle intersection diameter must be measured very carefully in order to reduce the error in

N_V. An estimation of ΔN_V using equation (2.1) is given in Appendix A1.

2.2.4 Crystal growth measurements

Crystal growth measurements were carried out by measuring the diameter of maximum size cross-sections of spherical particles. In the case of cubic particles the measurements were made of the side of the largest square cross-section. The glasses were previously nucleated for a short time (approximately 20 minutes) to obtain enough nuclei to be able to choose the largest cross section in a large population of crystals.

2.3 Electron Microscopy

2.3.1 Transmission electron microscopy (TEM)

Transmission electron microscopy was used to study the morphology of the crystals internally nucleated in the glasses. It was also used to measure crystal growth rates in samples heat treated isothermally and to follow metallic precipitation (Pt or Ag) in glasses. Although some work was carried out with the replication technique only the results obtained using thin glass foils will be described here.

Thin glass sections for TEM were prepared using the ion beam thinning technique. First a thin parallel foil of glass (approximately 15 μm thick) was prepared by grinding as follows. The glass sample was cemented to a glass slide with Canada Balsam. Six other pieces of glass (200 μm thick) were also cemented to the slide and surrounding the first sample. The

sample and glass pieces were then ground flat with 600 grade SiC and polished with cerirouge. Next the sample was turned over and cemented to a new slide together with 100 μm thick glass pieces as before. Grinding was carried out until the edges of the 100 μm glass pieces started to disappear. After this stage the grinding was continued with 3 μm diamond until the final 15 μm thickness was obtained.

The foil was removed from the slide using methanol and cemented to a copper grid. The grid was placed in a vacuum chamber on a rotating plate in an Edwards IBMA2 ion beam thinning machine. After a vacuum pressure of 10^{-4} Torr was reached the glass was bombarded with Ar ions until a small hole appeared in the sample. The thin foils were examined either in a Hitachi HU-11A instrument (at 75 kv and 100 kV), Phillips 301 electron microscope (at 75 kv and 100 kv) or in a high voltage (1000 kv) electron microscope at the Swinden Laboratories of the British Steel Corporation in Rotherham (at 800 kv and 1000 kv).

The magnifications used were checked with a replica of a diffraction grating with 2160 lines per mm. For electron diffraction the camera length was obtained from diffraction patterns of MoO_3 crystals.

2.3.2 Scanning electron microscopy (SEM)

The scanning electron microscope used was a Cambridge M4 (25 kv) instrument. This microscope was useful in obtaining nucleation densities of glasses which were only given a single stage nucleation treatment. It was also used for examining fracture

surfaces, as well as the effects of etching on glasses.

The etched samples were prepared as described in the optical microscope section. The samples were then stuck to flat cylindrical holders with silver paint, and a thin layer of gold was evaporated onto their surfaces to produce a conducting path for the electrons. The magnifications were checked by placing a droplet (on the specimen surface) of a fine liquid dispersion of spheres of polystyrene latex of known size (0.527 μm diameter with standard deviation ±0.0027 μm).

2.4 Differential Thermal Analysis (DTA) Measurements

This technique provided information on the glass transformation temperature Tg ('DTA Tg'), heats of crystallization, heat of melting and also heats involved in polymorphic transformations.

A Standata 625 instrument was used with a high temperature platinum wound furnace. A heating/cooling rate of 10°C/minute was used for most runs. The reference material was AR calcined alumina. Glass for examination was crushed in a percussion mortar and ground in an agate mortar to 300 B.S. mesh size. The powder was compressed around the tip of the platinum crucible in the DTA apparatus. The same amount of glass was always used (300 mg). By measuring the area under the melting peaks for AR NaF and AR NaCl the heats of fusion for the unknown compositions were estimated. By a similar procedure the heats of crystallization were also obtained. The heats of fusion of the standard materials were taken from JANAF tables (2.4).

2.5 Liquidus Temperature (T_L) Measurements

The T_L value was measured by the quenching technique. This method consisted in holding the glass, contained in a small platinum crucible, at constant temperature for approximately one hour and quenching it very rapidly (approximately at 700 - 1000°C s^{-1}) by dropping the crucible into water (or oil). Then the specimen was examined either visually or in a low power microscope for the presence (or absence) of crystals. The use of more sensitive instruments capable of detecting crystals such as the X-ray diffractometer or the petrological microscope (polarized light) was not found to be necessary in this work. By simply looking for the presence of opalescence due to crystallization it was possible to determine the liquidus temperature very accurately. The increase or decrease in T_L for different glasses was also checked in a hot stage microscope illuminated with polarized light. However the values of T_L were not as accurate as determined by the quenching experiment.

Although a horizontal tube furnace was occasionally used most of the work was carried out in a specially mounted vertical tube furnace. Two lateral guides (see Figure 2.1) allowed the furnace to be moved up and down very quickly. A platinum wire frame held the crucible and the thermocouples (touching one side of the crucible) in exactly the same position for every run. A Eurotherm controller ensured a control of the temperature to ±0.2°C. The temperature was measured with a Cambridge potentiometer using an ice/water cold junction.

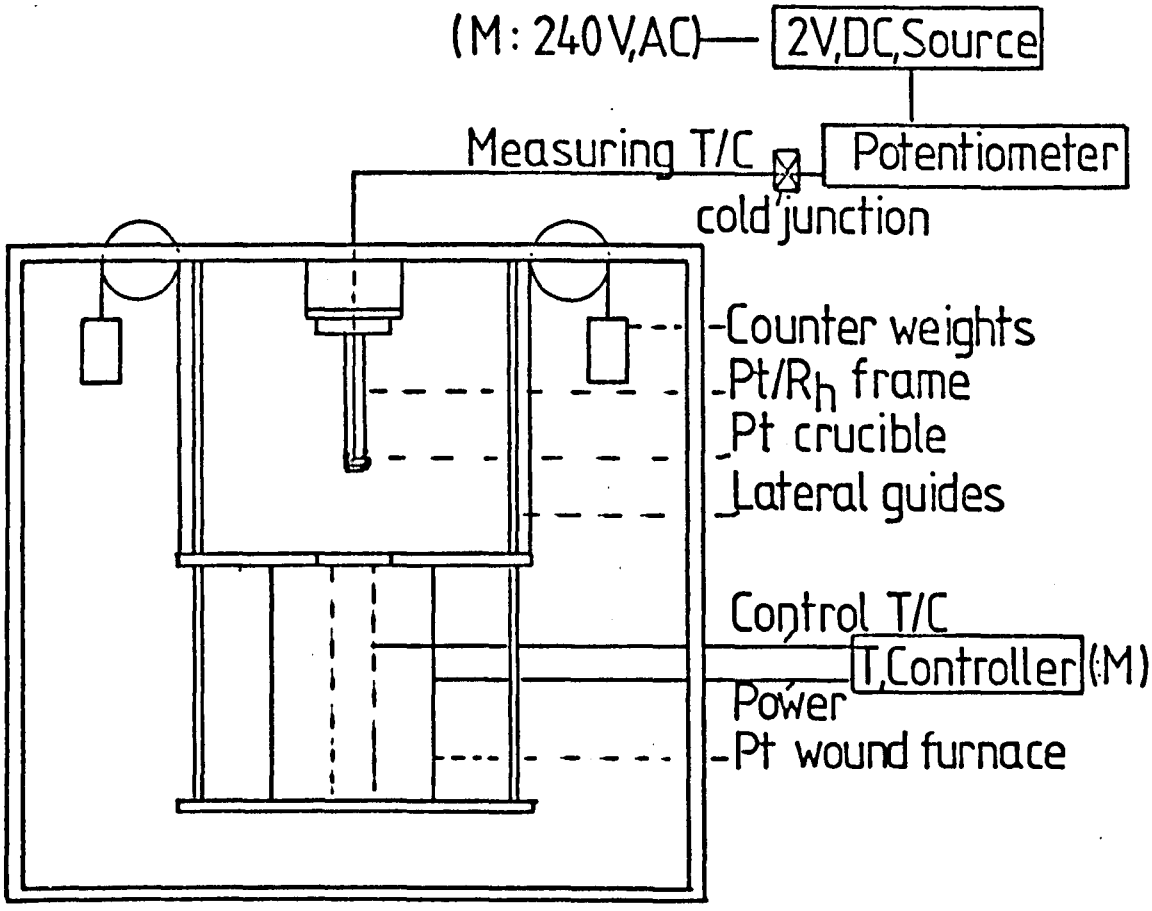

FIGURE 2.1 Quenching furnace for liquidus temperature(T_L) measurements.

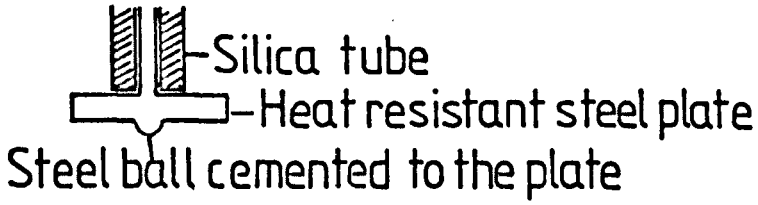

FIGURE 2.2 Penetrator assembly used in the penetration viscometer.

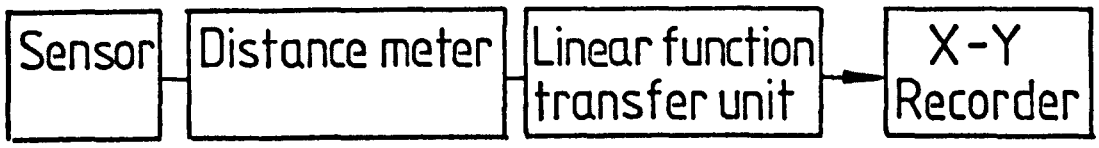

FIGURE 2.3 Block diagram for displacement measurements (penetration viscometer)

2.6 X-Ray Diffraction

A Philips diffractometer was used to determine the crystalline phases present after the heat treatments. Samples were heated at the maximum nucleation temperature for 60 minutes followed by 15 minutes at 730°C to crystallize them. They were then crushed and passed through a 300 B.S. mesh sieve.

X-ray diffraction was also used to estimate the percentage of crystals precipitated in certain glasses. This was achieved by either measuring the area under a particular X-ray peak or its height and comparing with the corresponding peak obtained from a known mechanical mixture of crystal and glass. The standard NC_2S_3 crystalline material was prepared from very pure AR Na_2CO_3, AR $CaCO_3$ and silquartz. Each component was weighed to an accuracy of 10^{-4} g. The components were ground and mixed in an agate mortar. The mixture was placed in a platinum crucible with lid and held in the temperature range 900°C - 1000°C for 7 hours. The whole sintered mass was removed from the crucible, crushed and ground to 300 B.S. mesh size and X-rayed to assess the formation of the NC_2S_3 compound. After repeating this process five times the area and heights of the peaks reached maximum values. The final 300 B.S. mesh size powder (always kept in a desiccator) was diluted with glass and vigorously mixed in a small glass bottle. Ten dilutions in the range 10% to 100% crystals were prepared. The diffraction angles covered were from $2\theta = 19°$ to 28° where two well separated NC_2S_3 peaks, suitable for measurements, could be found.

2.7 Chemical Analysis and Chemical Durability Test

2.7.1 Chemical analysis

A number of the glasses melted were analysed for Na_2O, CaO and F. For Na_2O determination either the flame photometry technique or the Triple Acetate method was used. The latter was preferred for obtaining absolute Na_2O content. For Cao determination either the flame photometry technique or the EDTA titration method was used, the titration technique being preferred. For the glass NC_2S_3 the level of Al_2O_3 and total Fe were determined by EDTA titration and the thioglycolic acid method respectively. The fluoride contents in certain of the glasses were estimated from a technique which involved measuring the potential difference between two electrodes, one as reference electrode and the other a F^- permeable electrode of lanthanum fluoride crystal. Further details are given in Appendix A2.

The details of the measurements as well as the preparation of the reagents are given in Appendix A2.

2.7.2 Chemical durability

Chemical durability was assessed by measuring the amounts of SiO_2 and Na_2O extracted from glass grains after attack by known solutions for one hour at 98°C. The glasses and corresponding glass ceramics (crystallized by a two stage heat treatment schedule) were crushed in a mortar and passed through a 35 B.S. mesh sieve and retained in a 45 B.S. mesh sieve. The grains were washed with AR Acetone and stored in desiccators. Accurately known amounts of the grains were transferred to 50 ml volumetric flasks

and 40 ml of either distilled water or 0.024 M HCL (prepared from AR 36.5% HCl, i.e. approximately 12 molar HCl) acid solution was added to them. Next the tops of the flasks were covered with polythene and the flasks transferred to a autoclave containing water for one hour at approximately 98°C. After the flasks had cooled to room temperature, they were filled with the appropriate attacking solution to the graduation mark. The extracts were then collected and the grains were washed with acetone and dried for further use. The extracts were analysed for Na_2O by flame photometry and for SiO_2 by the colorimetric molybdate method. The results for various glasses and corresponding glass ceramics are presented in Chapter 5. The SiO_2/Na_2O determinations are described in Appendix A3.

2.8 Viscosity Measurements

It was considered necessary to obtain viscosity data in order to provide a better understanding of the crystal nucleation and growth process in soda-lime-silica glasses. For glasses which crystallize fairly easily it is very difficult to obtain accurate viscosities in the range 10^2 - 10^8 Poises. However it is often possible to obtain data at high temperatures, i.e. for viscosities in the 10 - 10^3 P. range by the rotating cylinder method and at low temperatures (i.e. 10^9 - 10^{13} P) by the penetration, parallel plate or beam bending methods. In this section the theory and operation of three viscometers are described.

2.8.1 Penetration viscometer

The technique consists in measuring at a given temperature the penetration into the glass by a rigid sphere, under the action of a load.

2.8.1a Apparatus

Briefly the apparatus (2.5) consisted of:

(i) A tube furnace (Kanthal wound) which could be moved in a vertical direction.

(ii) A silica column on which the sample was placed but separated from the column by a platinum (or mica) foil.

(iii) A penetrator made of silica tubing clamped to a saddle on which the weights were placed. The ball was inserted into the lower end of the penetrator as shown in Figure 2.2. After several trials it was decided to use a total load of 2256.5 g and a ball of diameter 0.3175 cm to obtain deformations corresponding to vicosities in the 10^9 -10^{13} P. range.

(iv) A measuring device: a capacitance sensor with accessories as shown in Figure 2.3. The calibration was such that a penetration of 0.1 cm corresponded to 10 cm in the y axis or the recorder.

(v) An hydraulic system allowing the saddle to be released.

The furnace temperature was controlled to ±0.2°C and the measuring thermocouple (chromel/alumel) was placed touching the steel plate very near to the sample. The annealed glass samples were cylinders of approximately 1 cm diameter and 0.3 cm thickness. They were ground flat and parallel with several grades of SiC and

polished with cerirouge. The polishing was necessary in order to inspect the samples for visible cracks, cords, etc.

2.8.1b Operation

With the sample and furnace in position a stabilisation period between 15 and 30 minutes was required. Although 30 minutes stabilisation was usually employed, a time of only 15 minutes was allowed for samples tested at high temperatures where the danger of crystallization was greater. During the holding time the y axis magnification was checked and the x axis pen speed set according to the total deformation expected. Then the saddle was loaded and simultaneously both the recorder and the stop watch started. The sample temperature was measured at regular intervals during the course of the experiment. At the end of the experiment the time on the stop watch was recorded, the saddle lifted and the sample was taken out. It was found useful to examine the specimens for crystals after the viscosity measurements. (See section 2.2.3). A typical deformation curve is shown in Figure 2.4.

2.8.1c Theory

This is based upon the solution from elasticity theory in which the rate of strain and the coefficient of viscosity have been substituted for the strain and the rigidity modulus respectively (2.6). Thus for a viscous body penetrated by a sphere of infinite rigidity at constant temperature, the following formula can be obtained:

$$\frac{dy}{dt} = \frac{3P}{16a\eta} \qquad (2.3)$$

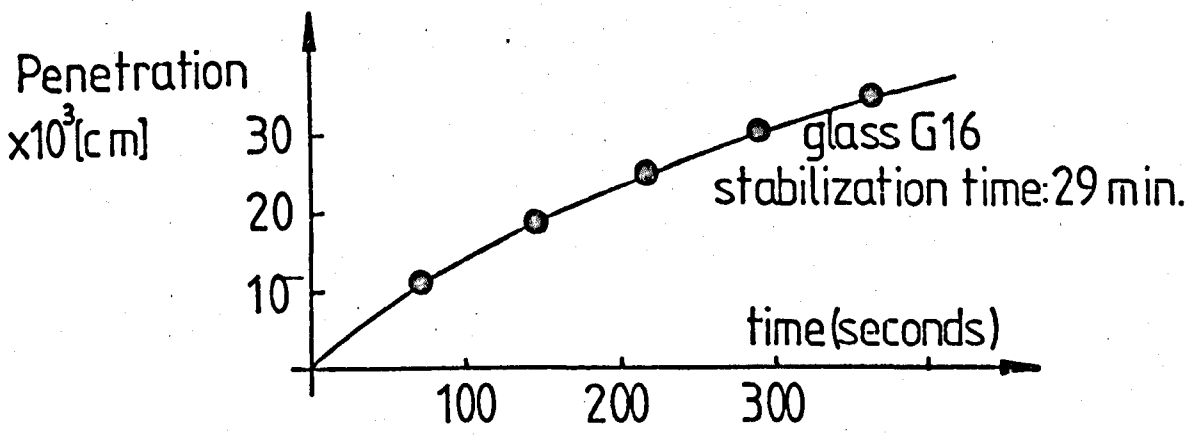

FIGURE 2.4 Typical deformation curve for penetration viscometer.

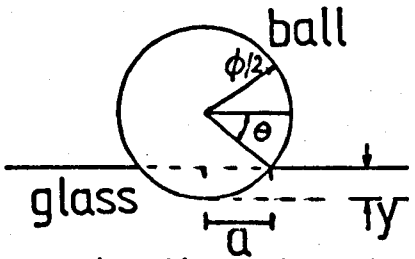

FIGURE 2.5 Ball penetrating glass (penetration viscometer)

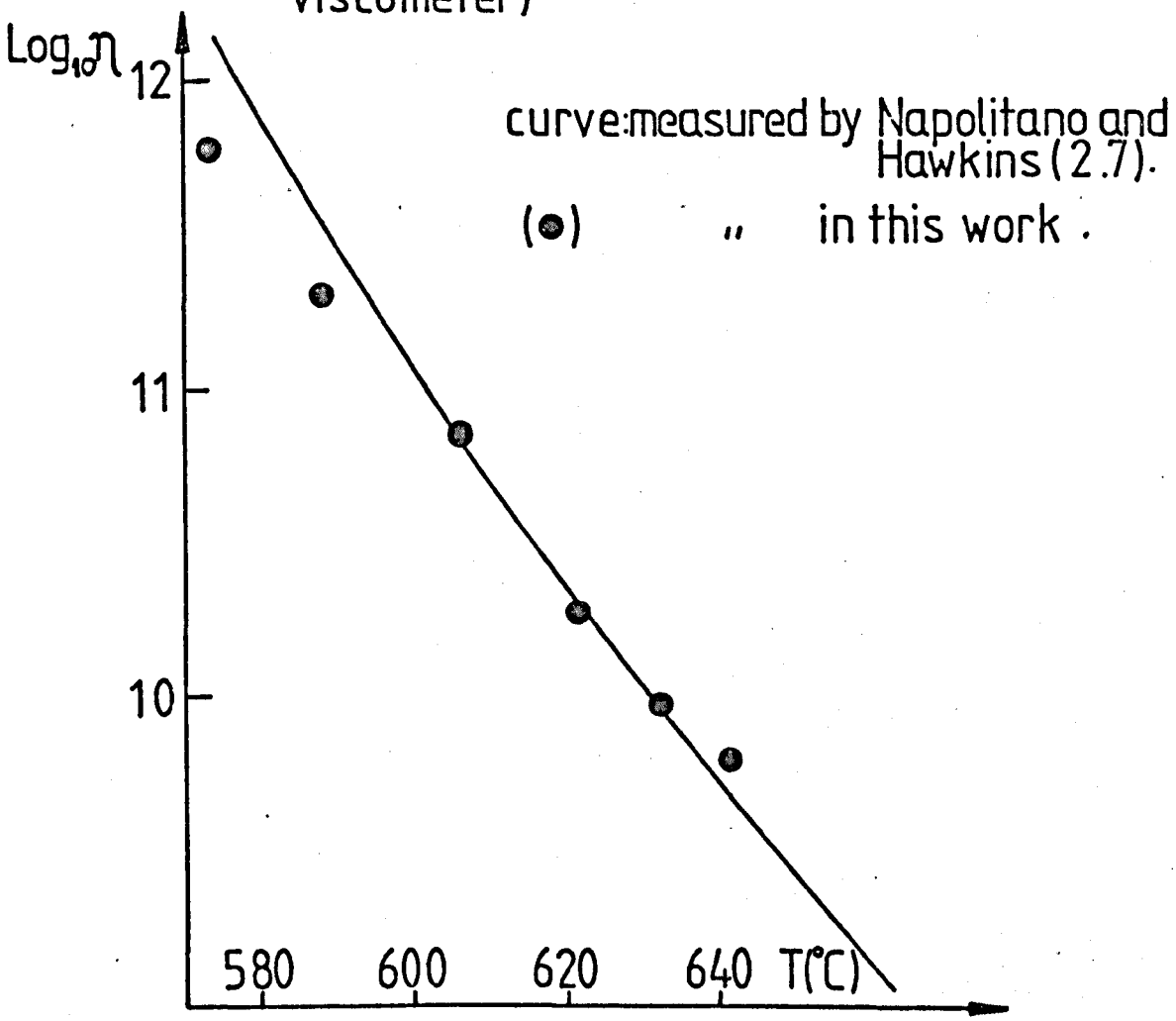

FIGURE 2.6 Comparison of $\log_{10}\eta$ vs. T(°C) data obtained in (2.7) and in this work.

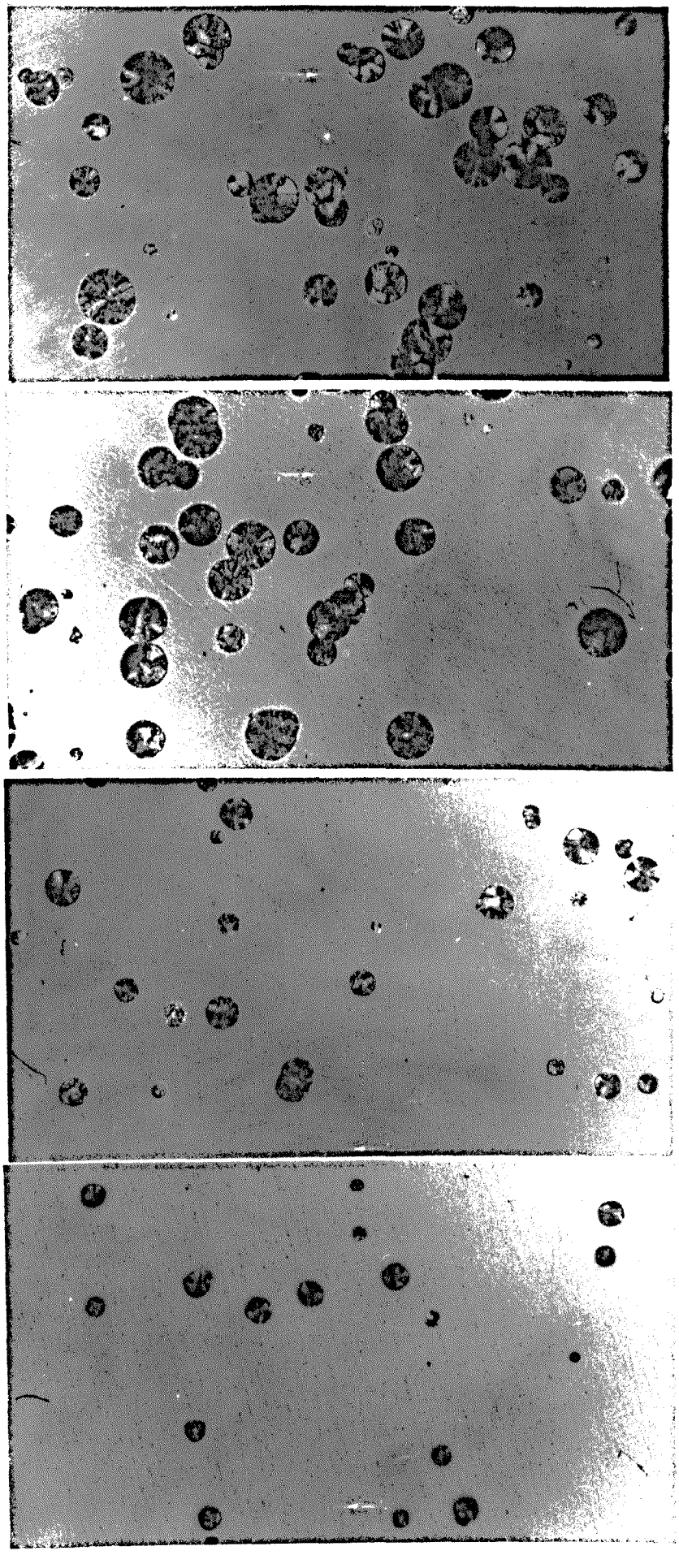

Figure 3.22a, b, c and d

Optical micrographs of G2 heated at 654°C for (a) 90, (b) 75 (c) 60 and (d) 45 min. Mag X504.

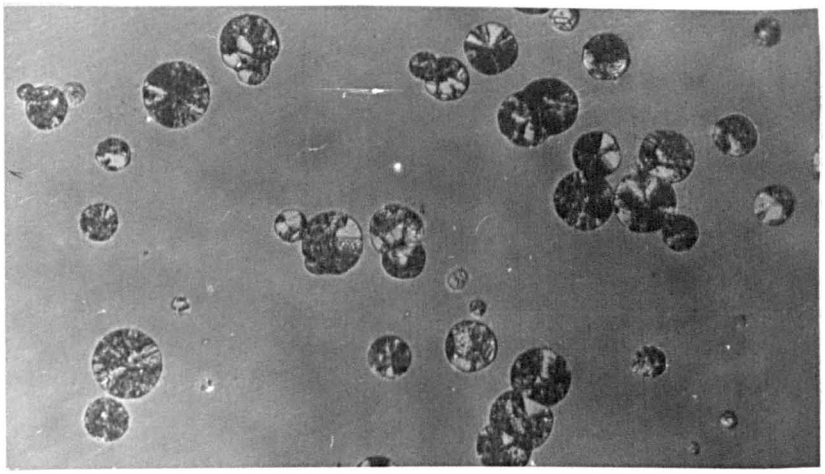

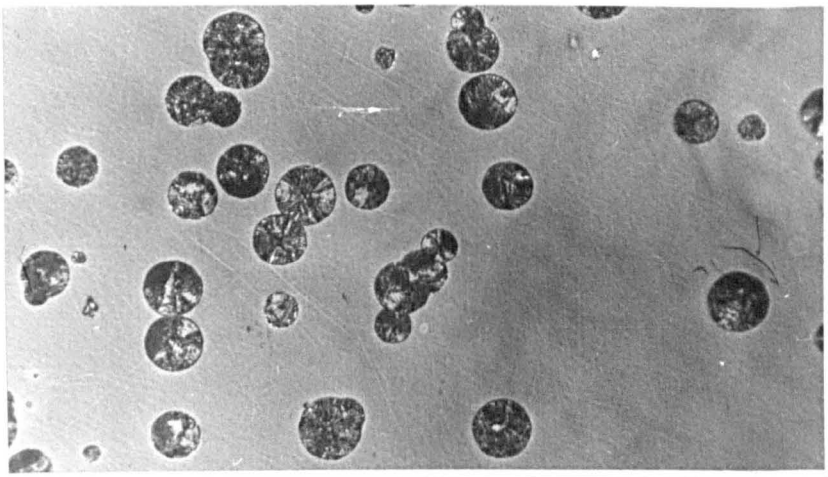

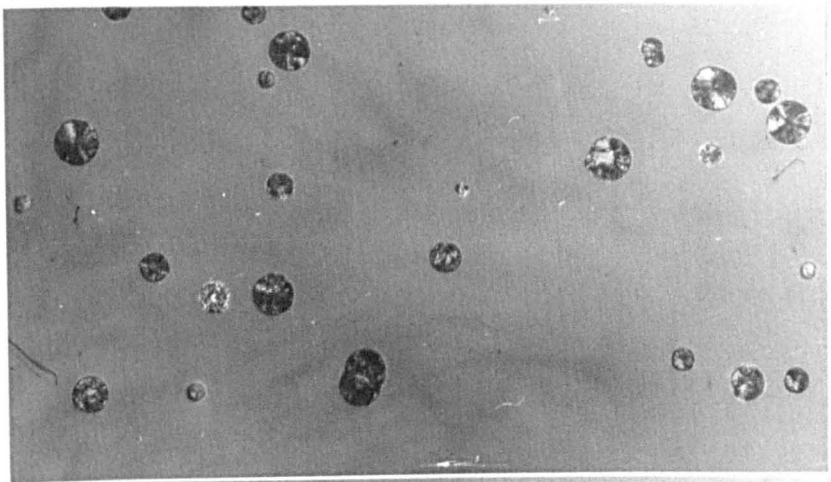

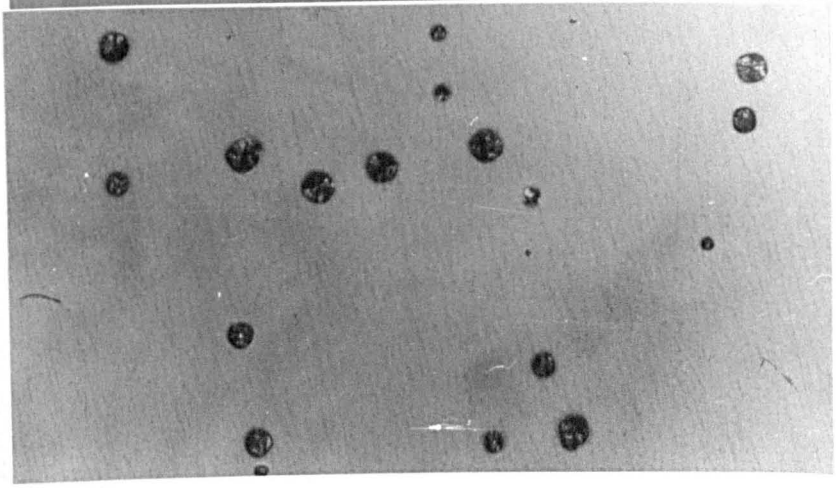

FIGURE 3.34 $Log_{10}\eta$ AS A FUNCTION OF TEMPERATURE FOR G19, G18 and G17

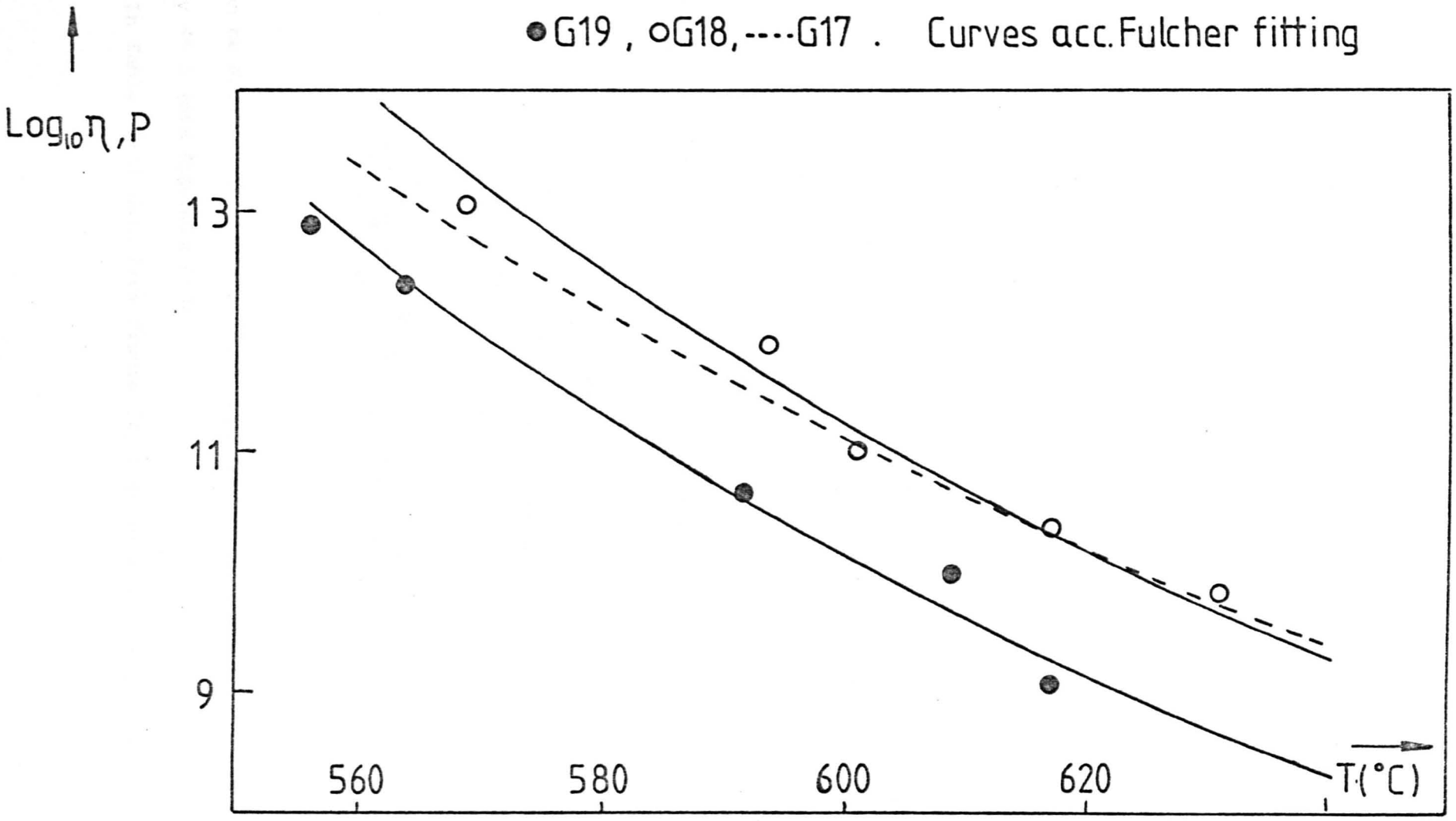

where (see Figure 2.5) $\frac{dy}{dt}$ is the rate of penetration (cm s^{-1}), P is the total load in dynes, $a = \sqrt{\phi y - y^2}$ is the radius of the circle of contact in cm, ϕ is the ball diameter and η is the coefficient of viscosity in Poise. For small deformations $y << \phi$, so

$$a \simeq \phi^{\frac{1}{2}} y^{\frac{1}{2}} \tag{2.4}$$

By integrating equation (2.3) and rearranging we obtain:

$$\frac{9Pt}{32\eta\phi^{\frac{1}{2}}} = y^{3/2} \tag{2.5}$$

Although this was the basic formula used, equation (2.3) can be <u>exactly</u> solved even for deformations not satisfying equation (2.4). The viscosity coefficient can be calculated, by using the following change of variables (see Figure 2.5).

$$y = \frac{\phi}{2} - \frac{\phi}{2}\sin\theta \; ; \; \begin{matrix} y = 0, \; \theta = \pi/2 \\ y = y, \; \theta = \theta_y \end{matrix} \; ; dy = -\frac{\phi}{2}\cos\theta d\theta \; ; \; a = \sqrt{\phi y - y^2} = \frac{\phi}{2}\cos\theta$$

Hence equation (2.3) can be integrated to give:

$$\frac{9}{32}\frac{P}{\eta\phi^{\frac{1}{2}}}t = \frac{3}{32}\phi^{3/2}[\pi - 2\theta_y - \sin 2\theta_y] \tag{2.6}$$

or

$$\frac{9}{32}\frac{Pt}{\eta\phi^{\frac{1}{2}}} = \frac{3}{16}\phi^{3/2}[\frac{\pi}{2} - \theta_y - \frac{2}{\phi}(1 - \frac{2y}{\phi})(\phi y - y^2)^{\frac{1}{2}}] = f(y) \tag{2.7}$$

It can be shown that equation (2.6) approaches equation (2.5) when $y << \phi$ (see Appendix A5d).

In Table (2.2) data from Figure (2.4) is presented together

TABLE 2.2 FROM DATA IN FIGURE 2.4

t (seconds)	y (cm x 10^3)	$y^{3/2}/t$ (x 10^6) from equation (2.5)	$f(y)/t$ (x 10^6) from equation (2.7)
73	11.4	16.67	16.31
145.9	19.0	17.95	17.59
218.9	25.1	18.17	17.81
291.8	30.9	16.61	18.12
364.8	35.7	18.49	17.85
Mean value		17.98×10^{-6}	17.53×10^{-6}
σ_{n-1} standard deviation		0.78×10^{-6}	0.70×10^{-6}
$\log_{10}\eta$		10.788	10.798
$\Delta(\log_{10}\eta)$		0.004	0.004

$$\sigma_{n-1}^2 = \frac{\Sigma x^2 - \frac{(\Sigma x)^2}{n}}{(n-1)}$$ where n = number of values (5)

with the viscosities calculated from equations (2.5) and (2.7), where $\frac{9}{32}\frac{P}{\phi^{\frac{1}{2}}}$ was taken as 1.104×10^6 (cm)$^{3/2}$ Poise s^{-1}. It can be seen that (i) the differences between equation (2.5) and the more exact equation (2.7) are greater for the larger deformations, (ii) the more accurate equation (2.7) gives less scatter than the equation (2.5) as shown by the values of the standard deviations given in the table. However, the $\log_{10}\eta$ values are very close for both equations. The relative errors $\frac{\Delta\eta}{\eta}$ and $\frac{\Delta\log_{10}\eta}{\log_{10}\eta}$ obtained using equation (2.5) can be estimated as 0.044 and 0.0044 respectively (see Appendix A5e).

In Figure (2.6) the $\log_{10}\eta$ values vs temperature for the NBS 710 soda-lime-silica standard glass measured in this work are presented as well as the values measured by Napolitano and Hawkins (2.7). Although at low temperatures the penetration viscometer tends to give lower values compared with the data from reference (2.7), it is seen that in the viscosity range $10^{9.5}$ to 10^{11} Poises the agreement is excellent. Hence it was decided to use the $\frac{9}{32}\frac{P}{\phi^{\frac{1}{2}}}$ value quoted above for all the measurements.

In general the calculations for either equation (2.5) or (2.7) were performed on a computer. A least squares fit of the $y^{3/2}$ or $f(y)/t$ values was obtained, from which the viscosity coefficient was calculated.

A fit to the viscosity vs temperature data for each glass was obtained by using the Fulcher equation:

$$\log_{10}\eta = A + \frac{B}{T-T_o} \qquad (2.8)$$

where A, B and T_o are adjustable parameters and $T(T_o)$ is in °C. The Fulcher constants were calculated in a computer through a least squares fit of the following function obtained from equation (2. 8) by substituting

$$T_i = x_i \quad ; \quad \log_{10}\eta_i = y_i \quad ; \quad B - A\,T_o = C$$

$$f_i = x_i y_i = Ax_i + T_o y_i + C \tag{2.9}$$

where x_i and y_i are assumed to be independent variables. In the least squares method values of the constants A, T_o and C are required such that the quantity

$$\varepsilon = \sum_{i=1}^{N} \varepsilon_i^2 = \sum_{i=1}^{N} [f_i - (Ax_i + T_o y_i + C)]^2$$

is a minimum where N is the number of experimental points. By partially differentiating ε with respect to the constants A, T_o and C and equating to zero the following system of linear equations is found:

$$\begin{aligned}
A\sum_{i=1}^{N} x_i^2 + T_o\sum_{i=1}^{N} x_i y_i + C\sum_{i=1}^{N} x_i &= \sum_{i=1}^{N} x_i f_i \\
A\sum_{i=1}^{N} x_i y_i + T_o\sum_{i=1}^{N} y_i^2 + C\sum_{i=1}^{N} y_i &= \sum_{i=1}^{N} y_i f_i \\
A\sum_{i=1}^{N} y_i + T_o\sum_{i=1}^{N} y_i + CN &= \sum_{i=1}^{N} f_i
\end{aligned} \tag{2.10}$$

This system can be solved by the Cramer rule if the determinant D given by

$$D = \sum_{i=1}^{N} x_i^2 \Big(N\sum_{i=1}^{N} y_i^2 - \Big(\sum_{i=1}^{N} y_i\Big)^2\Big) - \sum_{i=1}^{N} x_i y_i \Big(N\sum_{i=1}^{N} x_i y_i - \sum_{i=1}^{N} x_i \sum_{i=1}^{N} y_i\Big)$$

$$+ \sum_{i=1}^{N} x_i \Big(\sum_{i=1}^{N} x_i y_i \sum_{i=1}^{N} y_i - \sum_{i=1}^{N} x_i \sum_{i=1}^{N} y_i^2\Big)$$

is different from zero. For example the constant A is given by:

$$A = \frac{1}{D}\Big[\sum_{i=1}^{N} x_i f_i \Big(N \sum_{i=1}^{N} y_i^2 - \Big(\sum_{i=1}^{N} y_i\Big)^2\Big) - \sum_{i=1}^{N} x_i y_i \Big(N \sum_{i=1}^{N} y_i f_i - \sum_{i=1}^{N} y_i \sum_{i=1}^{N} f_i\Big)$$

$$+ \sum_{i=1}^{N} x_i \Big(\sum_{i=1}^{N} y_i \sum_{i=1}^{N} y_i f_i - \sum_{i=1}^{N} f_i \sum_{i=1}^{N} y_i^2\Big)\Big] \qquad (2.11)$$

The computer program (in Fortran) to calculate A, B and T_o is given in Appendix A4. This program was checked with the viscosity data published in Reference (2.8). For example the Fulcher constants obtained by us from the data presented by laboratory D (Reference (2.8) p.87) for the soda-lime-silica glass were: $A = -3.604$, $B = 8616.95$ and $T_o = -92.52$ whereas the values quoted by laboratory D (by a least squares fit) were: $A = -3.586$, $B = 8566$ and $T_o = -89$.

2.8.2 Rotating cylinder method

The method, as used in this work, consisted of (i) sharing the viscous liquid between two concentric cylinders and (ii) measuring the torque required (on the inner cylinder) to maintain a constant relative velocity.

2.8.2a Apparatus

The apparatus is shown schematically in Figure 2.7. The three suspension wires allow the torques produced by different viscous drags to be measured. The inner and outer cylinders (made of platinum) are cemented concentrically to sillimanite tubes. The top tube has a mirror and a threaded metallic rod where the

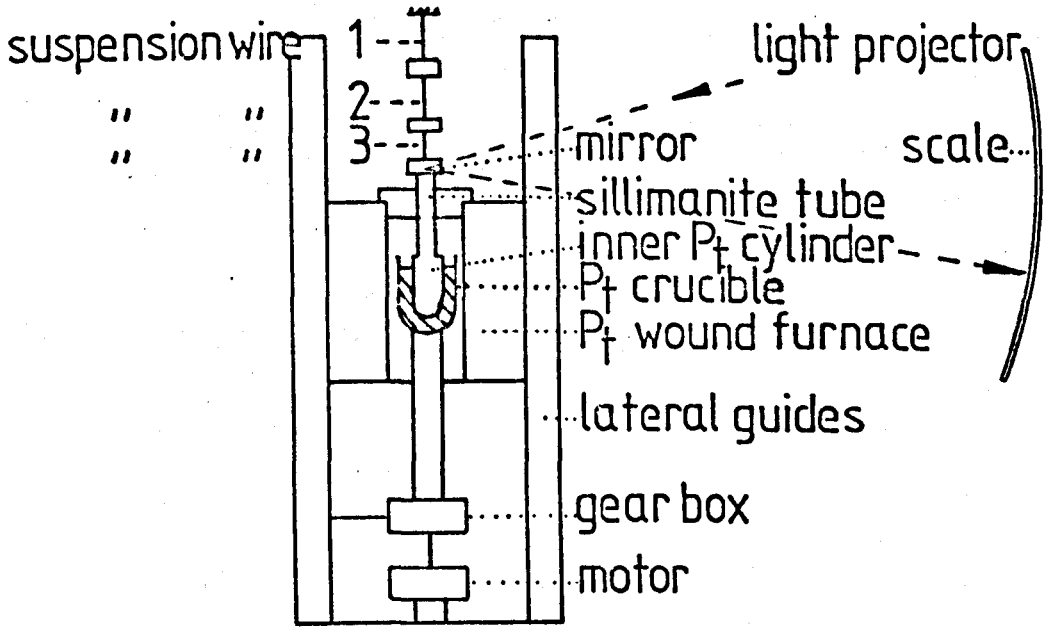

FIGURE 2.7 Rotating cylinder apparatus.

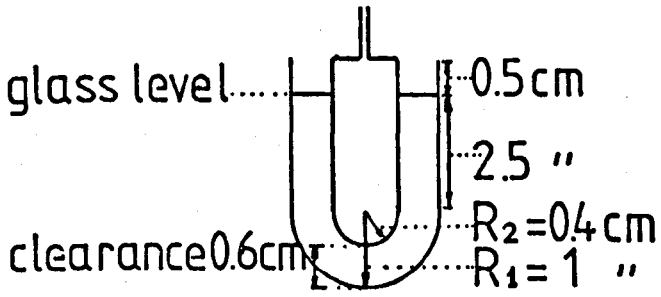

FIGURE 2.8 Inner and external cylinder configuration.

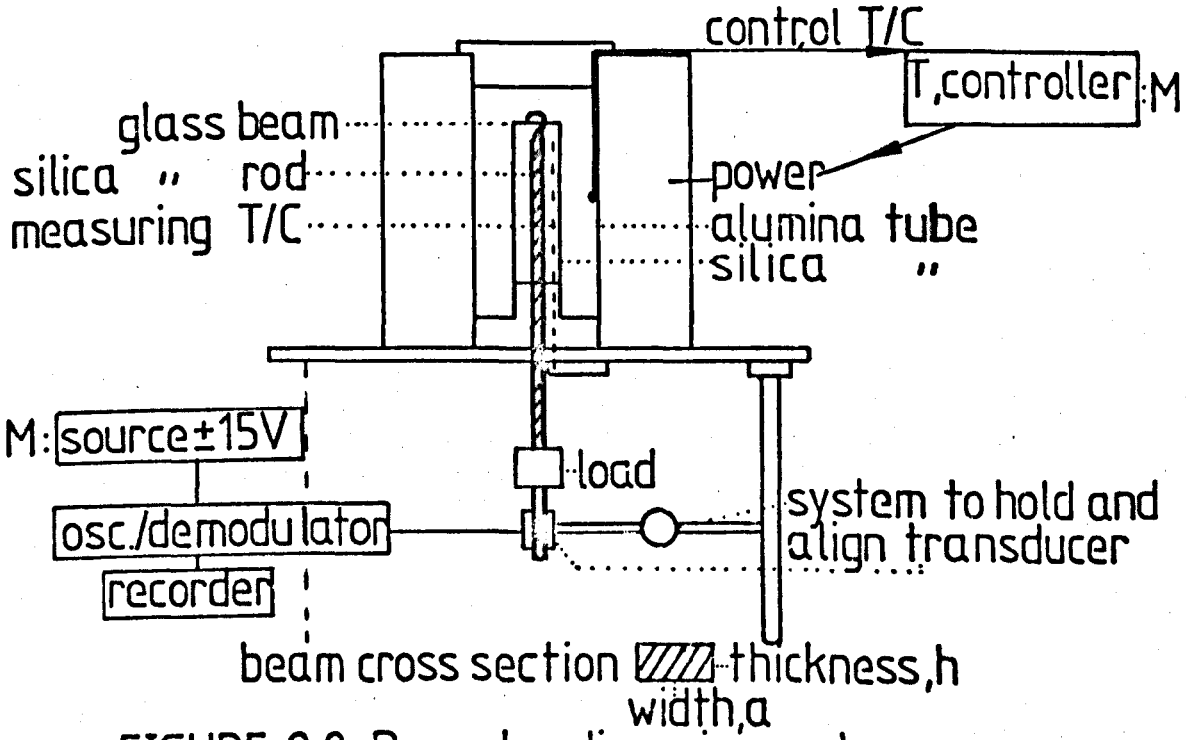

FIGURE 2.9 Beam bending viscometer.

calibration plate cylinders (see section 2.8.2c) can be attached. The measuring thermocouple is inserted into the top tube and passed through to the bottom tip of the inner cylinder. The working characteristics (top and bottom clearances) are shown in Figure 2.8. The platinum wound furnace (three independent windings) can be moved up and down. The bottom sillimanite tube is clamped to a chuck joined to a gear box; this in turn is connected to an electric motor which can rotate in either direction.

2.8.2b Operation

After the desired temperature was obtained a stabilization period of approximately 30 minutes was allowed. The temperature was measured and the thermocouple disconnected. The motor was started and the light spot position on the scale recorded. It was possible to record for the same settings, the deflection to the left as well as the deflection to the right (with the motor reversed) and the equilibrium zero (see section 2.8.2c). Reasonable large deflections (approximately 15 cm on the scale) were produced by choosing both the correct number of suspension wires and rotating crucible speed. Then the temperature was recorded again and the average between the two readings (before and after) was taken as the temperature of the measurement. A typical chart of readings is shown in Appendix A5a. The average between left and right deflection was taken as the deflection to be used in calculating the torque.

2.8.2c Theory

It can be shown (2.9,2.10) that the viscosity coefficient at constant temperature is given by:

$$\eta = \frac{T}{C\Omega L} \tag{2.12}$$

where (see Figure 2.8) T is the torque in ($g\ cm^2\ s^{-2}$) ; $C = 4\pi\frac{R_1^2R_2^2}{R_1^2-R_2^2} = 2.394\ cm^2$, R_2 and R_1 are the internal and external radii; Ω the angular velocity ($1.564\ rad\ s^{-1}$) and $L = L_C + \frac{2}{3}R_2 = 2.767$ cm. The torque T can be expressed as:

$$T = K\theta \tag{2.13}$$

where K is the torsional rigidity of the suspension wire(s) and θ is the angle of twist. The constant K can be determined for each wire combination by the use of two flat cylinders of different sizes and masses. Then

$$K = 4\pi^2\ \frac{(I_1-I_2)}{(t_1^2-t_2^2)} \tag{2.14}$$

where $I = \frac{1}{2}\ m\ r^2$, m the mass of cylinder in g and r the radius of cylinder in cm, t is the period of oscillation of the rotating pendulum consisting of the wire and weight attached. The values for K_j (j = number of wires) are given in Appendix A5b. By inserting the values previously stated and the K_j constants in the formula $\eta = \frac{K\theta}{C\Omega L}$ we obtain

for $K = K_1$ $\eta = 99.13\ (g\ cm^{-1}\ s^{-1}\ rad^{-1}) \times \theta\ (rad)$

for $K = K_2$ $\eta = 622.50 \times \theta$

for $K = K_3$ $\eta = 1829.43 \times \theta$

where θ is calculated from $\langle \theta \rangle = \frac{(\theta_R - \theta_{cR}) + (\theta_{oL} - \theta_L)}{2}$ where $\theta_i = \frac{x_i}{U}$, x_i is the deflection on the scale and U is the mirror scale distance; θ_{oR} (θ_{oL}) is the zero deflection just before the right (left) deflection was measured (see Appendix A5a). In Appendix A5c the results of measurements on the NBS 710 standard glass are quoted using equation (2.13). Also given are values obtained from

$$\eta = \alpha_R \theta \qquad (2.15)$$

using an averaged value of α_R in the range 1398 - 1490.5°C obtained by inserting the accepted viscosities of the NBS 710 glass in (2.15) and the experimental deflections measured with the three wire arrangement. This averaged value of α_R was found to be $\langle \alpha_R \rangle = 143.14$. It can be seen that over the whole temperature range the agreement with the NBS data is good showing the uniform behaviour of the instrument at different temperatures (column 6, Appendix A5c). It can also be seen from the same table that the best agreement between the values calculated from the physical constants and the published data for the standard glass is found in the working mode of three wires. For one wire and two wires the results are a little higher.

2.8.3 Beam bending technique

This method consists in measuring the mid-point deflection of a glass beam supported at each end.

2.8.3a Apparatus

The apparatus is shown schematically in Figure 2.9. The

sample glass beam rests in grooves in the top of a silica glass tube. A silica glass hook is placed on the centre of the beam, the hook being connected to a glass rod and transducer. The load is applied to the other end of the transducer armature. The furnace temperature is regulated by a Eurotherm controller to an accuracy of 0.2°C. The measuring thermocouple can be moved vertically as well as horizontally (this was convenient for checking the transverse temperature profile of the furnace). The transducer holder has a mechanical device which can align the transducer parallel to the apparatus axis. The deflections are measured with a LVDT (Linear variable differential transformer) unit and an oscillator/demodulator device (D5/200 and D11 RDP Electronics respectively); a typical sensitivity is 2 mV per V per 0.001". The output signal is fed to a standard recorder.

2.8.3b Theory and operation

It can be shown (2.11) that the glass viscosity at constant temperature is given by

$$\eta = \frac{gL^3}{2.4I_c v}\left[M + \frac{\rho AL}{1.6}\right] \qquad (2.16)$$

where η is given in Poise, g is the acceleration due to gravity (cm s^{-2}), I_c the cross sectional moment of inertia (cm^4), v the mid-point deflection rate of the beam (cm min^{-1}), M the load in g, ρ the glass density in g cm^{-3}, A the cross sectional area of the glass beam (cm^2) and L is the support span (cm). I_c is given by $\frac{ah^3}{12}$ (see Figure 2.9). The sample was placed in the

grooves on the silica tube (furnace already at testing temperature). The hook was placed in the middle of the beam, the furnace closed, the transducer attached and the load placed over a laboratory jack. After a given time had elapsed (approximately 20 minutes) the weight (approximately 300 g) was released and the deflection recorded vs time. Temperature readings were recorded during the experiment.

To illustrate the capabilities of this system to measure viscosities let us calculate the expected total mid-point beam deformation at a given time for a square cross section beam of glass G2 with the following characteristics: density ρ = 2.75 g cm^{-3}, a = h = 0.2 cm, M = 300 g, L = 5 cm. Then from eqn. (2.16) $\eta = \frac{1.149 \times 10^{11}}{v}$

so for $\eta = 10^{12}$ P $\quad v = 0.1149$ cm/minute; $\quad x = 11.49$ mm

$\eta = 10^{13}$ P $\quad v = 0.01149$ " ; $\quad x \simeq 1.15$ mm

$\eta = 10^{14}$ P $\quad v = 0.001149$ " ; $\quad x \simeq 0.115$ mm

where x is the total mid-point beam deflection in 10 minutes. Although measurements can be made in the range $10^{12.5}$ P to 10^{14} P it should be remembered that appreciable η vs time behaviour is expected in the glass transformation range (2.12). For example for a glass rapidly cooled through the transformation range the viscosity at temperatures in the transformation range is expected to increase as the heat treatment time increases (fictive temperature higher than temperature of measurement).

2.9 Other Experimental Techniques

2.9.1 Water content determination by infra-red (IR) spectroscopy

The method consists in adding the amounts of water which contribute to each wave length band in the IR absorption spectra following the technique developed by Scholze (2.13).

2.9.1a Apparatus

A Grubb-Parson double beam spectrophotometer was used. The wave length range covered was from 2 μm to 5 μm. After the spectrum was recorded the following corrections were made: (i) Subtract the background curve which in theory should be zero and may be considered as instrumental behaviour in the particular range of wave lengths; (ii) Discount the approximately constant level of absorption due to general scattering of the sample and reflectivity from sample surfaces. Then the curves were analysed in a Digital Curve Resolver to obtain the main peaks which matched with the normal peak positions in glasses due to OH^- vibrational groups. The peak heights of the assumed Gaussian peaks as well as the peak positions were used in the water content calculations.

2.9.1b Theory and calculation

Following Scholze (2.13) water is incorporated into the structure of glass and gives rise to absorption bands of different strengths. Scholze confirmed that the 2.75 to 2.95 μm and 3.35 to 3.85 μm bands were due to OH^- groups associated with the structure and found that the 4.25 μm band was not due to CO_3^{2-} but water. He showed that the positions of the bands do not depend on water content but

in general depend on the glass structure itself. Also the greater the wave length of a particular OH band the stronger is the hydrogen bridge bond which joins to a neighbouring oxygen and the smaller the interval between the two oxygens linked by the hydrogen bridge bond. Table 2.3, taken from Scholze (2.13), compares the O-O distances and the bond energies for some OH bands that occur in glasses. In general with increasing wave length of a band, the bond energies are larger and hence the absorption increases and the extinction coefficient increases. This fact plus the assumption that the extinction coefficients depend mainly on the wave length and do not vary with glass composition provide the basis of the method of determining the quantity of water in glasses.

As mentioned above the experimental IR curve is corrected for reflection losses and absorption in the sample and background absorption from the air and is resolved into the main peaks. For example in Figure 2.10 the uncorrected absorption curve for the G14 glass direct from the spectrophotometer is shown and in Figure 2.11 the result are shown after applying the corrections. In Table 2.4 the detailed data and corrections are given for the G14 glass.

The transmitted intensities for these peaks are read off and using the extinction coefficients determined by Scholze the water concentration C can be calculated from the Lambert-Beer equation:

$$C = \frac{1}{\varepsilon d} \log \frac{I_o}{I} \qquad (2.17)$$

where C is concentration in mole cm^{-3}, ε is the extinction coefficient in cm^2 $mole^{-1}$, d is the thickness of the glass in

TABLE 2.3 ABSORPTION BANDS DUE TO OH FROM REFERENCE (2.13)

Position of the OH^- bands (μm)	O-O distance (Å)	Bond energies (kcal/mole)
2.75	3.20	0.0
2.85	2.95	2.2
3.55	2.65	6.8
4.25	2.55	10.0

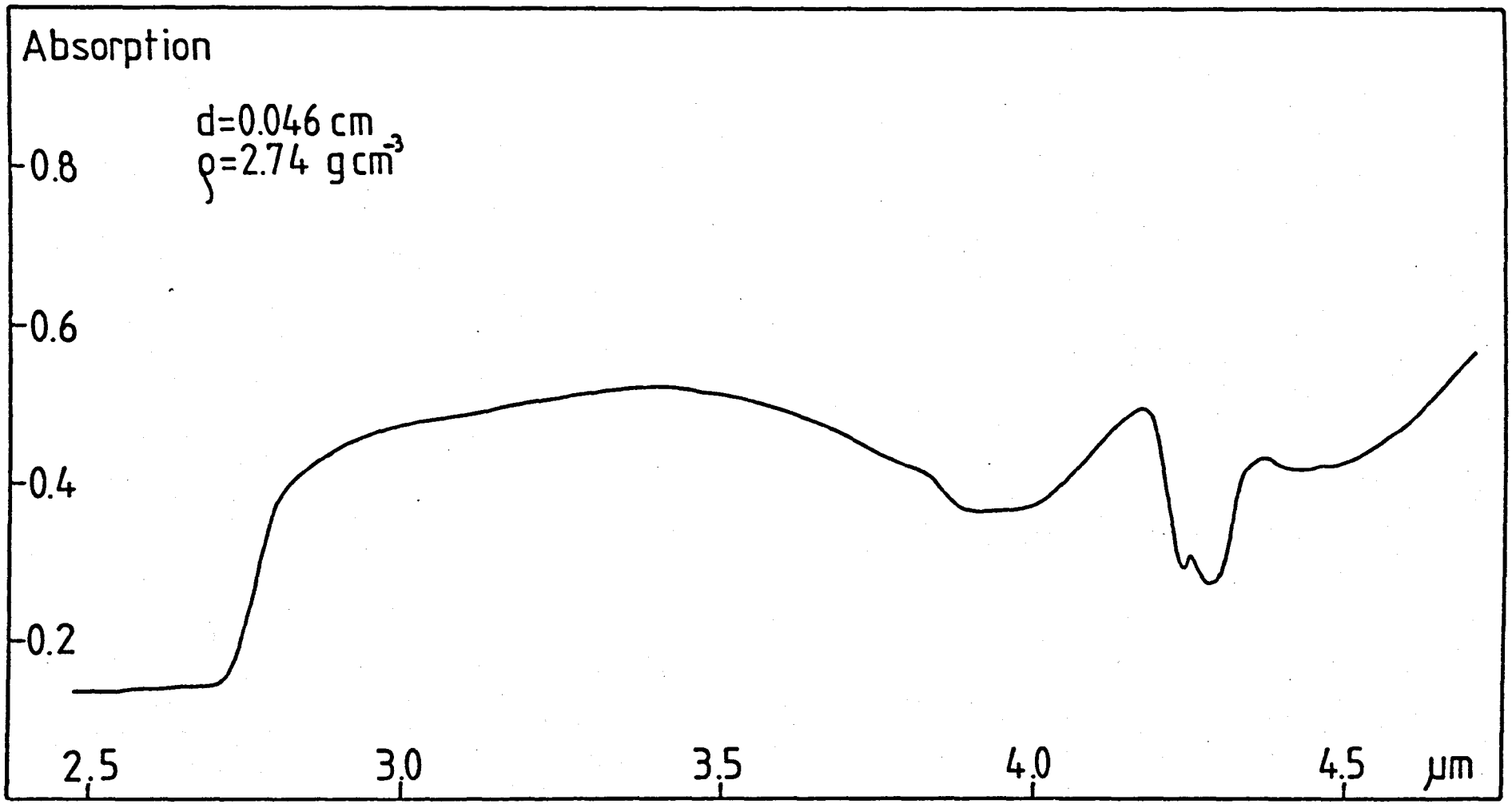

FIGURE 2.10 ABSORPTION AS A FUNCTION OF WAVELENGTH FOR GLASS G14

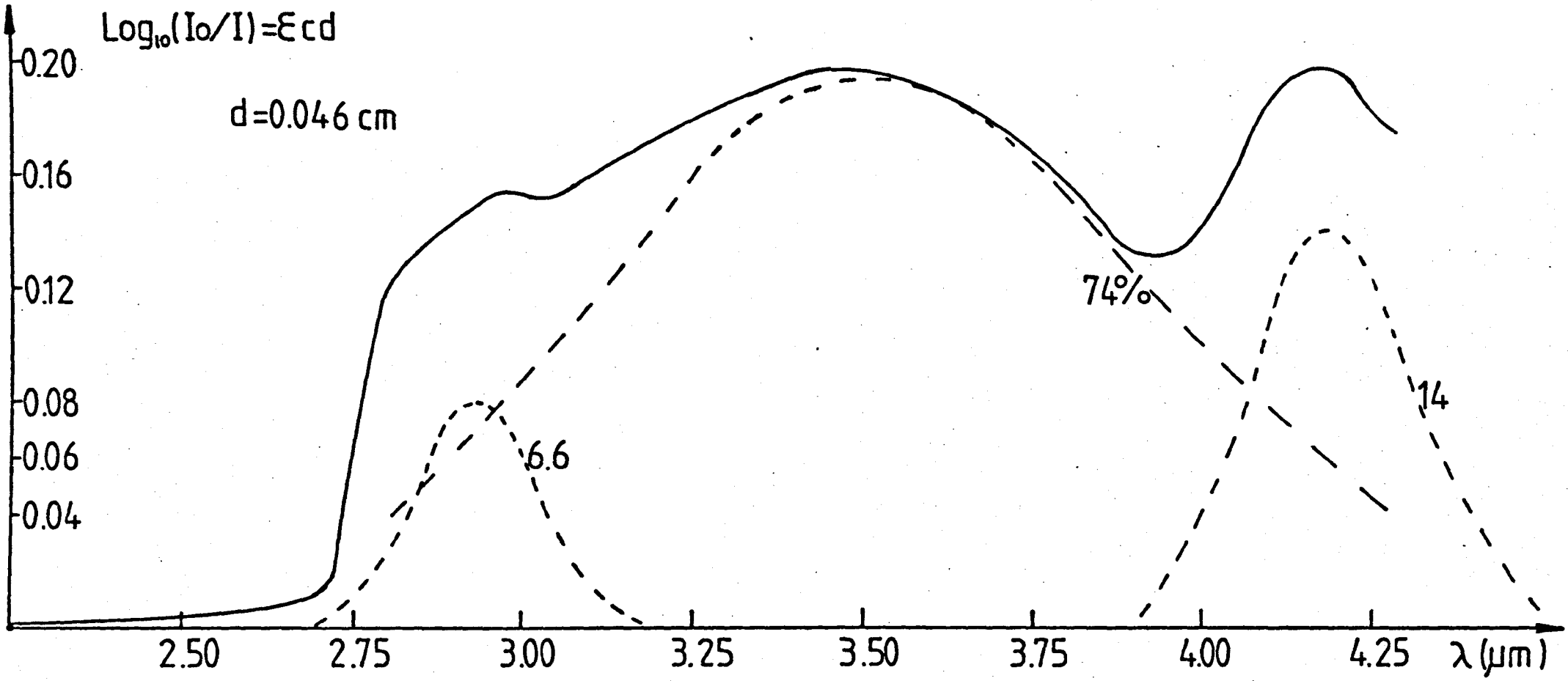

FIGURE 2.11 CORRECTED INFRA RED SPECTRA FOR GLASS G14

TABLE 2.4 DETAILED IR ABSORPTION AND CORRECTION DATA FOR G14 IN THE 2.6 TO 2.9 μm RANGE

Wave Length (μm)	Air Absorption	G14 Absorption	Correction Air Absorption	t_A Correction G14	$\log_{10}\left[\frac{100}{100-t_A}\right]$
2.600	8.5	21.0	12.50	1.50	0.0066
2.625	7.5	20.0	12.50	1.50	0.0066
2.650	7.2	20.0	12.80	1.80	0.0079
2.675	7.0	20.0	13.00	2.00	0.0088
2.700	7.0	20.5	13.50	2.50	0.0109
2.725	7.0	24.0	17.0	6.0	0.0268
2.750	7.0	30.0	23.0	12.0	0.0555
2.775	7.2	38.0	30.8	19.8	0.0958
2.800	7.0	42.0	35.0	24.0	0.1192
2.825	7.0	43.5	36.5	25.5	0.1278
2.850	7.2	44.5	37.3	26.3	0.1325
2.875	7.5	45.5	38.0	27.0	0.1367
2.900	7.2	46.1	38.9	27.9	0.1461

cm and I_o,I are the incident and transmitted intensities respectively. To obtain C in wt.% the following conversion formula can be used.

$$C(wt.\%) = C(mol/litre) \times \frac{1.8}{\rho} \qquad (2.18)$$

where ρ is the glass density. The densities were determined using the Archimedes method

$$\rho = \left[\frac{W_a}{W_a - W_w}\right] \qquad (2.19)$$

where W_a and W_w are the weights of the sample in air and water respectively. The corrected density is given by:

$$\rho_c = \rho(\rho_w - \sigma) + \sigma \qquad (2.20)$$

where ρ_w and σ are the densities of water and dry air at 27.5°C and 757.5 mm Hg Barometric pressure, which are

$$\rho_w = 0.9978 \text{ g cm}^{-3}$$

and $$\sigma = 1.157 \times 10^{-3} \text{ g cm}^{-3}$$

For example, the corrected densities for glasses G2 and G14 rapidly quenched were: 2.728 g cm^{-3} and 2.736 g cm^{-3} respectively. The water contents for the G2 and G14 glasses are presented in Table 2.5 as typical results.

2.9.2 Mechanical properties

Breaking strength tests on glass ceramic beams with rectangular cross sections were carried out in a universal Instron machine. The beams were fractured at room temperature under

TABLE 2.5 WATER CONTENT RESULTS FOR GLASSES G2 AND G14

Glass	$\nu(\frac{1}{cm})$	$\lambda(\mu m)$	$\log_{10}\frac{I_o}{I}$	% Area of Resolved peaks	$\varepsilon(cm^2/mole)$	$C_{PARTIAL}$ (mole/litre)	C_{TOTAL} mole/litre	wt.%
G14	3 448	2.90	0.080	6.6	75	0.0232		
	2 857	3.50	0.196	74	150	0.0284		
	2 386	4.19	0.140	14	310	0.0098	0.0614	0.040
G2	3 448	2.90	0.012	12	75	0.0043		
	2 857	3.50	0.025	74.5	150	0.0047		
	2 386	4.19	0.019	13.5	310	0.0017	0.0107	0.007

normal atmosphere on a four point bending jig, as shown in Figure 2.12, with 0.6 cm span between the inner rods and 2 cm span between the outer rods. The samples were cut after the nucleation and growth heat treatments with a diamond impregnated circular copper saw. They were then ground and polished with SiC (several grades) and 6 μm diamond paste (wetted with a mixture of oil and paraffin). The polishing operation was necessary in order to inspect the glass ceramic for visible cracks. This operation was also timed (approximately 4 minutes) in order to provide approximately the same surface condition for all of the beams. After polishing the samples were stored in a desiccator with silica gel. The final size of the beams was approximately 1.9 mm x 2.1 mm x 30 mm.

The machine was calibrated up to a total load of 5 kg including the weight of the bottom part of the jig and the weight of the sample. The cross-head speed was 0.005 cm per minute and the chart speed was 10 cm per minute.

The glass beams always fractured between the inner rods where the applied stresses were a maximum. Assuming that the fracture stress is the maximum applied stress the former can be calculated (2.14) from the following equation:

$$\sigma_{max} = \frac{My}{I} = \frac{Fxg}{2} \times \frac{(\ell_2-\ell_1)}{2} \times \frac{h}{2} \times \frac{1}{\frac{ah^3}{12}} = \frac{Fg(\ell_2-\ell_1)}{4} \frac{}{\frac{ah^2}{6}} \qquad (2.21)$$

where (see Figure 2.12) $M = \frac{Fg}{2} \cdot \frac{(\ell_2-\ell_1)}{2}$ is the bending moment (Nm), y (= h/2) is the distance from the neutral axis to the

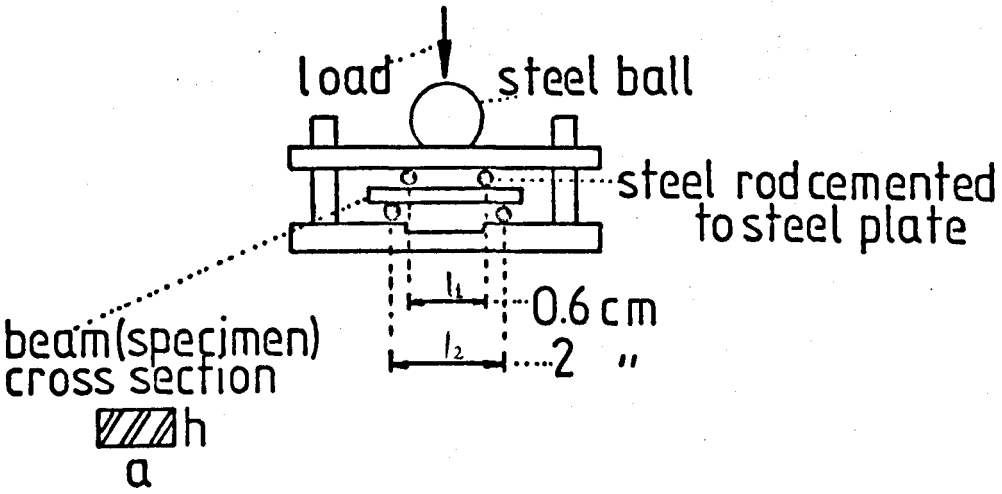

FIGURE 2.12 Jig designed for strength measurements.

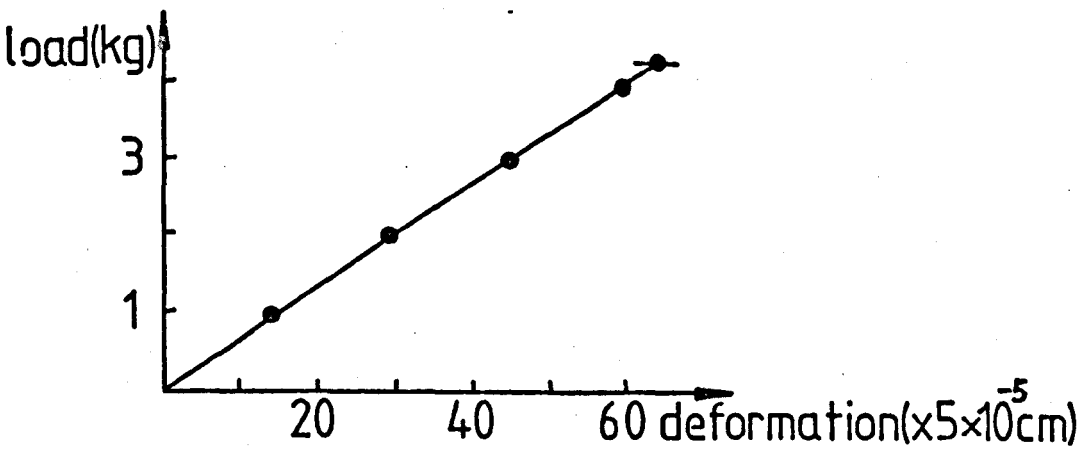

FIGURE 2.13 Typical deformation curve from Instron machine.(schematic)

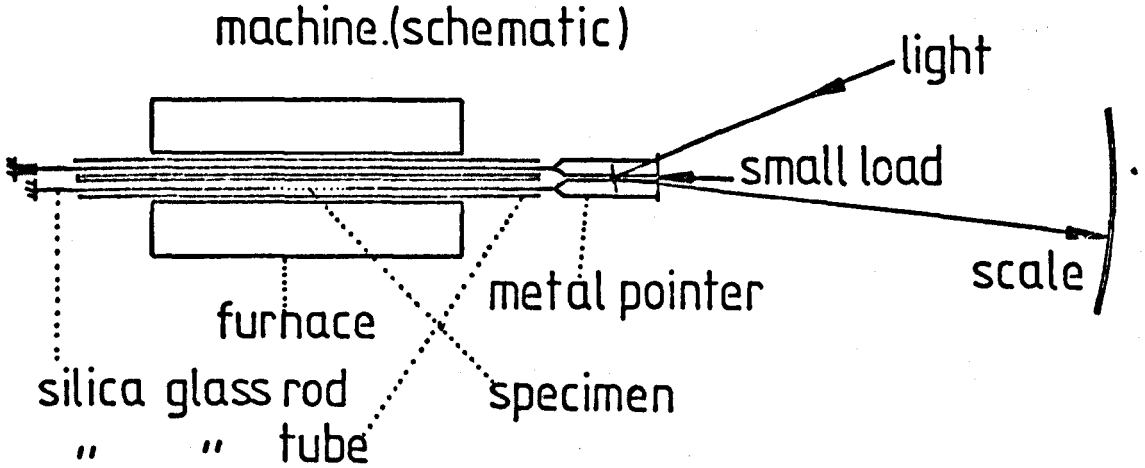

FIGURE 2.14 Thermal expansion apparatus.

surface (m), $I = \frac{ah^3}{12}$ is the second moment of the beam cross section about the neutral layer (m^4) and σ_f is in MN m^{-2}. A typical deformation curve is shown in Figure 2.13. The Young's modulus E can also be calculated (2.14) by noting that the beam between the inner rods is in pure bending (no shear stresses); the deflection of the beam (at the mid-point) can be approximated for small deflections by

$$\delta \simeq \frac{\ell_1^2}{8s} \tag{2.22}$$

where δ is the maximum deflection (m), ℓ_1 is the distance between inner rods (m) and s is the radius of curvature of the beam under the action of load F (see Figure 2.12), s is given by

$$s = \frac{EI}{M} \tag{2.23}$$

From equations (2.22) and (2.23)

$$E = \frac{3}{8} \frac{Fg\ell_1^2(\ell_2-\ell_1)}{\delta\ ah^3} \tag{2.24}$$

2.9.3 Thermal expansion measurements

The linear coefficient of thermal expansion α was determined for a number of the glasses and the corresponding glass ceramics. Expansion measurements were also useful to compare other thermally dependent properties. For example the thermal expansion transformation temperature Tg and softening point of the glasses could be determined. For the glass ceramics polymorphic phase transformations could also be detected, as will be described later.

The coefficient α is given by

$$\alpha = \frac{1}{\ell} \frac{\Delta \ell}{\Delta T} \qquad (2.25)$$

where ℓ is the original length, $\Delta \ell$ is the increase in length and ΔT is the temperature interval. The apparatus used (2.15) is shown schematically in Figure 2.14. The method consisted in comparing the elongation of the sample with the elongation of a silica glass rod. The heating rate was 3.3°C per minute. The deflections were read off the scale after each 10°C increase in temperature. To the deflection observed was added the deflection of a silica glass rod (α approximately 5×10^{-7} $°C^{-1}$) of the same length as the sample tested. The glass samples were prepared by cutting strips (approximately 8.4 cm in length) from annealed glass discs. The calculation of the coefficient α for different temperature ranges as well as typical $\frac{\ell - \ell_0}{\ell_0}$ vs temperature (°C) plots will be given in a later chapter.

CHAPTER 3

EXPERIMENTAL RESULTS

$Na_2O.2CaO.3SiO_2$ glass composition and glasses close to this composition

As discussed in Chapter 1, previous work (3.1) has shown that the glasses around the stoichiometric compositions NC_2S_3 and N_2CS_3 exhibit internal crystal nucleation. In the present work detailed study was made of the crystallization kinetics of glasses whose compositions were very close to the NC_2S_3 composition. In this chapter several soda-lime-silica glasses around the exact NC_2S_3 composition are experimentally analysed in detail.

3.1 Glass G2

This glass (and also G1) was melted from a batch with the stoichiometric composition $Na_2O.2CaO.3SiO_2$. From chemical analysis the final composition of G2 was 17.07 wt.% Na_2O (16.27 mole % N), 31.40 wt.% CaO (33.07 mole % C) and 51.53 wt.% SiO_2 (50.66 mole % S). (Appendix A2, Table A2.1). So it was close to NC_2S_3 but there was approximately a 0.2 wt.% loss in CaO and 0.4 wt.% loss in Na_2O. This small change in composition was not significant for most of the present work since similar losses were expected for the other glasses (including those with additions of other components to NC_2S_3). Hence straight comparisons could be made. Also, the influence of changes in the Na_2O, CaO and SiO_2 components from the exact NC_2S_3 composition on both nucleation rates and viscosities was clearly established from independent work to be described later.

During a preliminary study of the internal crystallization in this glass the optimum etching technique was developed for observation of the crystals in the optical microscope, which involved neither 'over' etching nor 'under' etching. Although previous

workers used 0.03 vol.% HNO_3 for 5 seconds (3.1) or 1 vol.% HF, 0.2 vol.% HCl for 5 seconds (3.2) for similar compositions, in this work the best etching solution was found to be 0.001 vol.% HF, 0.0005 vol.% HCl with an etching time of approximately 120 seconds. It was found that the crystals were etched more rapidly than the glass as can be seen in Figure 3.1 which shows scanning electron micrographs of the etched glass. This behaviour toward acids is supported by the results of the chemical durability experiments to be presented in a later chapter. Thus the NC_2S_3 glass ceramic when tested for attack by hydrochloric acid gave higher extracts of Na_2O than the NC_2S_3 glass, indicating that the glass was more durable to acids. The larger etching effect on the crystals may also explain the considerable difficulty experienced in preparing carbon replicas for electron microscopy from this glass. Carbon was evaporated under vacuum onto fractured or polished surfaces of the glasses. The final replicas (after "floating off" in either warm water or a very dilute HF solution) contained many holes corresponding to the location of crystals in the glass surface. A probable explanation for these holes is that in the very rough cavities produced by the etching of the crystals the carbon layer is not easily detached by the "floating off" technique, so the replica is torn around the crystal-glass boundary leaving a hole. Although this problem was partly overcome by etching for shorter times the replicas were not of good quality due to the lack in contrast (see Figure 3.1c).

Figure 3.1a,b

Stereoscan micrographs of G2 heated at 620°C for 150 min.
Etched for: (a) 45 s in acid (see text). Mag X7,400.
(b) 90 s in acid (see text). Mag X14,100.

Figure 3.1c (left)

Electron micrograph of a replica of G2 heated at 578°C for 20 hr then etched in acid (see text) for 20 s. Mag X11,700.

Figure 3.3a (right)

Optical micrograph of G2 nucleated at 621°C for 60 min and grown at 730°C. Mag X504.

Figure 3.3b

Electron micrographs of G2 heated at 578°C for 20 hr
Mag X29,500; X26,800.

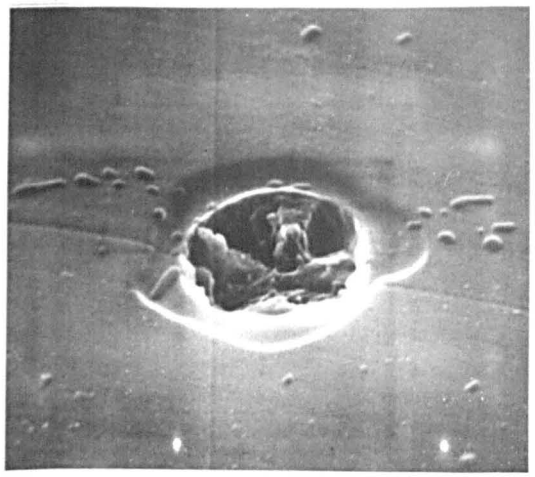

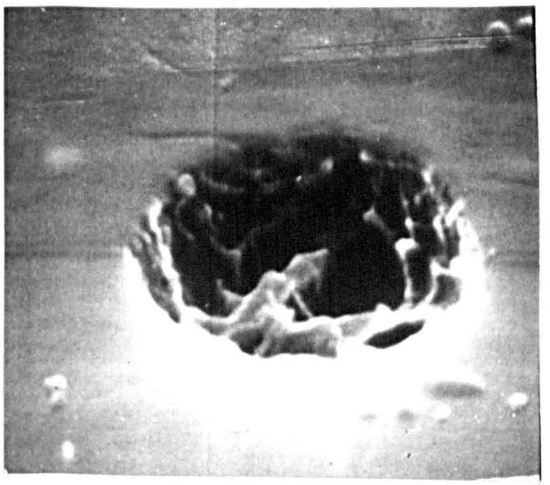

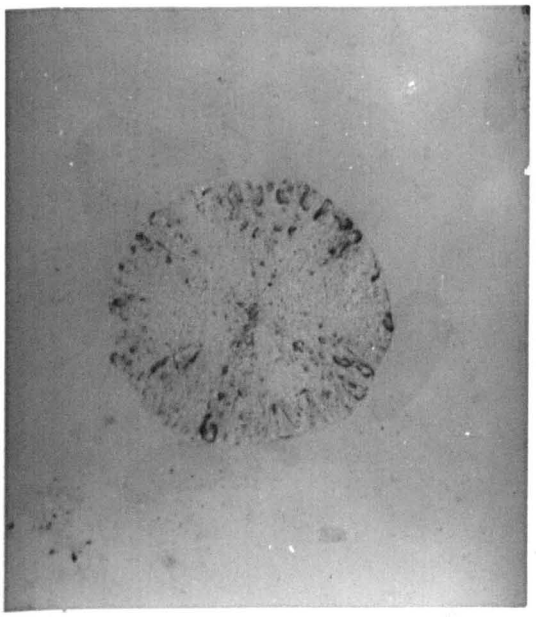

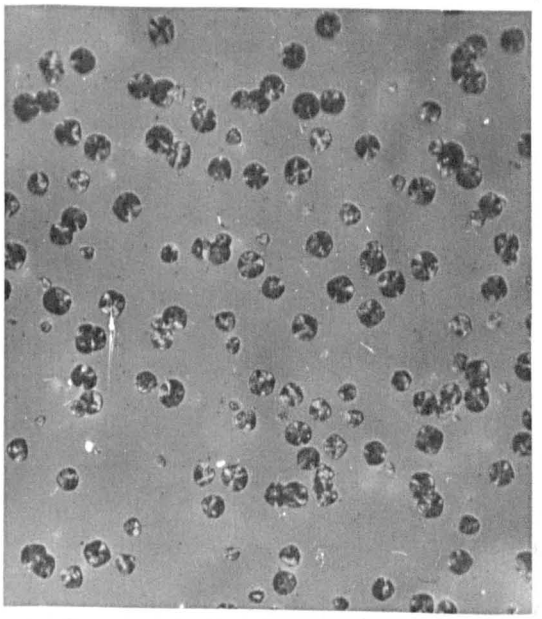

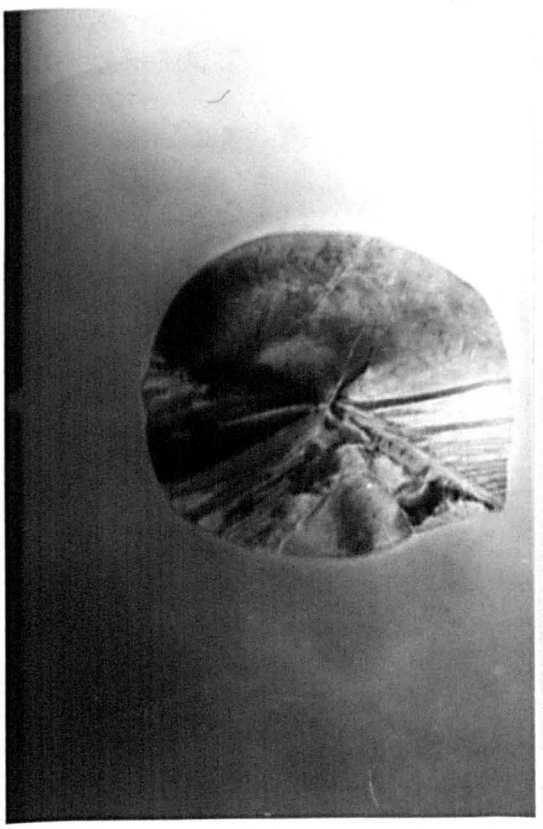

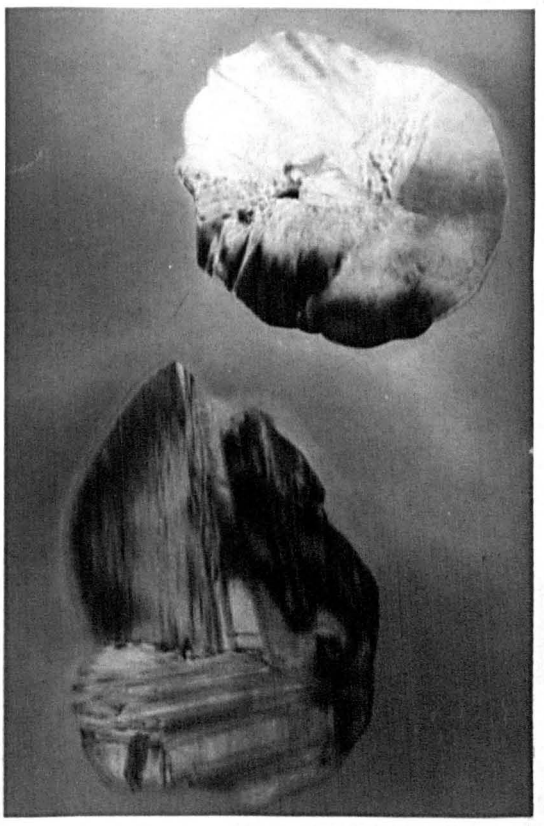

3.1.1 Nucleation Rates (G2)

The nucleation data for glass G2 obtained using the equations (2.1) and (2.2) are summarized in Table 3.1 and Figure 3.2. In Figure 3.3a a typical optical micrograph is shown, and Figure 3.3b shows transmission electron micrographs of NC_2S_3 crystals. The crystal morphology will be discussed later.

In Figure 3.2 are shown plots of $\log_{10}(\frac{N_V}{t})$ versus temperature, where N_V is the number of nucleated crystals per unit volume at the given temperature (°C) after a time t of 40 minutes. N_V/t may be regarded as the 'average' nucleation rate over this time interval. These values are probably close to the 'steady state' nucleation rates except for the results at the lower temperatures where incubation time effects can cause appreciably non linear N_V versus t (3.3). Thus at the lower temperatures the N_V/t value will probably be an underestimate of the steady state nucleation rate. This effect will be further discussed later in this chapter.

The N_V/t or 'nucleation rate' curve shows three main features:

(i) A maximum of 1.259×10^4 nuclei mm^{-3} min^{-1} is found at approximately 617°C.

(ii) A 'cut off' at about 570°C and a high temperature 'cut off' at about 710°C where the frequencies were below 10^2 nuclei mm^{-3} min^{-1}

(iii) A range of approximately 140°C where the nucleation process was clearly detected.

In order to check the values of N_V obtained using equations (2.1) and (2.2) the particle size distribution method was employed.

TABLE 3.1 NUCLEATION RESULTS FOR GLASS C2

T(°C)	Time t, mins	N' number of particles inter-sections	b' (mm)	Magnifi-cation	A' plate area (mm^2)	$\log_{10}\left(\frac{N' \times M^3}{A' \times b' \times t}\right)$	$\log_{10}\left(\frac{2}{\pi}\frac{M^3}{A' \times t}\left\langle\frac{1}{b}\right\rangle\right)$	$\log_{10}\left(\frac{N_{V\,TOTAL}}{t}\right)$ Due to Schwartz
580	40	70(71)	3.4	148.8	17120	1.99	1.89	-
600	"	346	2.3	2976	"	3.75	3.67	-
620	"	104	5	744	"	4.10	4.03	-
640	"	44(44)	6	744	"	3.66	3.68	-
660	"	225	5.5	297.6	"	3.19	3.22	-
680	"	369	4.1	148.8	"	2.64	2.62	2.67
700	"	147	11	148.8	"	1.80	1.73	-
710	"	142	12.5	148.8	"	1.74	1.66	-

FIGURE 3.2 $LOG_{10}(Nv/t)$ AS A FUNCTION OF TEMPERATURE FOR GLASS G2

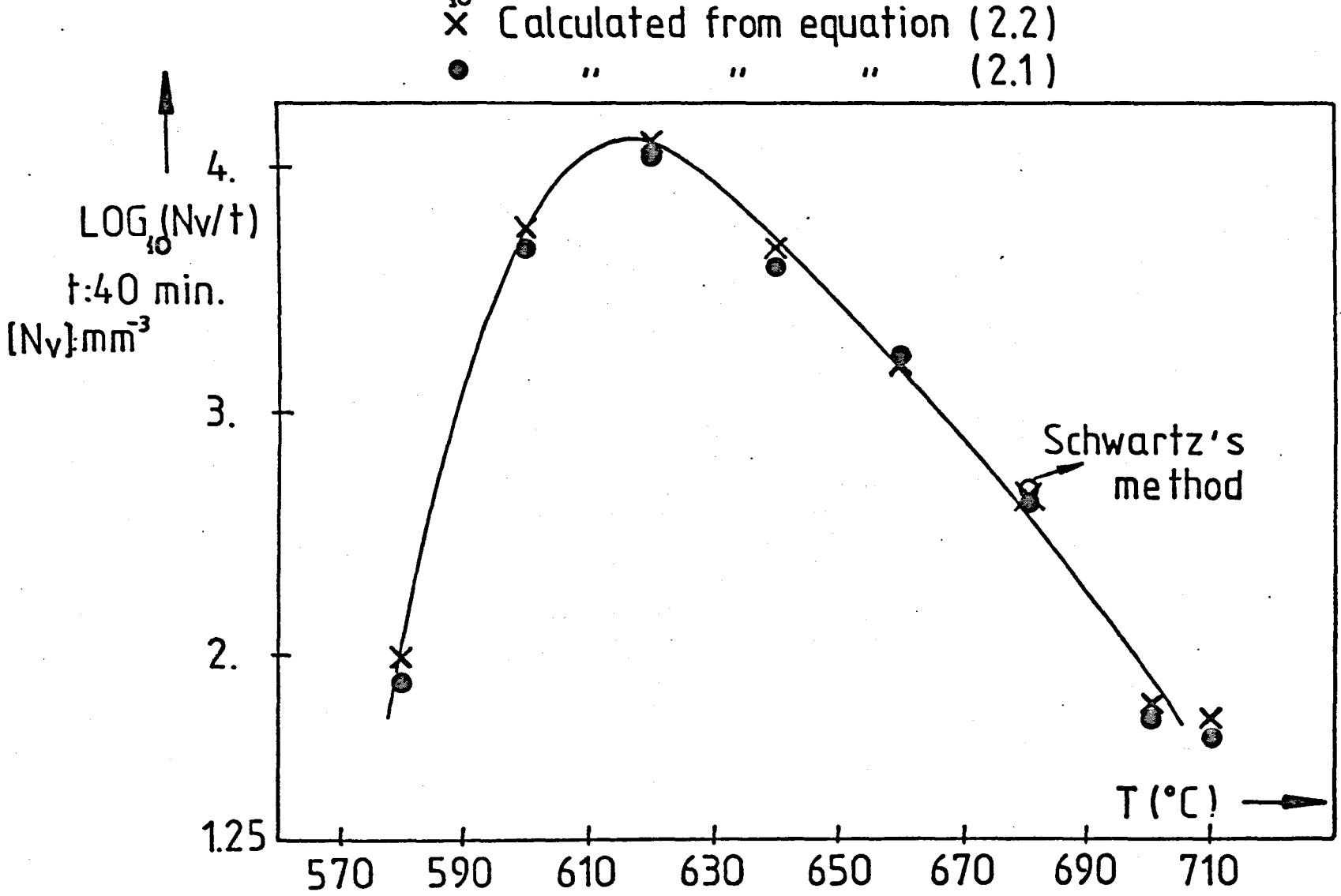

In this method due to Saltykow and Schwartz (3.4) the particle size distribution is first estimated. A sample of the glass G2 given a nucleation treatment at 680°C for 40 minutes followed by a growth treatment at 730°C for 3 minutes was chosen. For this sample a distribution of particle sizes was expected because of the appreciable crystal growth rate at the nucleation temperature (approximately 0.7 $\mu m\ min^{-1}$). The $\log_{10}(N_V/t)$ value, using equation (2.2) and assuming a diameter of 4.1 mm for the largest cross section was 2.64. Following the Saltykow method the number of size intervals k was chosen as 8. The width of each interval $\overline{\Delta}$ was 0.528 mm such that $k \times \overline{\Delta} = 4.23$ mm. The print magnification M was 148.8 and the print area A' measured was 17120 mm^2. The number of particles in each size interval are given in Table 3.2. Also given are the calculated number of particles per unit volume $N_V(k)$ for each interval k except for the first four intervals where their sum is quoted. The sum of the $N_V(k)$ for all the intervals gave the total $N_V(N_V(T))$. The value of $\log_{10}(\frac{N_V(T)}{t})$ with t = 40 minutes is 2.67, which is in close agreement with the values calculated from the two previous methods described (equations (2.1) and (2.2)), i.e. 2.64 from equation (2.2) and 2.62 from equation (2.1).

TABLE 3.2 PARTICLE SIZE ANALYSIS FOLLOWING SCHWARTZ'S METHOD

k	Range $k\bar{\Delta}$ (mm)	n:number of particles	$\frac{N_A(k)}{\Delta} = \frac{(148.8)^3 n}{\bar{\Delta} \times 17120}$
1	0.00 ↔ 0.53	0	0.0
2	0.53 1.06	14	5094.97
3	1.06 1.59	20	7278.53
4	1.59 2.12	55	20015.95
5	2.12 2.64	46	16740.62
6	2.64 3.17	79	28750.19
7	3.17 3.70	84	30569.82
8	3.70 4.23	84	30569.82

$$N_V(1) + N_V(2) + N_V(3) + N_V(4) = 950.97$$

$$N_V(5) = 0.3333 \frac{N_A(5)}{\Delta} - 0.1161 \frac{N_A(6)}{\Delta} - 0.0366 \frac{N_A(7)}{\Delta} - 0.0168 \frac{N_A(8)}{\Delta} = 609.32$$

$$N_V(6) = 0.3015 \frac{N_A(6)}{\Delta} - 0.1081 \frac{N_A(7)}{\Delta} - 0.0346 \frac{N_A(8)}{\Delta} = 4305.87$$

$$N_V(7) = 0.2773 \frac{N_A(7)}{\Delta} - 0.1015 \frac{N_A(8)}{\Delta} = 5371.12$$

$$N_V(8) = 0.2582 \frac{N_A(8)}{\Delta} = 7893.13$$

$$N_V(T) = N_{VTOTAL} = \frac{N_A(1)}{\Delta} + 0.4227 \frac{N_A(2)}{\Delta} + 0.2583 \frac{N_A(3)}{\Delta} + 0.1847 \frac{N_A(4)}{\Delta} + 0.1433 \frac{N_A(5)}{\Delta} + 0.1170 \frac{N_A(6)}{\Delta} + 0.0988 \frac{N_A(7)}{\Delta} + 0.0856 \frac{N_A(8)}{\Delta}$$

$$= \sum_{i=1}^{N} N_V(i) = 1913041 \text{ nuclei per mm}^3, \text{ where } \Delta = \frac{\bar{\Delta}}{(148.8)^3} \text{ and}$$

$N_A(k)$ is the number of particle intersections in class k.

3.1.2 Growth Rates (G2)

Growth rates were measured using the crystals internally nucleated after a single heat treatment at a given temperature. A typical linear plot of the maximum cross sectional diameter vs. time at a given temperature (678°C) is shown in Figure 3.4. The growth measurements are summarized in Table 3.3 and Figure 3.5. Figure 3.5 shows the crystal growth rate ($\mu m\ min^{-1}$) vs. temperature (°C). There is a considerable overlap of the growth rate curve with the high temperature side of the nucleation rate curve (Figure 3.2). In fact this composition crystallizes very rapidly for temperatures higher than the nucleation rate maximum at 617°C. To demonstrate this point an approximate calculation of the time required to crystallize the glass (to a certain level of crystallinity) at different temperatures will be made using the Johnson-Mehl equation

$$X = 1 - \exp(-\frac{\pi}{3} I U^3 t^4) \qquad (3.1)$$

where X is the volume fraction transformed, I is the nucleation rate, U is the growth rate and t is the transformation time. For the assumptions involved in this equation see for example reference (3.5). From Figures 3.2 and 3.5 at 640°C, $I = 5.01 \times 10^3$ nuclei $mm^{-3}\ min^{-1}$ and $u = 10.5 \times 10^{-5}$ mm min^{-1}. From equation (3.1) with $X = 0.98$ (98% crystallinity) t is found to be 159.3 min. It should be stressed that equation (3.1) is only an approximation because the incubation times in both nucleation and growth rates (which will be further analysed later in this chapter) are not considered in its derivation. However in the temperature range where the present calculations were

FIGURE 3.4 MAXIMUM DIAMETER AS A FUNCTION OF TIME FOR GLASS G2 AT 678 °C

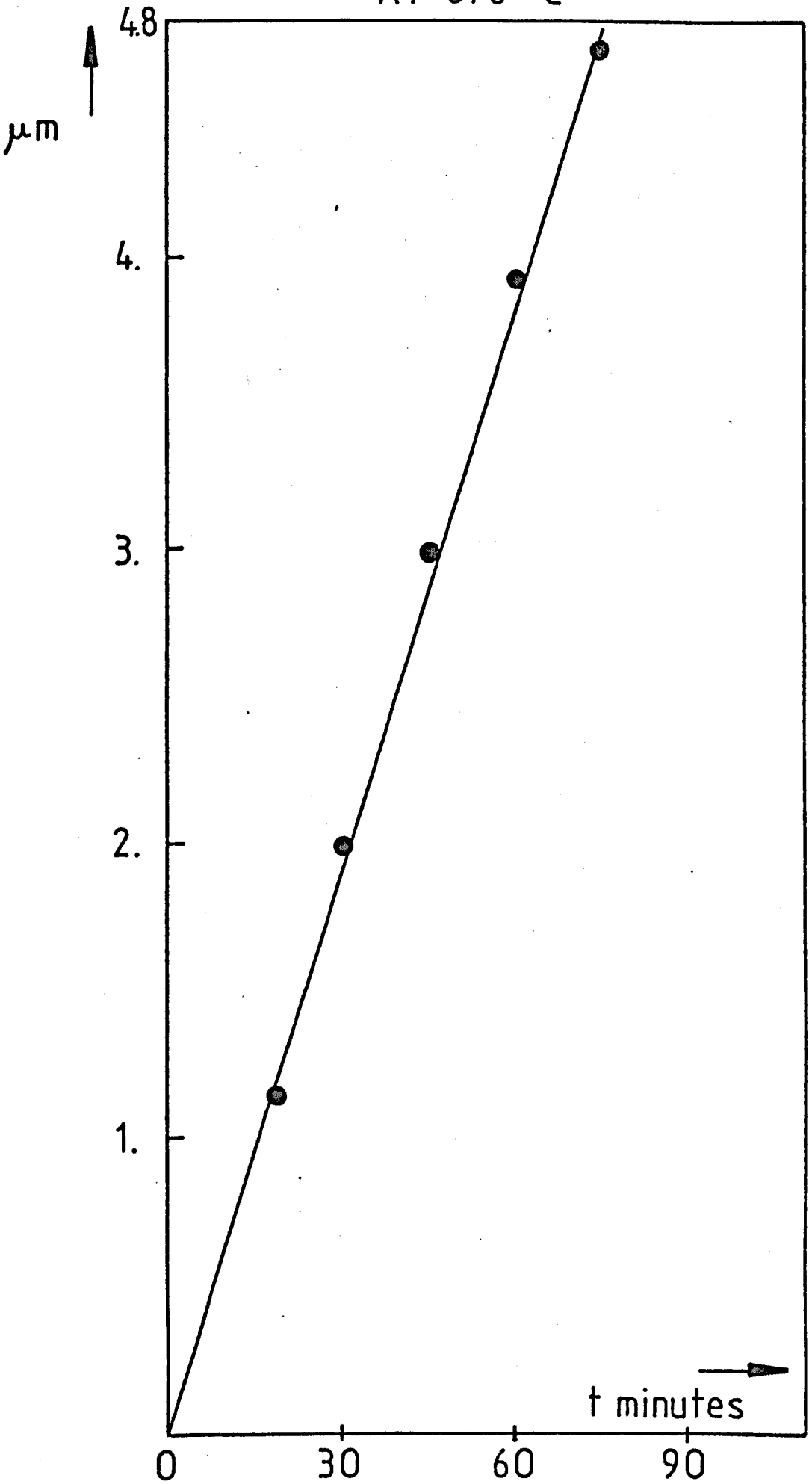

TABLE 3.3 GROWTH RATES vs. TEMPERATURE

T(°C)	Growth rate u ($\mu m\ min^{-1}$)
606.5	0.0066
619	0.0330
631	0.0506
654	0.2366
678	0.6357
692	1.1800
710	1.9100

Estimated error: $\frac{\Delta\mu}{\mu} \times 100 = 9\%$

TABLE 3.4 TIMES TO REACH 98% CRYSTALLINITY CALCULATED FROM EQUATION (3.1)

T(°C)	I (nuclei $mm^{-3}\ min^{-1}$)	u ($mm\ min^{-1}$) x 10^5	t(min)
618	1.995×10^4	2.8	303.9
640	5.011×10^3	10.5	159.3
650	2.812×10^3	19.5	115.6
660	1.413×10^3	31.5	95.9
670	7.498×10^2	47.1	83.1
680	3.548×10^2	69.5	74.8
690	1.778×10^2	110.0	63
710	3.981×10	191.0	60.6

FIGURE 3.5 GROWTH RATE AS A FUNCTION OF TEMPERATURE FOR GLASS G2

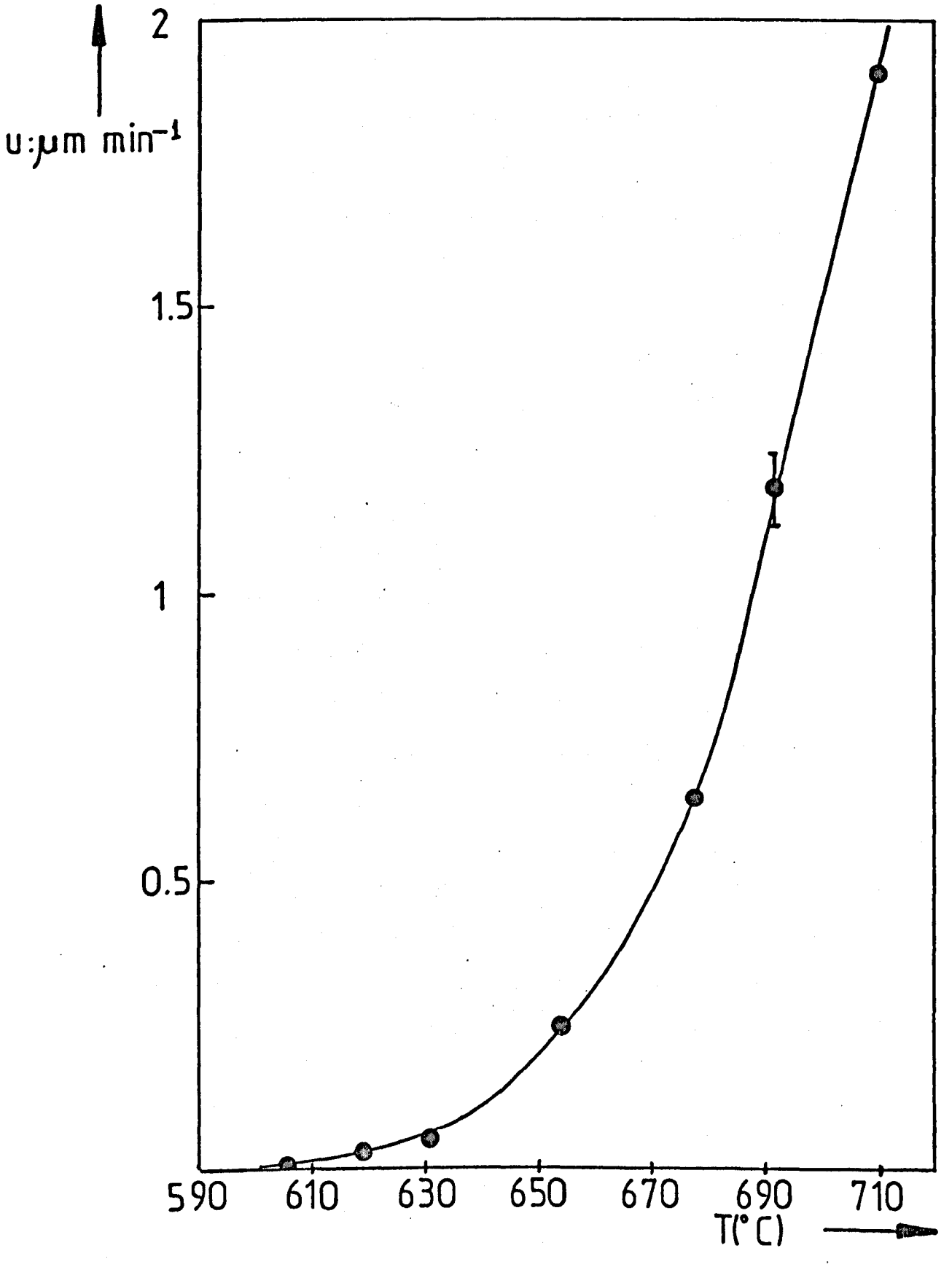

performed these effects are considerably diminished. Table 3.4 gives further calculations from equation (3.1) at other temperatures.

3.1.3 Viscosity Measurements

Viscosity data (measured as described in section 2.8) were obtained for the glass G2 in two different temperature ranges; the low temperature range from 570°C to 650°C and the high temperature range from 1260°C to 1370°C. The viscosity values as calculated from the deformation curves (see section 2.8.1b) are summarized in Table 3.5 and Figure 3.6. These curves were such that the total deformation satisfied equation (2.4) and so equation (2.5) was used to calculate the viscosity coefficient.

Table 3.5 shows the measured viscosities in both temperature ranges. Also shown are the Fulcher parameters (equation (2.8)) obtained with both the low and high temperature data (column 5) as well as the same parameters for only the low temperature data. The Fulcher equation for glass G2 for the whole temperature range is:

$$\log_{10}\eta = -3.86 + \frac{4893.3}{T-274.4} \qquad (3.2)$$

Figure 3.6 shows the complete viscosity curve as determined in this work. The intermediate points were obtained using the Fulcher equation fitted for the whole temperature range. The extrapolated dotted line was constructed using the Fulcher equation from the lower temperature range data only. On the same plot is also shown the curve for the glass NFS 710. It can be observed that glass G2

TABLE 3.5 VISCOSITY DATA AND FULCHER PARAMETERS FOR GLASS G2

T(°C)	$\log_{10}\eta$	Fulcher Parameters	$570 \leq T \leq 650$	$570 \leq T \leq 1370$
572	12.34	A	5.54	-3.86
591	11.59	B	721.11	4893.3
610	10.71	T_o	468.5	274.4
629	9.96			
645	9.62			
1264.5	0.99			
1286.3	0.93			
1303.3	0.88			
1318.0	0.82			
1338.0	0.79			
1370.0	0.70			

FIGURE 3.6 $LOG_{10}\eta$ AS A FUNCTION OF TEMPERATURE FOR GLASS G2

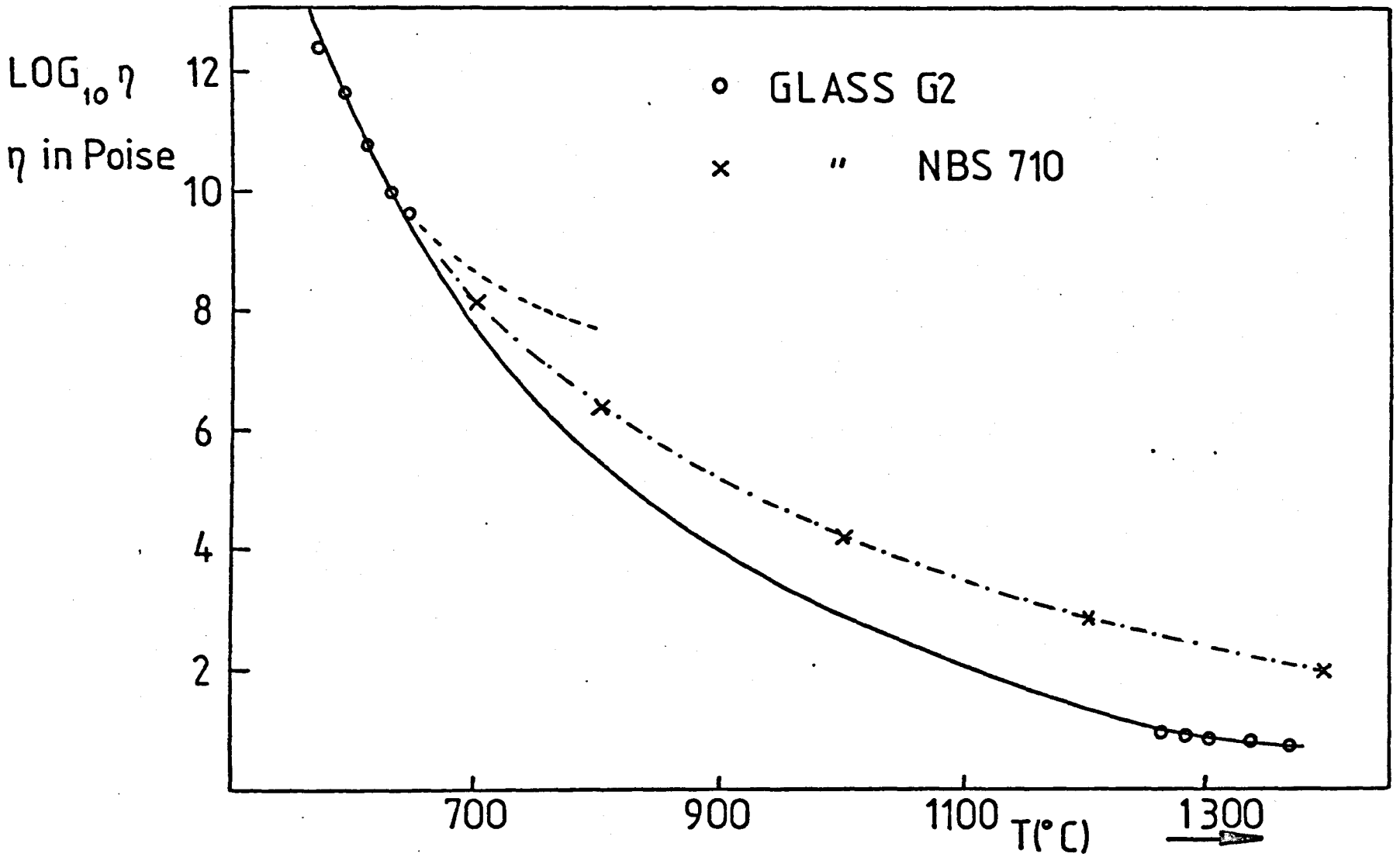

is very fluid at high temperatures; for example at its liquidus temperature (T_L = 1276°C) $\log_{10}\eta \cong 1$ and at T = 1370°C $\log_{10}\eta \cong 0.7$. The temperature at which $\eta = 10^{13}$ Poises is found to be T = 564.7°C when the Fulcher equation for the whole range of temperature is used and T = 565.2°C when the Fulcher equation for only the lower temperature range is used.

3.1.4 DTA and T_L Results

The DTA traces for glass G2 for the heating cycle and for the cooling cycle (both at 10°C per minute) are shown in Figure 3.7. The following are observed: for the heating cycle an endothermic peak and peaks due to crystallization and melting, and for the cooling cycle peaks due to crystallization and a reversible polymorphic transformation.

3.4.1a Transformation range of glass

From the endothermic peak due to changes in specific heat and usually associated with the annealed glass a temperature can be defined to represent the 'DTA Tg' as shown in Figure 3.7. The 'DTA Tg' was 579°C ±3°C, the estimated error being based on the observed scatter for several runs at the same heating rate and with similar sample and reference characteristics. It is interesting to compare this value with the value obtained from isothermal viscosity measurements where 10^{13} Poise corresponds to 564.7°C. Also for glass G17 (slightly different in composition from G2) the 'DTA Tg' was 578°C and the temperature at which $\eta = 10^{13}$ P was 565.7°C. The latter

FIGURE 3.7 DTA TRACE FOR GLASS G2 (300mg)

Reference Material - Al_2O_3 (300 mg), Heating/Cooling Rate 10°C min^{-1}

ΔT Sensitivity - 100 μV - Full Scale Deflection

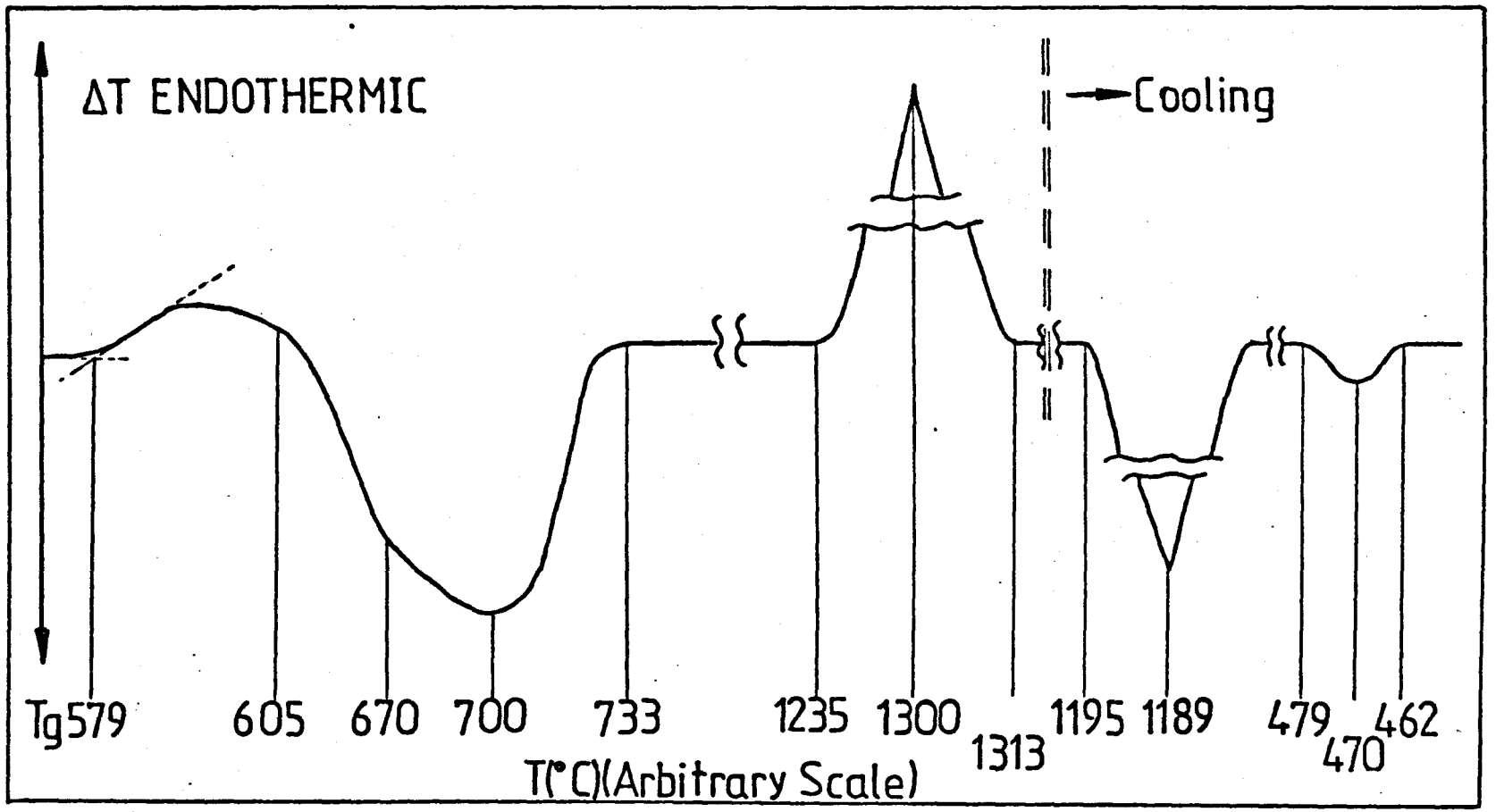

value was calculated from the Fulcher equation for glass G17

$$\log_{10}\eta = -3.44 + \frac{4338.6}{T-301.8}$$

where

the low temperature data for G17 and the high T data for G2 were used. For the glass G17 also thermal expansion data (at approximately 3°C per min heating rate) was obtained. The thermal expansion 'Tg' was 563.5°C in close agreement with the value of 565.7°C mentioned above. Other workers have also measured the DTA Tg for glasses similar in composition to G2 and G17. For example Frischat (3.6) quoted 575°C and Sadeghi (3.2) quoted 587°C.

Using the Fulcher equation for the whole temperature range for glass G2 (Equation (3.2)) the 'DTA Tg' temperature of 579°C corresponds to a viscosity level of $\log_{10}\eta = 12.20$.

3.1.4b Heats of crystallization, fusion and polymorphic transformations

To measure these quantities from a DTA trace it is necessary to obtain a relationship between the heat of reaction and, for example, the area under the peak produced by the reaction. This is a very difficult problem. It involves the solution of differential equations such as:

$$\rho(i)c_p(i)\left(\frac{\partial T}{\partial t}\right) = \lambda_i\left[\frac{\partial^2 T}{\partial x^2} + \frac{\partial^2 T}{\partial y^2} + \frac{\partial^2 T}{\partial z^2}\right] \qquad (3.4)$$

where i indicates a given medium and ρ, c_p and λ are the medium density, specific heat and thermal conductivity respectively. The Heat Equation (3.4) gives the distribution of temperature as a function of position and time in the given medium. However, it has been

shown both theoretically and empirically that the following approximated relationship applies:-

$$K\,B = k \int_a^b \Delta T(t)dt = \Delta H \qquad (3.5)$$

where B is the area under the peak, K is a proportionality factor and ΔH the heat of reaction per unit mass. This equation can be used provided it is possible to evaluate the factor K with known substances. A more elaborate version of equation (3.5) due to Kerr (quoted by Blazek in reference (3.7)) is:

$$\int_a^b \Delta T dt = \frac{M_a \Delta H}{g\ \lambda_{sm}} \qquad (3.6)$$

which can be obtained by solving equation (3.4) assuming cylindrical symmetry. Here $M_a\Delta H$ is the heat of reaction, M_a is the mass of sample, g is a geometrical factor and λ_{sm} is the coefficient of thermal conductivity of the sample. In deriving equation (3.6) the temperature gradients in the sample and the dependence of the area on the specific heat are neglected.

In this work expression (3.5) has been used to determine the heat of reaction. The calibration constant was obtained using both AR NaCl (melting point : 801°C, heat of melting ΔH_f = 6.69 kcal $mole^{-1}$ = 114.46 cal g^{-1}) and AR NaF (m. pt. 996°C, ΔH_f = 7.97 kcal $mole^{-1}$ = 189.81 cal g^{-1}). The values adopted are from JANAF tables (3.8). However it should be noted that:-

(i) the factor K is not constant with temperature, but tends to increase with increasing temperature. A possible explanation is

that the higher the temperature the greater the heat transference by a radiation mechanism (3.7).

(ii) In general in order to obtain good peaks (base line nearly the same before and after the reaction) it is often necessary to dilute the sample with an inert material (for example the reference material Al_2O_3). The sample particle size, density, specific heat and packing determine the thermal conductivity and this in turn should be nearly equal to the thermal conductivity of the reference material in order to avoid big shifts in the base line.

(iii) It is not easy to find a diluent material that will not interact with the sample to be measured or the standards.

In view of the complexities mentioned above it was decided to prepare several dilutions of NaCl (NaF) with Al_2O_3 keeping the same total mass (300 mg) and to use Al_2O_3 (300 mg) as the reference material. The areas under the peaks were measured by cutting and weighing a copy in tracing paper of the peak. No problem was found in defining these areas because the base line did not shift. In Figure 3.8 the weights of the peaks vs. the % of NaCl (NaF) is plotted. Although some scatter was found in the case of NaCl, the calibration factor K appeared to be unique: K = 150.2 cal per g of paper and independent of % NaCl. Hence it is reasonable to conclude that no interaction between NaCl and Al_2O_3 has occurred up to the melting point of NaCl. For NaF the situation is not so clear. Apparently there is a curvature (see Figure 3.8) for concentrations of NaF higher than 30%. Perhaps

FIGURE 3.8 AREA UNDER THE MELTING PEAK OF NaCl(NaF) VERSUS wt% OF NaCl(NaF) KEEPING THE SAME TOTAL MASS (300mg)

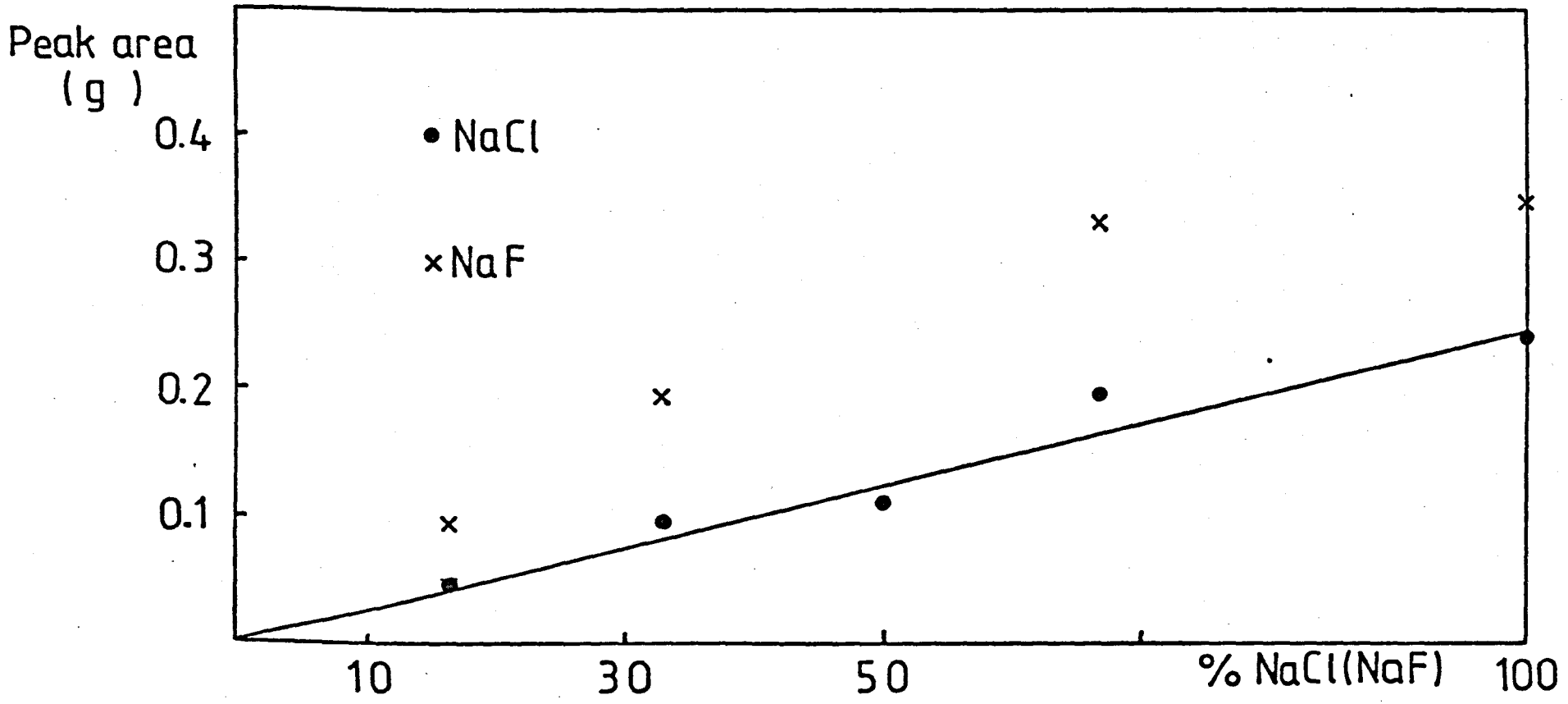

some interaction of NaF with Al_2O_3 could explain this behaviour but more research is needed to clarify this point. On the whole this method is attractive since it is simple to calibrate the apparatus and to obtain a good estimation of the heats of crystallization and melting in glass systems. As mentioned above the calibration factor obtained from NaF/Al_2O_3 dilutions increased with NaF content, so it was decided to use the calibration factor corresponding to 100% NaF (K = 164.39 cal per g of paper). This factor is greater than the one obtained from $NaCl/Al_2O_3$ dilutions, showing the probable trend of K increasing with temperature. The heats of crystallization, fusion and the low temperature reversible transformation for glass G2 were calculated from both factors. The results are listed in Table 3.6. The values quoted are the mean values obtained from three separate runs on the same glass.

In fact, high temperature calorimetric data for the $Na_2O.2CaO.3SiO_2$ composition is also available. The value for ΔH_f quoted by Kröger (3.9) is 21.8 ±0.1 kcal $mole^{-1}$ in good agreement with the present technique. Also this value provides the opportunity of estimating the probable error involved in using the DTA technique; it seems reasonable to qualify these measurements with a relative error of ±5%. So the heats of crystallization, fusion and polymorphic transformation can be taken to be: ΔH_c = 12.7 ±0.7 kcal $mole^{-1}$, ΔH_f = 20.6 ±1.1 kcal $mole^{-1}$ and ΔH_t = 0.98 ±0.05 kcal $mole^{-1}$ respectively by using the present DTA technique. All these values are the averages from NaCl and NaF calibration in Table 3.6. It should be noted that the heat of crystallization refers to measurement at approximately 700°C,

TABLE 3.6 ΔH_c (620 to 730°C), ΔH_f AND ΔH_r FOR GLASS G2

Standard	ΔH_c average heat of crystallization in the range 620 to 730°C		ΔH_f heat of fusion		ΔH_r Polymorphic transformation	
	kcal $mole^{-1}$	cal g^{-1}	kcal $mole^{-1}$	cal g^{-1}	kcal $mole^{-1}$	cal g^{-1}
NaCl	12.14	34.24	19.71	55.61	0.94	2.65
NaF	13.28	37.48	21.57	60.86	1.03	2.90

TABLE 3.7 STRUCTURES OF LOW AND HIGH FORMS OF CRYSTALLINE NC_2S_3

Structure		Maki (low form)	Maki (high form)	Mileson (low form)	Present work (low form)
Hexagonal	a(A)	10.47		10.48	10.5o
	c(A)	13.17		13.19	13.19
	Z	6		6	6
Rhombohedral	a(A)	7.472	7.53	7.48	7.49
	α(°)	88°58'	89°07'	88°59'	89°01'
	Z	2	2		

the maximum of the exothermic crystallization peak. It is interesting to calculate the viscosity levels at the beginning, maximum and end of the crystallization peak in Figure 3.7. From equation (3.2) the following viscosities were obtained:

at 605°C $\log_{10}\eta$ = 10.94 (onset of crystallization),

at 700°C $\log_{10}\eta$ = 7.64 (maximum of peak), and

at 733°C $\log_{10}\eta$ = 6.81 (end of crystallization).

Finally, the liquidus temperature T_L measured for glass G2, was 1277 ±2°C. No value was obtained for glass G17. However, Glasser (3.10) quoted 1288 ±1°C as the liquidus temperature. The water content of glass G2 was 0.007 wt.% H_2O. The effects of water on the kinetics of crystal nucleation and growth as well as on the general properties of the glasses will be fully analysed in a later chapter.

3.1.5a X-ray diffraction results

The diffraction pattern for glass G2 (fully crystallized) matched exactly the pattern for the low temperature form of the standard $Na_2O.2CaO.3SiO_2$ crystalline compound (see section 2.6) in both peak positions and relative intensities. This compound was previously analysed by Maki and Sugimura (3.11) and Mileson and Glasser (3.12). Maki and Sugimura also studied the high temperature form at 500°C. In Table 3.7 the different results are quoted. The low temperature form is hexagonal, however the strongest peaks can also be fitted by assuming a rhombohedral structure. In fact there is a great similarity between the

structures of the low (hexagonal) and high (rhombohedral) forms.

In this work the pattern derived for the low temperature form could be indexed in terms of a hexagonal structure. The following formula (3.13) was used

$$\sin^2\theta = A(h^2 + k^2 + hk) + Cl^2 \qquad (3.7)$$

where $A = \frac{\lambda^2}{3a^2}$, $C = \frac{\lambda^2}{4c^2}$, the wavelength $\lambda = \lambda_{CuK\alpha_1} = 1.5404$ Å and a, c are the hexagonal constants of the unit cell. The A and C values were 7.174×10^{-3} and 3.408×10^{-3} respectively. These are very important quantities because they determine the (hk.ℓ) indices and when found allow the unit cell constants to be calculated. The number of 'formula units' Z inside the unit cell can also be calculated if the density of the compound is known. Thus $Z = \frac{\Sigma A}{M} = \frac{\rho V}{1.66} \times \frac{1}{M}$ where ΣA is the total mass inside the unit cell, M is the molecular weight (354.40 g), ρ is the density (2.80 g cm^{-3}) and $V = 0.886\ a^2c$ is the volume of the unit cell in $Å^3$. The unit cell constants were a = 10.50 Å, c = 13.193 Å and Z = 5.99 ≃ 6. In Table 3.8 are shown the calculated and experimentally obtained $\sin^2\theta$ values together with the Miller indices assigned.

3.1.5b Electron Diffraction Results

$Na_2O.2CaO.3SiO_2$ crystals precipitated from glass G2 are shown in Figures 3.3b,9. Regions of different contrast as well as some kind of crystalline imperfections can be observed. To obtain further information on the internal configurations it was decided to carry out some more detailed work using selected area

TABLE 3.8 NC_2S_3 LOW FORM X-RAY DATA

	$-h+k+\ell = 3n$	h	k	ℓ	$\sin^2\theta \times 10^3$	d (Å)	2θ	$\sin^2\theta \times 10^3$ Exp.	$d_{Exp.}$	2θ Exp.	$I_{REL.}$	Maki (3.11) h	k	ℓ	
		1	0	0	7.174	9.093	9.72	7.15	9.11	9.70	1.5				
*		1	0	1	10.58	7.487	11.81	10.50	7.519	11.76	20				
		1	0	2	20.806	5.340	16.59	20.80	5.342	16.58	14				
*		1	1	0	21.522	5.250	16.87	21.40	5.260	16.81	10				
		1	1	1	24.93	4.880	18.17	24.90	4.886	18.14	20				
*		0	0	3	30.67	4.393	20.173	30.70	4.397	20.18	46.5				
		1	1	2	35.15	4.110	21.613	35.30	4.099	21.66	6.0				
		1	0	3	37.85	3.96	22.436	37.9	3.955	22.46	14.0				
		2	0	-2	42.33	3.74	23.745	43.6	3.690	24.10	95.0				
*		2	0	2											
		1	2	0	50.22	3.44	25.90	50.4	3.432	25.94	23.0				
*		1	1	3	52.19	3.37	26.41	52.6	3.358	26.52	92.0				
*		2	1	1	53.63	3.33	26.78	54.2	3.309	26.92	138.0				
		2	0	3	59.37	3.16	28.20	59.5	3.157	28.24	7.5				
		1	2	2	63.85										
*		3	0	0	64.57	3.031	29.44	64.5	3.033	29.42	19.0	1	2	2	
		3	0	1	67.97	2.954	30.225	68.3	2.947	30.30	8.0				
		1	1	4	76.05	2.793	32.02	76.5	2.784	32.12	9.5				
		2	1	3	80.89	2.708	33.05	80.8	2.709	33.04	20.0				
		0	2	4	83.22	2.670	33.53	83.7	2.662	33.64	178.0				
*		2	0	4											
*		2	2	0	86.09	2.625	34.12	86.7	2.616	34.25	162.0				
		2	2	1	89.496	2.57	34.81	90.0	2.567	34.92	14.5	> 0	1	5	d = 2.53 ($I_{REL.}$ MAKI = 10)
		3	1	0	93.26	2.522	35.56	93.1	2.522	35.54	22.0				
		1	3	0											
*		3	0	3	95.24	2.496	35.95	95.8	2.489	36.06	10.0				
*		1	3	1	46.67	2.48	36.23	97.2	2.470	36.34	12.0				
		3	1	1											
*		2	1	4	104.75	2.38	37.77	105.3	2.373	37.88	8.0				
*		3	1	2	106.89	2.356	38.17	107.5	2.349	38.28	27.0				

TABLE 3.8 (continued)

	-h + k + ℓ = 3n	h	k	ℓ	$\sin^2\theta$ x 10^3	d (Å)	2θ	$\sin^2\theta$ x 10^3 Exp.	$d_{Exp.}$	2θ Exp.	$I_{REL.}$	Maki (3.11) h	k	ℓ	
		4	0	0	114.78	2.273	39.61	114.6	2.275	39.58	9.5	2	0	5	
		2	2	5	113.90										
		4	0	1	118.19	2.232	40.38	118.8	2.235	40.32	15.0	4	0	1	
		3	0	4	119.09										
		0	0	6	122.70	2.188	41.23	123.8	2.189	41.20	13.5	0	0	6	
		3	1	3	123.93										
		0	4	2	128.42							1	3	3	d = 2.181 (I_{REL} = 3) MAKI
		3	0	5		2.137	42.25	129.6	2.140	42.20	22.0	0	4	2	
		1	0	6	129.86										
		3	1	5	135.42	2.086	43.33	136.6	2.084	43.38	11.0	1	2	5	
		3	2	0	136.31										
		3	2	1	139.71	2.053	44.05	140.6	2.054	44.04	11.5	3	2	1	
		2	2	4	140.62										
		1	1	6	144.21	2.019	44.84	145.8	2.017	44.90	9.0	1	1	6	
		4	0	3	145.46										
		1	3	4	147.80	1.990	45.54	148.8	1.997	45.38	15.0	1	3	4	
		3	0	5	149.80										
		4	1	1	154.06	1.962	46.22	154.9	1.957	46.36	12.5				
		4	1	2	164.29	1.900	47.82	165.3	1.895	47.98	7.0				
		4	0	4	169.31	1.861	48.90	170.5	1.865	48.78	101.0	4	0	4	
		2	2	5	171.29										
*		1	0	7	174.17	1.846	49.33	175.0	1.841	49.46	14.0				
*		1	4	3	181.33	1.809	50.41	182.9	1.801	50.64	21.0	0	5	1	d = 1.797 (I_{REL} = 9) MAKI
*		3	2	4	190.83	1.763	51.81	191.88	1.758	51.96	7.0				
		3	3	0	193.70	1.741	52.51	194.90	1.745	52.40	11.0	3	3	0	
		2	0	7	195.67										
		3	3	0	193.70	1.741	52.51	196.57	1.737	52.64	15.0	3	3	0	
		2	0	7	195.67										
		1	4	4	205.18	1.700	53.87	206.35	1.696	54.03	14.0				

TABLE 3.8 (continued)

-h + k + ℓ = 3n	h	k	ℓ	$\sin^2\theta \times 10^3$	d (Å)	2θ	$\sin^2\theta \times 10^3$ Exp.	$d_{Exp.}$	2θ Exp.	I_{REL}	Maki (3.11) h	k	ℓ
*	2	2	6	208.78	1.686	54.38	211.18	1.676	54.72	7.5			
*	1	2	7	217.21	1.653	55.56	218.63	1.647	55.76	16.5			
	2	1	7										
*	1	0	8	225.29	1.623	56.67	223.57	1.629	54.44	10.0			
	3	2	5	221.51	1.636	56.15							
	3	0	7	231.56	1.601	57.53	232.94	1.596	57.72	8.0			
	1	5	2	236.03	1.581	58.23	237.38	1.581	58.32	7.0	1	5	2
	4	0	6	237.47									
	1	1	8	239.63	1.573	58.62	238.71	1.576	58.49	7.0			
	4	0	6	237.47	1.581	58.33							
*	2	0	8	246.81	1.55	59.58	248.61	1.545	59.82	19.0			
*	2	4	4	255.4	1.524	60.71	256.49	1.521	60.85	28.5			
*	6	0	0	258.26	1.510	61.35	259.86	1.511	61.30	18.5	6	0	0
	3	1	7	260.25									
*	3	4	1	268.85	1.485	62.46	270.35	1.481	62.66	9.0			
	1	2	8	268.33	1.487	62.40							
	3	4	3	296.11	1.415	65.93	295.65	1.416	65.88	5.8			
*	1	1	9	297.57	1.412	66.12	298.04	1.411	66.18	5.0			
	3	2	7	303.30	1.395	67.01	305.09	1.394	67.06	18.0	3	2	7
	2	0	9	304.74									
*	5	2	3	310.46	1.380	67.84	312.17	1.379	67.94	12.5	5	2	3
	1	3	8	311.37									

> Means appearance in Maki test but not in this work

——— Means non appearance in Maki data

Figures 3.9 (top left), 3.10a (top right), 3.10b (bottom left)
3.10c (bottom right).

Electron micrographs of G2 heated at 578°C for 20 h (3.9) and 23 h (3.10).
Mag X15,000; X32,100
Mag X31,500; X40,600

The 3.10c micrograph was taken at an electron accelerating voltage of 1,000,000 V.

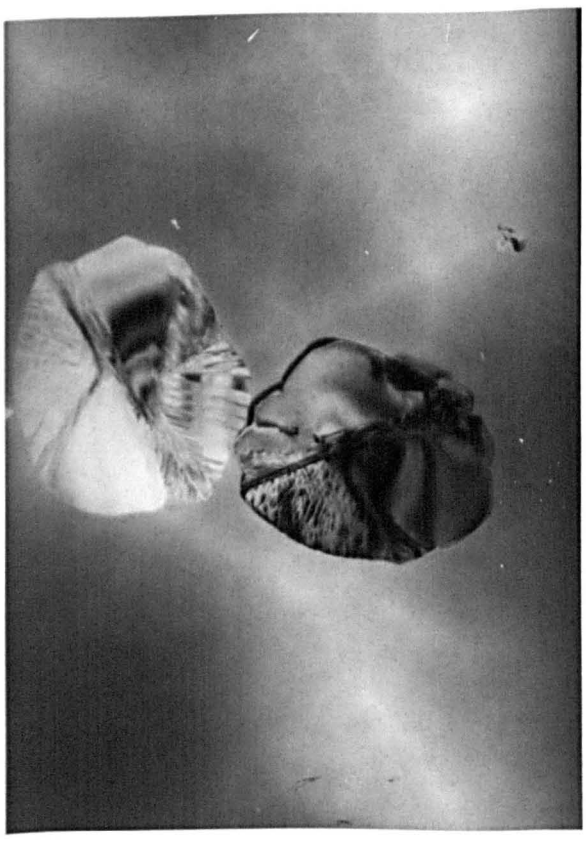

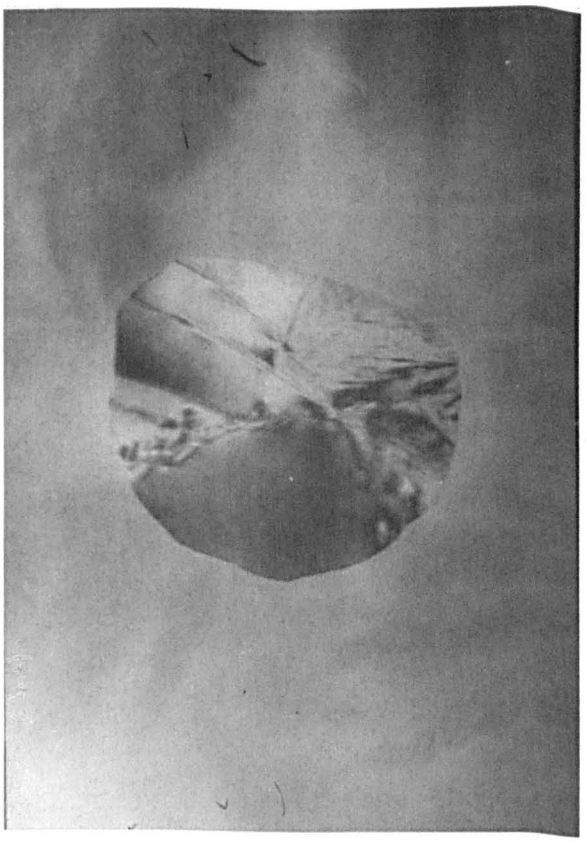

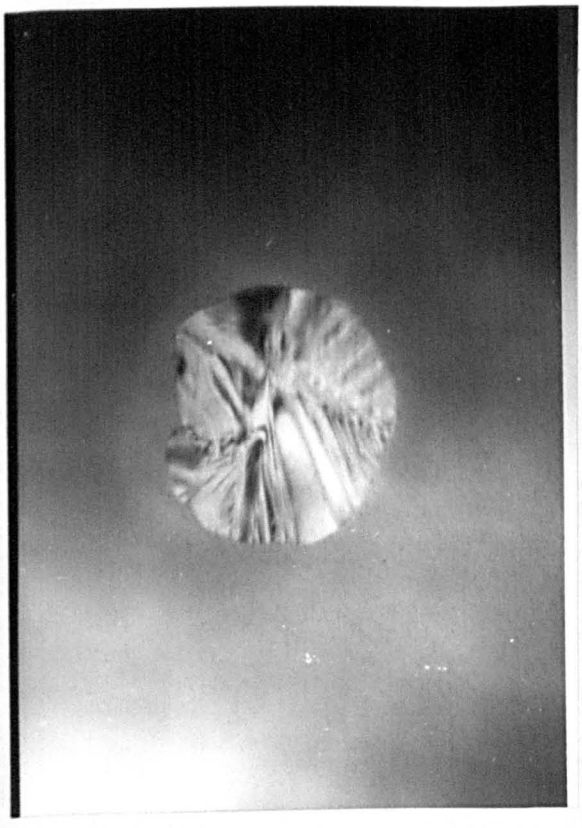

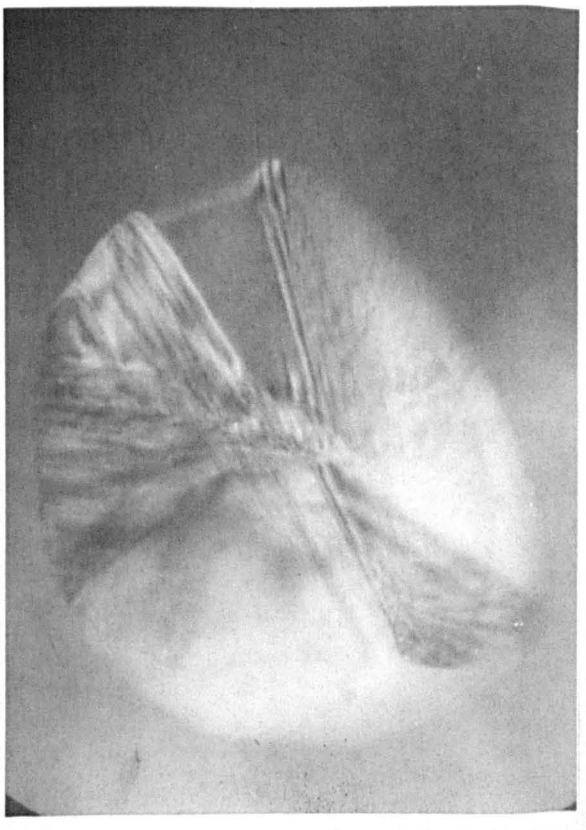

diffraction (SAD). In some cases it was also possible to use dark field microscopy. In general the glasses were given a long single nucleation treatment at low temperatures, in order to produce a large number of small crystals.

The d spacings were calculated from R(mm) x d(Å°) = L(mm) x λ(Å°) = C is the camera constant, L is the effective camera length, λ is the electron wavelength, R is the distance from the particular spot to the central one and d is the interplanar distance corresponding to that diffraction spot. The value of C was determined by taking diffraction patterns of orthorhombic α MoO_3 crystals using the same electron microscope settings. Very good diffraction patterns can be obtained for these crystals and very accurate d-spacing data exist.

In order to check the crystalline phase precipitated from the glasses G2 and G14, d-spacings were listed for all the diffraction patterns. The results for both glasses are shown in Table 3.9. There is very good agreement, within the experimental errors, between the d-spacings determined from the electron diffraction patterns and those obtained from X-ray diffraction for the low form of NC_2S_3.

A set of micrographs of crystals precipitated from glass G2 is shown in Figure 3.10a, b, c. The crystal in Fig. 3.10d gave a very strong diffraction pattern (Fig. 3.10e) which when indexed gave the zone axis (direction of electron beam) as [UV.W] = [00.1]. The diameter of the selected area for diffraction, as determined by the diameter of the diffraction aperture was 0.87 μm. Also

TABLE 3.9 LOW FORM $Na_2O.2CaO.3SiO_2$ d-SPACINGS FROM ELECTRON DIFFRACTION

d(E.M), A°		d(X-Rays), A°, *, Relative Intensity (X-Rays)
G2	G14	
7.38	7.40	7.519 30
5.32	5.34	5.342 14
5.26	5.22	5.260 10
4.27	4.26	4.397 46.5
4.16	4.14	4.099 6
	3.97	3.955 14
3.35	3.35	3.358 92
	3.29	3.309 138
3.15	3.19	3.157 7.5
3.01	3.04	3.033 19
2.93		2.947 8
2.63		2.616 162
	2.51	2.522 22
	2.49	2.489 10
2.37		2.373 8
2.27	2.26	2.275 9.5
	2.21	2.235 15
	2.13	2.140 22
2.08		2.084 11
	2.01	2.017 9
	1.98	1.997 15
1.93	1.96	1.957 12.5
1.86		1.865 101
1.73	1.73	1.737 15
	1.67	1.676 7.5
1.64		1.647 16.5
	1.61	1.596 8
1.57		1.576 7
1.52		1.521 28.5
	1.45	1.481 9
	1.43	1.416 5.8
1.41		1.411 5.0
1.39		1.394 18.0

* See Table 3.8

Figure 3.10d

Bright field electron micrograph of G2 heated at 578°C for 23 hr. Mag X45,260.

Figure 3.10e

Selected area diffraction pattern of crystal in Figure 3.10d.

Figure 3.10f

Dark field electron micrograph taken with the diffracting aperture around the ($4\bar{2}.0$) reflection. Mag X49,000.

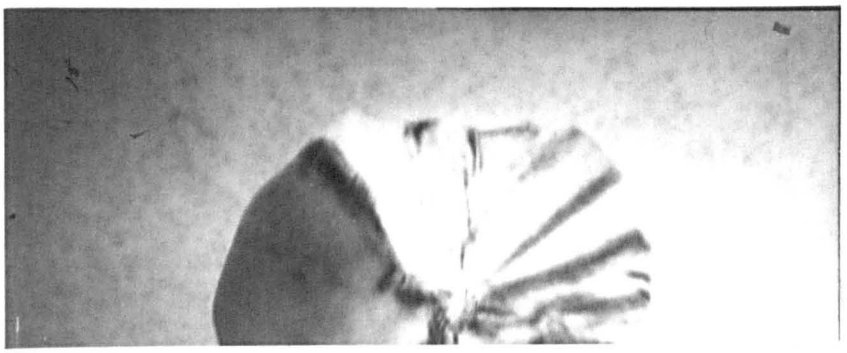

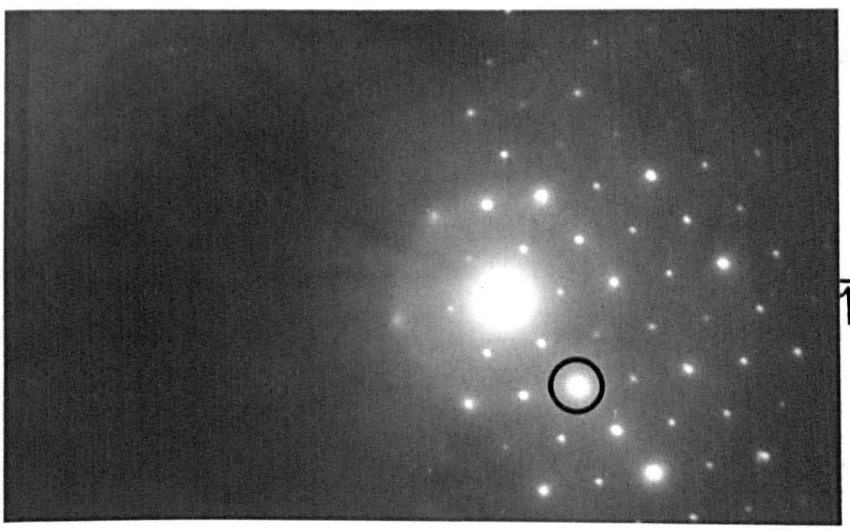

[U V.W]=[00.1]

$\bar{1}2.0$ ● 00.0

11.0 • • $2\bar{1}.0$

$4\bar{2}.0$

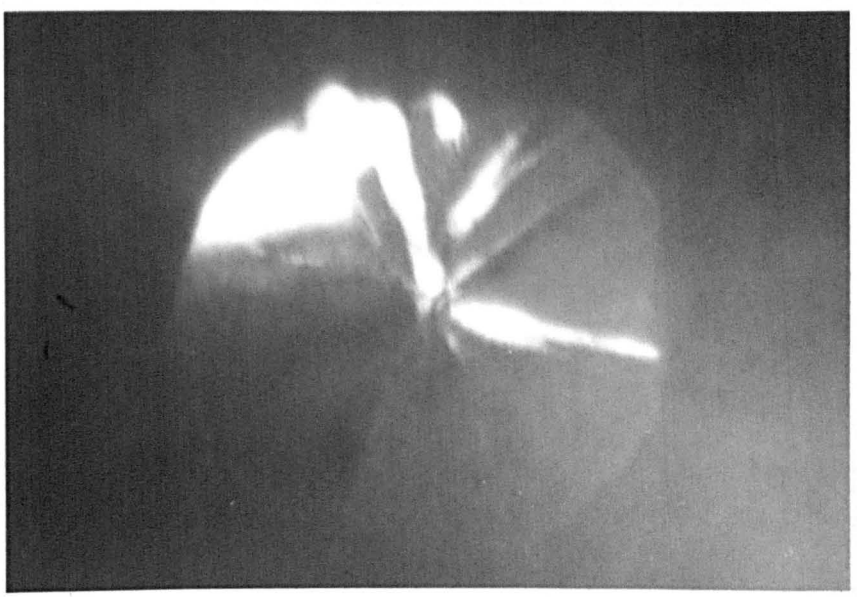

this applies to all the patterns that follow. The low resolution dark field micrograph of Fig. 3.10f was taken by placing the objective aperture around the $(4\bar{2}.0)$ spot. No attempt was made to obtain high resolution dark field micrographs by tilting the diffraction spots to the microscope axis, due to the beam damage giving insufficient time. The bright regions of the crystal are those diffracting particularly strongly with the $(4\bar{2}.0)$ reflection. Since only one diffraction pattern was detected it is suggested (tentatively) that this crystal was single and not compcsed of several crystals with different orientations.

For the crystal in Fig. 3.11a selected area diffraction patterns were taken in positions 1, 2 and 3. These are shown in Figures 3.11b, c and d respectively. The patterns are essentially the same. The spots in Figure 3.11d are streaked in the direction perpendicular to the band aa' in Figure 3.11a. This suggests the presence of planar defects, possibly stacking faults, in that band. No further observations on this crystal were made due to electron beam damage.

For the crystal in Figure 3.12a diffraction patterns were taken in regions 1, 2 and 3. In region 1 a single undistorted pattern was obtained (Figure 3.12b). Region 2 gave a few weak spots (Figure 3.12c). The pattern obtained from Region 3 (Figure 3.12d) is different from that for region 1 and also some streaking of the spots can be observed. Twinning may be present in this crystal.

Finally, diffraction patterns were taken from regions 1, 2 and 3 of the crystal in Figure 3.13a. The patterns were closely

Electron micrographs of G2 heated at 578°C for 23 hr

Figure 3.11a (top) Mag X24,800

Figure 3.12a (middle) Mag X24,800

Figure 3.13a (bottom) Mag X24,800

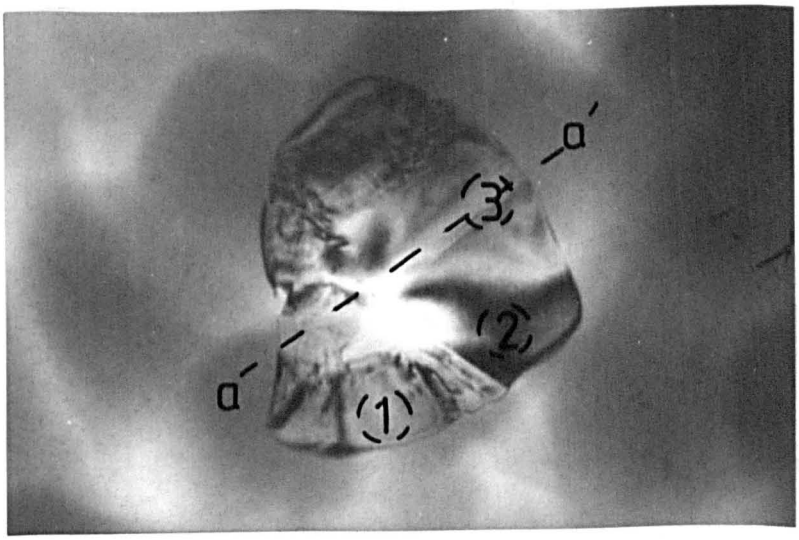
a'
3
2
a
1

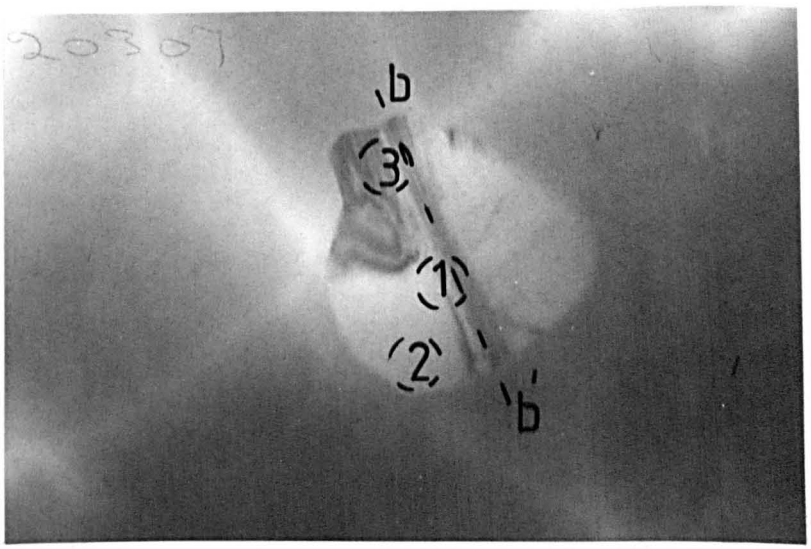
20307
b
3
1
2
b'

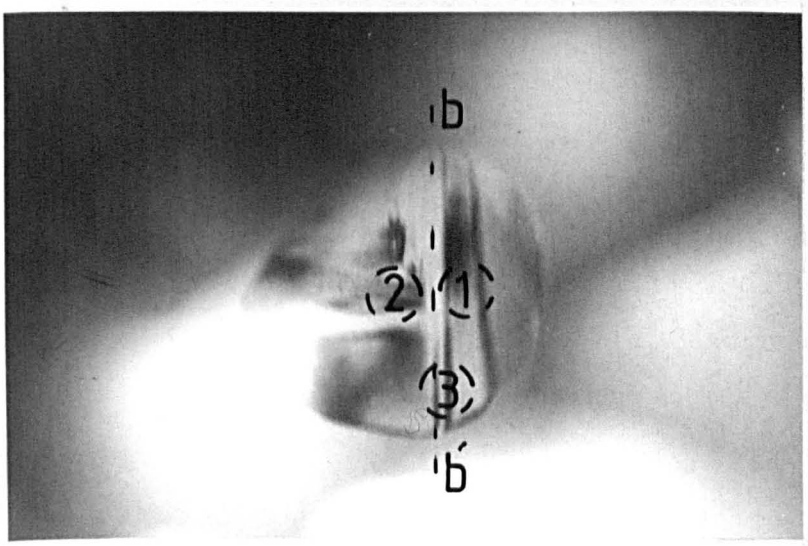
b
2
1
3
b'

Figures 3.11b,c and d

Selected area diffraction patterns (SAD) of crystal in Figure 3.11a.

Figure 3.12b,c and d

SAD of crystal in Figure 3.12a.

Figure 3.13b, c and d

SAD of crystal in Figure 3.13a.


①
②
③

similar suggesting essentially the same crystal orientation in all the regions. However in regions 1 and 3 pronounced streaking of the spots and the presence of double spots was observed. The streaking occurred also perpendicular to the band bb'. In region 2 little or no streaking could be observed. This suggests again the presence of stacking faults or twinning

Unfortunately, due to the beam damage, the chances of getting more than 3 or 4 different selected area diffraction patterns from the same crystal were very limited. However from this study some tentative conclusions can be drawn:-

(i) The crystalline phase detected in the early stages of growth is the same as that obtained from X-ray diffraction of fully crystallized bodies (the low form of NC_2S_3)

(ii) The crystals are probably single crystals containing imperfections. The most probable defects are stacking faults and/or twins.

(iii) No branching of the crystals was observed, i.e. the formation of branches with different orientations from the parent crystal as found, for example, for lithium disilicate (3.14).

(iv) The shape of the crystals is not a unique feature. Some crystals show a polyhedral shape whereas others are roughly spherical. Further information on this subject will be presented during the analysis of glass G16.

Further work is needed to understand the features observed. Hot stage electron microscopy studies might assist in the interpretation of the origin of the imperfections. It is possible that

the low form-high form polymorphic transformation observed at 480°C has a strong influence on the kind of defects detected.

3.2 Glass G16

The batch for this glass was prepared with high purity SiO_2 ('SILQUARTZ'). Glass G16 was melted in an attempt to assess the effect of trace elements on crystal nucleation and growth rates. The final composition is quoted in Appendix A2, (Table A2.1). The Na_2O content was 16.85 wt.% (16.06 mole%), the CaO content was 31.54 wt.% (33.21 mole%) and the SiO_2 content was 51.61 wt.% (50.73 mole%). This was close to the composition of glass G2 previously studied. The steady state nucleation rates and crystal growth rates were measured for this glass. In addition it was decided to check the nucleation rates obtained from the standard double stage heat treatment by counting the number of crystals produced after a single nucleation treatment directly in the transmission electron microscope. Although the nucleation rates for this glass were reasonably high, (for example compare the values in Figure 3.16 with the results for the $Li_2O.2SiO_2$ glass obtained by James (3.3)), at the magnifications needed to observe the crystals in the electron microscope the number of crystals in the field of view was very low. Therefore to count a reasonable number of crystals (say a hundred) it was necessary to obtain a large number of electron micrographs using a number of foils of the same glass. Thus the use of thin sections was impractical due to the long time required to prepare a ion beam thinned foil (on average 8 hours) and the large number of EM negative plates

needed. Carbon replication of the glass was not attempted because of the extra complications mentioned earlier in this chapter.

However determination of the number of crystals per unit volume N_v in glasses given a single stage nucleation treatment was possible using a stereoscan electron microscope. As in the case of the optical microscopy determinations, random cross sectional planes of the glass samples were analysed through equations (2.1) and (2.2) in order to obtain N_v.

3.2.1 Nucleation Rates

The number of crystals versus time at a given temperature calculated from equation (2.1) are presented in Figures 3.14, 3.15. The steady state nucleation rates and 'approximated' nucleation rates (N_v/t for 40 min) determined from optical microscopy as well as those from the SEM analysis are presented in Figure 3.16 and Table 3.10.

It can be observed from Figure 3.14 that appreciable non-steady state nucleation is present at lower temperatures. The lowest temperature analysed was 585°C where an intercept to of approximately 37.5 min (Table 3.10) was obtained. The slope of the plot at longer times gives the steady state nucleation rate (3.3) and the intercept (to) with the time axis gives an idea of the degree of the non classical nucleation effect (see Chapter 1). The slopes of the plots at a given temperature were analysed by the least squares method. For the plot at 585°C the points used were from (see Figure 3.14) 60 min upwards where the linearity is

FIGURE 3.14 CRYSTAL NUCLEATION DENSITIES Vs. TIME AT T=585 °C AND T=606.5 °C FOR GLASS G16

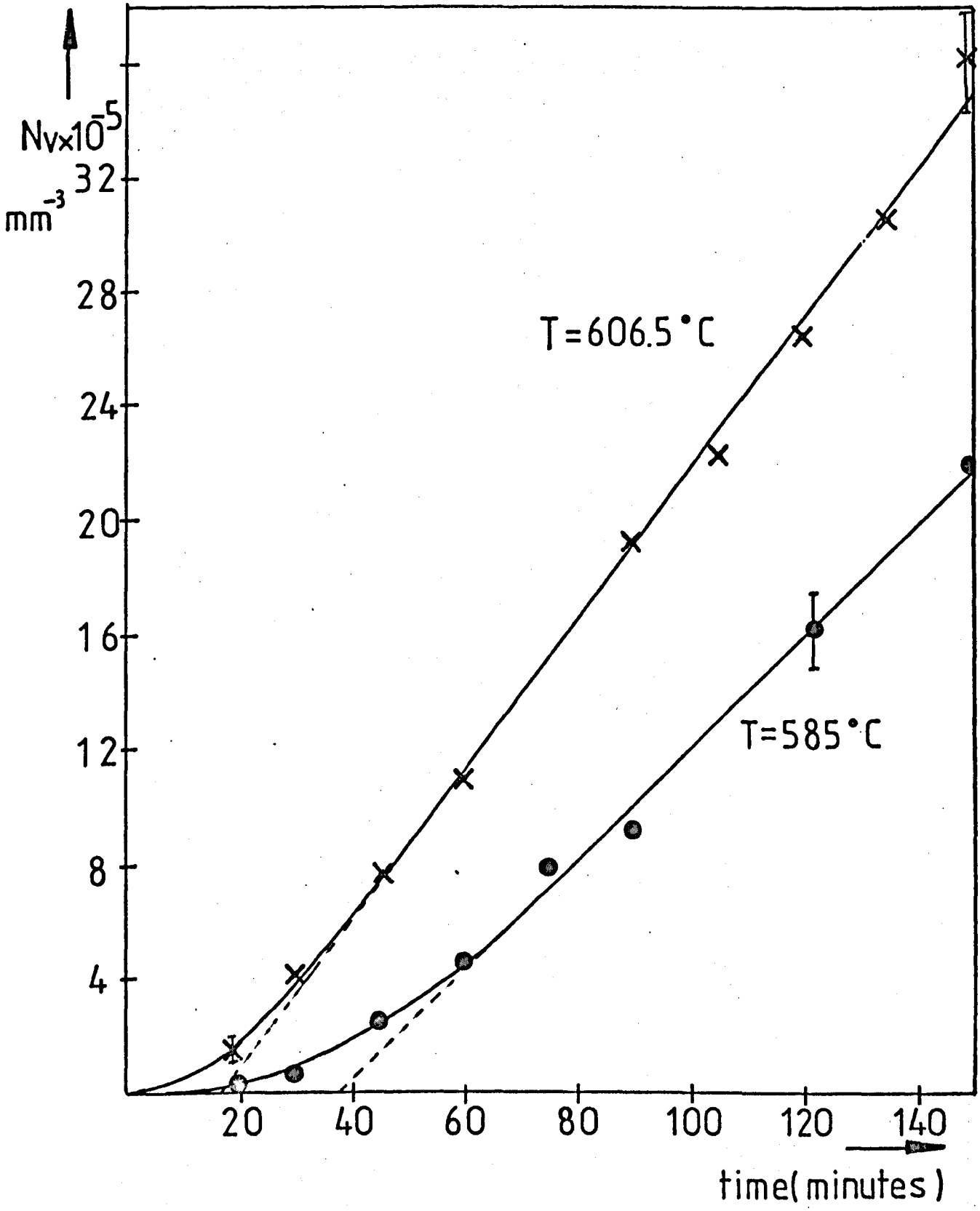

Error bars represent 10% relative uncertainty

$$\frac{\Delta Nv}{Nv} \times 100 = 10\%$$

FIGURE 3.15 CRYSTAL NUCLEATION DENSITIES Vs. TIME AT 620, 631.5 AND 655°C FOR GLASS G16

● 620°C, D.S ▲ 631.5°C, D.S × 655°C, D.S

○ " S.S △ " S.S + " S.S

S.S : Single stage heat treatment

D.S : Double " " "

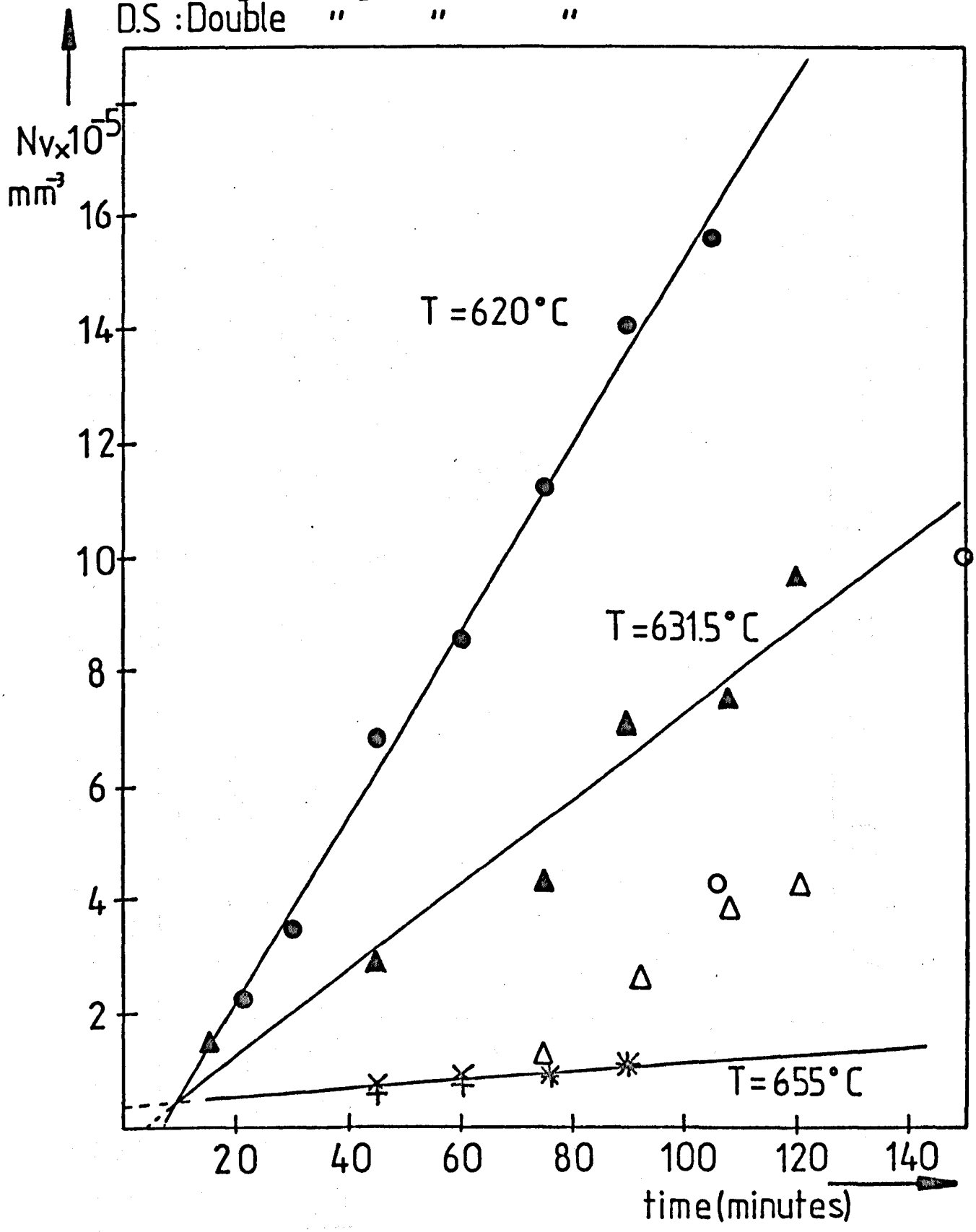

FIGURE 3.16 STEADY STATE NUCLEATION RATES AND APPROXIMATED NUCLEATION RATES AFTER 40min. FOR GLASS G16 AS A FUNCTION OF TEMPERATURE

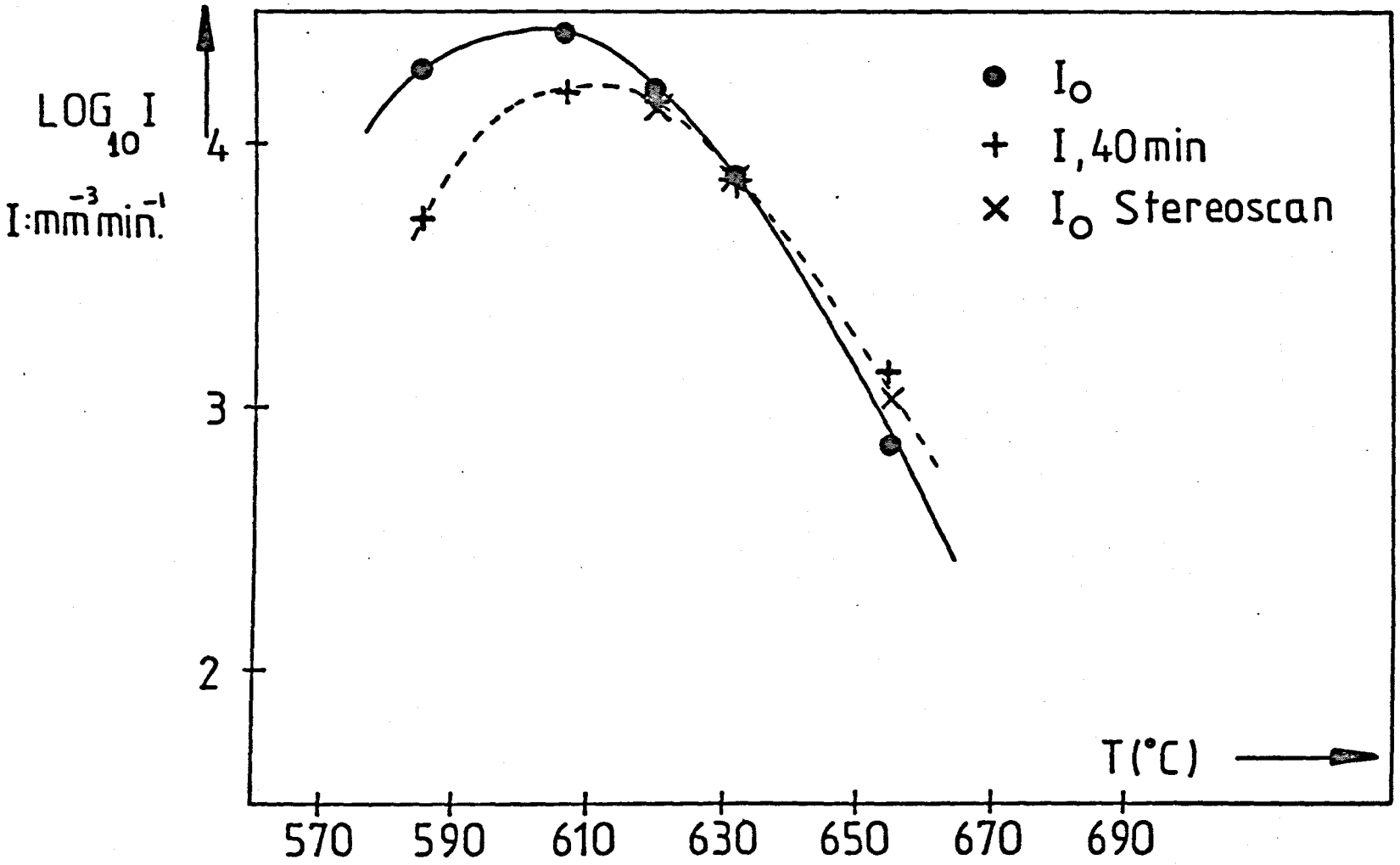

TABLE 3.10

NUCLEATION DENSITIES DATA FOR GLASS G16

Experimental technique	T(°C)	Steady state nucleation rate in nuclei mm^{-3} min^{-1}		Approximated nucleation rate after 40 min heat treatment in nuclei mm^{-3} min^{-1}		Intercept with time axis (see text) (min)
		I_o	$\log_{10} I_o$	$I = N_v/t$	$\log_{10} I$	
Double stage heat treatment	585	19225.3	4.28	5000	3.70	37.48
	606.5	26243.9	4.42	15250	4.18	17.08
	620	16331.1	4.21	13625	4.13	7.02
	631.5	7578.4	3.88	7000	3.85	4.24
	655	723.8	2.86	1625	3.21	-50.8
Single stage heat treatment	620	12970.3	4.11			
	631.5	6999.4	3.85			
	655	1068.9	3.03			

apparent. Increasing temperature gave shorter intercepts. For example at T = 606.5°C t_o was 17 min, at T = 620°C 7 min and at T = 631.5°C 4 min.

The steady state nucleation rate shows a maximum ($\log_{10}I_o \simeq 4.43$) at approximately 605°C. Increasing the temperature by 50°C above the maximum causes a drop in I_o of about one and a half orders of magnitude. The SEM results are also plotted in Figures 3.15 and 3.16. The agreement of the steady state nucleation rates from this method with the double state (DS) heat treatment method is good. However it should be noted that the number of crystals observed from the SEM analysis (single stage (SS) heat treatment) are lower than those produced by the DS heat treatment method for T = 620°C and T = 631.5°C. At T = 655°C it is difficult to detect any difference between the two methods, although least squares analysis gave a slightly higher steady state nucleation rate for the SS method (Table 3.10).

From nucleation theory (see Chapter 1) the size of the critical nucleus increases with increasing temperature. Hence critical nuclei at the lower (nucleation) temperature are smaller than the critical size at the upper (growth) temperature and should dissolve when the temperature is raised to the growth temperature (for G16 the nucleation range was 570-690°C and the growth range 720-730°C). In fact during the nucleation treatment the nuclei grow, often to an appreciable size. For example, consider the growth data from Figure 3.21 at 620, 631.5 and 655°C (the intercepts on the time axis will be discussed shortly). For these temperatures after times of 25, 19 and 0 min respectively the growth rates reach

constant values of 0.023, 0.065 and 0.240 μm min^{-1} respectively. Hence for a nucleation time of 100 min the corresponding sizes expected for the nuclei first formed (at t=0) are 2.11 μm (= (100-25) x 0.028) at 620°C, 5.2 μm at 631.5°C and 24 μm at 655°C. For a nucleation time of 30 minutes the corresponding sizes would be 0.14 μm (= (30-35) x 0.028), 0.69 μm and 7.2 μm at the three temperatures. The size of the critical nuclei for the NC_2S_3 glass cannot be computed at this stage because the interfacial free energy σ is not known (this will be estimated from the theoretical analysis of the nucleation rates in a later chapter). However the ratio of the critical sizes at two different temperatures can be estimated from the formula for a spherical nucleus $r(T) = -\frac{2\sigma V_m T_m}{\Delta H_f (T_m - T)}$ (see Chapter 1) by assuming that changes in σ V_m with temperature are negligible. Hence $\frac{r(T')}{r(T)} = \frac{1561-893}{1561-1003} = 1.197$ where T_m = 1501°K (1288°C), T' = 1003°K (730°C) and T = 893°K (620°C). If, as an approximation we take a reasonable value of 20 Å (see Reference (3.3)) for the critical radius at say 620°C, this would give at 730°C a critical radius of approximately 24 Å. So it can be seen that the great majority of the crystals should have reached sizes larger than the critical size at the growth temperature before the second stage treatment. A second assumption involved in the DS method is that the nucleation rate at the growth temperature is negligible (see Reference (3.3)). This condition was also satisfied for the glasses studied in this work.

The number of crystals obtained with the stereoscan are never

larger than the number of crystals obtained from the DS method. In fact the stereoscan values are very low at low temperatures compared with the DS values. The reason for this effect is the very small sizes of the crystals as can be seen from the analysis above giving the maximum sizes expected for a typical nucleation time of 100 minutes. The smaller the crystals, the more difficult they are to detect in a random cross-sectional plane through the specimen. Since the stereoscan has a limited resolution a large number of the small crystals will not be observed. In fact it can be observed (see Figure 3.15) that at higher temperatures (where the growth rates are higher) both methods gave similar results.

Finally it is interesting to compare the steady state nucleation rates with the approximated nucleation rates calculated from N_V/t where t is the nucleation time. It can be seen in Figure 3.16 that the agreement between both is very good for temperatures higher than approximately 610°C. Below 610°C the agreement is not as good, the difference being half an order of magnitude at 585°C

Further analysis of the 'incubation time' effect in this glass will be presented in the discussion chapter.

3.2.2 Growth rates

Growth rates were obtained by measuring the maximum diameter of the particle cross sections in the optical microscope. The glasses were heat treated at a given temperature for different periods of time. The crystal sizes were also measured in thin

glass foils with the electron microscope. The electron microscope showed clearly the crystal morphology in the early stages of growth. For non-spherical particles the size measured was the largest calliper diameter that could be found.

In Figure 3.17 a series of optical micrographs of glass G16 shown for different times at 631.5°C. In Figure 3.18 the corresponding electron micrographs are shown.

The crystal sizes vs time for each temperature are summarized in Figures 3.19 and 3.20. It is apparent that these plots are linear. There is also a positive intercept with the time axis at 655°C, 631.5°C, 620°C and 606.5°C. The slopes of the plots (growth rates) and the intercepts were calculated by least squares analysis. The results are given in Table 3.11. The crystal growth rates as a function of temperature are plotted in Figure 3.21. Although the intercepts tend to increase with decreasing temperature the intercept at 606.5°C (approximately 20 min) is smaller than the intercept at 620°C. In order to check this behaviour the experiment was repeated for glass G2. Because of the lack of time only optical microscopy was used. A series of micrographs for G2 heated for different times at a given temperature are shown in Figure 3.22. The plots of size vs time are shown in Figures 3.23 and 3.24. The plot for glass G2 at T = 678°C was presented in Figure 3.4 earlier in this chapter. The growth rates and intercepts (again using least squares analysis) are given in Table 3.12. Although the growth rates for glasses G2 and G16 are close (see Figures 3.5 and 3.21) the intercepts are significantly different. For example glass G2 gives an inter

cept of 42.3 min at T = 619°C (growth rate = 0.330 x 10^{-1} μm min^{-1}) whereas glass G16 at T = 620°C gives 24.6 min (growth rate = 0.286 x 10^{-1} μm min^{-1}). An attempt to explain the origin of these intercepts will be presented in a later chapter.

Finally let us consider the crystal morphology of G16. First a change of crystal morphology occurred with temperature. For example, glass G16 when heated at 631.5°C for 75 min or when heat treated at 655°C for 45 min (Figure 3.25), showed crystals with an almost perfect spherical shape. However for the same glass heated at lower temperatures, for example at T = 620°C for 75 min (Figure 3.26), the crystals had a polyhedral shape.

Secondly a change in morphology with time at constant temperature was observed at lower temperatures. For example, G16 heated at T = 620°C for 75 min (Figure 3.26) showed crystals with a sharp edged polyhedral shape whereas after 90 min the crystals had a more rounded polyhedral shape (Figure 3.27). It must also be stressed that even the latter morphology was different from the spherical shape obtained at higher temperatures (Figure 3.28) for similar heat treatment times.

3.2.3 Viscosity measurements

Viscosity data for G16 obtained between 570°C and 650°C as previously described, is shown in Figure 3.29. The Fulcher equation, fitted to the low temperature data for G16 and to the high temperature range data of the glass G2 (it was assumed that the viscosities of G16 and G2 were close at high temperatures) was as follows:

Figure 3.17a,b

Optical micrographs of G16 heated at 631.5°C for (a) 122 min and (b) 108 min. Mag X504.

Figure 3.18a (top right), b (bottom left), c (middle) and d (bottom right)

Electron micrographs of G16 heated at 631.5°C for (a) 122, (b) 108, (c) 92 and (d) 75 min. Mag X2838.

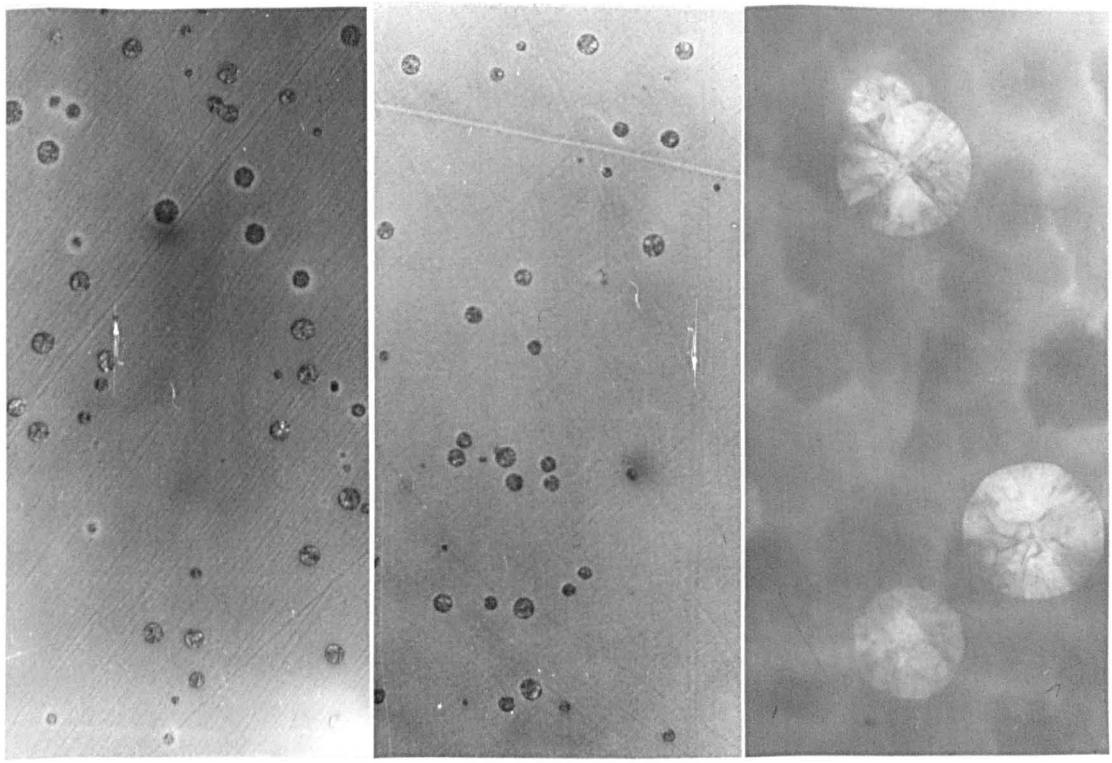

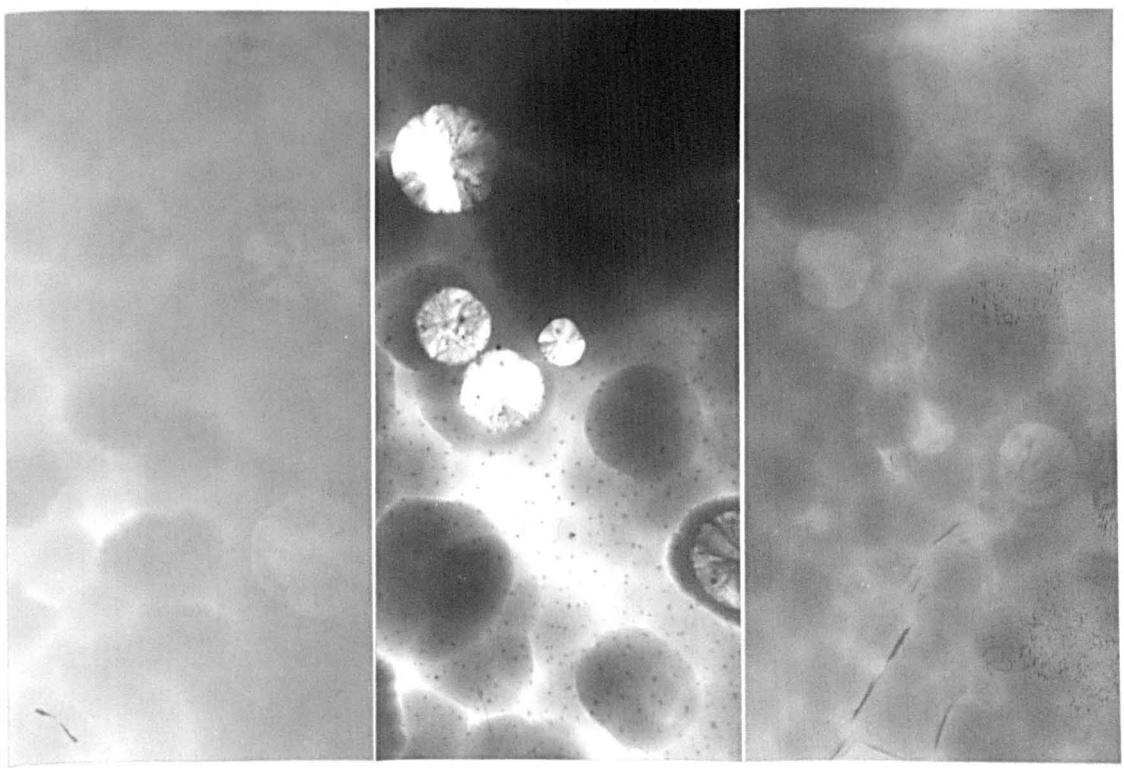

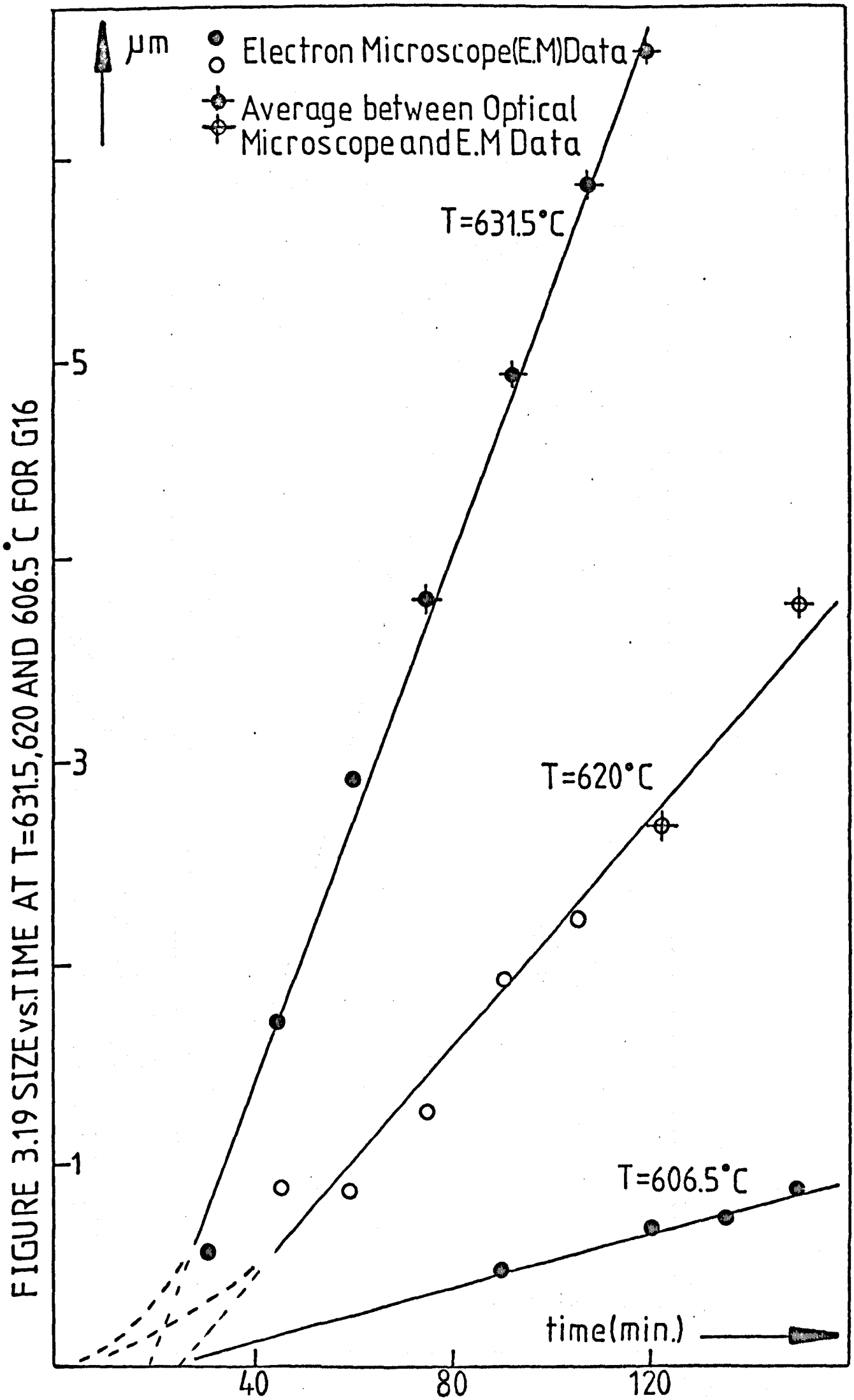

FIGURE 3.19 SIZE vs TIME AT T=631.5, 620 AND 606.5 °C FOR G16

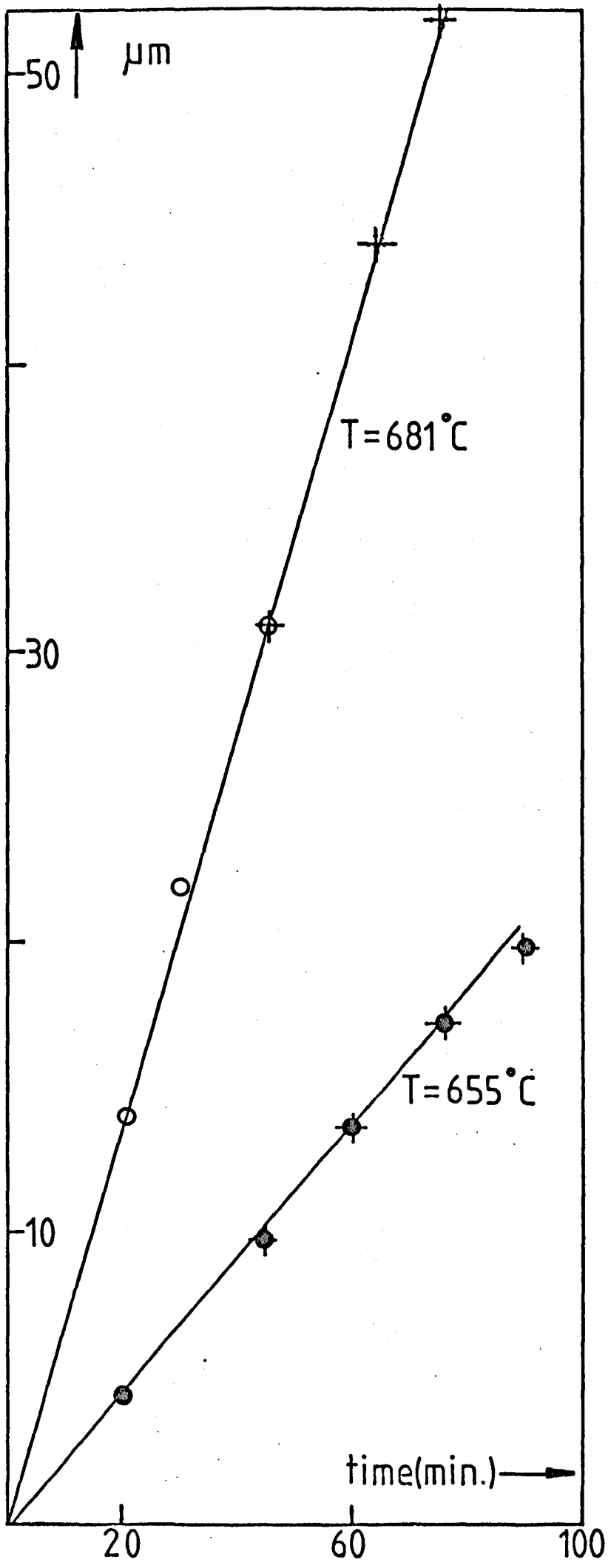

FIGURE 3.20 SIZE vs. TIME AT T=681 and 655 °C FOR GLASS G16
o, ● Electron Microscope Data
+ Optical " "

TABLE 3.11

'STEADY' GROWTH RATES AND INTERCEPTS DATA FOR GLASS G16 AFTER LEAST SQUARES ANALYSIS

T(°C)	Growth rate $\mu \times 10^3$ ($\mu m\ min^{-1}$)	Intercept (minutes)
606.5	0.665	20.69
620	28.64	24.62
631.5	66.39	19.33
655	232.00	- 0.01
681	675.60	0.00

TABLE 3.12

'STEADY' GROWTH RATES AND INTERCEPTS DATA FOR GLASS G2 AFTER LEAST SQUARES ANALYSIS

T(°C)	Growth rate $\mu \times 10$ ($\mu m\ min^{-1}$)	Intercept (minutes)
619	0.330	46.29
631	0.506	9.43
654	2.366	11.56
678	6.357	-0.42

FIGURE 3.21 GROWTH RATE AS A FUNCTION OF TEMPERATURE FOR GLASS G16

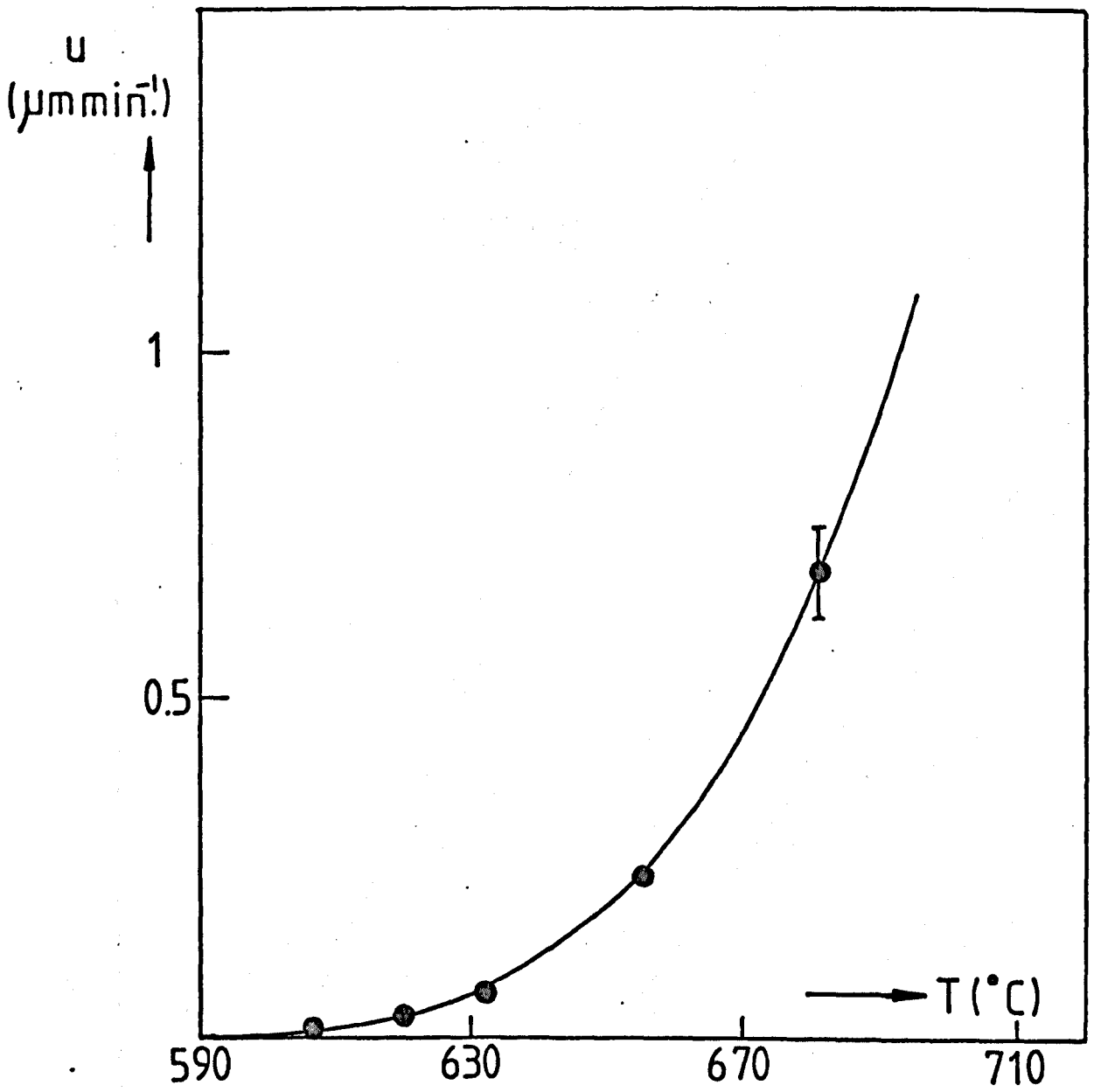

FIGURE 3.23 SIZE vs. TIME AT T=631 and 619°C
FOR GLASS G2

× Optical Microscope Data

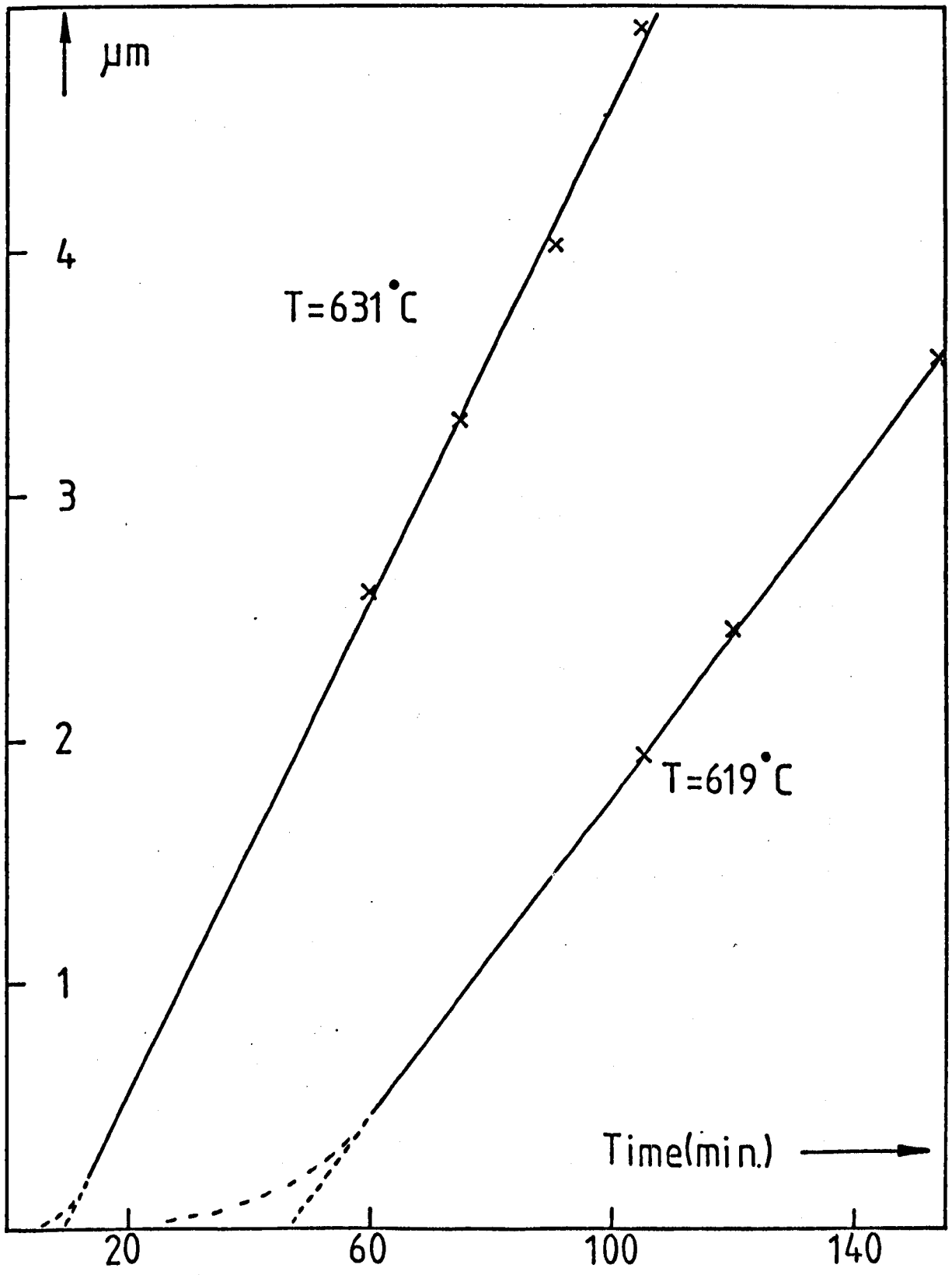

FIGURE 3.24 SIZE vs.TIME AT T=654°C FOR G2

× Optical Microscope Data

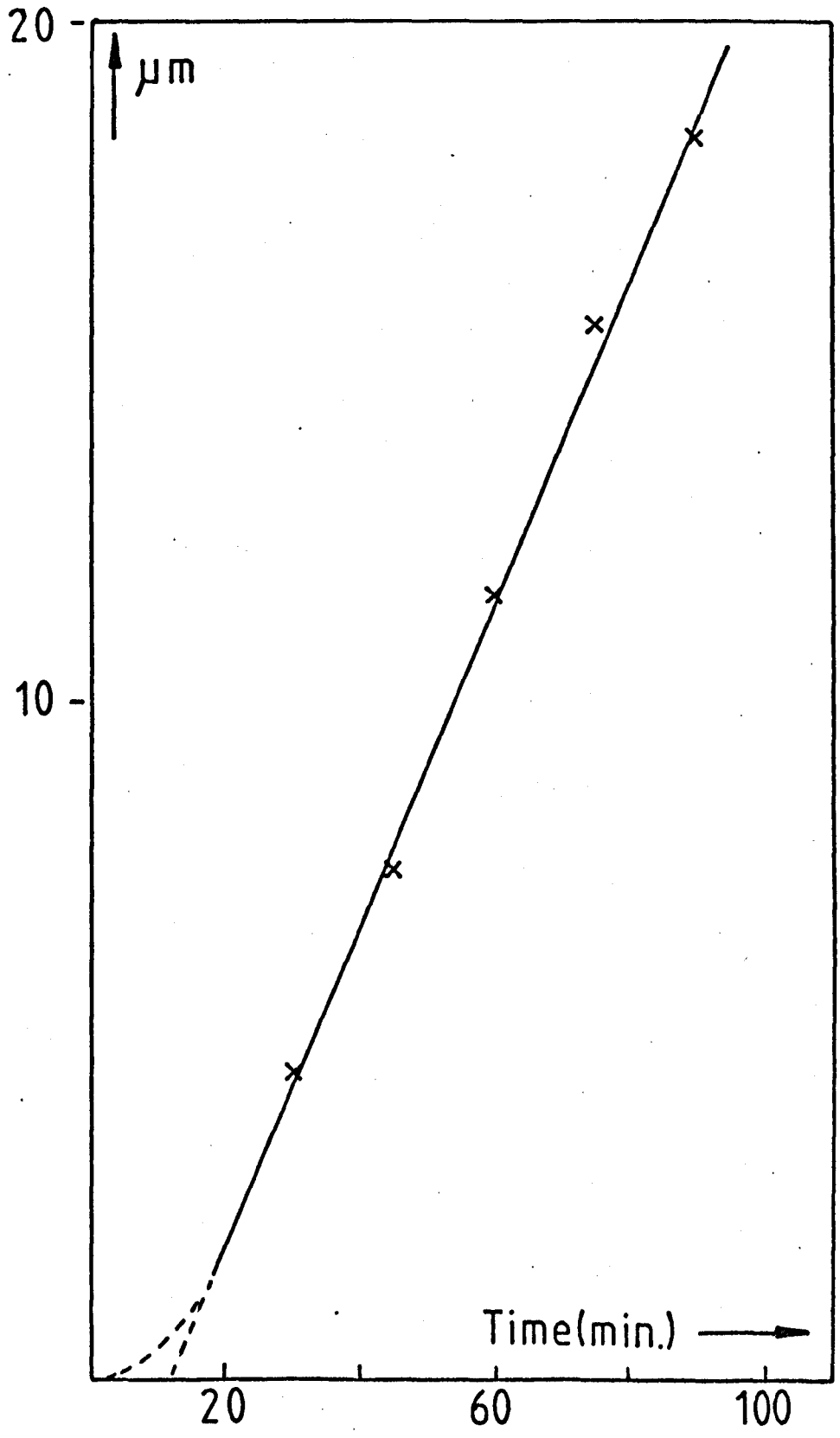

Figure 3.25

Electron micrograph of G16 (see text). Mag X16,000

Figures 3.26, 3.27 (top right)

Electron micrographs of G16 (see text). Mag X16,900; 10,600

Figure 3.28

Electron micrograph of G16 heated at 631.5°C for 92 min
Mag X21,000

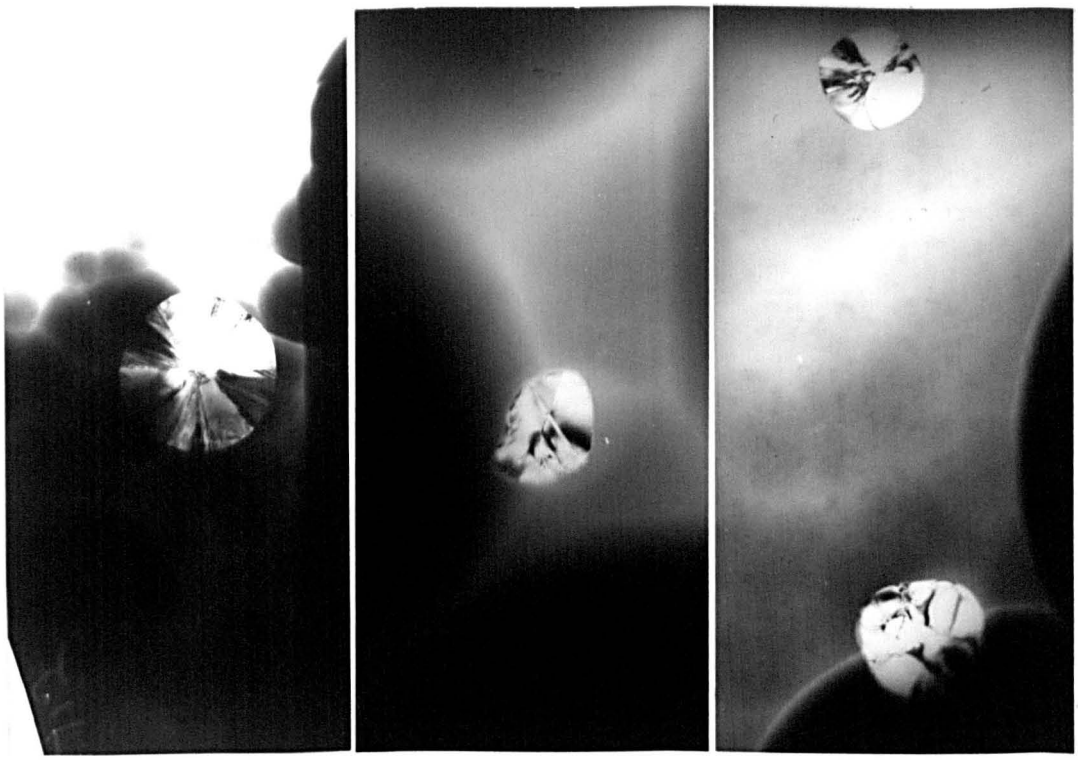

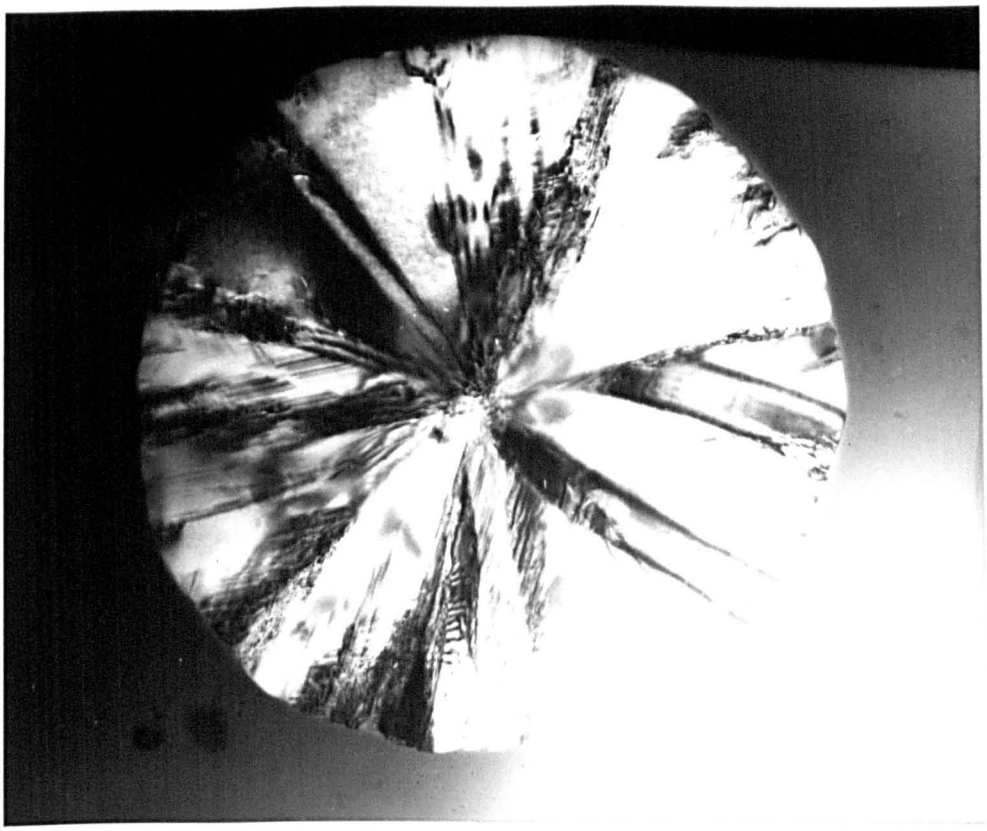

FIGURE 3.29 $Log_{10}\eta$ AS A FUNCTION OF TEMPERATURE FOR GLASSES G16 AND G17

● G16
○ G17

Curves Acc.To Fulcher Equations(see text)

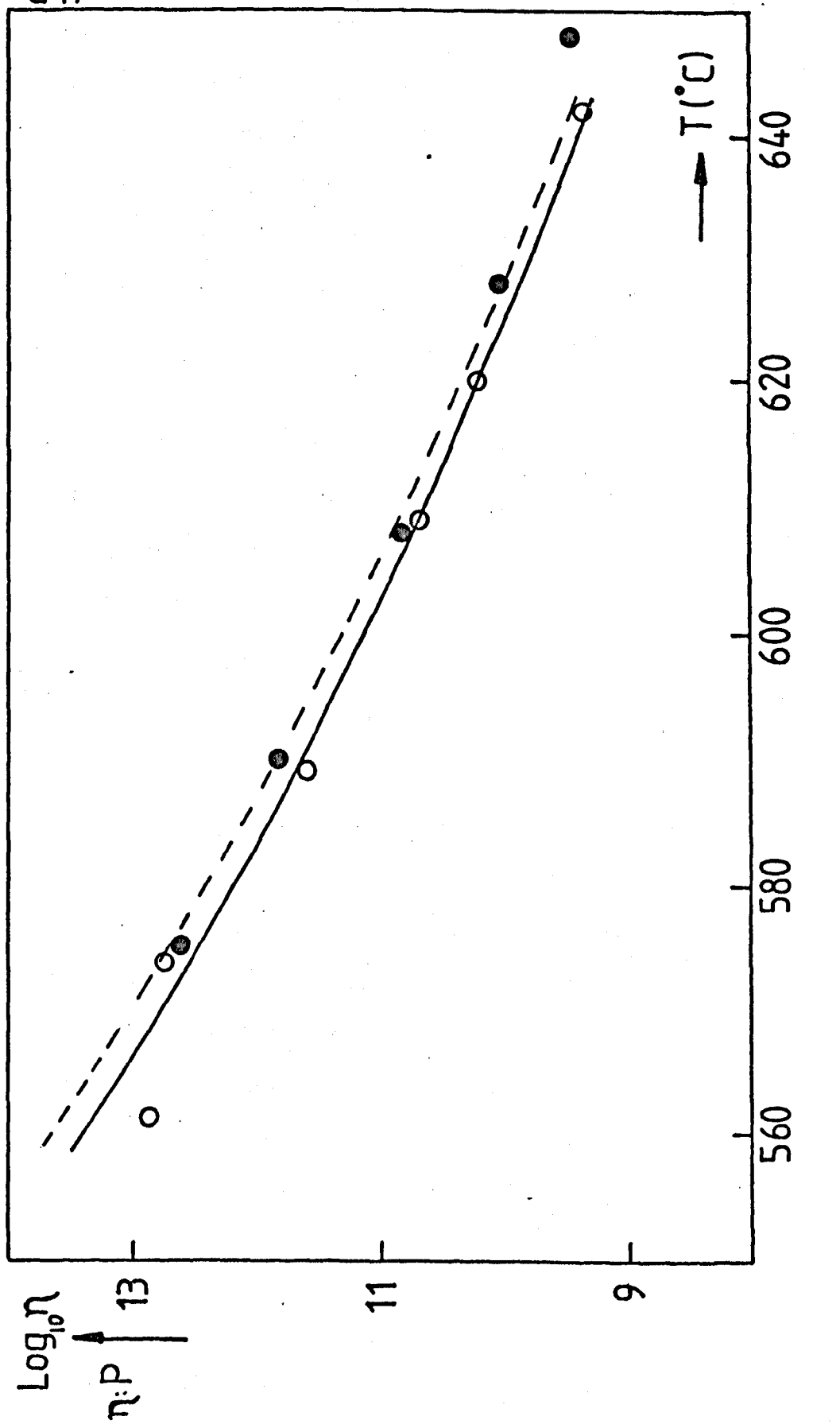

$$\log_{10}\eta = -3.367 + \frac{4224.9}{T-311.9} \qquad (3.8)$$

From equation (3.8) $\log_{10}\eta = 13$ corresponds to 570°C. The values obtained for G2 and G17 were 564.7°C and 565.7°C respectively. In Figure 3.29 the viscosity curve for G17 (from equation (3.3)) is also plotted for comparison purposes. G16 is slightly more viscous than G17 at low temperatures. However the difference in the $\log_{10}\eta$ values is never larger than 0.3. More information on the effect of glass composition on the viscosities at lower temperatures, for glasses near to the stoichiometric $Na_2O.2CaO.3SiO_2$ composition, will be presented later in this chapter. It should be mentioned that two values obtained at approximately 650°C and 660°C for G16 were discarded due to the presence of crystallization as confirmed by the optical microscope.

3.2.4 DTA and X-ray diffraction results

The 'DTA Tg' value obtained was 582.5°C. This is higher than the 579°C obtained for G2 but the difference in values is small when the uncertainty of ±3°C is considered (section 3.1.4a).

The DTA charts for G16 and G2 were very similar. The peak corresponding to the high form to low form transformation of the $Na_2O.2CaO.3SiO_2$ phase was clearly observed. Following the procedure explained in section 3.1.4b the heats of crystallization (ΔH_c), fusion (ΔH_f) and high to low transformation (ΔH_r) were determined. The values, which correspond to the average obtained from the NaCl and NaF calibrations, were as follows:

$$\Delta H_f = 20.6 \pm 1.0 \text{ kcal mole}^{-1}$$

$$\Delta H_c = 13.5 \pm 0.7 \text{ kcal mole}^{-1}$$

and $$\Delta H_r = 0.91 \pm 0.05 \text{ kcal mole}$$

Within the experimental errors these values are the same as obtained for G2.

Finally X-ray diffraction confirmed that the crystalline phase precipitating in G16 was the low temperature form of $Na_2O.2CaO.3SiO_2$.

3.3 Glasses around the stoichiometric $Na_2O.2CaO.3SiO_2$ composition

Little information was available on the effect of glass composition on the kinetics of crystal nucleation for glasses close to the NC_2S_3 composition. It was decided to investigate this point by studying six glasses close to the G17 glass (nominally the NC_2S_3 composition). The nominal compositions of these glasses are given in Table 2.1. Although these glasses were not chemically analysed it is probable that the final compositions are very close to the nominal ones. Thus on the basis of the losses of 0.4 wt.% Na_2O and 0.2 wt.% CaO found after chemical analysis of G2, it is reasonable to assume that approximately the same losses apply to these glasses. Additional amounts of Na_2CO_3 and $CaCO_3$ were added to the nominal batches to correct for the expected losses of Na_2O and CaO. The six chosen glasses consisted of three 'pairs' of compositions. For each pair the oxide content of one component was decreased (first composition) by 1 mole% and increased (second

composition) by 1 mole% with respect to the nominal oxide content for the exact NC_2S_3 composition. In other words the point on the ternary diagram NC_2S_3 was joined to either the 100% Na_2O, CaO or SiO_2 corner, and on each line a pair of compositions, placed symmetrically on either side of NC_2S_3 were selected. The compositions are shown schematically in Figure 3.30 and listed in Table 3.13.

Low temperature viscosity data was obtained for each of the six glasses. It was assumed that the viscosities at high temperatures were very close to G2. Although there are no high temperature viscosity data in this region of the system it seems reasonable to assume that the above approximation holds to within a 0.2 change in $\log_{10}\eta$. Support for this assumption may be drawn from a consideration of the high temperature isokoms in the soda-lime-silica system quoted in Morey's book (3.15). As will be shown later in this chapter the final least squares fitting of the Fulcher equation (2.8) using the measured low temperature viscosities and the approximated high temperature data for the six glasses produced a very reasonable interpolation of the experimental points at low temperatures.

In the following sections the viscosities of the glasses G18 to G23 are compared in each case with the viscosity of G17 which was closest to the exact NC_2S_3 composition. G17 was melted under the same conditions as G18-G23 with the same correction for expected losses of Na_2O and CaO. The Fulcher constants A, B and T_o and the temperature at which $\log_{10}\eta = 13$ for the glasses G18 to G23 are listed in Table 3.14. The nucleation results for glasses G18 to G23

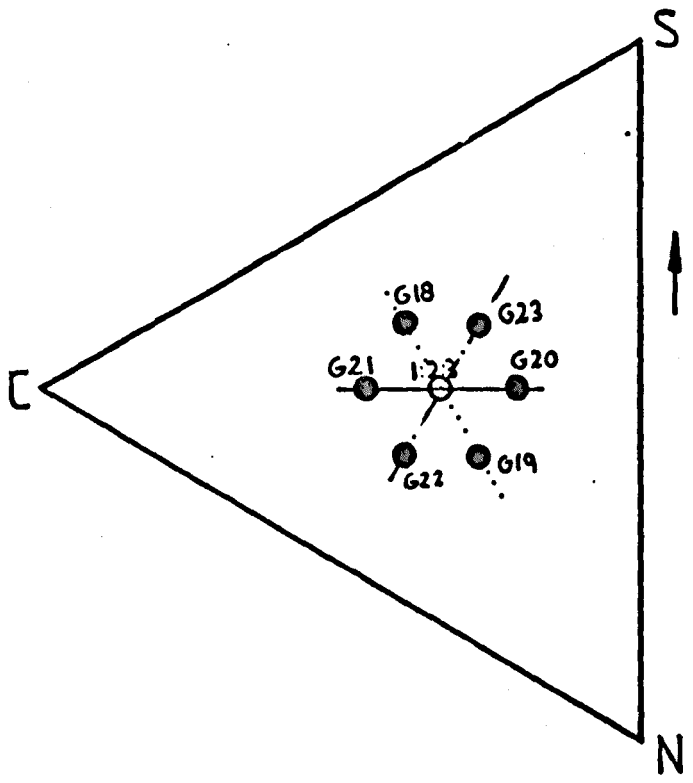

FIGURE 3.30

Schematic positions, in the N-C-S system, for the glasses in section 3.3.

TABLE 3.13

Glass Code	Nominal oxide compositions in mole% Na_2O	CaO	SiO_2
G18	15.65	33.74	50.61
G19	17.65	32.93	49.41
G20	16.92	32.33	50.75
G21	14.62	34.33	49.25
G22	17.0	34.0	49.00
G23	16.33	32.7	51.00

TABLE 3.14

Glass Code	Fulcher Parameters A	B	T_o(°C)	Temperature (°C) at which $\log_{10}\eta = 13$
G18	-2.667	3356.7	359	573.3
G19	-2.124	2800.6	371.5	556.7
G20	-2.398	3079.0	365.3	565.3
G21	-2.796	3576.4	332.6	559.0
G22	-2.502	3220.8	352.7	560.5
G23	-3.067	3859.9	328.5	568.8

were compared with G2 which was also close to the NC_2S_3 composition and had already been extensively studied. The DTA and growth rates results are summarized in Table 3.15.

3.3.1 Glass G18

The composition of this glass was 15.65 mole% Na_2O, 33.74 mole% CaO and 50.61 mole% SiO_2.

3.3.1.1 Nucleation rates

Approximated nucleation rates were obtained as described previously for a nucleation time of 40 min by using the two stage heat treatment method. The nucleation rates are shown in Figure 3.31 and data for G2 are also shown for comparison. The nucleation rates for this glass were less than for G2. The maximum occurred at about the same temperature as for G2 (617°C) and the maximum nucleation rate was 3.72×10^3 mm^{-3} min^{-1}.

A typical optical micrograph used for the nucleation rate determinations is shown in Figure 3.32. The crystals were generally spherical. For the particular nucleation treatment used (675°C for 40 min) there was no need of a second stage growth treatment. Thus the growth rate at 675°C could be estimated. This was 0.56 μm min^{-1} which was slightly lower than the growth rate for G2 at the same temperature (approximately 0.58 μm min^{-1}). An electron micrograph for G18 nucleated for 40 min at 603°C and grown at 730°C for approximately 3 min is shown in Figure 3.33. Again the crystal shape appeared to be almost perfectly spherical.

TABLE 3.15

Glass Code	ΔH_c (cal/g)	ΔH_f (cal/g)	'DTA Tg' (°C)	Growth rates at 675°C in $\mu m\ min^{-1}$
G18	38.4 ±1.9	50.5 ±2.5	590	0.56
G19	35.8 ±1.8	59.3 ±3.0	571	0.52
G20	37.0 ±1.8	49.4 ±2.5	578	0.97
G21	35.8 ±1.8	62.4 ±3.1	578	0.46
G22	38.1 ±1.9	61.5 ±3.1		0.56
G23	33.0 ±1.7	45.4 ±2.3	585	0.67
G2	35.9 ±1.9	58.2 ±2.9	579	0.58

FIGURE 3.31 $Log_{10}(Nv/t)$ AS A FUNCTION OF TEMPERATURE FOR G19, G18 and G2

⊕ G19, ● G2, ○ G18

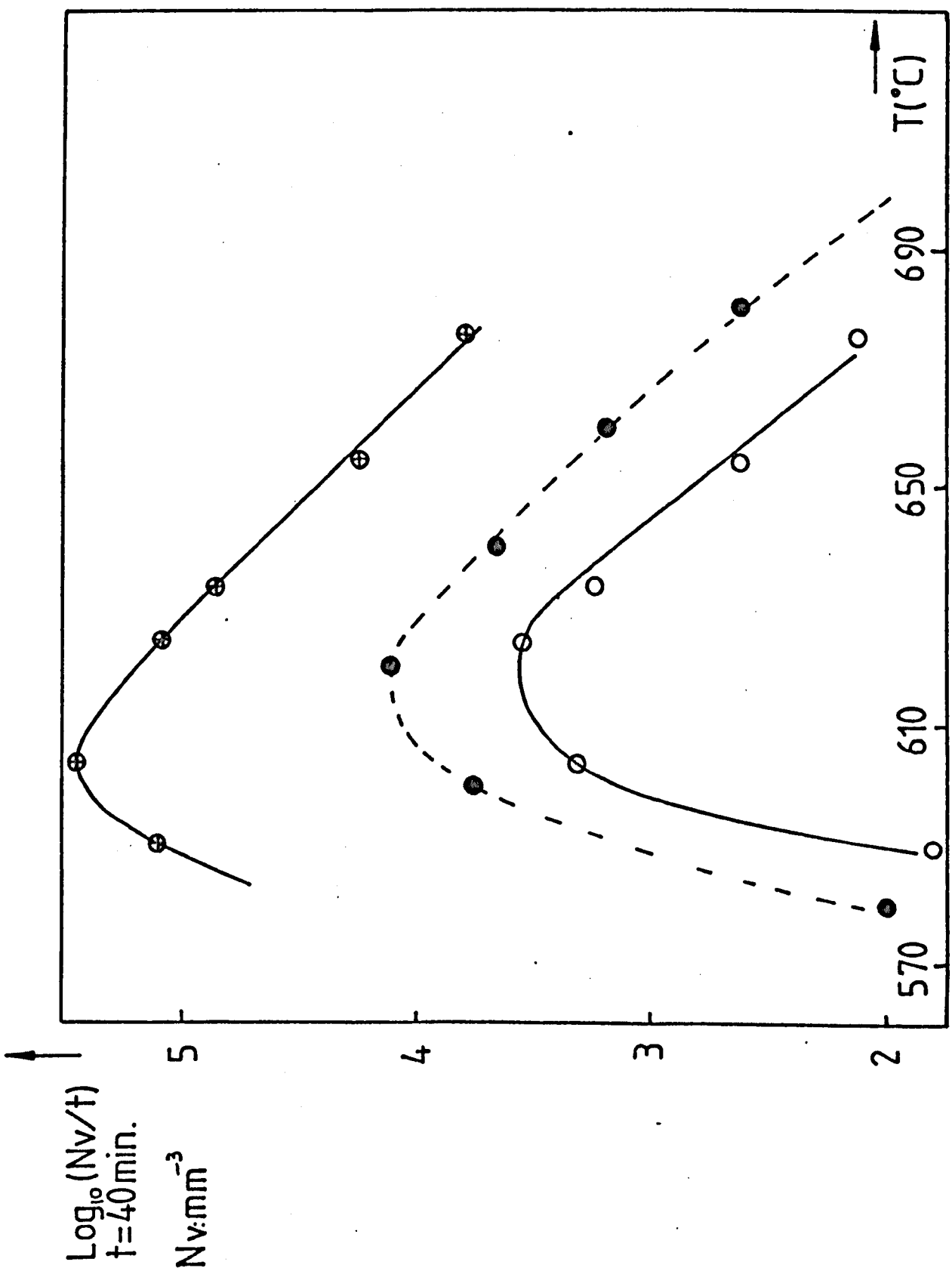

Figure 3.32 (top left)

Optical micrograph of G18 (see text). Mag X101.

Figure 3.33 (top right)

Electron micrograph of G18 (see text). Mag X7,300.

Figure 3.35 (bottom left)

Optical micrograph of G19 heated at 675°C for 40 min. Mag X504.

Figure 3.36 (bottom right)

Electron micrograph of G19 (see text). Mag X48,200.

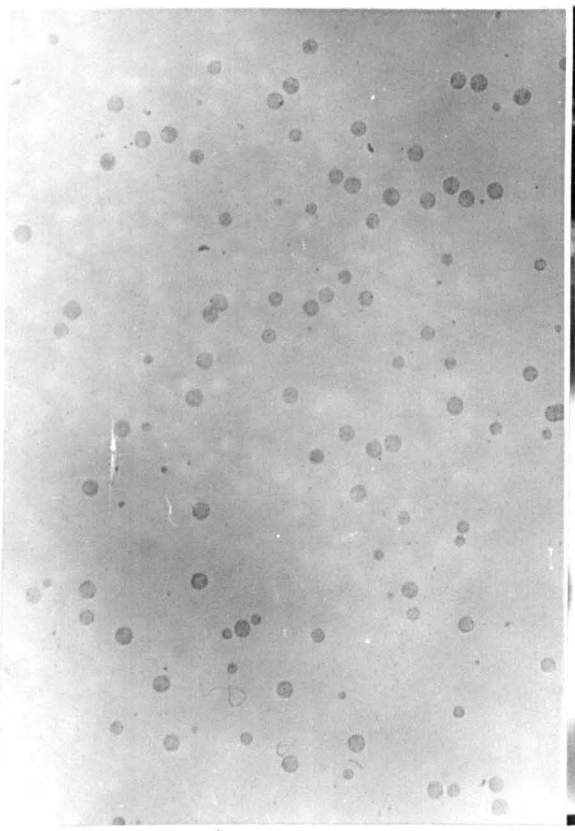

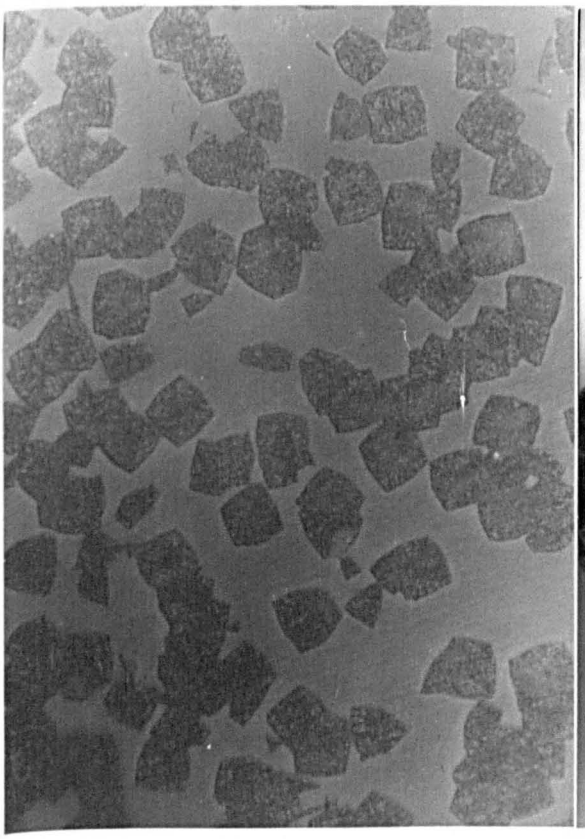

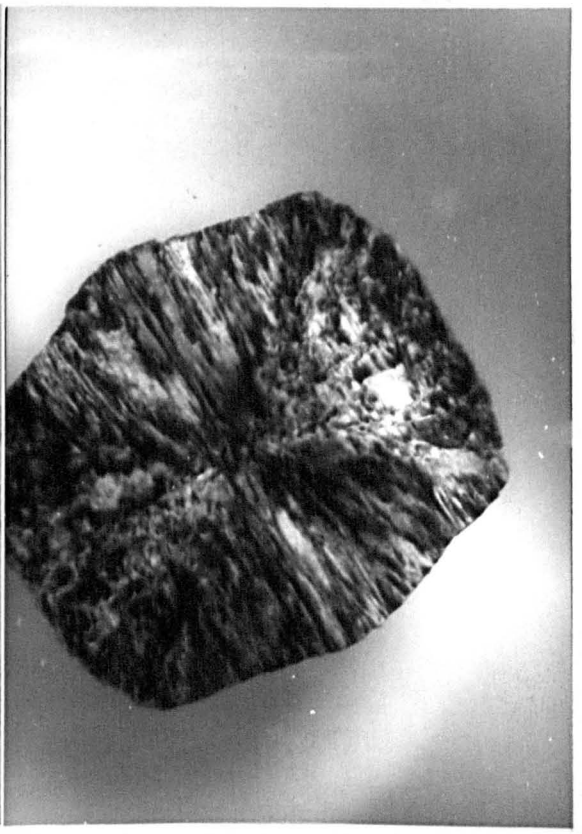

3.3.1.2 Viscosity data

The measured viscosities are shown in Figure 3.34. The curve resulting from fitting the data to the Fulcher equation is also plotted. The Fulcher constants are listed in Table 3.14.

The viscosity curve for glass G17 is also shown for comparison. The viscosity for G18 is higher than G17 particularly at low temperatures, at 570°C the difference in $\log_{10}\eta$ being about 0.5.

3.3.1.3 DTA

The DTA trace for G18 was very similar to that for G2. It was also possible to observe on the cooling cycle (10°C min^{-1}) the peak corresponding to the reversible transformation mentioned in sections 3.1 and 3.3. The 'DTA Tg' for this glass was 590, 10°C higher than for C2. The melting peak was at about the same temperature for both glasses, 1302°C for G18 and 1303°C for G2. We shall see shortly that for some of the glasses around the NC_2S_3 composition two melting peaks have been observed.

The heats of crystallization and fusion (see section 3.1.4b) obtained from the peak areas were ΔH_c = 38.4 ±1.9 cal g^{-1} and ΔH_f = 50.5 ±2.5 cal g^{-1}. The ΔH_c was greater than the value for G2 and the ΔH_f was less than the value for G2.

3.3.2 Glass G19

The composition of G19 was 17.65 mole% Na_2O, 32.93 mole% CaO and 49.41 mole% SiO_2.

3.3.2.1 Nucleation Rates

A typical optical micrograph used for the nucleation rate determination is shown in Figure 3.35. The crystal shape was approximately cubic with slightly rounded faces. When calculating N_v using equation (2.2) b' was taken as the side of the maximum square cross section observed. More details of the morphology can be seen in Figure 3.36 which shows an electron micrograph for G19 heated at 603°C for 40 min and grown at 730°C for 2 min. Again rounded faces can be clearly observed.

The approximated nucleation rates are shown in Figure 3.31. On comparing this curve with that for G2 a large increase in the nucleation rates is evident. The maximum nucleation rate of 2.69×10^5 mm^{-3} min^{-1} is at 603°C. Hence the maximum rate is increased by approximately 1.3 orders of magnitude and the temperature of the maximum is lowered by 14°C. Also the nucleation is increased more at the lower temperatures than at higher temperatures. When the nucleation rates for this glass are compared with those for G18 the following observations can be made:

i - A shift of 14°C in the position of the maximum to lower temperatures.

ii - The maximum nucleation rate if 1.9 orders of magnitude larger than that for G18.

It was possible to estimate the growth rate at 675°C from the glass given a single heat treatment for 40 min at this temperature. The growth rate was obtained from the maximum diagonal distance that could be found in the distribution of particle cross sections

in a random plane. The growth rate was 0.52 μm min^{-1}. This value is slightly smaller than the growth rate for G18.

3.3.2.2 Viscosity Data

The measured viscosities are shown in Figure 3.34 and also the curve resulting from fitting the Fulcher equation (see Table 3.14) to the data. The $\log_{10}\eta = 13$ value occurred at 556.7°C which is approximately 9°C lower than the corresponding value for G17. There is an overall decrease in viscosity when compared with G17. Thus at 640°C the difference in $\log_{10}\eta$ is 1.1. It is interesting to note that the curves for G18 and G19 are almost parallel.

3.3.2.3 DTA

The DTA trace for G19 (see Figure 3.51) was different from that for G18 and G2. First, the crystallization peak (maximum at 723°C) does not show the shoulder observed for G2. Second, at the melting temperature two overlapping peaks appeared. The first (and smaller) occurred at 1264°C and the second at 1294°C. Third, the polymorphic transformation was no longer observed.

The 'DTA Tg' for this glass was 571°C, 8°C lower than that for G2.

The heats of crystallization and melting were $\Delta H_c = 35.8 \pm 1.8$ cal g^{-1} and $\Delta H_f = 59.3 \pm 3.0$ cal g^{-1}. For this glass ΔH_c was the same as that for G2. With reference to the melting peak the area considered was the whole area enclosed by the two overlapping peaks. The ΔH_f value was slightly larger than that for G2.

3.3.3 Glass G20

The composition for this glass was 16.92 mole% Na_2O, 32.33 mole% CaO and 50.75 mole% SiO_2.

3.3.3.1 Nucleation Rates

The nucleation rates for glass G20 were determined from glass specimens nucleated for 40 minutes at various temperatures. The results are shown in Figure 3.37 and compared with those for G2. The rates were higher for G20 at lower temperatures whereas at higher temperatures they were very similar for both glasses. A maximum rate of 3.89×10^4 mm^{-3} min^{-1} was found at T = 606°C. This temperature is 11°C lower than that for G2.

A typical optical micrograph for this glass is shown in Figure 3.38. The crystal morphology was nearly spherical. An electron micrograph for G20 heated at 603°C for 40 min and grown at 730°C for approximately one minute is shown in Figure 3.39. Crystalline defects similar to those found for G2 were observed.

The crystal growth rate at 675°C was 0.97 μm min^{-1}. This value is larger than the value for glass G2 at 675°.

3.3.3.2 Viscosity Data

The low temperature viscosity results are shown in Figure 3.40. The Fulcher parameters for this glass are shown in Table 3.14. The $\log_{10}\eta = 13$ value occurred at 565.3°C. The viscosity of G20 is lower than that for G17 over almost the whole range where measurements were carried out. However, at lower temperatures the difference in viscosities between both glasses was negligible.

FIGURE 3.37 $Log_{10}(Nv/t)$ AS A FUNCTION OF TEMPERATURE FOR G21, G20 and G2.

⊕G21, ○G20, ●G2

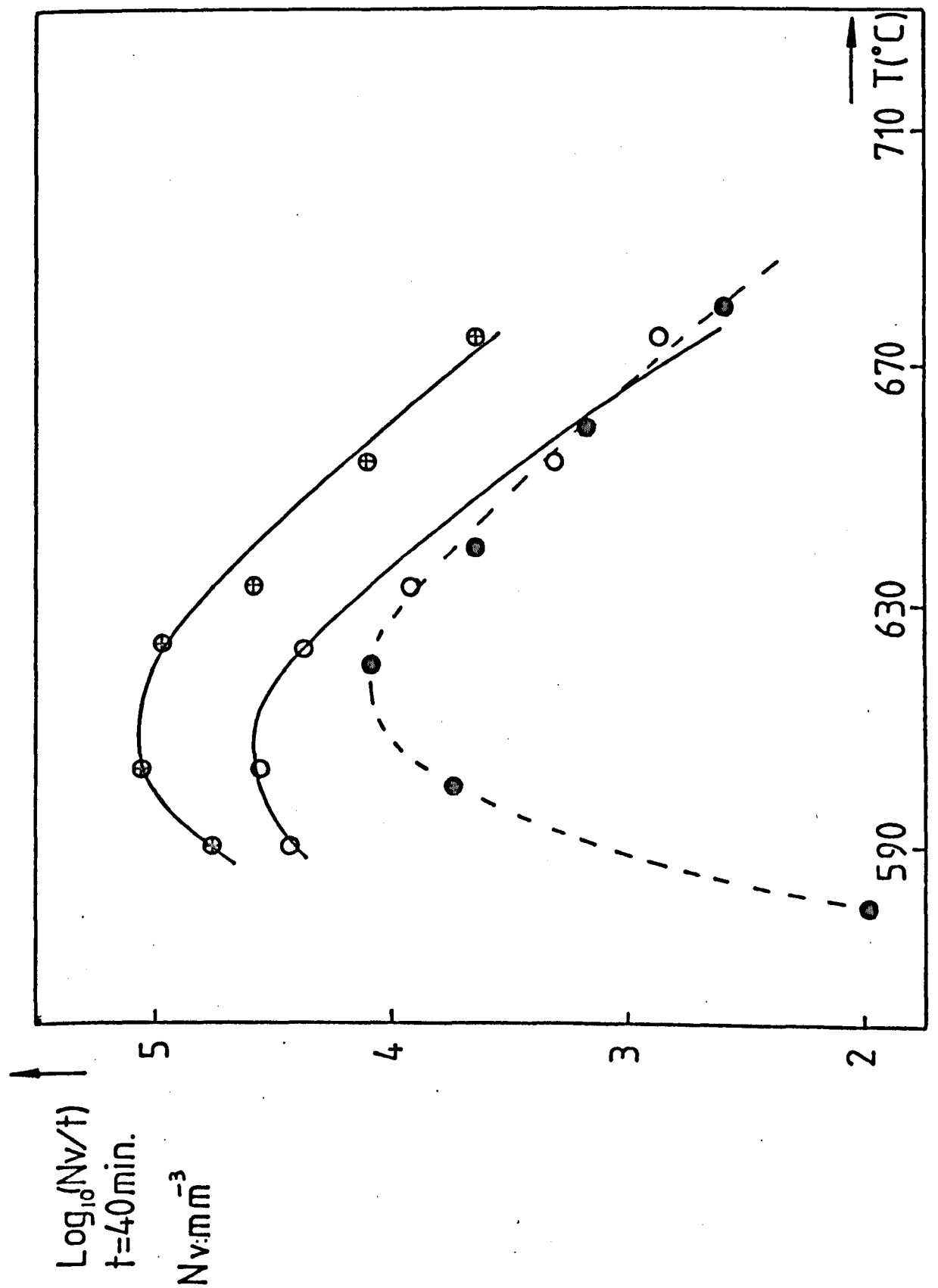

Figure 3.38 (top left)

Optical micrograph of G20 heated at 675°C for 40 min.
Mag X202.

Figure 3.39 (top right)

Electron micrograph of G20 (see text)
Mag. X17,500

Figure 3.41 (bottom left)

Optical micrograph of G21 heated at 675°C for 40 min.
Mag X202.

Figure 3.42 (bottom right)

Electron micrograph of G21 nucleated at 603°C for 40 min and grown at 730°C for 3 min.
Mag X24,800.

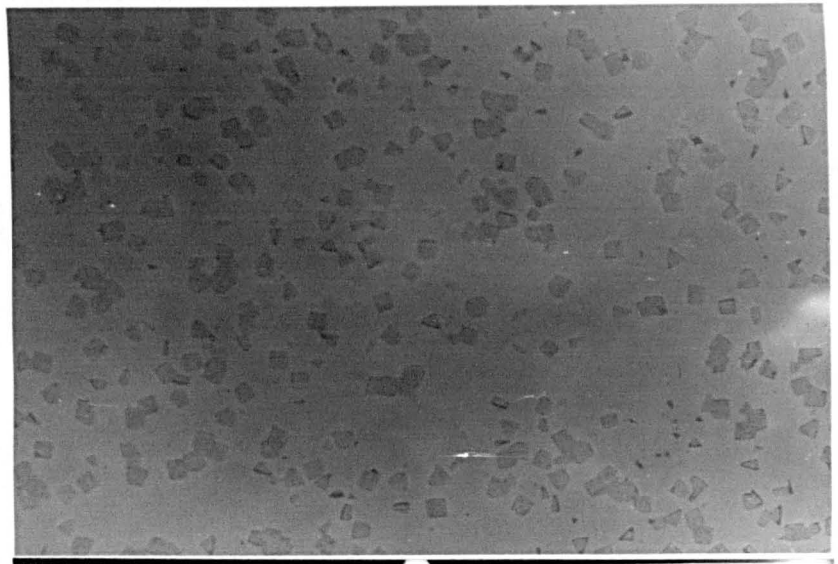

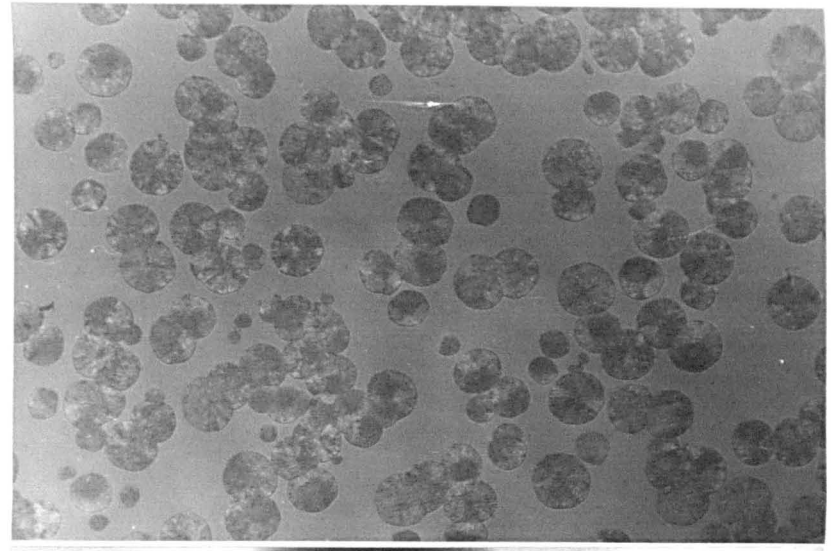

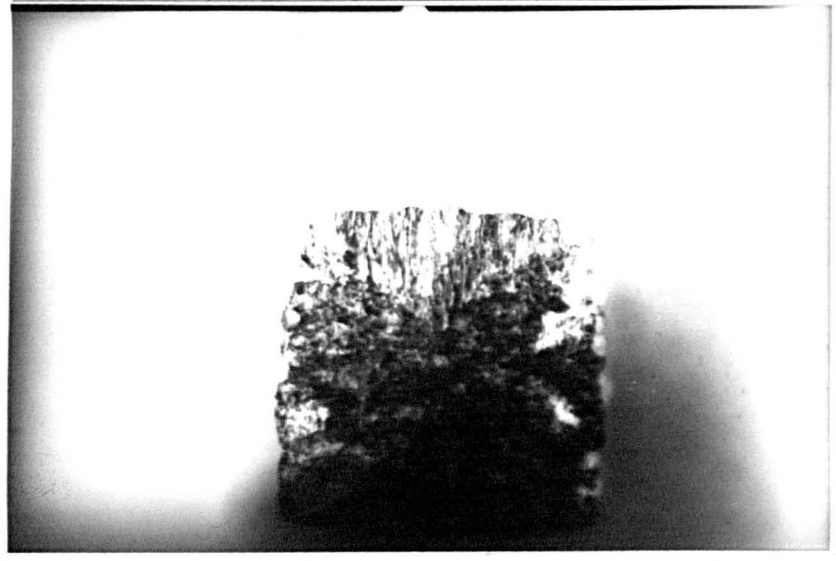

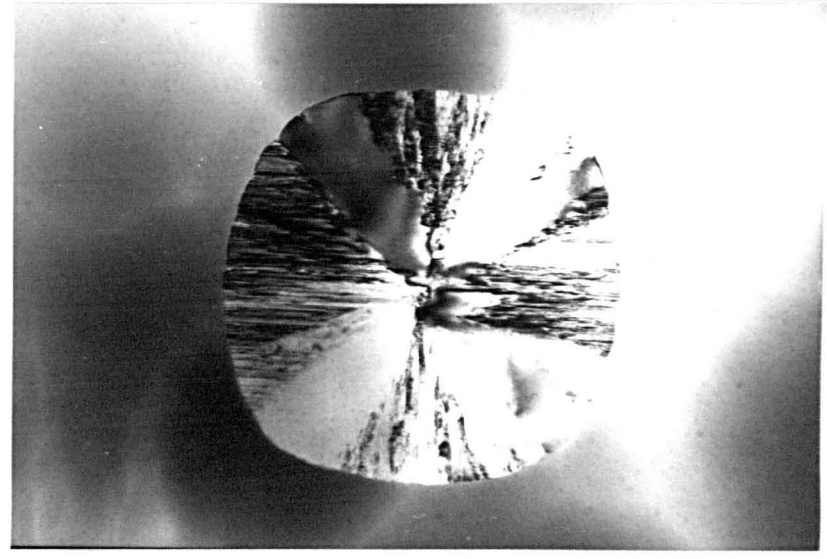

FIGURE 3.40 $Log_{10}\eta$ AS A FUNCTION OF TEMPERATURE FOR G21, G20 and G17

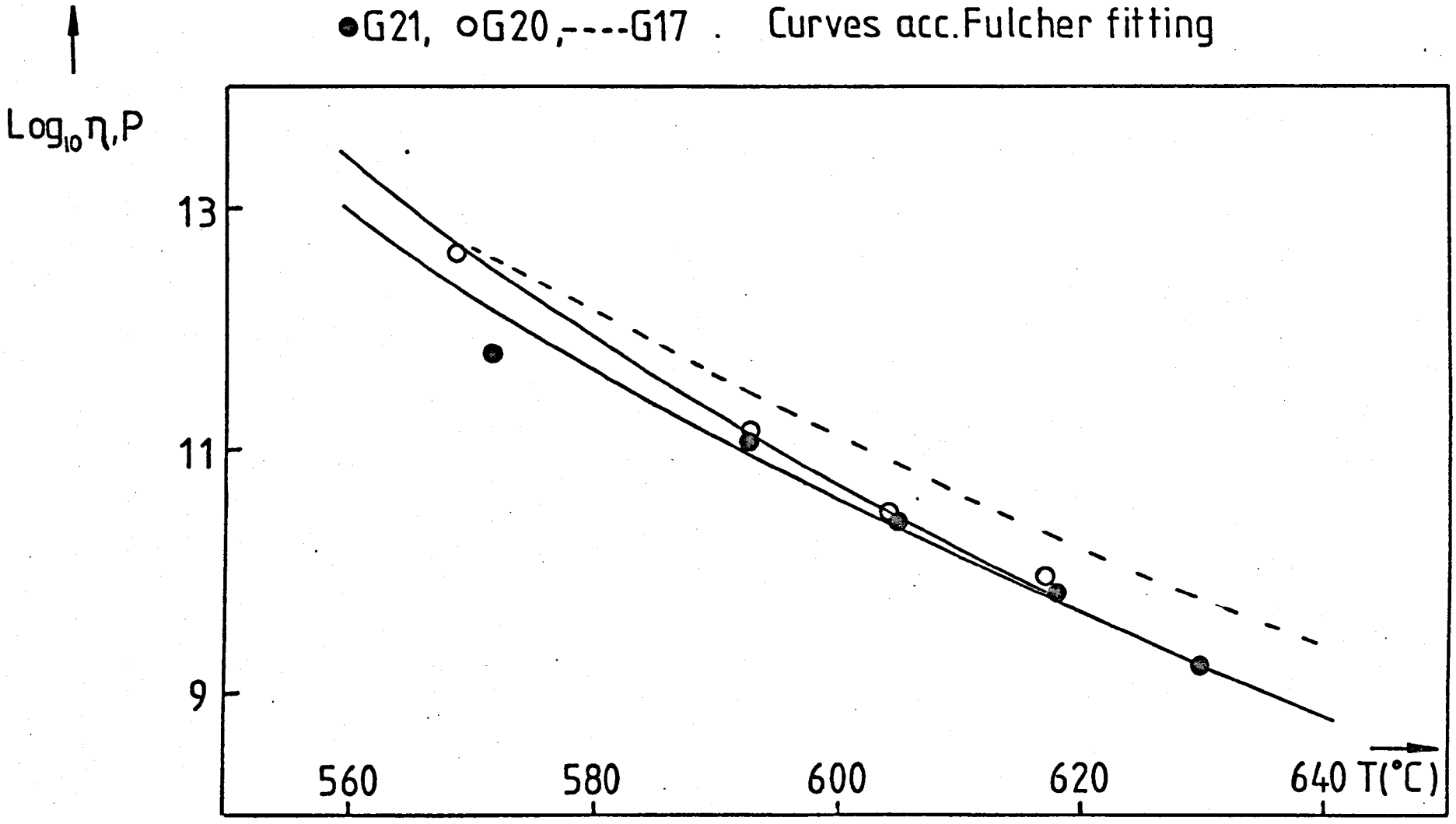

3.3.3.3 DTA

The DTA chart for this glass was very similar to that for G2. The 'DTA Tg' for this glass was 578°C, which was very close to that for glass G2. The heats of crystallization and fusion for glass G20 were ΔH_c = 37.0 ±1.8 cal g^{-1} and ΔH_f = 49.4 ±2.5 cal g^{-1}. An increase in ΔH_c and a decrease in the ΔH_f were observed for G20 relative to the values for G2.

3.3.4 Glass G21

The composition of this glass was 14.62 mole% Na_2O, 34.33 mole% CaO and 49.25 mole% SiO_2.

3.3.4.1 Nucleation Rates

A typical optical micrograph used for the nucleation measurements is shown in Figure 3.41. Every particle cross section observed corresponds to a random plane intersecting an almost perfect cube. This morphology was confirmed by electron microscopy, as shown in Figure 3.42. When using equation (2.2) to calculate $N_{v'}$ b' was taken as the side of the maximum particle square cross section that could be found on the micrographs.

The nucleation rates are shown in Figure 3.37. They are greater than those for G2, particularly at lower temperatures. The maximum nucleation rate of 1.19 x 10^5 mm^{-3} min^{-1} was at 607°C, 10°C lower than for G2. When compared with G20 the rates for G21 were larger over the whole temperature range and the maximum nucleation rate occurred at approximately the same temperature for both glasses.

The growth rate was estimated at 675°C, as described for the previous glasses. The maximum diagonal distance observed on the optical micrographs was used, giving a growth rate of 0.46 μm min^{-1}. This is lower than for G2 at 675°C and much smaller than for G20 at the same temperature.

3.3.4.2 Viscosity Data

The viscosity results are shown in Figure 3.40. The Fulcher parameters for this glass are listed in Table 3.14. The $\log_{10}\eta = 13$ corresponds to 559°C which is 6°C lower than for G17. The viscosity of G21 is lower than G2 over the whole temperature range. At high temperatures the viscosities for glasses G21 and G20 tend to coincide.

3.3.4.3 DTA

As for G19 the DTA trace for G21 was different from G2 (see Figure 3.51). The two melting peaks occurred at 1280°C (the smaller peak) and at 1297°C (the larger of the two peaks). The polymorphic transformation peak was not detected.

The 'DTA Tg' for this glass was 578 ±3°C. The heats of crystallization and fusion were ΔH_c = 35.8 ±1.8 cal g^{-1} and ΔH_f = 62.4 ±3.1 cal g^{-1} respectively. ΔH_c was the same as that for G2. However the ΔH_f value, which was determined from the total area of the two peaks, was larger than for G2.

3.3.5 Glass G22

The composition of this glass was 17.0 mole% Na_2O, 34.0 mole% CaO and 49.0 mole% SiO_2

3.3.5.1 Nucleation Rates

A typical optical micrograph for G22 heat treated at 675°C for 40 min is shown in Figure 3.43. The crystal shape appeared cubic. An electron micrograph of this glass heated at 603°C for 40 min and grown at 730°C for 2.5 min is shown in Figure 3.44. The N_v values were determined as described previously for G21.

The nucleation rates, which are shown in Figure 3.45, are much greater than those for glass G2. The maximum nucleation rate of 1.70×10^5 mm^{-3} min^{-1} was at 605°C, 12°C lower than for G2.

The growth rate for G22 at 675°C, which was estimated in the same way as for glass G21, was 0.56 μm min^{-1}. This was slightly lower than the value for G2 (0.58 μm min^{-1}).

3.3.5.2 Viscosity Data

The results are shown in Figure 3.46. The Fulcher parameters for glass G22 are listed in Table 3.14. The $\log_{10}\eta = 13$ value occurred at 560.5°C, 5°C lower than the temperature for G17. The viscosity of G22 was lower than G17 over the whole range of measurements.

3.3.5.3 DTA

The DTA trace for this glass showed two melting peaks, the first at 1273°C and the second at 1297°C. The polymorphic transformation peak found for G2 was not observed. The heats of crystallization and fusion were 38.1 ±1.9 cal g^{-1} and 61.5 ±3.1 cal g^{-1} respectively. These values are slightly larger than those for G2.

Figures 3.43 (top left), 3.44 (top right)

Optical and electron micrographs of G22 (see text)
Mag X202; X8,760

Figure 3.47 (left)

Optical micrograph of G23 heated at 675°C for 40 min.
Mag X101

Figure 3.48 (right)

Electron micrograph of G23 nucleated at 603°C for 40 min and grown at 730°C for 2 min.
Mag X20,400

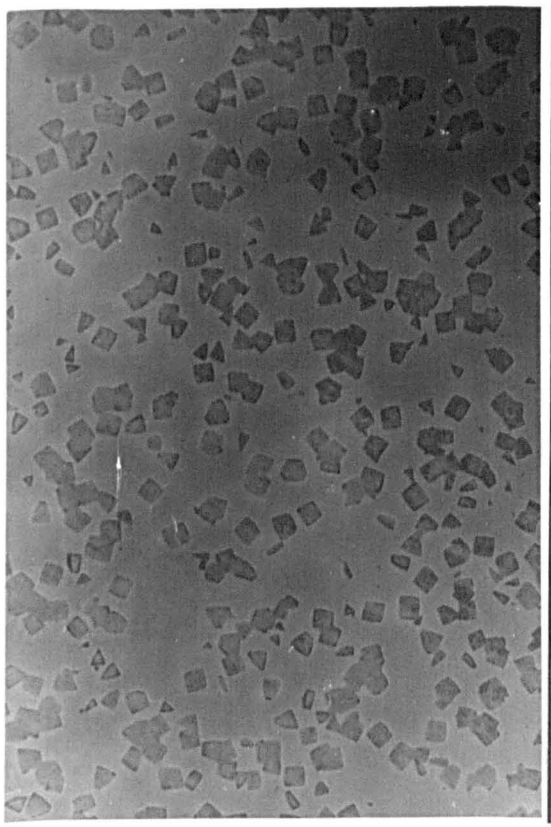

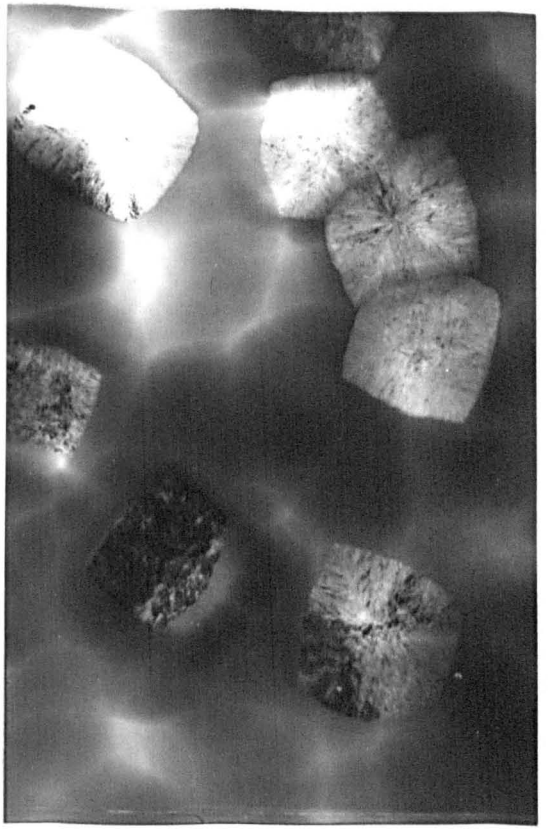

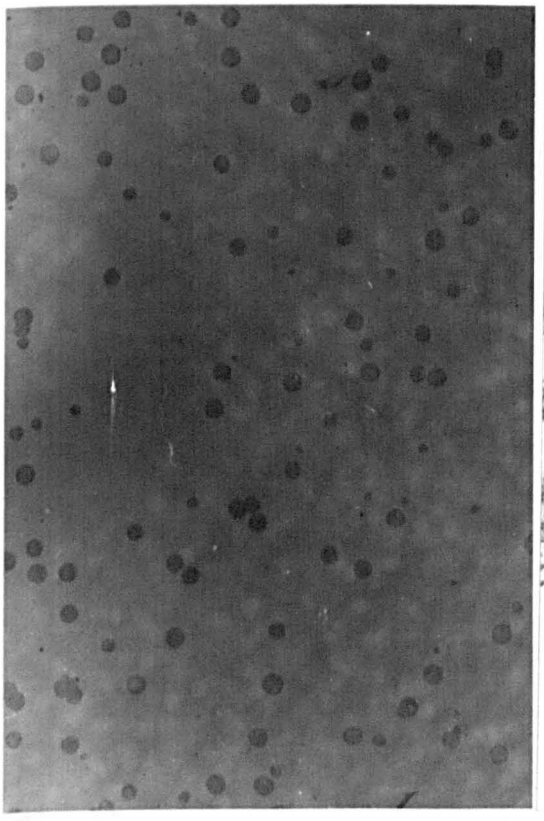

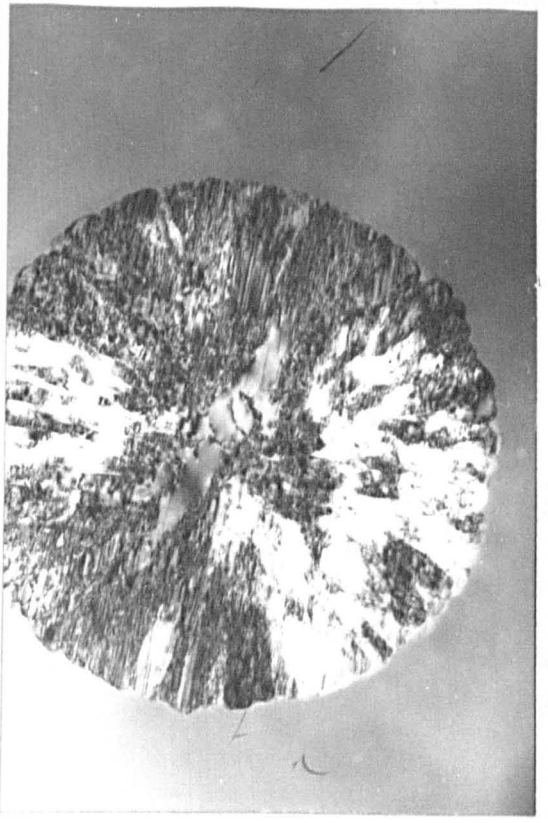

FIGURE 3.45 $Log_{10}(Nv/t)$ AS A FUNCTION OF TEMPERATURE FOR G23, G22 and G2

○G23, ⊕G22, ●G2

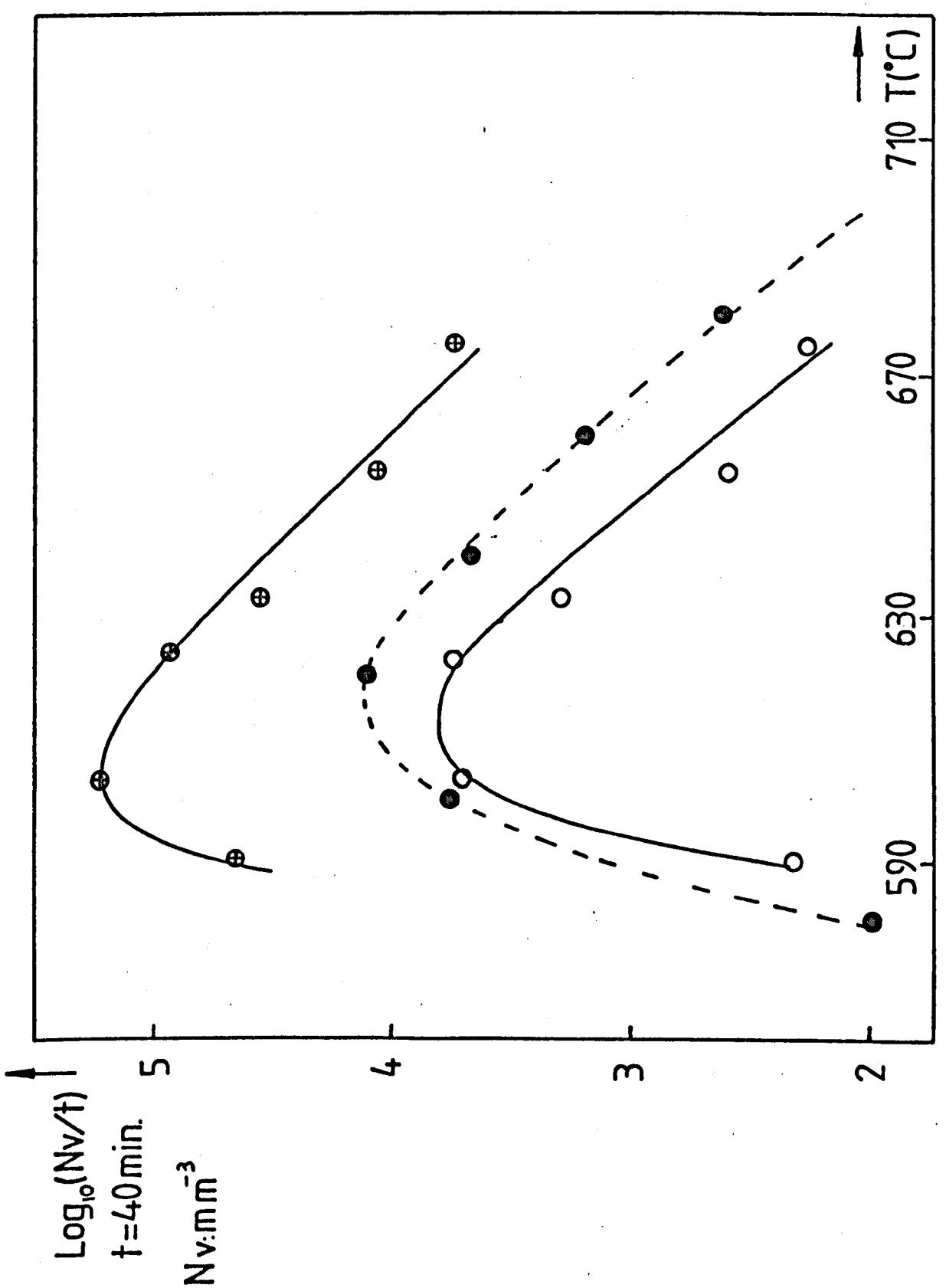

FIGURE 3.46 $Log_{10}\eta$ AS A FUNCTION OF TEMPERATURE FOR G23, G22 and G17

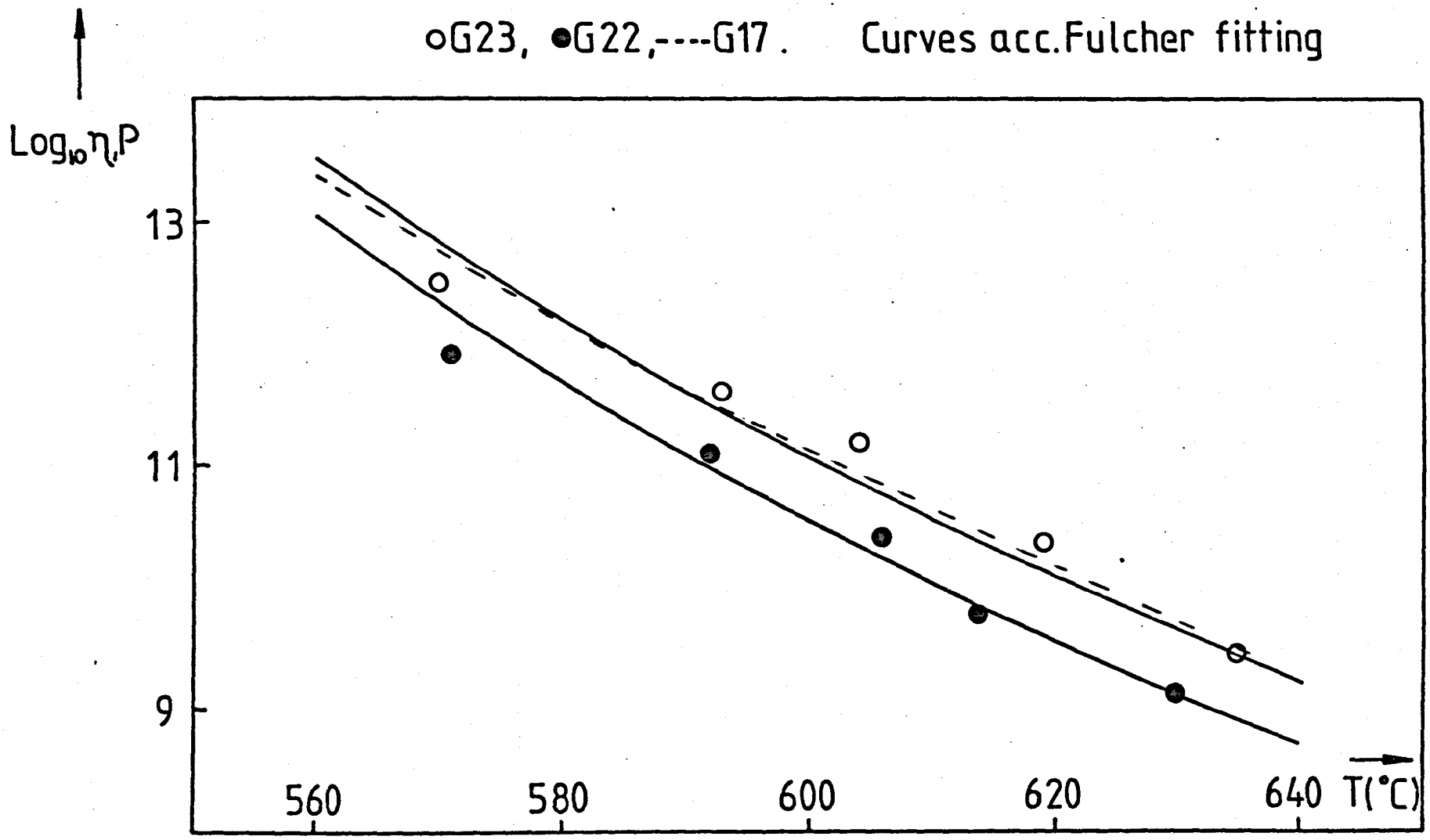

3.3.6 Glass G23

The composition for this glass was 16.33 mole% Na_2O, 32.7 mole% CaO and 51.00 mole% SiO_2.

3.3.6.1 Nucleation Rates

The nucleation rates for G23 (Figure 3.45) were less than those for G2. The maximum nucleation rate of 6.46×10^3 mm^{-3} min^{-1} was at 612°C.

A typical optical micrograph is shown in Figure 3.47. The particle cross sections are almost circular. An electron micrograph is shown in Figure 3.48.

The estimated growth rate at 675°C was 0.67 μm min^{-1}, which was larger than the corresponding values for both G2 and G22.

3.3.6.2 Viscosity Data

The viscosity results are shown in Figure 3.46. The Fulcher parameters for this glass are shown in Table 3.14. The $\log_{10}\eta = 13$ value occurred at 568.8°C, 3°C higher than the temperature for G17. The viscosity for G23 was slightly higher than the viscosity for glass G17. It is interesting to note that the curves for G17 and G23 are parallel to the curve for G22.

3.3.6.3 DTA

The DTA trace was similar to that for G2. The melting peak occurred at 1305°C and the polymorphic transformation peak was observed. The 'DTA Tg' for G23 was 585. The heats of crystalli-

zation and fusion, ΔH_c and ΔH_f, were 33.0 ±1.7 cal g^{-1} and 45.4 ±2.3 cal g^{-1} respectively. The ΔH_c for G23 was slightly lower than the value for G2. The ΔH_f for G23 was lower than the value for G2.

At this stage it is convenient to summarize the nucleation rate curves for all the glasses as well as the viscosities curves. The former are shown in Figure 3.49 and the latter are plotted in Figure 3.50. The DTA melting curves for glasses G19, G21 and G22 are compared in Figure 3.51. The DTA results for all the glasses have already been given in Table 3.15.

3.3.7 X-ray results for glasses in section 3.3

It has been mentioned already that for glasses G22, G21 and G19 two melting peaks were observed in the liquidus temperature range and that the polymorphic transformation peak was no longer observed in the DTA traces obtained at cooling rates of 10°C min^{-1}. In an attempt to understand the origin of the two melting peaks, X-rays diffraction was carried out for all the glasses in section 3.3. They were all nucleated for an hour at 620°C and grown at 750°C for 30 minutes. The results, shown in Table 3.16, should be compared with the results of Table 3.8 for the NC_2S_3 compound. According to Maki and Sugimura, (3.11) for the high form phase the following peaks (2θ) should disappear (up to a 2θ angle of 37°): 18.14, 22.46, 25.94, 28.24, 32.12, 33.04 and 34.92. For glasses G18, G20 and G23 the crystalline phase detected was the low form of the NC_2S_3 phase. For glasses G19 and G22 the data strongly

FIGURE 3.49 SUMMARY OF THE $Log_{10}(Nv/t)$ vs.T(°C) PLOTS FOR GLASSES IN SECTION 3.3

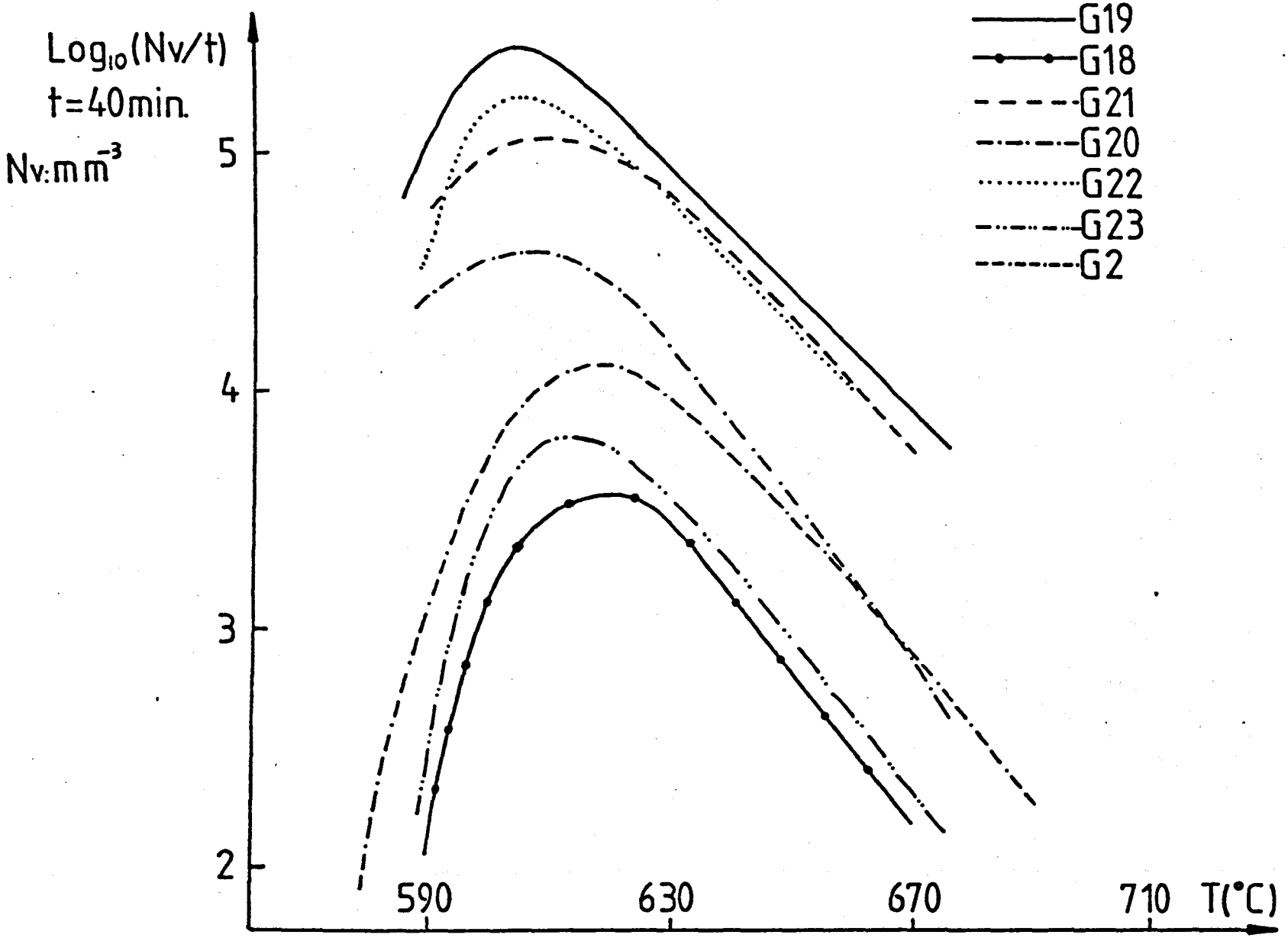

FIGURE 3.50 SUMMARY OF THE $Log_{10}\eta$ vs. T(°C) PLOTS FOR GLASSES IN SECTION 3.3

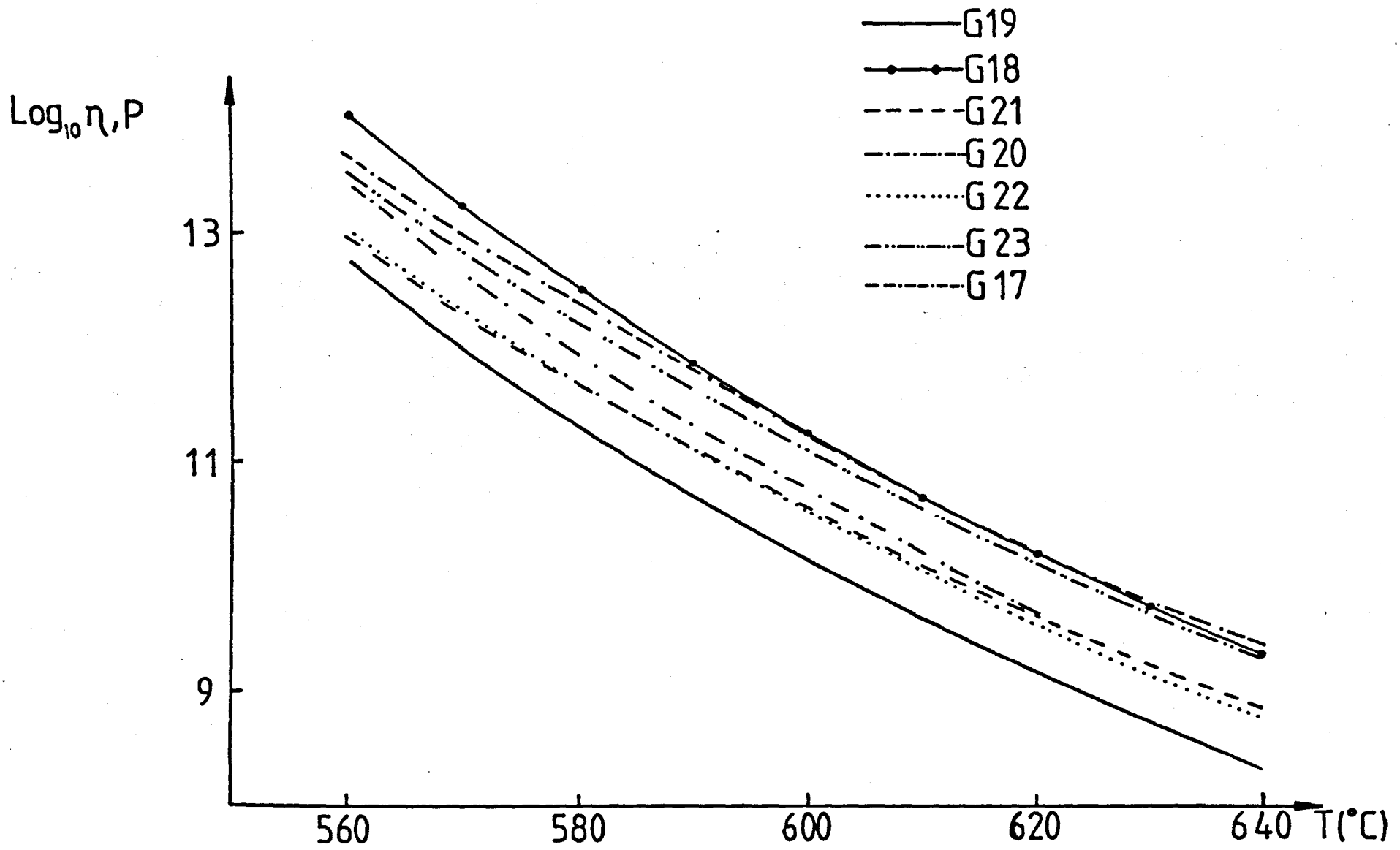

FIGURE 3.51 MELTING PEAKS(DTA) FOR GLASSES G19, G21 and G22 AND CRYSTALLIZATION PEAK FOR G19

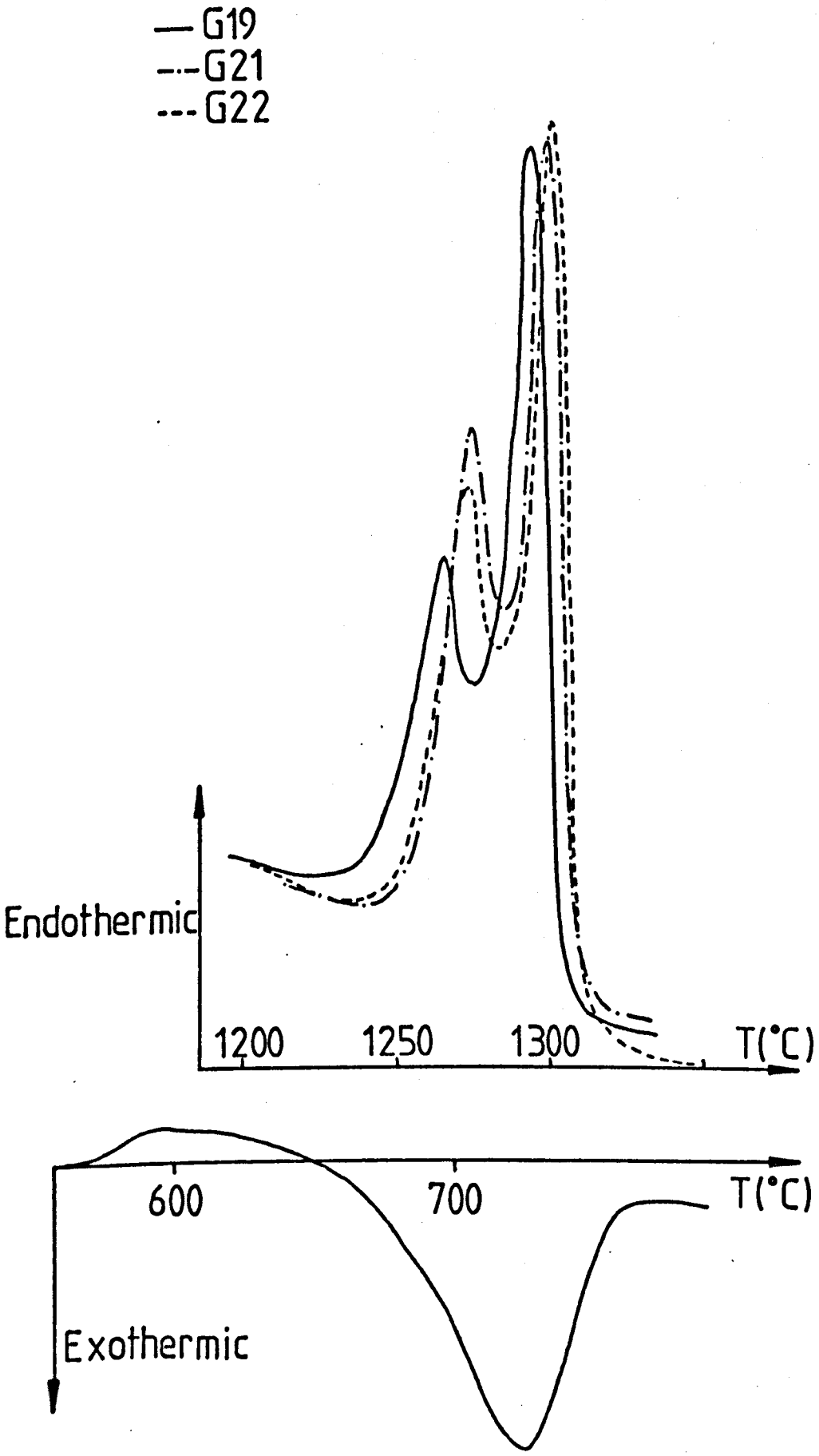

TABLE 3.16

X-RAYS DATA FOR GLASSES IN SECTION 3.3

G18			G19			G20			G21			G22			G23		
2θ	I	d	2θ	I	d	2θ	I	d	2θ	I	d	2θ	I	d	2θ	I	d
11.9	14	7.43	11.9	10.3	7.43	11.8	14	7.49	11.85	11.4	7.46	11.8	11	7.49	11.8	14.1	7.49
16.74	7.6	5.29	16.6	7.5	5.34	16.66	7.2	5.32	16.58	6.9	5.34	16.46	6.7	5.38	16.61	7.1	5.33
18.0	7.1	4.92	20.27	1.7	4.38	18.18	10.2	4.88	18.05	8.0	4.91	16.70	6.9	5.30	18.2	11.6	4.87
18.2	9.2	4.87	23.8	40.1	3.74	20.25	20.9	4.38	20.3	14.0	4.37	17.92	6.0	4.95	20.21	23.3	4.39
18.3	9.5	4.84	26.0	8.9	3.42	22.5	7.3	3.95	22.45	6.1	3.96	18.10	7.5	4.89	22.5	8.0	3.95
20.25	23.5	4.38	26.5	37.9	3.36	23.8	43.1	3.74	23.78	35.0	3.74	18.31	7.0	4.84	23.83	50.6	3.73
22.5	7.4	3.95	26.9	57.4	3.32	25.93	13.5	3.43	26.0	10.1	3.42	20.29	14.5	4.37	26.0	13.9	3.42
23.9	48.1	3.72	29.5	11.0	3.03	26.1	12.6	3.41	26.5	39.0	3.36	23.82	33.8	3.73	26.52	51.1	3.36
26.0	13.6	3.42	33.61	86.9	2.66	26.53	51.0	3.36	26.80	53.5	3.32	25.92	9.8	3.43	26.91	73.0	3.31
26.6	50.3	3.35	36.14	87.0	2.62	26.92	68.1	3.31	29.44	10.1	3.03	26.80	47.0	3.32	28.3	5.2	3.15
27.0	70.5	3.30	35.45	9.1	2.53	28.81	6.0	3.1	33.13	12.9	2.70	29.42	10.5	3.03	28.82	6.9	3.09
28.3	5	3.15				29.51	13.0	3.02	33.6	80.5	2.67	32.61	6.7	2.74	29.50	13.7	3.03
28.45	4.5	3.14				33.12	11.9	2.70	34.11	80.0	2.63	32.95	9.5	2.72	30.32	4.5	2.95
28.9	6	3.09				33.71	100>>	2.66	35.5	9.5	2.53	33.72	80	2.66	32.15	5.5	2.78
29.6	12.3	3.02				34.27	100>>	2.61	35.65	9.1	2.52	34.21	82.9	2.62	33.20	12.4	2.70
32.14	5.1	2.78				34.9	9.8	2.57				35.5	9.7	2.53	33.70	100>>	2.66
33.2	12.6	2.70				35.54	14.8	2.52				36.0	6.1	2.49	34.3	100>>	2.61
33.74	100>>	2.65				36.1	6.1	2.49							34.93	9.0	2.57
34.32	100>>	2.61				36.37	7.0	2.47							35.51	15	2.53
34.92	9.1	2.57													36.03	5.9	2.49
35.53	14.3	2.52													36.3	7.1	2.47
36.14	6.1	2.48															
36.31	7.8	2.47															

suggests the presence of the high form of the NC_2S_3 phase. However for glass G21 it is not clear whether the high form was present or not, since the 28.24, 32.12 and 34.92 peaks were not present and the 18.14, 22.46, 25.94 and 33.04 peaks were present (apart from a small shift).

CHAPTER 4

EXPERIMENTAL RESULTS. GLASSES WITH H_2O, NaF, ZrO_2, P_2O_5, TiO_2, MoO_3 and Pt ADDITIONS

In this Chapter the effect of additions of different oxides and compounds to the base glass composition NC_2S_3, on the crystal nucleation and growth rates will be considered in detail.

4.1 H_2O Additions

The melting technique (Chapter 2) was modified to enable a glass of higher water content to be produced. When the batch had reacted completely (after one hour) the melt was bubbled with steam for two to three hours. The steam was generated by electrically heating a spherical flask containing distilled water. The flask had two outlet tubes, one a safety tube. The other outlet tube was joined by a plastic tube to a sillimanite tube with a platinum tube cemented to its end. The platinum tube was inserted into the melt to a depth of 0.5 in. from the bottom of the crucible. The thermostat was set at 95°C which allowed a steady flow rate of steam into the molten glass (assessed by counting the number of bubbles per min rising to the melt surface) without activating the safety valve of the second output tube. The overall flow rate was approximately 1 litre per hour. The losses (wt.%) in Na_2O and Cao for glass G14 (nominal composition similar to G2) were 1.63 and 1.3 respectively (Table A2.1, Appendix 2). The chemically analysed compositions (Appendix 2) for various glasses considered in this section are given in Table 4.1. Due to the losses found for G14 it was decided, for comparison, to melt another glass (G15) under normal 'dry' conditions. G15 was closer in composition to G14 than to G2 (Table 4.1). Glasses L1,

TABLE 4.1 COMPOSITIONS OF GLASSES IN SECTION 4.1 AFTER CHEMICAL ANALYSIS

Glass Code	Composition (mole%) Na_2O	Cao	Li_2O	SiO_2 (by difference)
G2	16.30	33.10	-	50.70
G14	14.70	31.70	-	53.60
G15	14.30	31.60	-	54.10
L1	-	-	33.10	66.90
L2	-	-	-	-
L3			33.0	57.0

TABLE 4.2 WATER CONTENTS FROM EQUATION (4.3) FOR VARIOUS SODA-LIME-SILICA AND LITHIA-SILICA GLASSES

Class Code	Thick-ness (cm)	$T_{2.5}$	T	Water Concentration C(wt.%)	C(mole%)	Water Concentration After Accurate Method Chapter 2 C(wt.%)	C(mole%)
G2	0.0365	0.85	0.80	0.0067	0.023	0.00703	0.023
G5	0.098	0.93	0.74	0.0094	0.030		
G13	0.093	0.91	0.77	0.0072			
G14	0.048	0.81	0.47	0.0457	0.149	0.0404	0.132
G15	0.228	0.96	0.65	0.0069	0.022		
L1	0.117	0.91	0.675	0.0214	0.054		
L2						0.034	0.096
L3						0.136	0.377

and L2, L3 were originally melted and analysed by James (4.1) and Johnson (4.2) respectively. Additional experimental work on their glasses was carried out during the present study.

It was found possible to develop a more rapid method of determining water content that that described in Chapter 2. For glasses near the NC_2S_3 composition the water contents associated with the 2.8 μm, 3.5 μm and 4.2 μm bands were approximately 20%, 47% and 33% respectively of the total water present in the glass (section 2.9). Now, instead of using equation (2.17) valid for the final corrected I vs wavelength λ curve the following equation was used

$$T = K_\lambda \, 10^{-(\varepsilon cd + \varepsilon_o C_o d)} \qquad (4.1)$$

where T is the transmittance at wavelength λ and ε, C and d have the same meaning as in equation (2.17). K_λ accounts for surface reflectance losses and $\varepsilon_o C_o d$ for the intrinsic absorption of the sample at the wavelength of interest. It is reasonable to assume that $K_\lambda \, 10^{-\varepsilon_o C_o d}$ is approximately constant and is given by the transmittance value at shorter wavelengths than the main water absorption bands, for example at λ = 2.5 μm. So equation (4.1) becomes

$$T = T_{2.5} \, 10^{-\varepsilon C d} \qquad (4.2)$$

Thus from equations (4.2) and (2.18)

$$C(\text{wt.}\%) = \frac{1.8}{\varepsilon d \rho} \log_{10}\left(\frac{T_{2.5}}{T}\right) \qquad (4.3)$$

This equation can be used at a convenient peak, for example at

λ = 3.5 μm (2nd band) for those glasses near to the NC_2S_3 composition. So multiplying equation (4.3) by $\frac{100}{47}$ and putting ρ = 2.75 g cm^{-3} and $\varepsilon \simeq 150$ cm^2 $mole^{-1}$ we obtain

$$C(wt.\%) = \frac{1}{107.7} \times \frac{1}{d} = \log_{10}\left(\frac{T_{2.5}}{T}\right) \qquad (4.4)$$

The results for a number of glasses analysed in this Chapter are given in Table 4.2. In the case of glasses near the lithium disilicate ($Li_2O.2SiO_2$) composition the water contents associated with the 2.9, 3.6 and 4.2 bands (see (4.2)) were approximately 70.5%, 18.9% and 10.6% respectively. For these glasses it is more convenient to choose the band at 2.9 μm (1st band) for the calculations. For example for glass L1 (Figure 4.1) equation (4.3) multiplied by $\frac{100}{70.5}$ gave 0.0214 wt.% H_2O (thickness = 0.117 cm, ρ = 2.2078 g cm^{-3} and $\varepsilon \simeq 60$ cm^2 $mole^{-1}$). The following should be noted:-

(i) The results for G2 and G14 using the present method agree well with the longer method described in Chapter 2 (Table 2.5).

(ii) The bands at 3.5 μm and 2.9 μm (Figure 4.1) were selected for measurements for the soda-lime glasses and the lithia glasses respectively because for these bands little or negligible interference occurred from the other 'water' bands (for example see Figure 2.11)).

It can be observed, from Table 4.2, that G2 and G15 have approximately the same level of water whereas G14 (steam bubbled) has approximately six times more water than G2. Also, for the lithia glasses, the ratio of water contents between L3 (steam bubbled) and L1 (normal

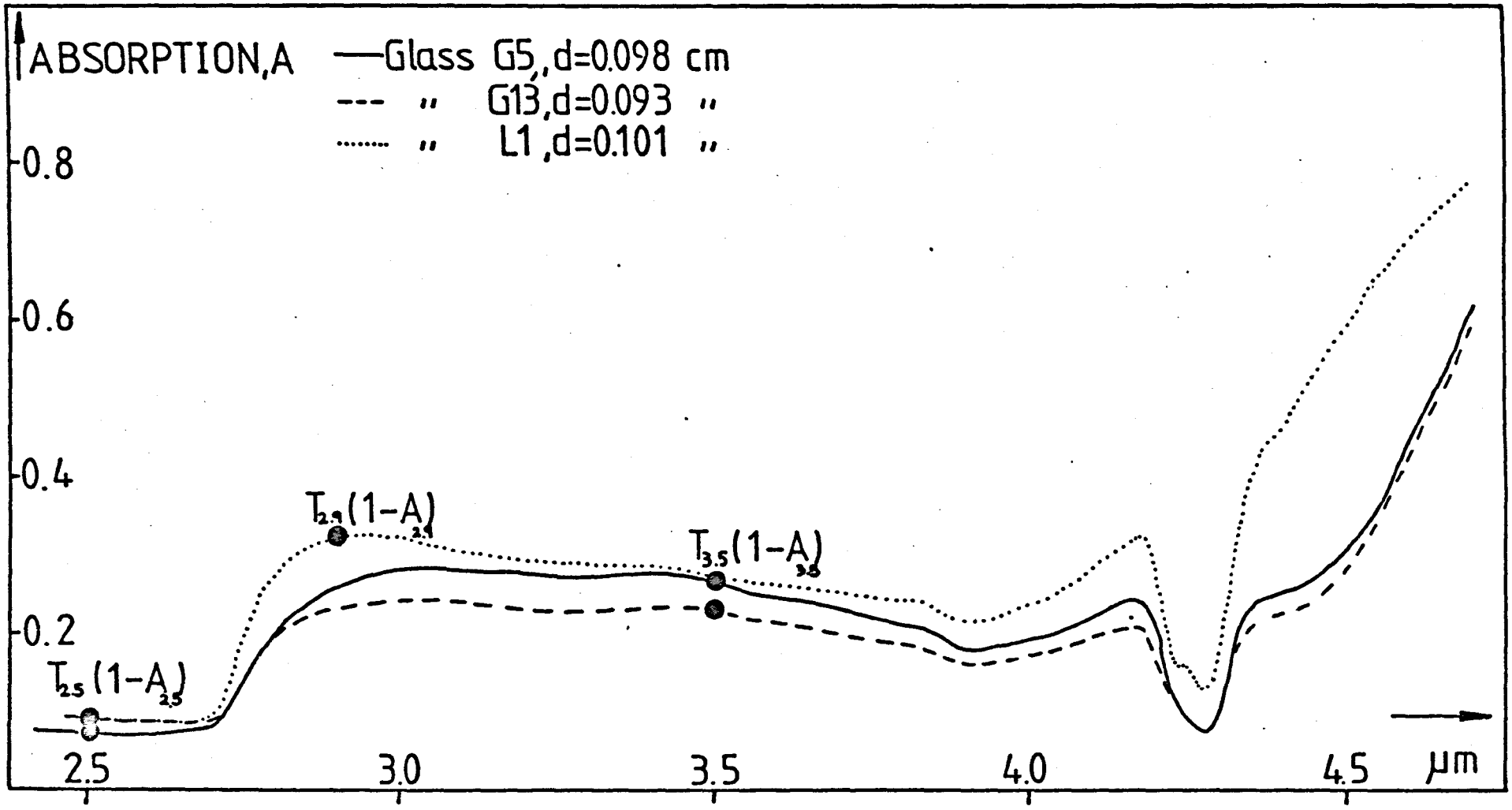

FIGURE 4.1 ABSORPTION AS A FUNCTION OF WAVELENGTH FOR GLASSES G5,G13' AND L1:

melting) is approximately seven. Glass L2, bubbled with wet air, had approximately 1½ times more water than L1. It is interesting to note that under normal melting conditions the water uptake for the lithia glasses is about 3 times larger than for the soda-lime glasses.

4.1.1 Nucleation Results

The nucleation 'rates' (N_v/t) for glasses G2, G14 and G15 are shown in Figure 4.2. The nucleation results for G14 are given in Table 4.3. The nucleation time for G14 was the standard 40 min whereas for G15, which had much lower nucleation densities, a nucleation time of 80 min was chosen. The position of the maximum rate is similar for G2 and G15. However for G14 the maximum rate of 9.77×10^5 mm^{-3} min^{-1} is at 574°C which is 43°C lower than for G2. The maximum rate for G14 is greater than that for G2 by 0.9 of an order of magnitude. For G15 the maximum rate is less than that for G2 by 2.7 orders of magnitude.

The nucleation data for glasses L1, L2 and L3 are plotted in Figure 4.2. Optical micrographs for G14 and G15 are shown in Figures 4.3 and 4.4. Electron micrographs for G14 (Fig. 4.5) show a different crystal morphology from glass G2. The crystals in G14 are more polyhedral in shape.

4.1.2 Growth rates

Growth rates were determined by measuring the maximum size of the internal crystals (previously nucleated) as a function of

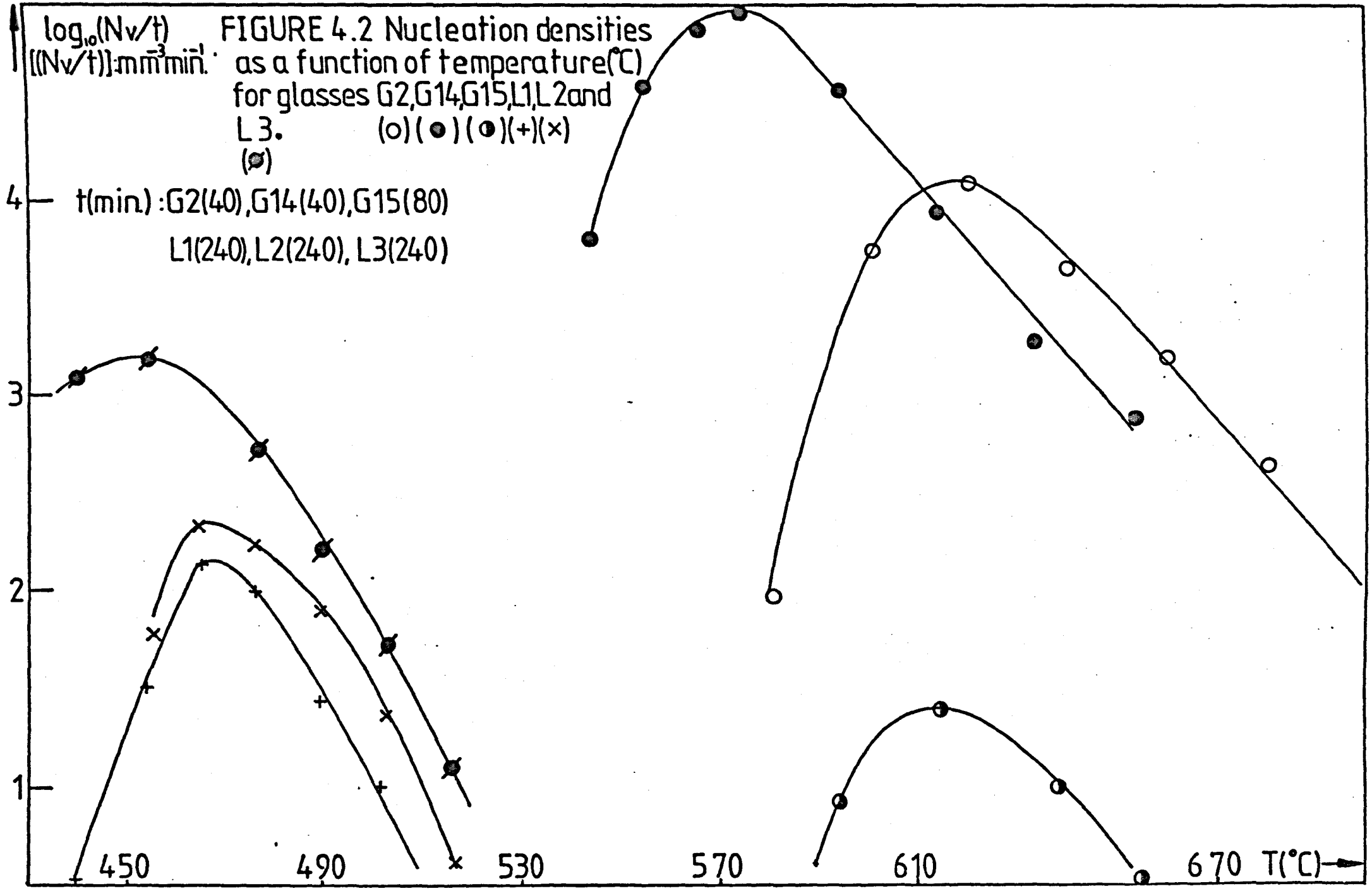
log10(Nv/t)
[(Nv/t)]:mm⁻³min⁻¹
FIGURE 4.2 Nucleation densities as a function of temperature(°C) for glasses G2,G14,G15,L1,L2and L3.
(o)(●)(◑)(+)(×)
(ø)
t(min.):G2(40),G14(40),G15(80)
L1(240),L2(240),L3(240)
4
3
2
1
450
490
530
570
610
670
T(°C)

TABLE 4.3 NUCLEATION DATA FOR GLASS G14 ACCORDING TO EQUATION (2.2) WHERE t : NUCLEATION TIME IN MIN, N : NUMBER OF PARTICLE INTERSECTIONS, b' : MAXIMUM CROSS SECTION DIAMETER, M : FINAL MAGNIFICATION AND A : PLATE AREA (mm^2)

T(°C)	t	N	b'	M	A	$\log_{10}\left(\frac{NxM^3}{Axb'xt}\right)$
544	40	581	3.27	305.4	18950.4	3.82
554	40	209	3.13	763.4	"	4.60
566	40	395	2.84	763.4	"	4.87
574	40	459	2.66	763.4	"	4.99
594	40	296	4.65	816	21967.2	4.59
613	40	490	2.09	326.4	"	3.96
633	40	267	5.28	326.4	"	3.27
653	40	219	9.50	326.4	"	2.92

TABLE 4.4 LIQUIDUS TEMPERATURES AND DTA RESULTS FOR GLASSES G2, G14, G15, L1 AND L3

Glass Code	Liquidus Temperature (°C) T_L	Heat of fusion (DTA) ΔH_f (cal g^{-1})	DTA Tg (°C)
G2	1276	58.2 ±3	579
G14	1273	60.0 ±3	571
G15	1268		
L1	1036		451
L3	1034		441

Figure 4.3 (top left)

Optical micrograph for G14 nucleated at 575°C for 40 min and grown for a short time at 725°C Mag X500.

Figure 4.4 (top right)

Optical micrograph for G15 nucleated at 638°C for 80 min and grown for 4 min at 750°C. Mag X50.

Figure 4.5a,b,c

Electron micrographs of G14 heated at 579°C for

(a) 14 hr (middle left) Mag X17,300
(b) 14 hr (middle right) Mag X17,000
(c) 10 hr (bottom) Mag X18,000

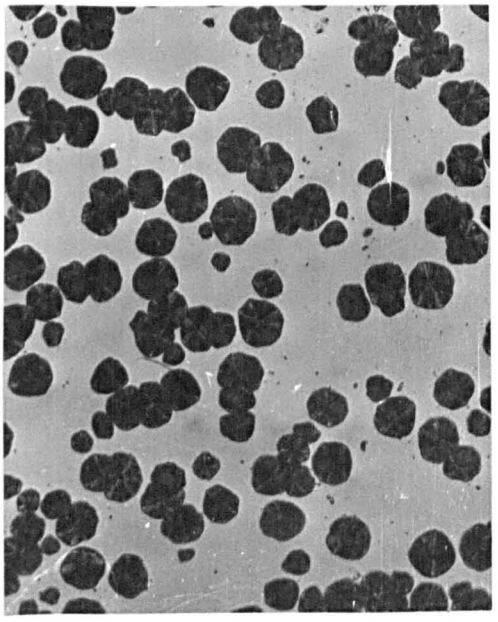

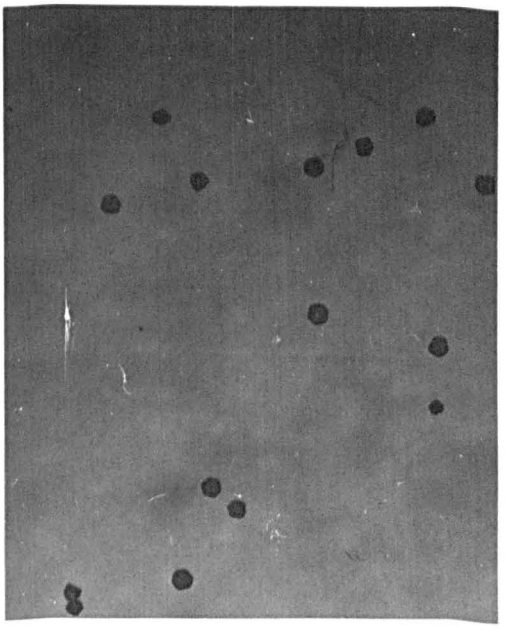

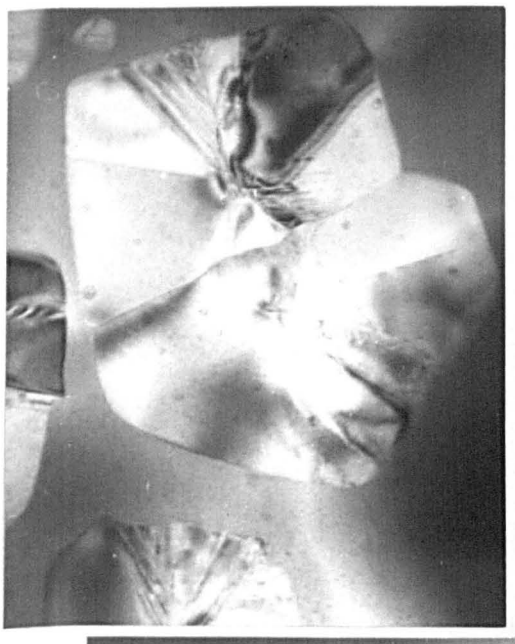

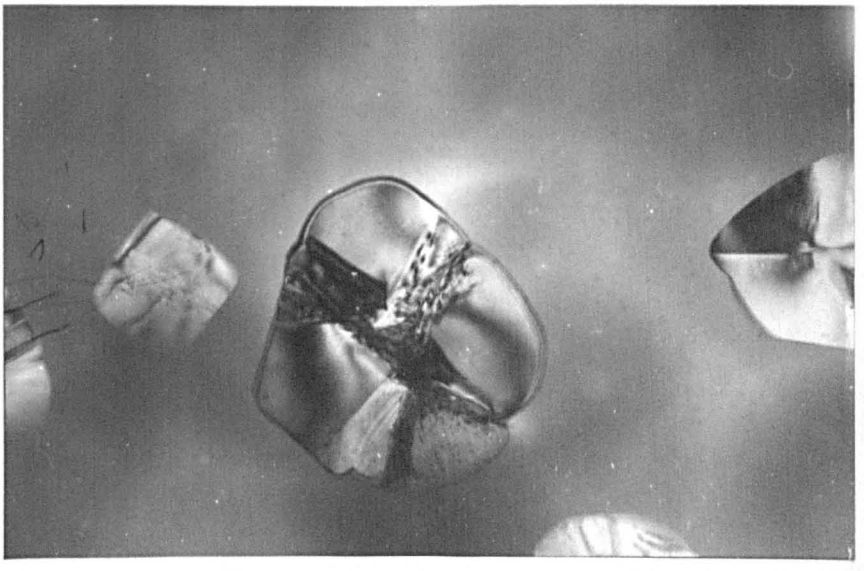

time. Figure 4.6 shows plots of the size vs time at a series of temperatures for G14. In Figure 4.7 the growth rates as a function of temperature are shown for glasses G2, G14, L1 and L3. It is clear that addition of water causes a marked increase in the growth rates for both the soda-lime glasses and the lithia glasses. The growth rates in the latter glasses were determined by measuring the thickness of the surface crystalline layer vs time. The size vs time plots were linear.

4.1.3 Viscosity measurements

The results are given in Figure 4.8. For both sets of glasses the viscosity at lower temperatures decreased considerably with increase in water content. It should be noted that a good fit was obtained to the low temperature data for L1 and L3 with the Fulcher equation when the high temperature data for $Li_2O.2SiO_2$ obtained by Shartsis et al (4. 3) was used for both glasses. For the soda-lime glass G14 the Fulcher equation was fitted to the low temperature data for G14 and the high temperature data for G2. The fit, however, does not appear as good at low temperatures as that obtained by tracing a smooth curve through the experimental points. This is almost certainly due to the compositional difference between G2 and G14 (see Table 4.1). On the other hand L1 and L3 are much closer in composition and at high temperatures the viscosities of L1 and L3 are probably very close.

It is interesting to note that Scholze and Merker (4.4) found that the viscosity at 1300°C for a glass of 75 mole% SiO_2,

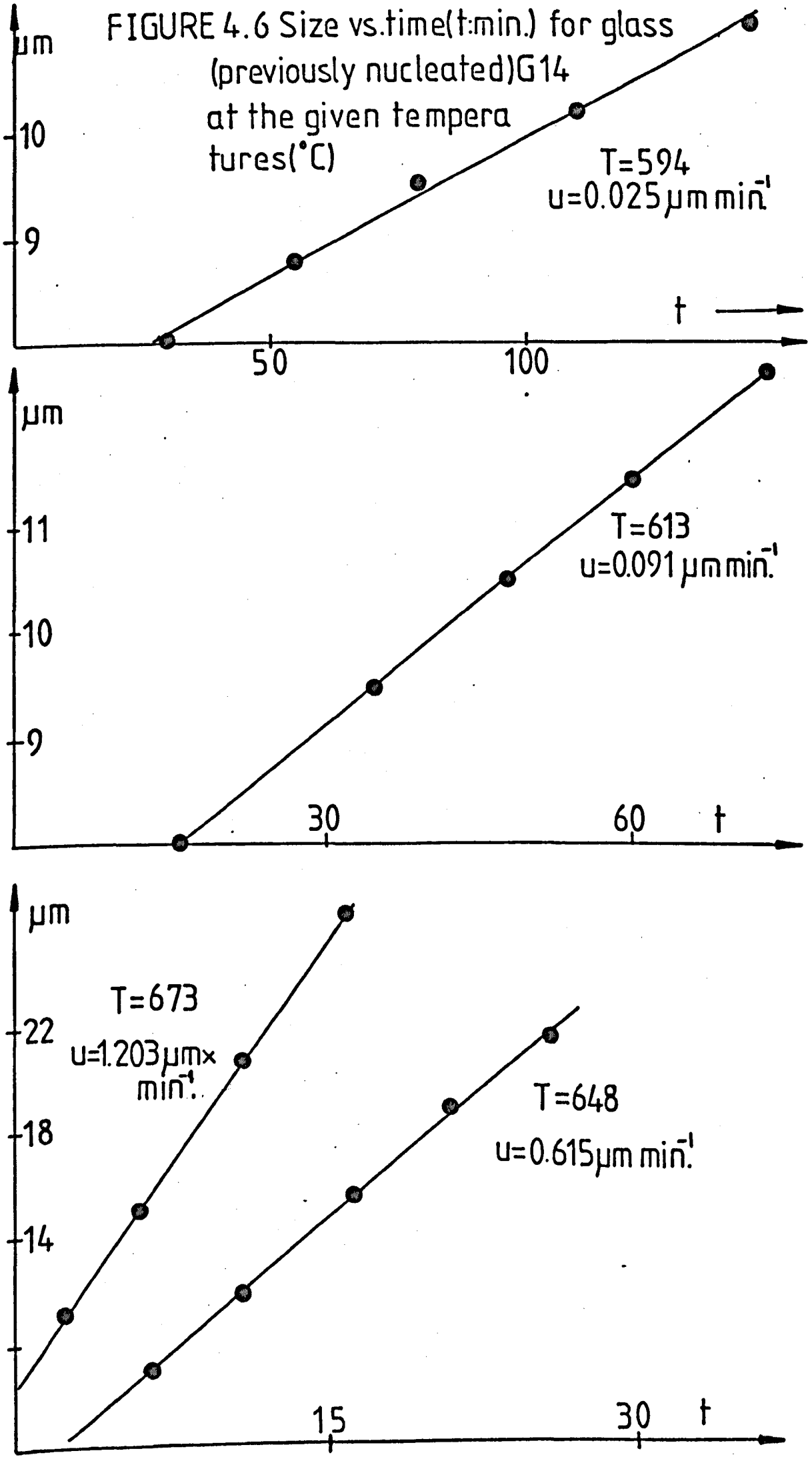

FIGURE 4.6 Size vs.time(t:min.) for glass (previously nucleated)G14 at the given tempera tures(°C)

FIGURE 4.7 Growth rates as a function of temperature for glasses G2, G14, L1 and L3.

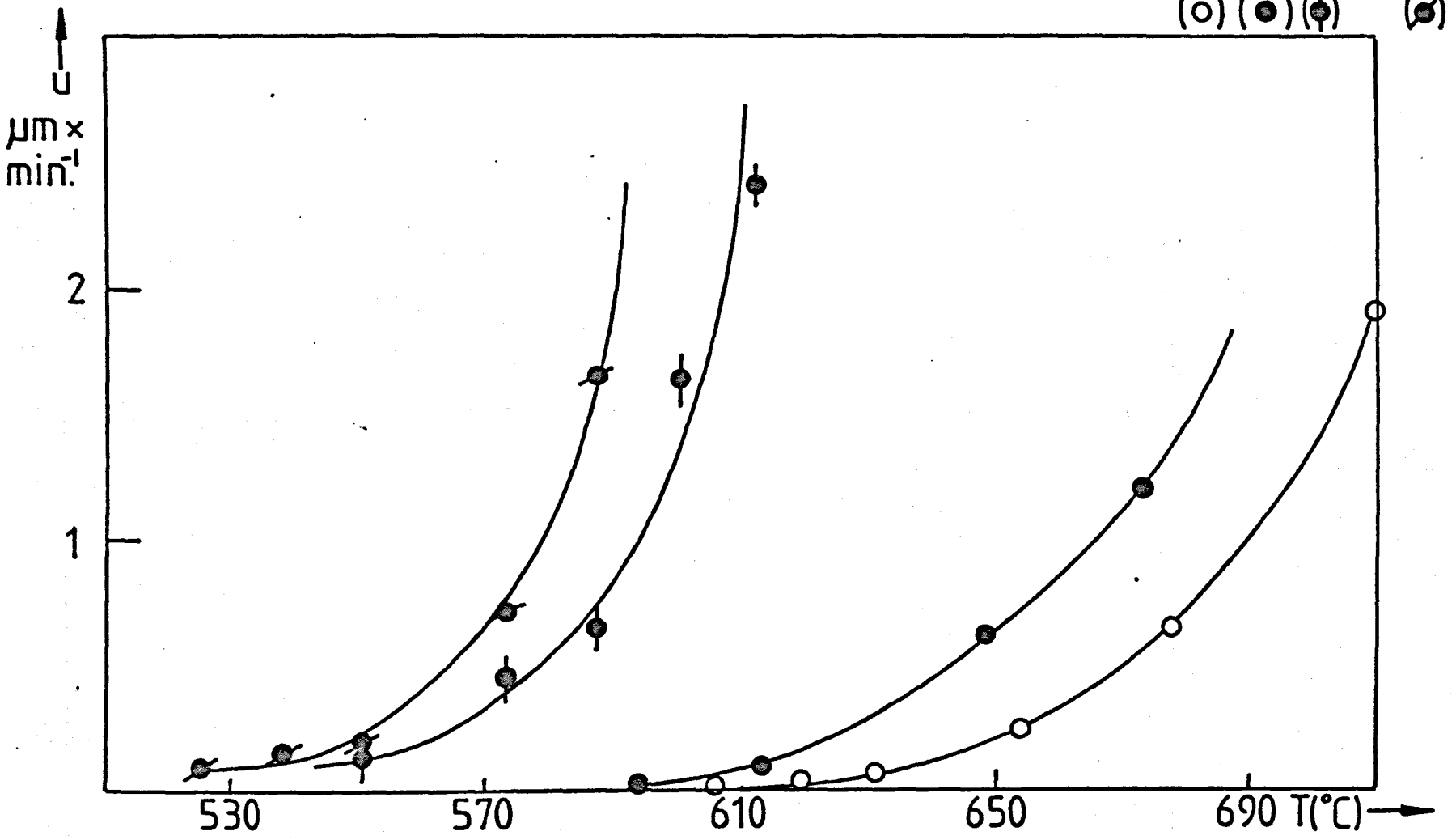

FIGURE 4.8 $\log_{10}\eta$ as a function of temperature for glasses G2, G14, G15, L1 and L3.
(○) (●) (◑) (◐) (⊘)

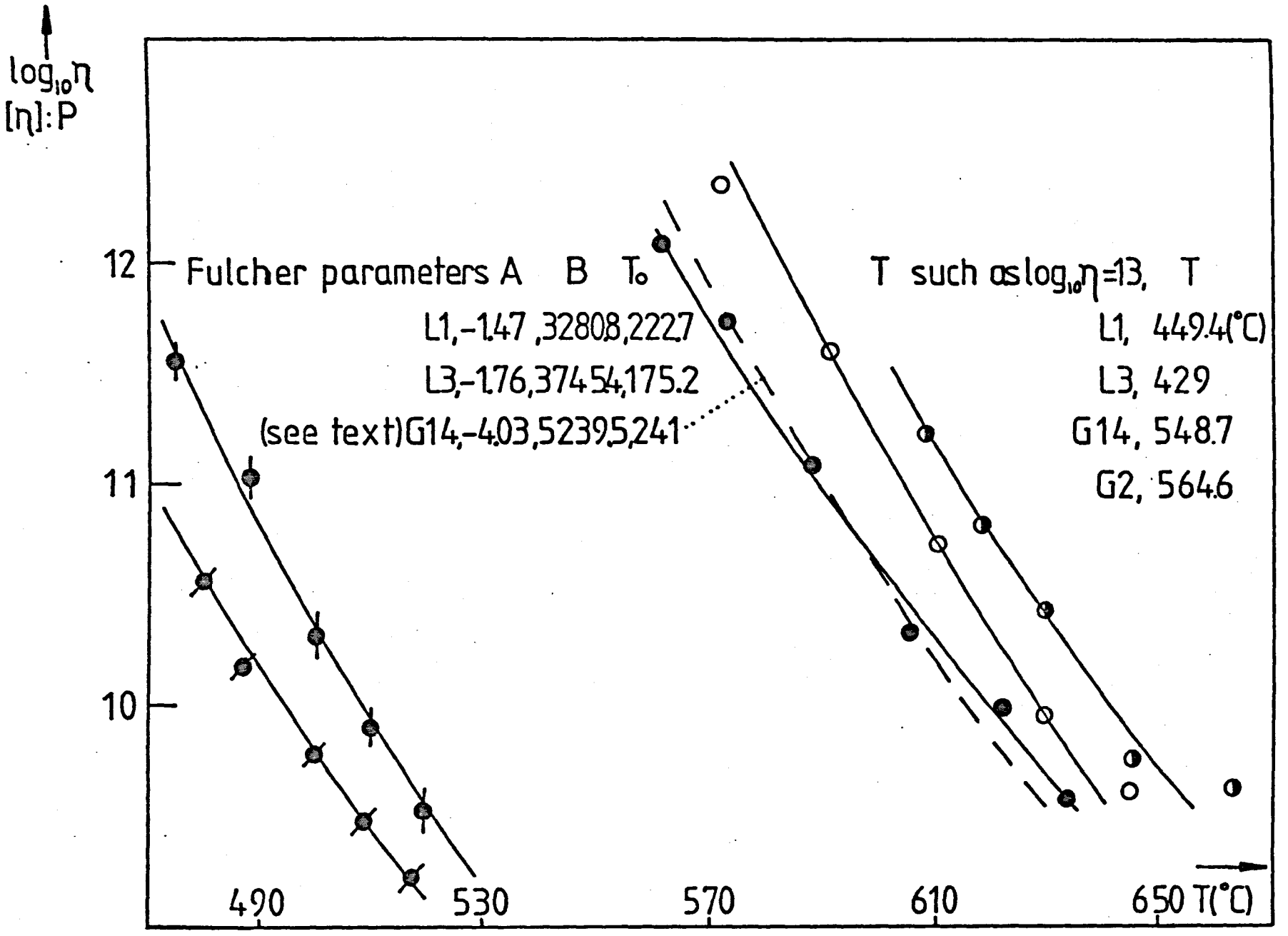

15 mole% Na_2O and 10 mole% CaO and containing 0.11 wt.% water was only a factor of 2 less than the same composition with a water content of 0.004 wt.%. However, at 560°C the corresponding reduction in viscosity was almost two orders of magnitude. This is consistent with our results. In the present study the maximum reduction in viscosity (for a similar viscosity range) was about one order of magnitude. However, in the work of Scholze and Merker the increase in water content was 30 times compared with only 6 times in our work.

4.1.4 Other results

The crystalline phase precipitated from G14 and G15 was the low temperature form of NC_2S_3. This was confirmed by electron diffraction for the early stages of growth in G14 (see Table 3.9). For the lithia glasses the primary crystalline phase was lithium disilicate.

The liquidus temperature and the 'DTA Tg' for glasses G2, G14, G15, L1 and L3 are listed in Table 4.4. The heats of fusion for G14 and G2 are also given. Clearly the DTA Tg show a decrease for the glasses with higher water contents, which is consistent with the viscosity behaviour. Only a slight decrease in T_L with water content, was observed.

4.2 NaF Additions

Five glasses were melted and the compositions are listed in Table 4.5 (see also Table 2.1). G3 to G6 belong to the series

TABLE 4.5 GLASSES CONTAINING F^-

Glass Code	Nominal glass composition
G3	$97(NC_2S_3)3NaF$
G4	$94(NC_2S_3)6NaF$
G5	$82(NC_2S_3)18NaF$
G6	$45(NC_2S_3)55NaF$
G7	$97\ (C_2S_3)95.5N3NaF$

TABLE 4.6 GROWTH RATES FOR G3, G4 AND G5

Glass	T(°C)	μ(μm min^{-1})
G3	590	0.025
	610	0.082
	650	0.273
	668	0.725
	691	1.744
G4	590	0.046
	610	0.100
	630	0.277
	650	0.390
	668	0.790
	691	2.375
	705	3.200
G5	590	0.318
	610	0.983
	634	1.479
	650	2.417
	668	4.827
	692	12.0

TABLE 4.7 DTA RESULTS

Glass Code	'DTA Tg' (°C)	ΔH_c (cal g^{-1})	ΔH_f (cal g^{-1})
B2	579	35.9 ±1.8	58.2 ±2.9
G3	579	38.0	59.6
G4	570	35.9	56.4
G5	552	32.5	54.3
G6	458		

(1-X) NC_2S_3.XNaF. G7 was intended to have the same Na_2O content as the composition NC_2S_3 on the assumption that the Na^+ from the NaF would combine with atmospheric oxygen to give Na_2O. For all glasses chemical analysis (see Appendix A2) revealed a considerable loss of fluoride during melting. For example, for G5 (nominal F content 1.15 wt.% ,see Table 2.1) the F content was 0.77 wt.% corresponding to a 33% loss. For higher nominal fluoride contents the losses increased. Thus for G6 (nominal F content 5.73 wt.%) the loss was 43%.

Since, as we have already seen, water content can strongly influence the kinetics of crystallization, it was decided to check the water content of one of the fluoride glasses. The water content for G5, measured using equation (4.4), was 0.0094 wt.% (see Table 4.2 and Figure 4.1) which is slightly higher than for G2. This may mean that the water uptake of fluoride glasses is higher than for non fluoride glasses, under normal melting conditions.

4.2.1 Nucleation rates

The nucleation results are given in Figure 4.9. For G3 (3 mole% NaF) the 'maximum nucleation rate' (N_V/t) was 2.3×10^4 mm^{-3} min^{-1} at 600°C significantly greater than the value for the base glass G2. For G4 (6 mole% NaF) a further increase in the maximum was observed (3.4×10^4 mm^{-3} min^{-1} at 590°C). For G5 (18 mole% NaF) the maximum was 40×10^4 mm^{-3} min^{-1} at 580°C. For increasing NaF content the nucleation curves show a systematic

FIGURE 4.9 $Log_{10}(Nv/t)$ as a function of temperature for glasses G2, G3, G4, G5, G6 and G7.
(○) (◐) (●) (⊠) (◪) (◑)

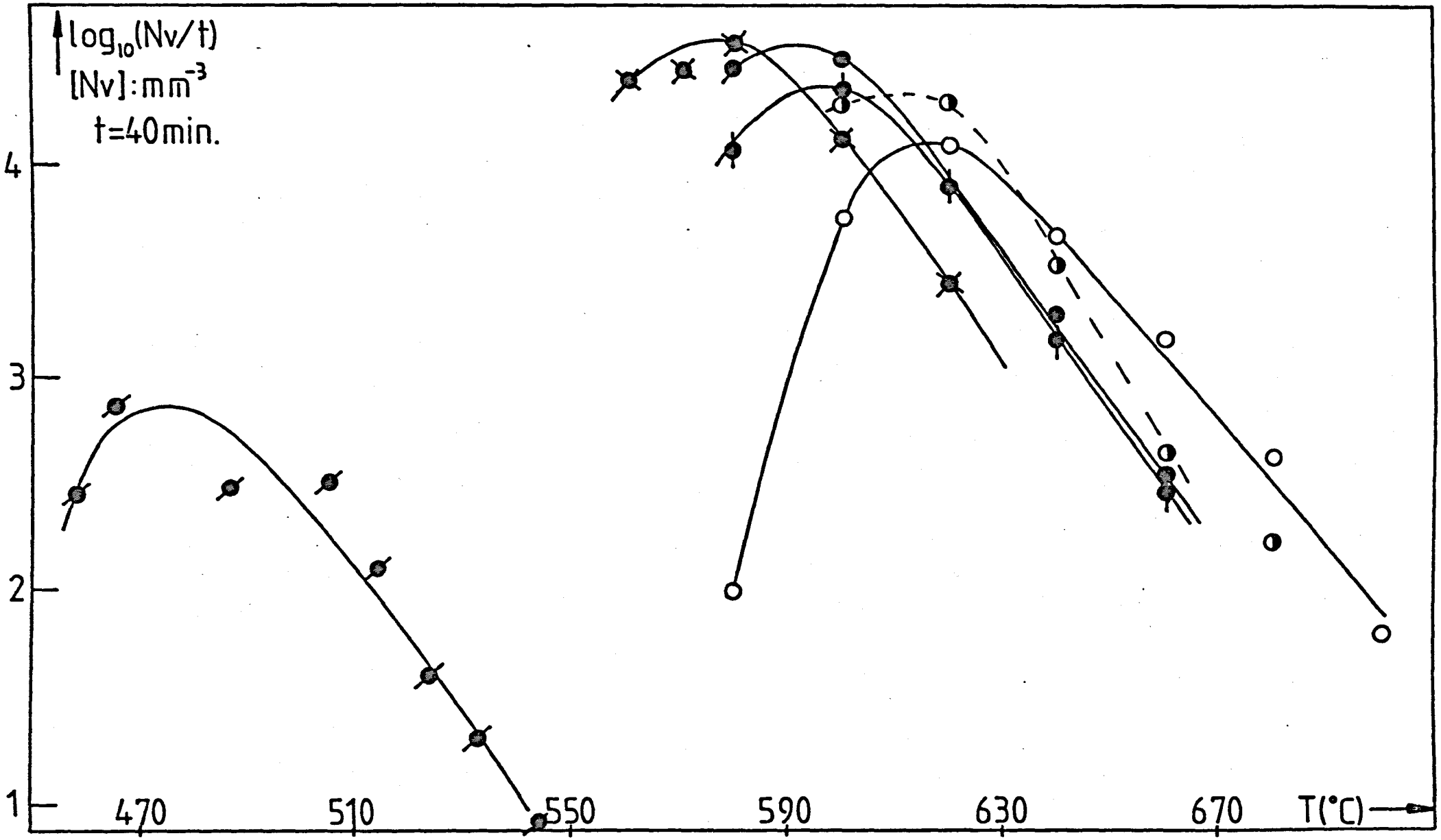

shift to lower temperatures and an increase in the maximum N_v/t. For C6, which contained a much larger amount of NaF than the other glasses, the shift in the maximum was as much as 140°C relative to G2, although the maximum N_v/t had now decreased to 0.75×10^3 mm^{-3} min^{-1}. G7, which was not in the same series as G3 to G6 (see above), also showed more nucleation at lower temperatures than G2 (but not at higher temperatures). The position of the maximum for G7 was similar to G2.

The crystals precipitated from these fluoride glasses were nearly spherical in shape. Optical micrographs for G7 and G5 are shown in Figures 4.10 and 4.11. Electron micrographs for G4 are shown in Figure 4.12.

For G6 (55 mol% NaF) the particles grew as spherulites up to a certain size and then appeared to change morphology (Figure 4.13). The origin of this effect is unknown but might be due to the formation of a new crystal phase (see X-ray results in section 4.2.4).

4.2.2 Growth Rates

Measurements were made for G3, G4 and G5. The maximum diameter of cross sections was measured for a series of times at the same temperature on previously nucleated glasses. The maximum diameter was found to grow linearly with time. A typical set of size vs time plots at different temperatures are shown in Figure 4.14 for G3, G4 and G5. The growth rates obtained by least squares analysis of the size versus time plots are given

Figure 4.10 (top left)

Optical micrograph of G7 heated at 710°C for 40 min
Mag X200.

Figure 4.11 (top right)

Optical micrograph for G5 nucleated at 620°C for 40 min and grown at 725°C.
Mag X500

Figure 4.12a,b

Electron micrographs of G4 nucleated at 620°C for 40 min and grown at 725°C.
(a) Mag X7,300; (b) X29,200.

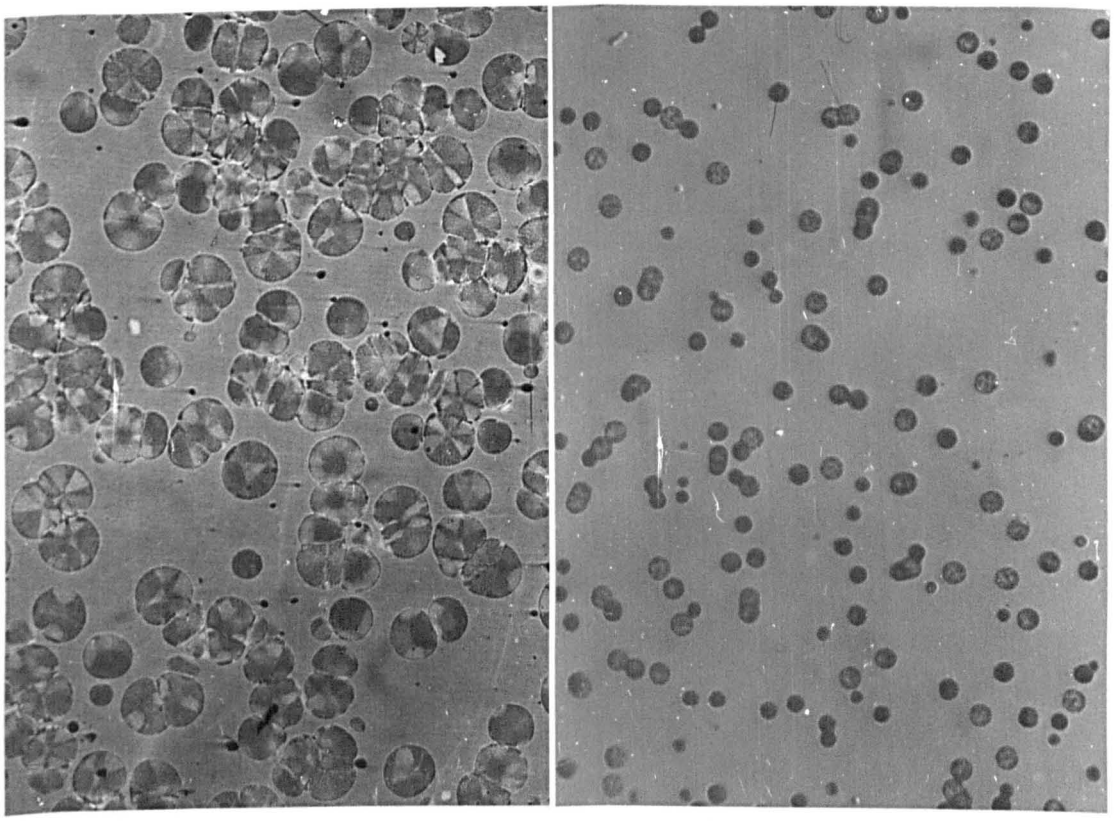

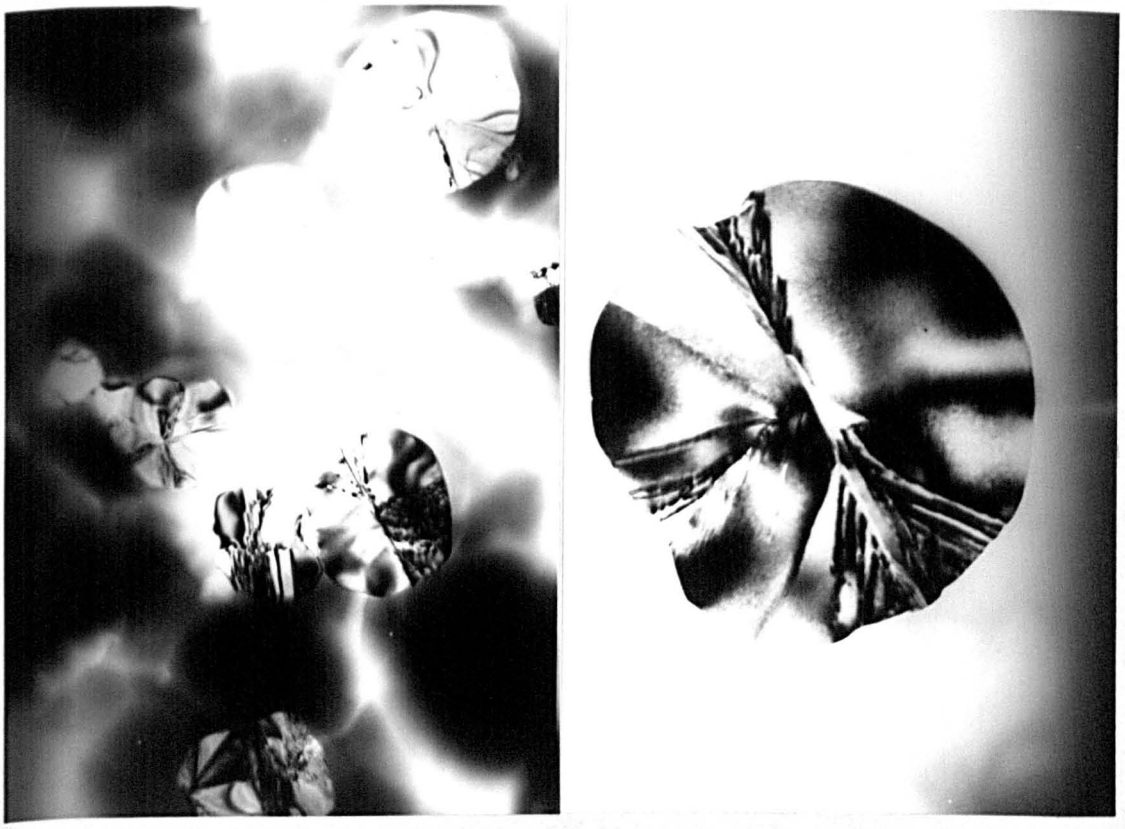

Figure 4.13a,b,c

(a) Optical micrograph (OM) of G6 nucleated at 486°C for 40 min and grown at 710°C. Mag X100

(b,c) OM of G6 heated at 610°C for 14 min. Mag X200.

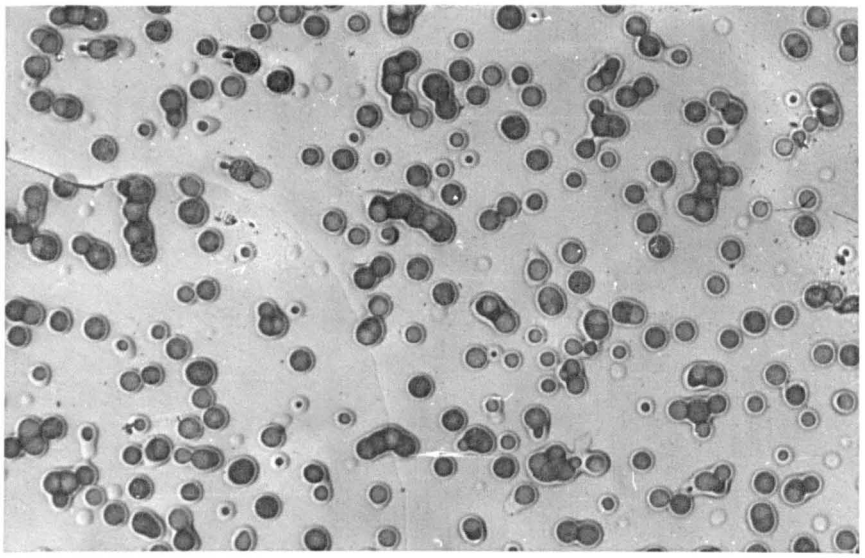

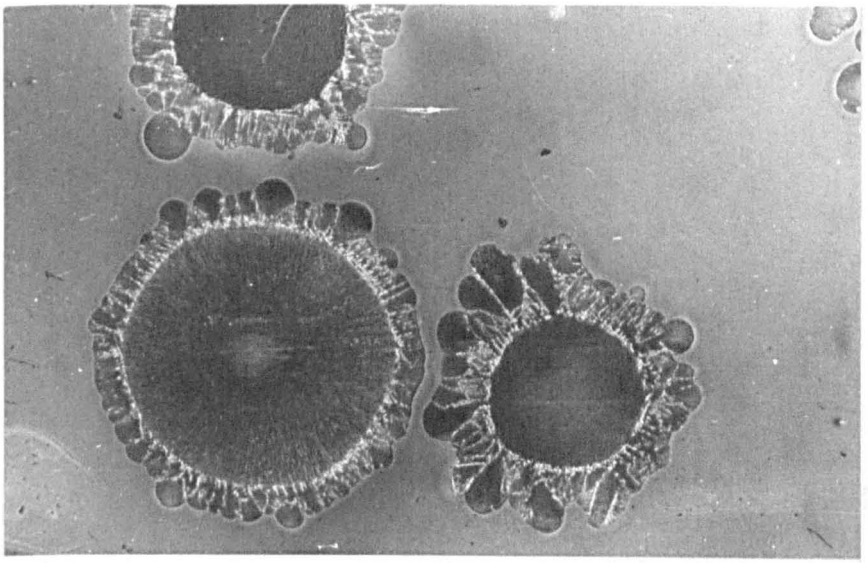

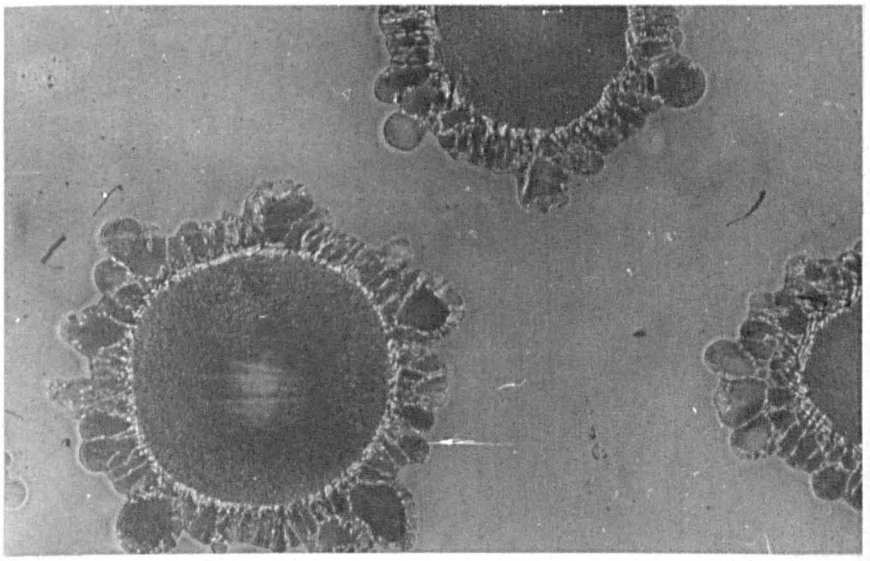

FIGURE 4.14 Size vs. time(t:min.), at the given temperatures, for glass(previously nucleated):G3

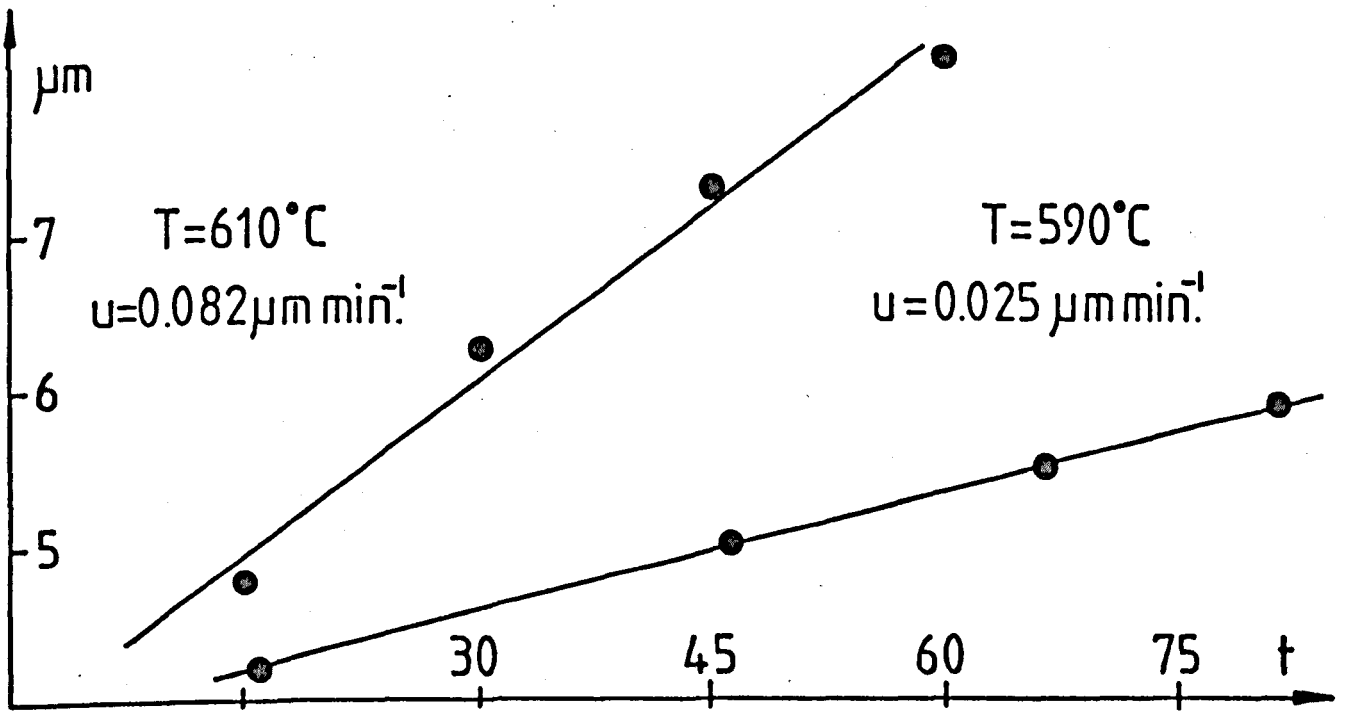

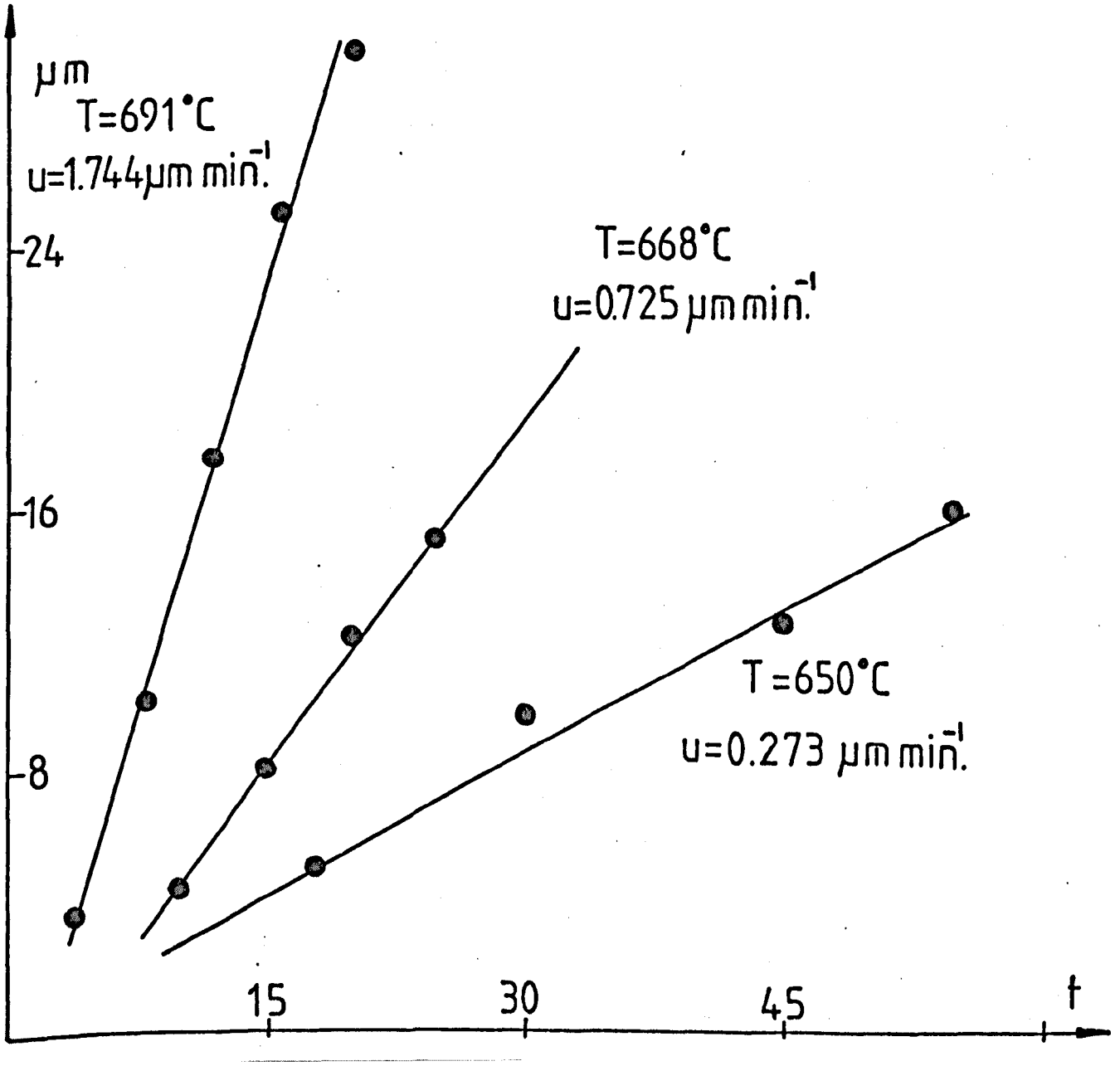

FIGURE 4.14 Continued: G4

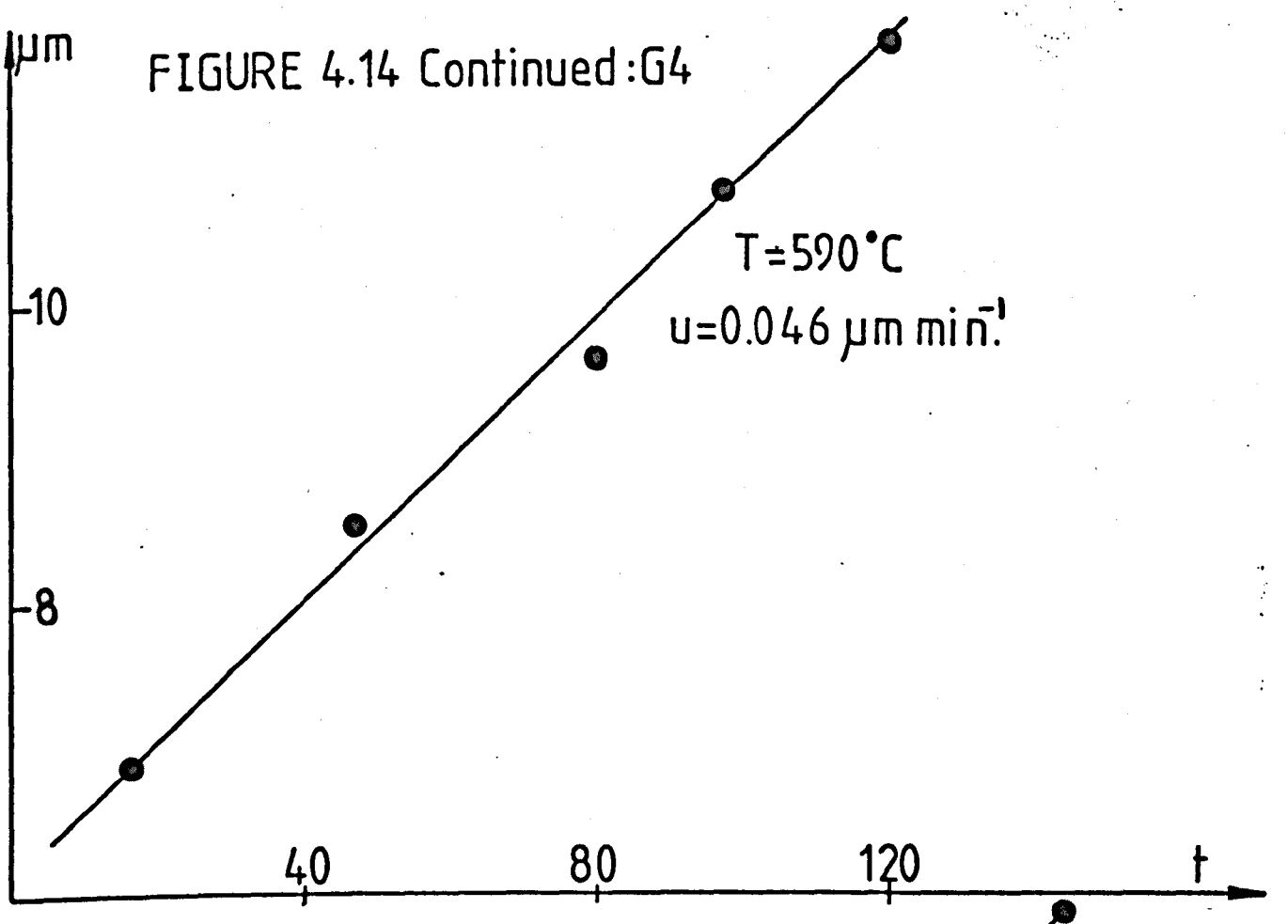

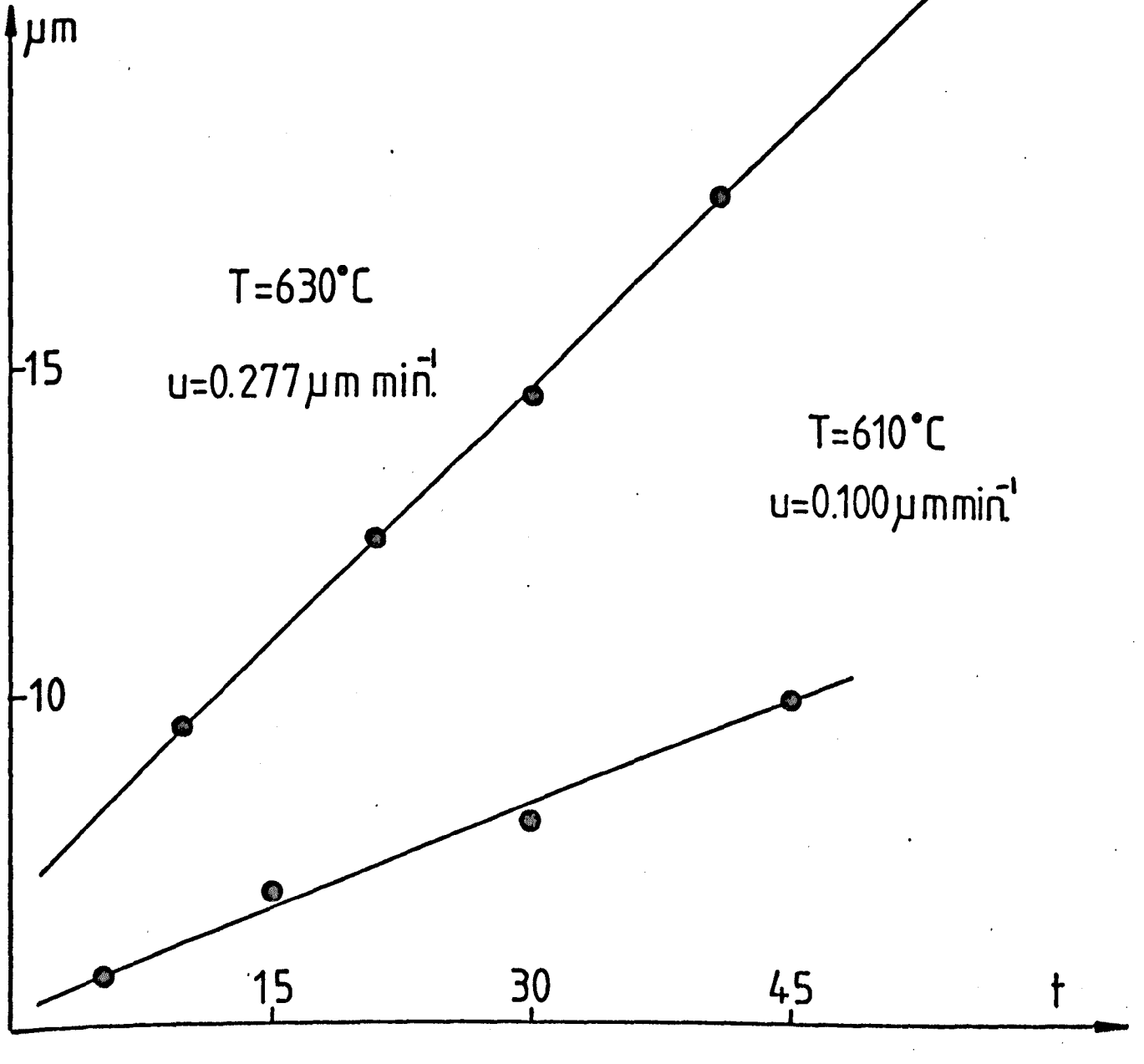

FIGURE 4.14 Continued: G4

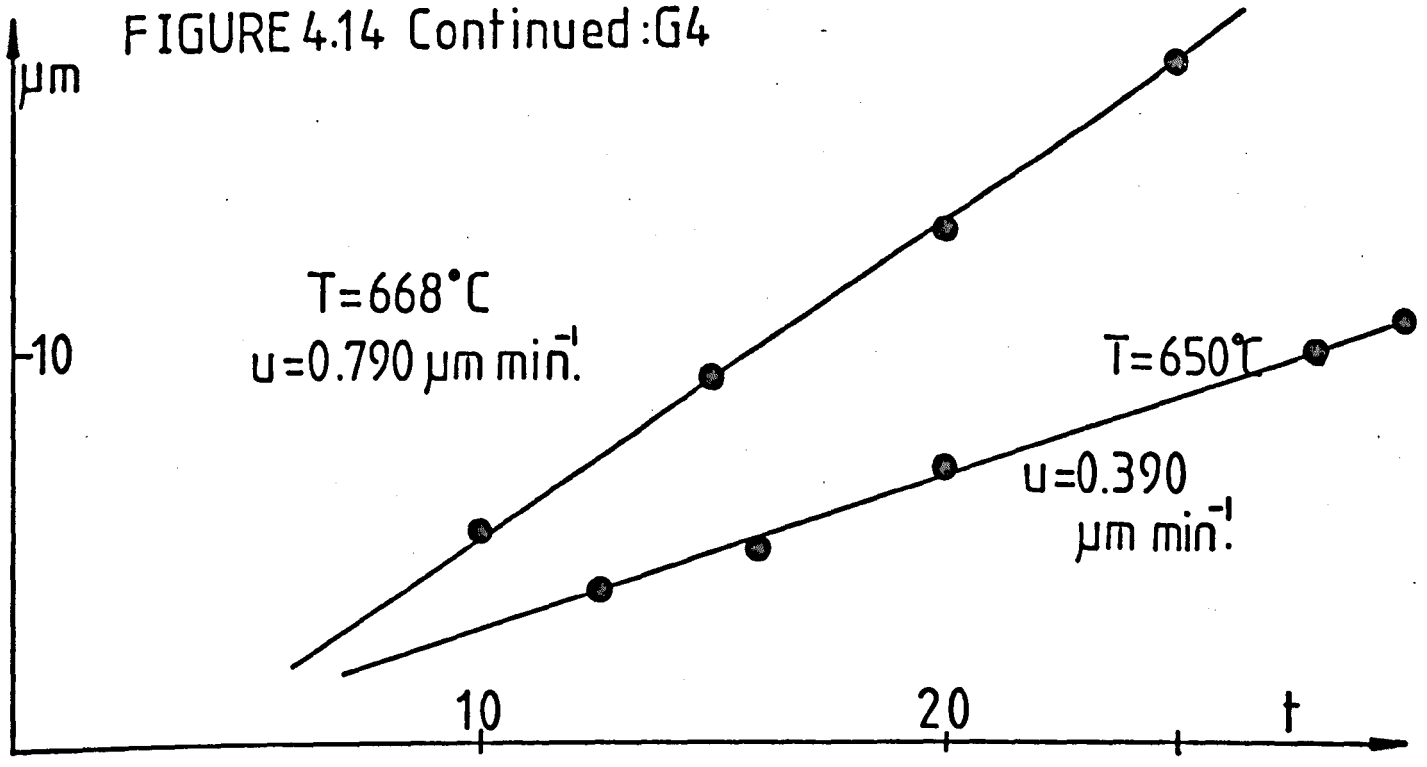

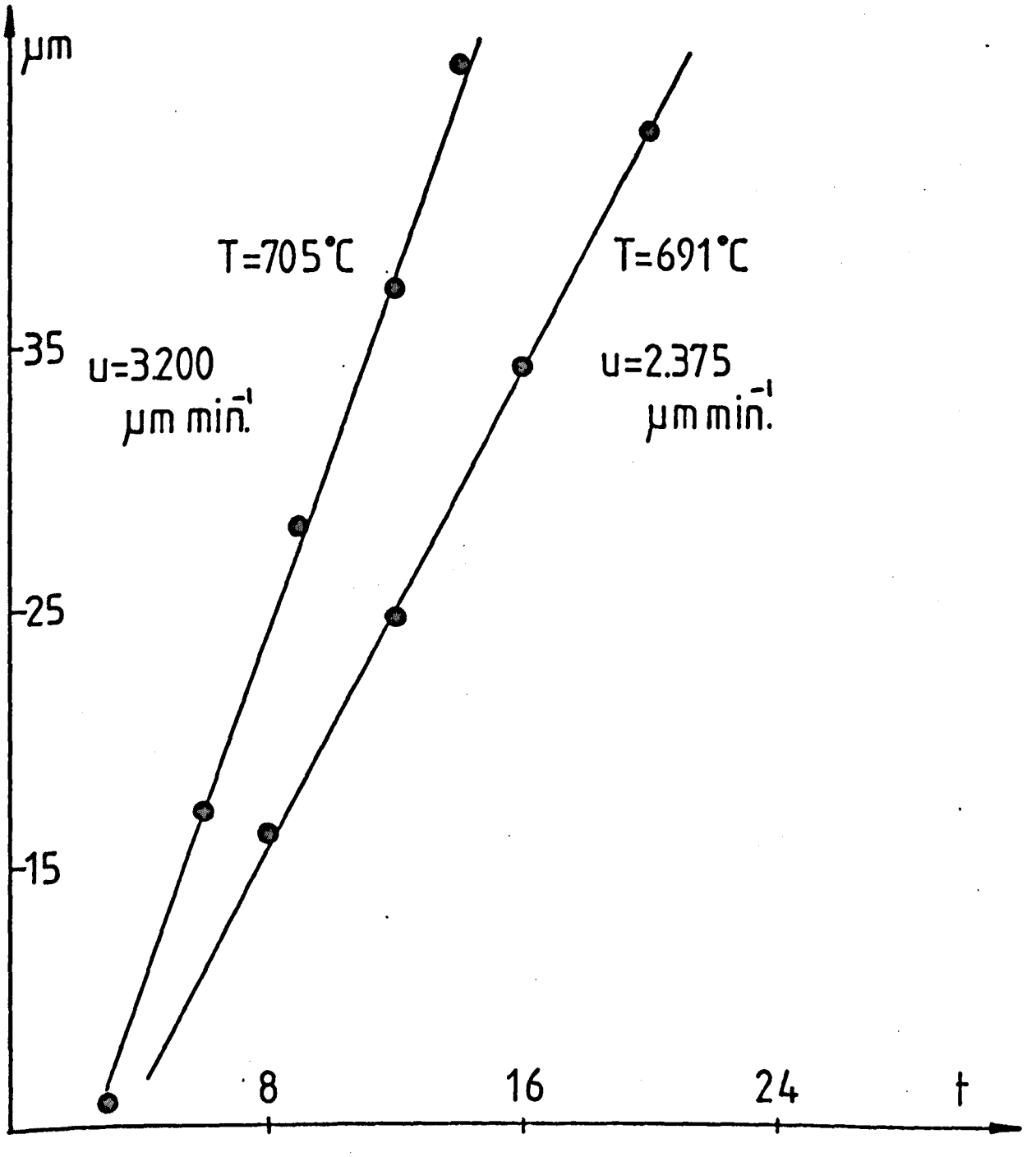

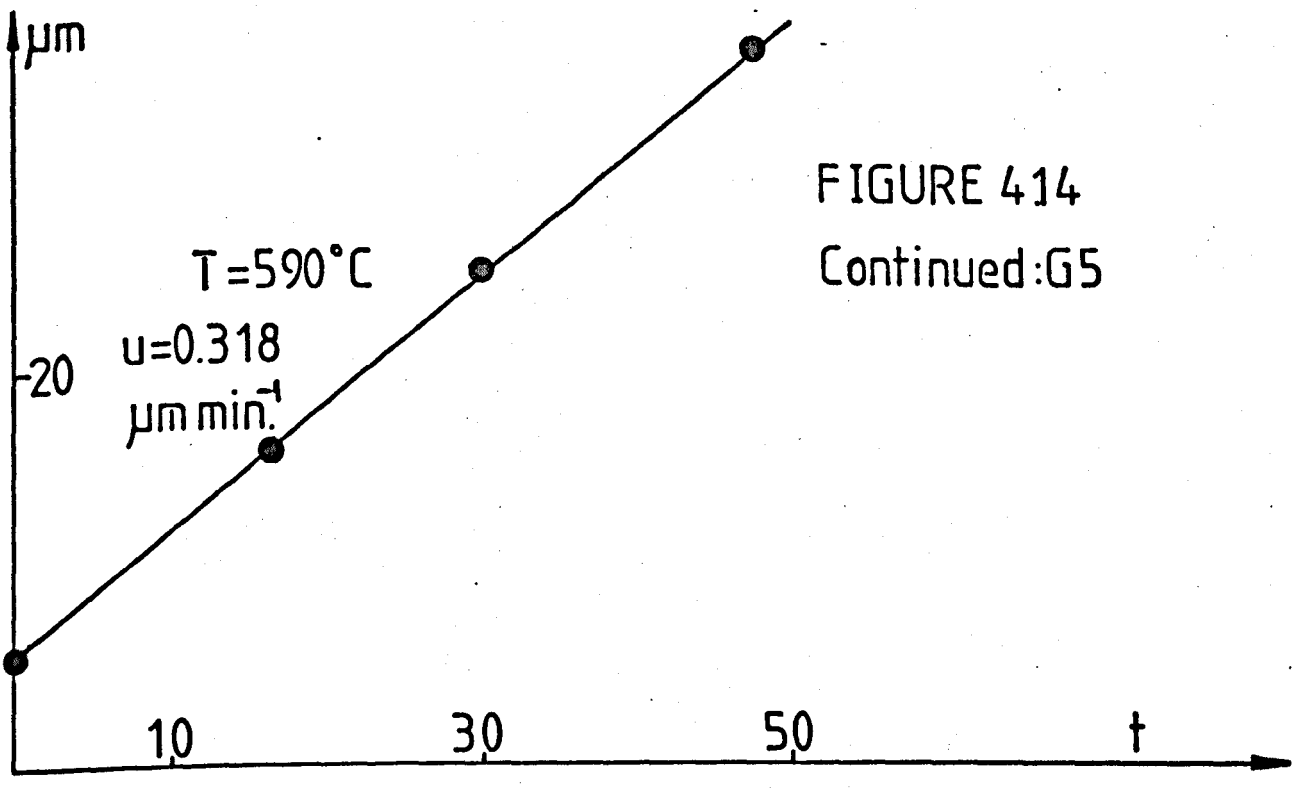

FIGURE 414
Continued: G5

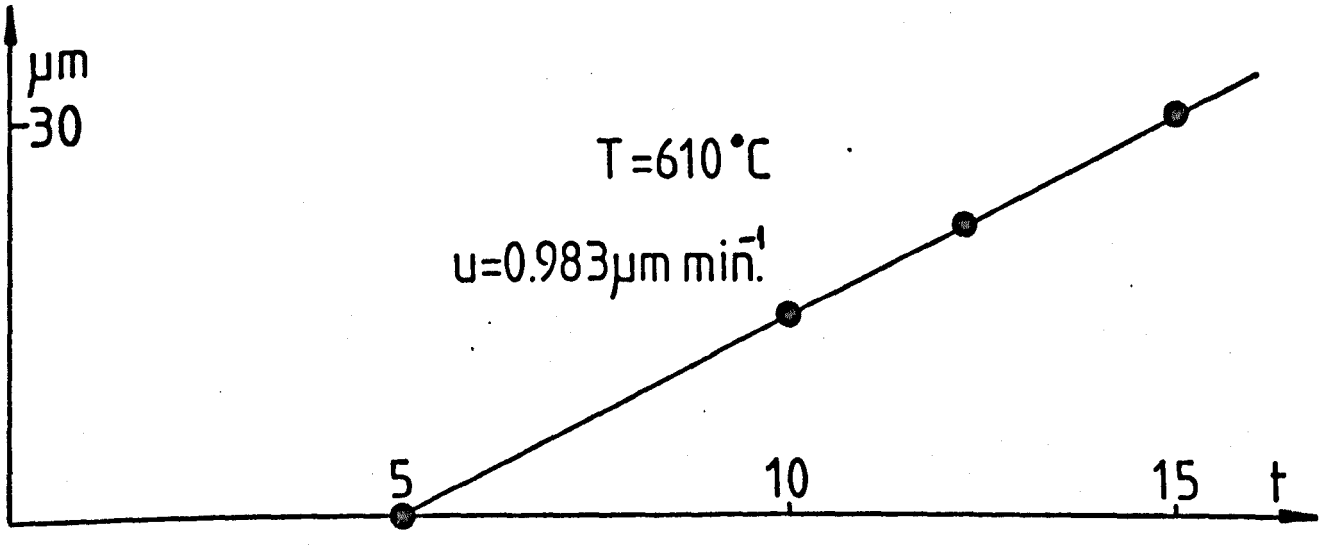

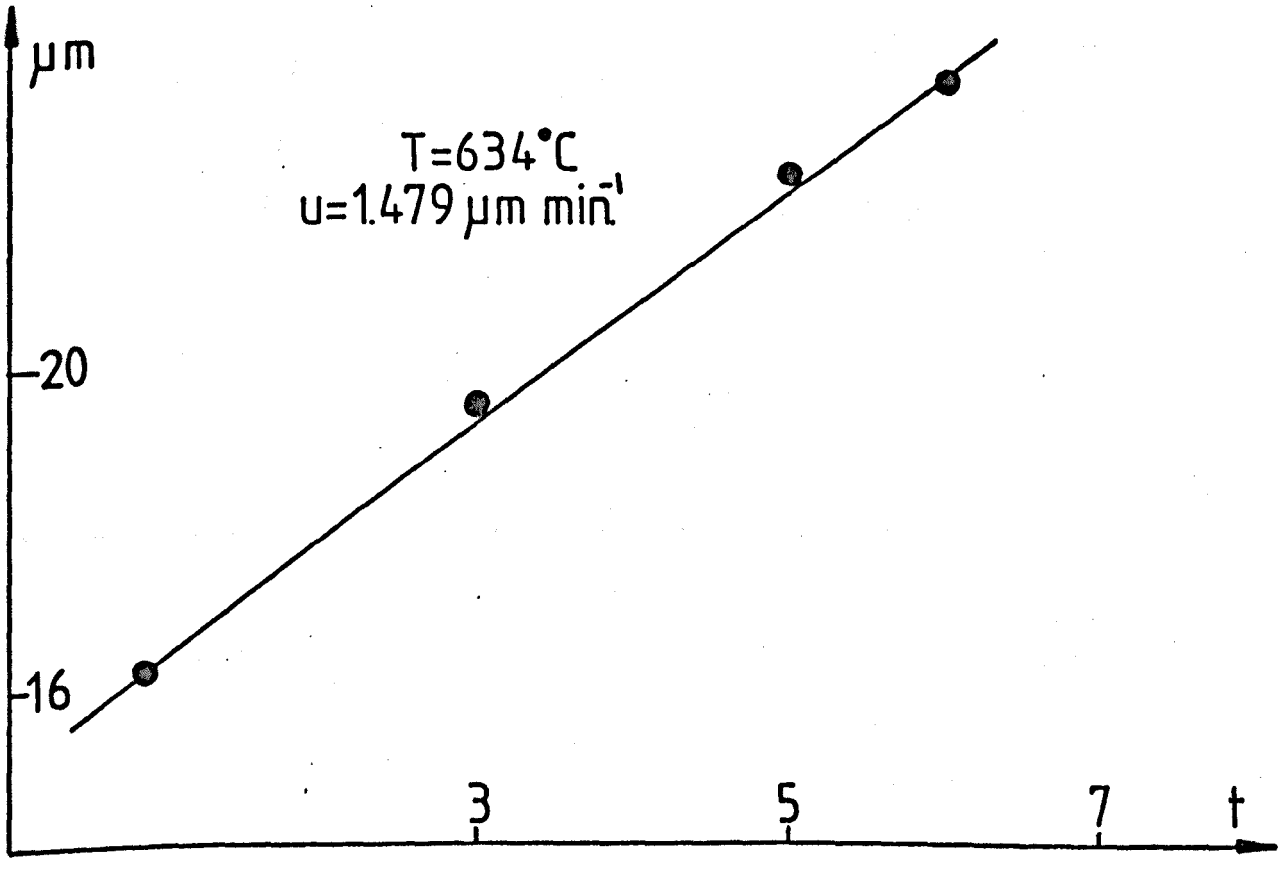

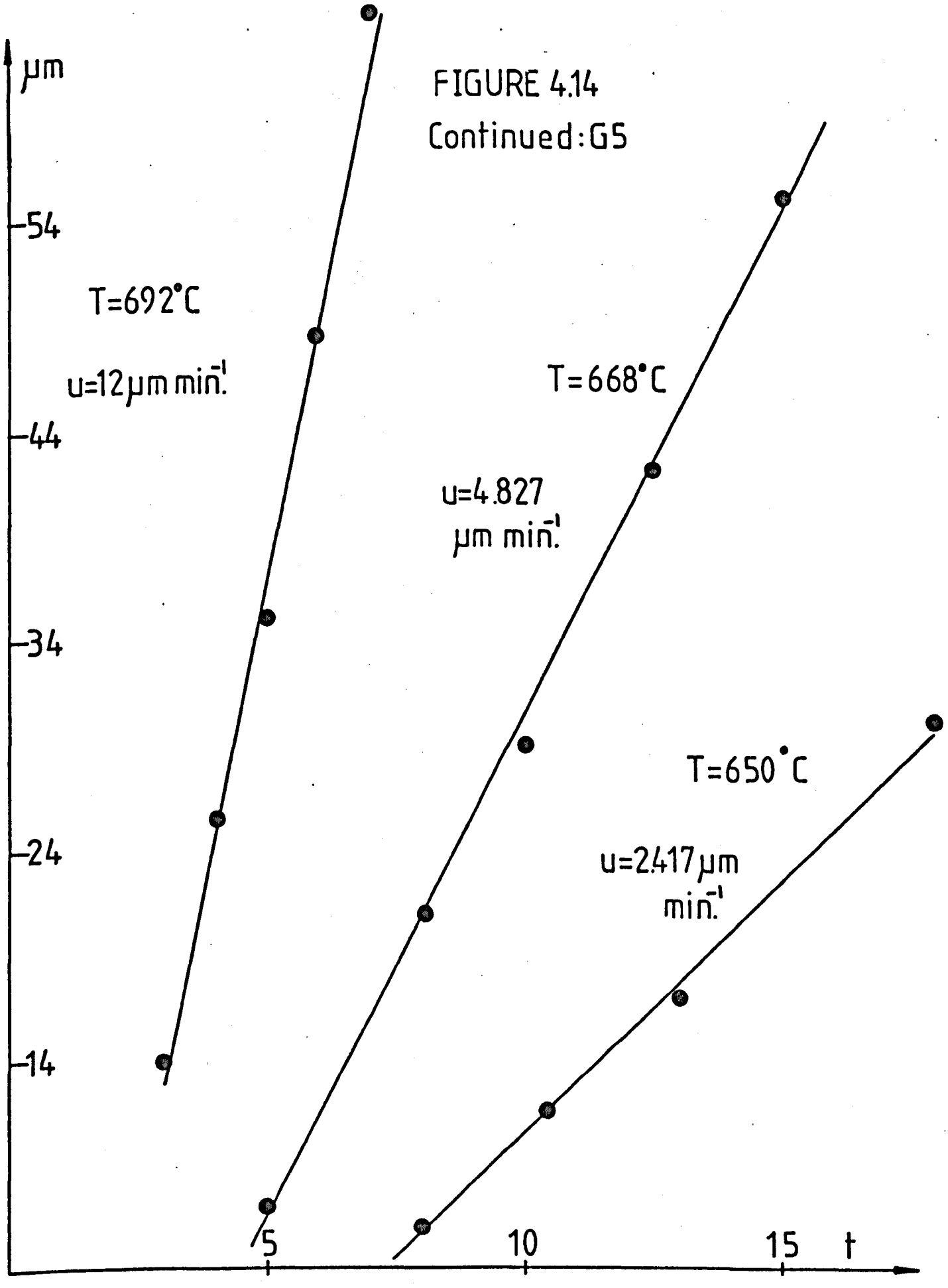
FIGURE 4.14
Continued: G5
μm
54
44
34
24
14
T=692°C
u=12μm min⁻¹
T=668°C
u=4.827
μm min⁻¹
T=650°C
u=2.417μm
min⁻¹
5
10
15
t

in Table 4.6. In Figure 4.15 the growth rates as a function of temperature are plotted for G3, G4, G5 and G2 (0% NaF). The growth rates showed a systematic increase with increasing NaF content.

4.2.3 DTA, viscosity and liquidus temperature results

The DTA results are given in Table 4.7. A marked drop in the 'DTA Tg' was observed for increasing NaF content suggesting a lowering of viscosity. The heats of crystallization and fusion remained constant within experimental error although there was an apparent decrease in the values from G3 to G5. The DTA traces for G3, G4 and G5 were very similar to G2. The reversible polymorphic transformation peak of the NC_2S_3 phase was also observed. However, the DTA trace for G6 (Figure 4.16) was different. The crystallization peak at 589°C exhibited a shoulder at higher temperatures and the apparent fusion peak at 842°C occurred at a much lower temperature. This behaviour may be due to the precipitation of more than one crystalline phase in this glass.

The viscosity results for G5 are shown in Figure 4.17. The curve for G5 corresponds to the Fulcher equation fitted to the low temperature range data for G5 and the high temperature range data for G2. The $\log_{10}\eta = 13$ value occurred at 537.3°C, 27°C lower than for G2. A difference of 27°C was also found in the 'DTA Tg' values. The viscosity of G5 was lower than G2, the curves for the two glasses being almost parallel.

FIGURE 4.15 Growth rates as a function of temperature for glasses G2, G3, G4 and G5 .
(×) (+) (○) (●)

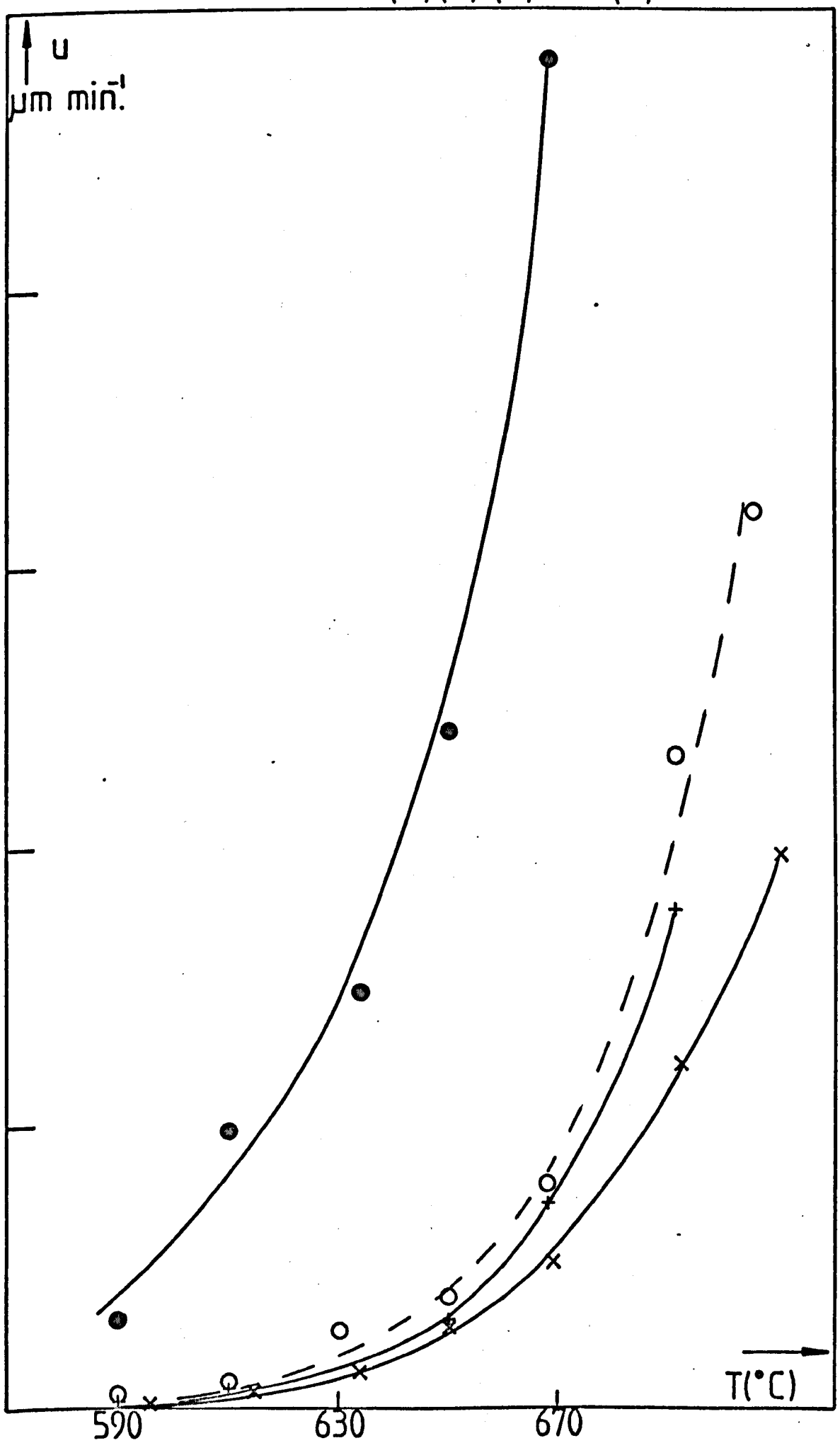

FIGURE 4.16 DTA TRACE FOR GLASS G6.

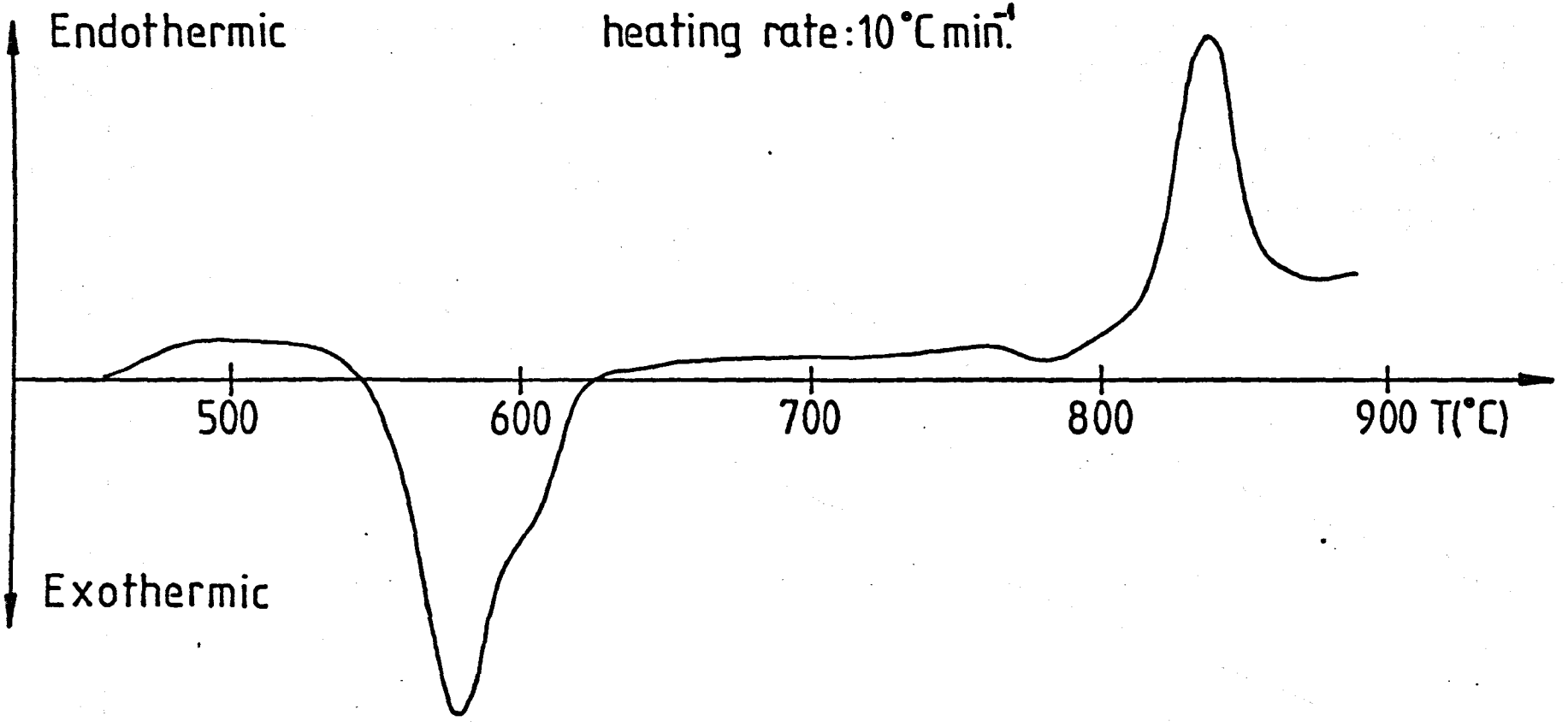

FIGURE 4.17 $Log_{10}\eta$ as a function of temperature for glasses G5 and G2.
(●) (○)

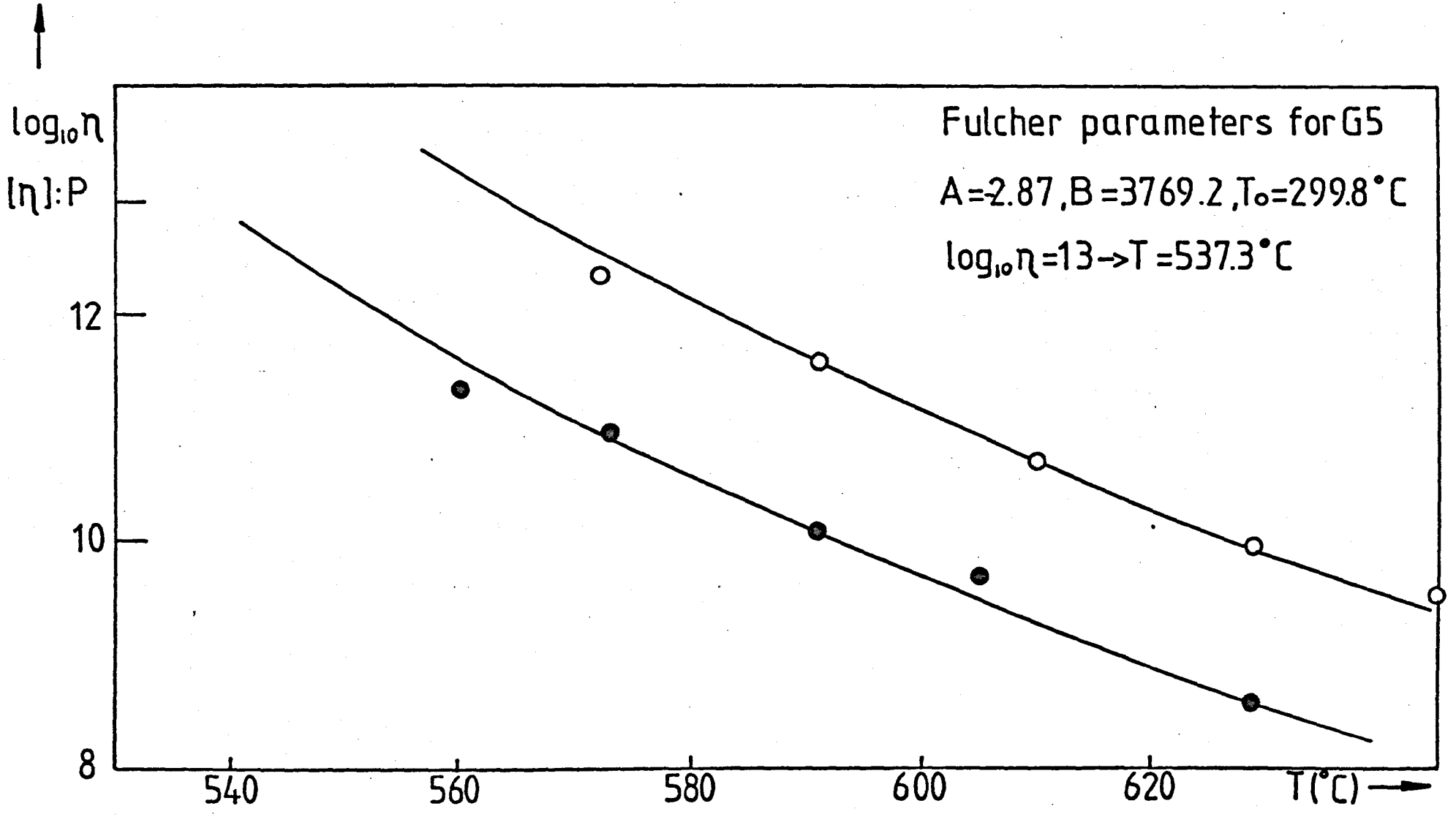

The liquidus temperature for G5 was 1266°C, 11°C lower than for G2.

4.2.4 X-ray Results

For the crystallized glasses G3, G4 and G5 the peak positions correspond to the low NC_2S_3 form. The only differences were in the relative heights of the peaks. For G6 the patterns were more complicated. Samples of G6 were heated at 595°C for times ranging from 15 to 240 min. The results are given in Table 4.8. The peak heights increased after the 15 min treatment. After 45 min little or no changes in the pattern could be detected. For the 30 min treatment the majority of the peaks correspond to the 'high' NC_2S_3 except for the peak at 2.63 Å where for NC_2S_3 two peaks should be observed. The peaks at 2θ = 38.85, 56.1 and 70.45 correspond to the following NaF d spacings: 2.32 (very strong reflection), 1.64 and 1.34 Å respectively. Also the peaks at 2θ = 28.35 and 47.10 correspond to the CaF_2 d spacings 3.153 and 1.931 Å (very strong reflection) respectively. Examination of the data for 15 min suggests that the first phase precipitated was high NC_2S_3.

The unusual appearance of the crystals for G5 (Figure 4.13) can be tentatively explained as follows. The first phase to be precipitated is NC_2S_3. Subsequently a layer forms on the existing NC_2S_3 crystals, which is probably rich in crystalline NaF and CaF_2.

G6 was also heated for 20 min at 560, 600 and 747°C. The X-ray results were very similar to those given in Table 4.8. The

TABLE 4.8

X-RAYS DATA FOR G7 HEATED AT 595°C FOR DIFFERENT TIMES

2θ	d(Å)	Relative Intensity for different heat treatment times t(min)				
		t 15	30	45	60	240
11.80	7.46		14.7	12.9	15.1	12.4
16.75	5.30		12.4	11.3	13.5	13.1
20.30	4.37	12.6	24	24.1	22.4	21.1
23.85	3.73	15.9	74.0	76.1	77.1	67.5
26.65	3.34	18.0	56.4	53.0		52.3
26.80	3.32		80.0	77.1	77.0	68.8
28.35	3.15		24.1	26.1	26.5	24.8
29.40	3.03		17.5	20.6	17.1	18.4
33.95	2.63	30.8	>>>100	>>>100	>>100	>>>100
35.70	2.51	17.9	10.4	10.0	11.8	10.8
38.20	2.35		18.1	18.9	17.2	19.5
38.85	2.32		35.8	40.3	40.3	37.0
39.60	2.27		10.0	10.8	10.2	10.3
40.25	2.24		11.0	10.8	10	10.6
41.20	2.19		10.5	10.3		9.5
42.0	2.15		15.6	15.7	15.3	16.5
43.3	2.09		10.0	9.2	9.4	8.5
45.0	2.01					9.2
47.10	1.93		21.8	21.0	18.3	20.9
48.75	1.87	16.5	82.9	83.4	87.2	78.1
49.8	1.83					10.3
50.65	1.80		15.4	14.0	16.3	16.5
52.85	1.73			10.0		10.2
56.10	1.64		22.2	21.9	21.7	20.0
59.95	1.54		15.3		14.3	14.3
60.85	1.52		24.1	23.9	24.1	23.0
67.15	1.39			10.0		11.3
67.80	1.38		10.3	9.5	10.0	9.6
70.45	1.34		10.6	9.8		11.2
71.5	1.32		10.0	9.5	10.5	9.9
71.95	1.31		10.0	9.2		10.0

percentage crystallinity was greater for the higher temperatures probably due to the higher growth rates.

For the heat treatment at 747°C two peaks were observed near to 2.63 Å instead of the single peak found for treatment at 595°C. Two strong peaks at 2.62 and 2.66 Å are expected for 'high' NC_2S_3 (see section 3.3.7).

4.3 ZrO_2 Additions

Two glasses were melted (see Table 2.1), G12 (3 mole% ZrO_2, 97 mole% NC_2S_3) and G13′ (6 mole% ZrO_2, 94 mole% NC_2S_3). The water content of G13′, estimated from the infra-red trace shown in Figure 4.1, (value obtained from equation (4.4)) was 0.0072 wt.%, which is almost the same as the value for G2 (see Table 4.2).

4.3.1 Nucleation Results

The nucleation kinetics of G12 and G13′ were determined by the double stage heat treatment method previously discussed. Typical optical micrographs for G12 and G13′ are shown in Figures 4.18 and 4.19 respectively. The crystallization centres in these glasses appeared to be close to cubic in shape, in contrast to G2 where they were spherical. The cubic shape was confirmed by transmission electron microscopy. Figure 4.20 shows NC_2S_3 particles in glass G13′ at an earlier stage of development than those shown on the optical micrographs. Each particle appears to be composed of a single crystal.

Figure 4.18 (top left)

Optical micrograph of G12 heated at 720°C for 40 min
Mag X100.

Figure 4.19 (top right)

Optical micrograph of G13′ nucleated at 600°C for 40 min
and grown at 720°C. Mag X200.

Figure 4.20

Electron micrographs of G13′ and G12

G13′ heated at 586°C for 51 h
and at 597°C for 41 hr
Mag X14,000

G12 heated at 580°C for 40 hr
Mag X20,440

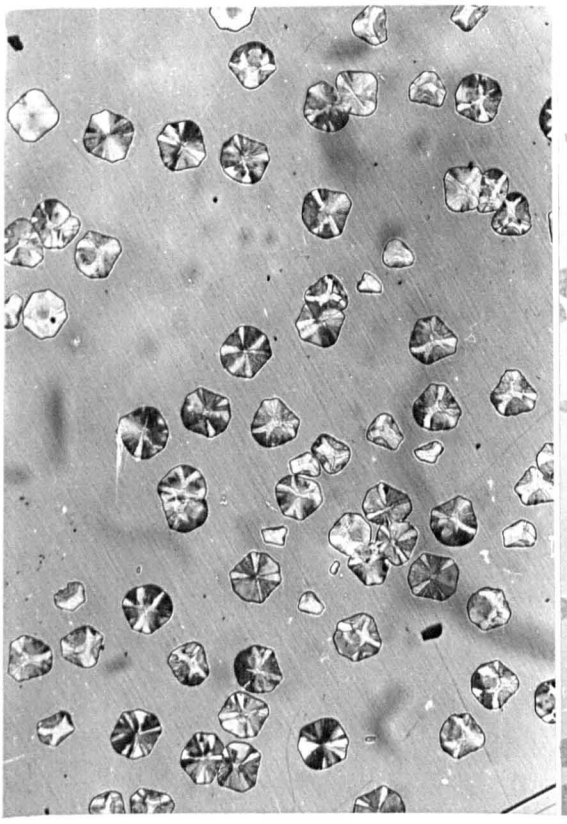

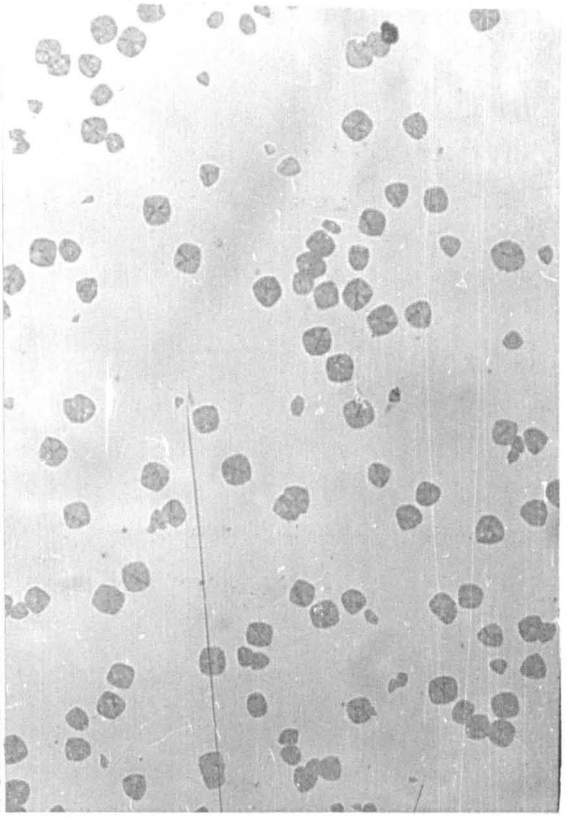

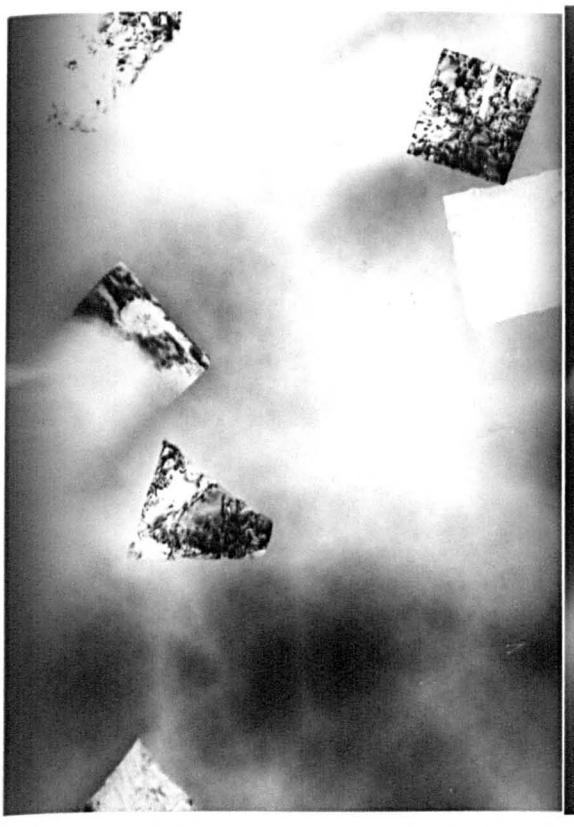

Since the particles were no longer spherical, to determine the nucleation densities N_V the procedure used was to measure the side of the longest square cross section observed. The results (obtained from equation (2.2)) for G2, G12 and G13′ are shown in Figure 4.21. The addition of 3 mole% ZrO_2 (G12) caused a small decrease in nucleation. Addition of 6 mole% ZrO_2 (G13′) caused a much larger decrease in N_V/t particularly at the higher temperatures but no significant change at the lower temperatures. Also the position of the maximum in the nucleation curve was not altered significantly, for G13′ the maximum rate being 4.68×10^3 mm^{-3} min^{-1}.

4.3.2 Growth Rates

The growth rates were obtained using the internal crystals and measuring the distance between parallel sides of the largest square sections observed. As before the size was found to be linear with time at a given temperature. Size vs time plots for G13′ are shown in Figure 4.22, and the growth rates vs temperature for G13′ and G2 are shown in Figure 4.23. The growth rates for G13′ were less than those for G2.

4.3.3 Viscosity, DTA and other results

The viscosities of G13′ and G2 are compared in Figure 4.24. Addition of ZrO_2 produced a considerable increase in viscosity in the low temperature range. The dashed curve corresponds to the Fulcher equation fitted to the low temperature data for G13′ and the high temperature data for G2. The $\log_{10}\eta = 13$ value

FIGURE 4.21 $Log_{10}(N_V/t)$ vs.T(°C) FOR GLASSES G12,G13′ and G2.
(●) (○) (×)

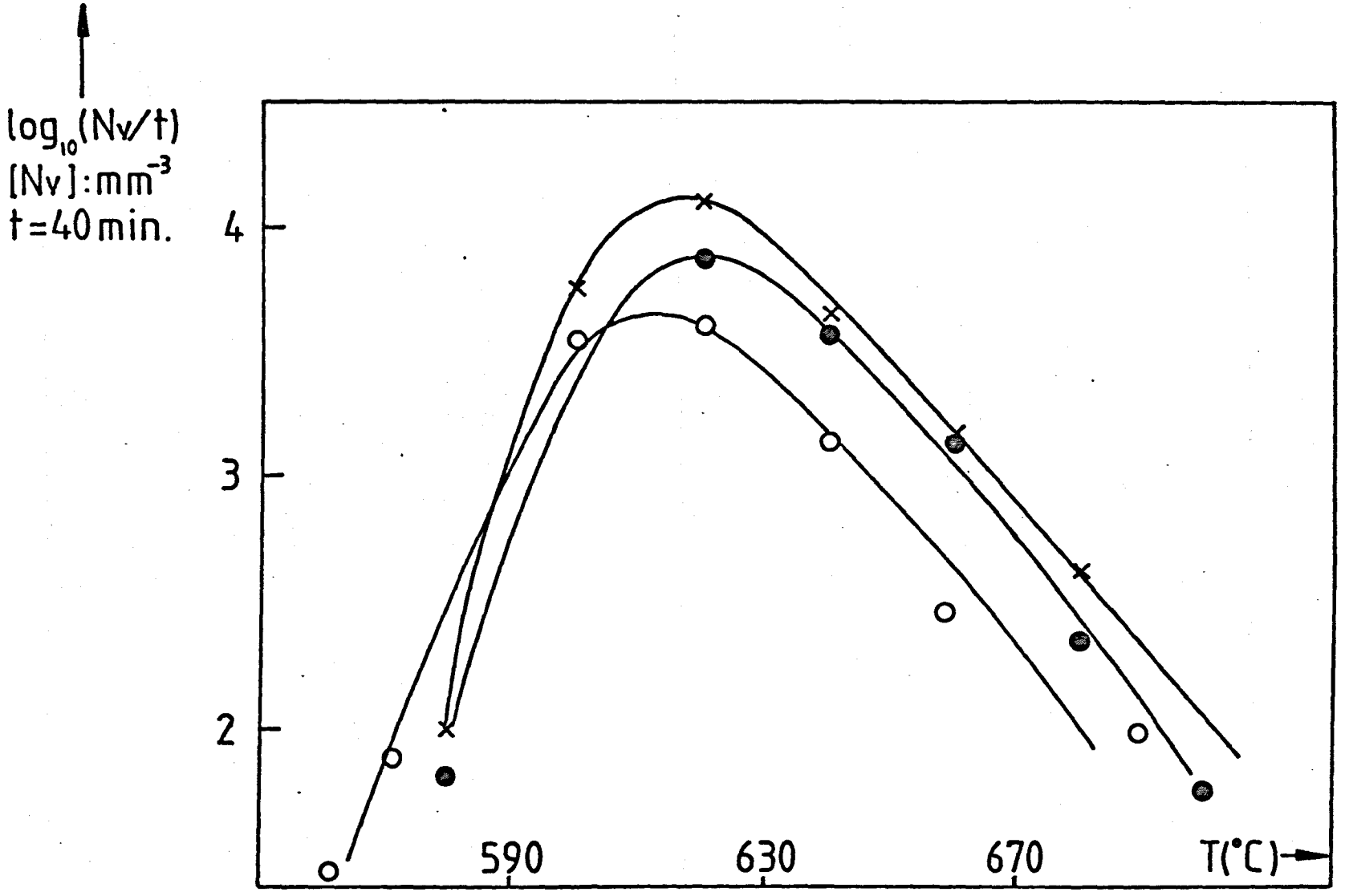

FIGURE 4.22 Size vs. time (t: min.), at the given temperatures, for glass (previously nucleated) G 13'.

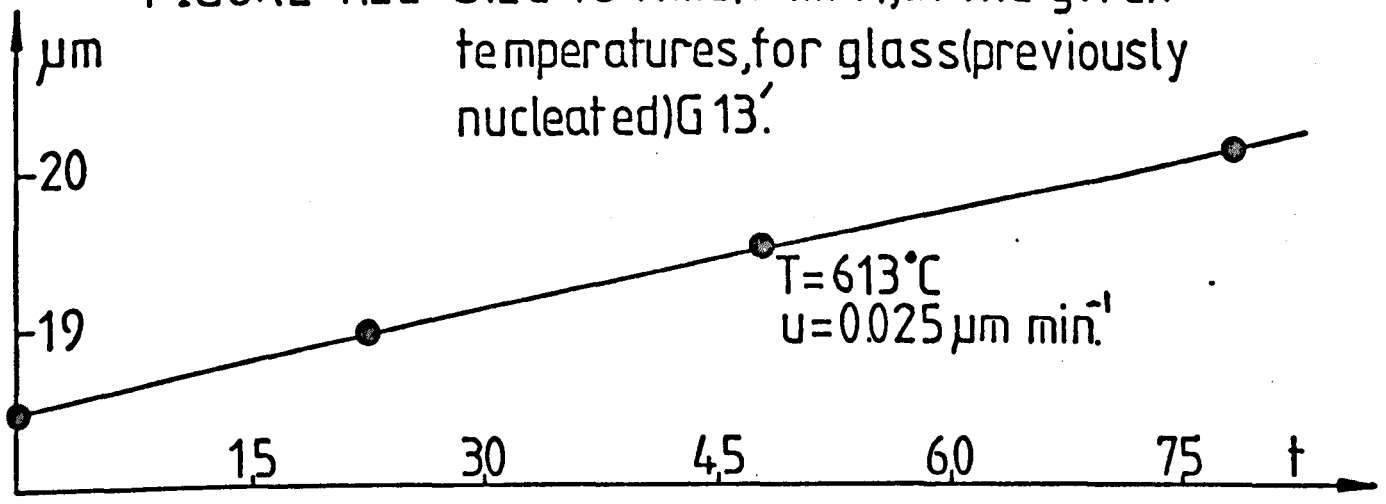

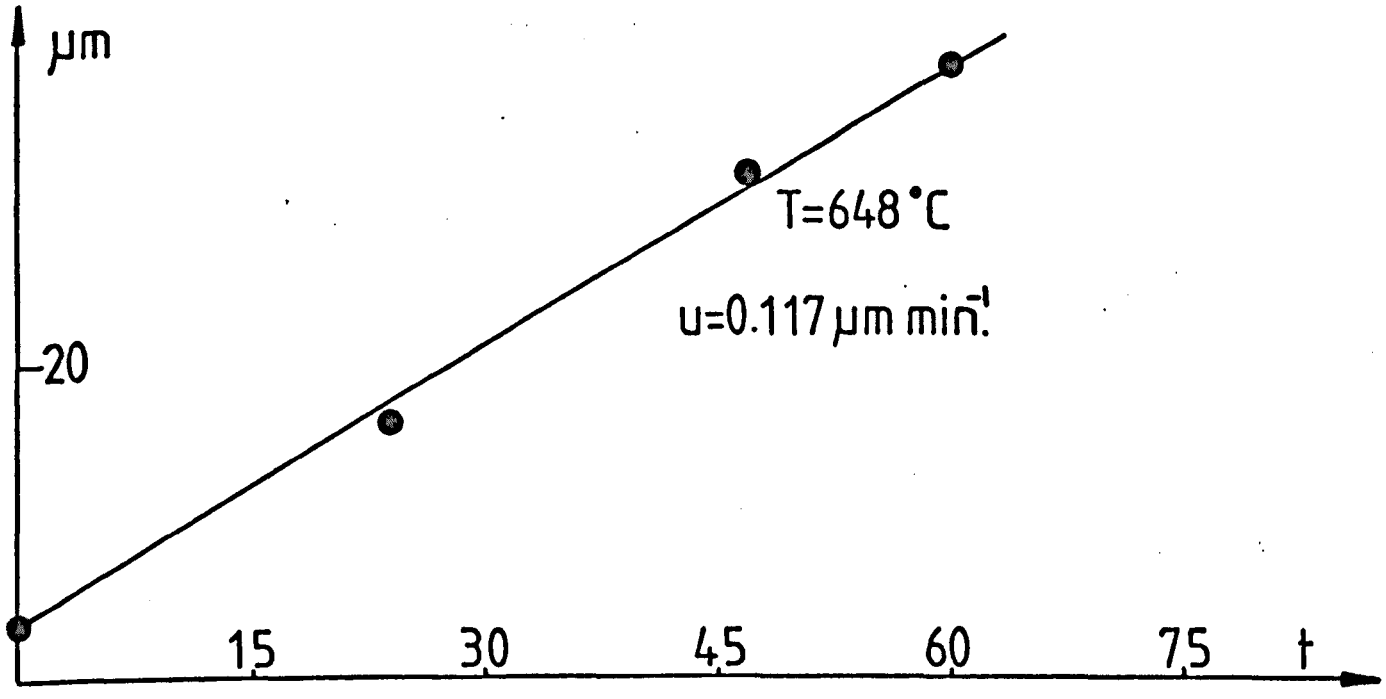

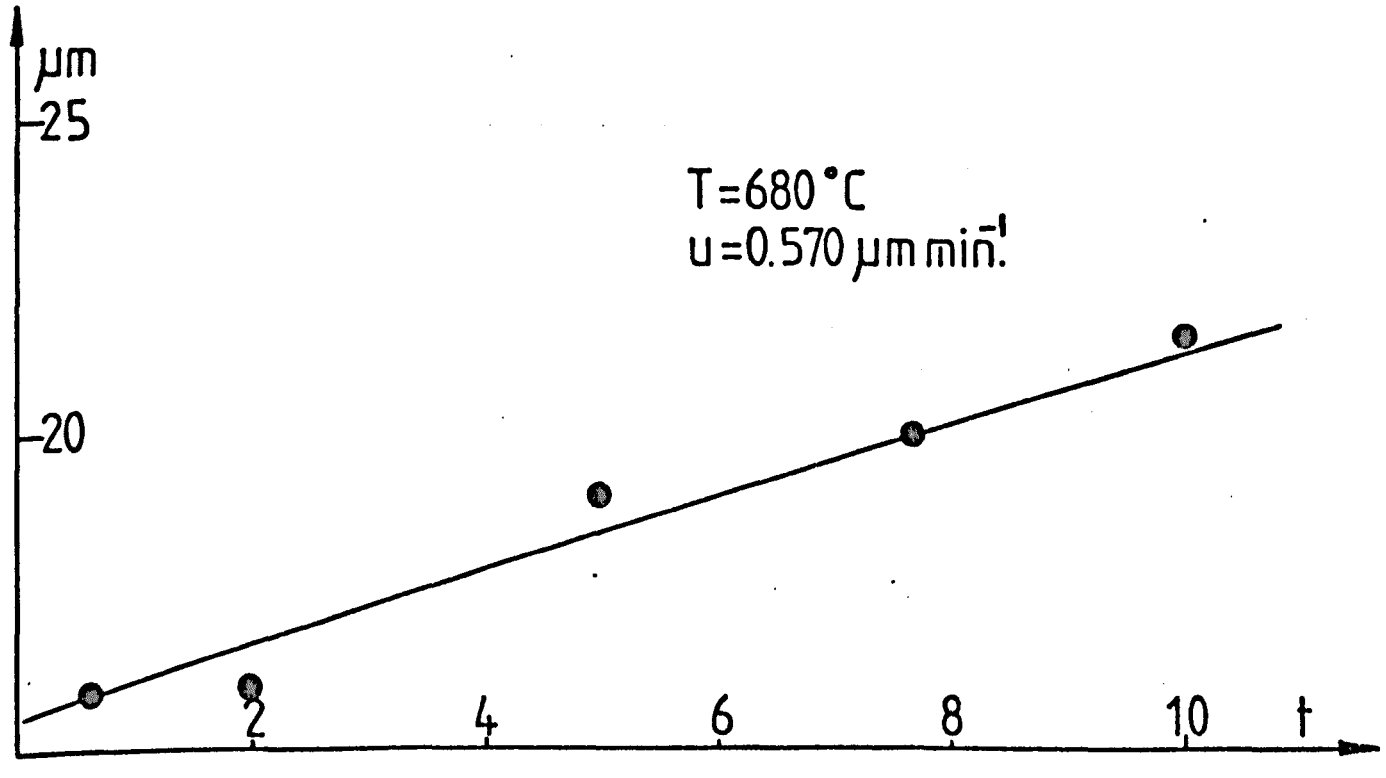

FIGURE 4.22 Continued;

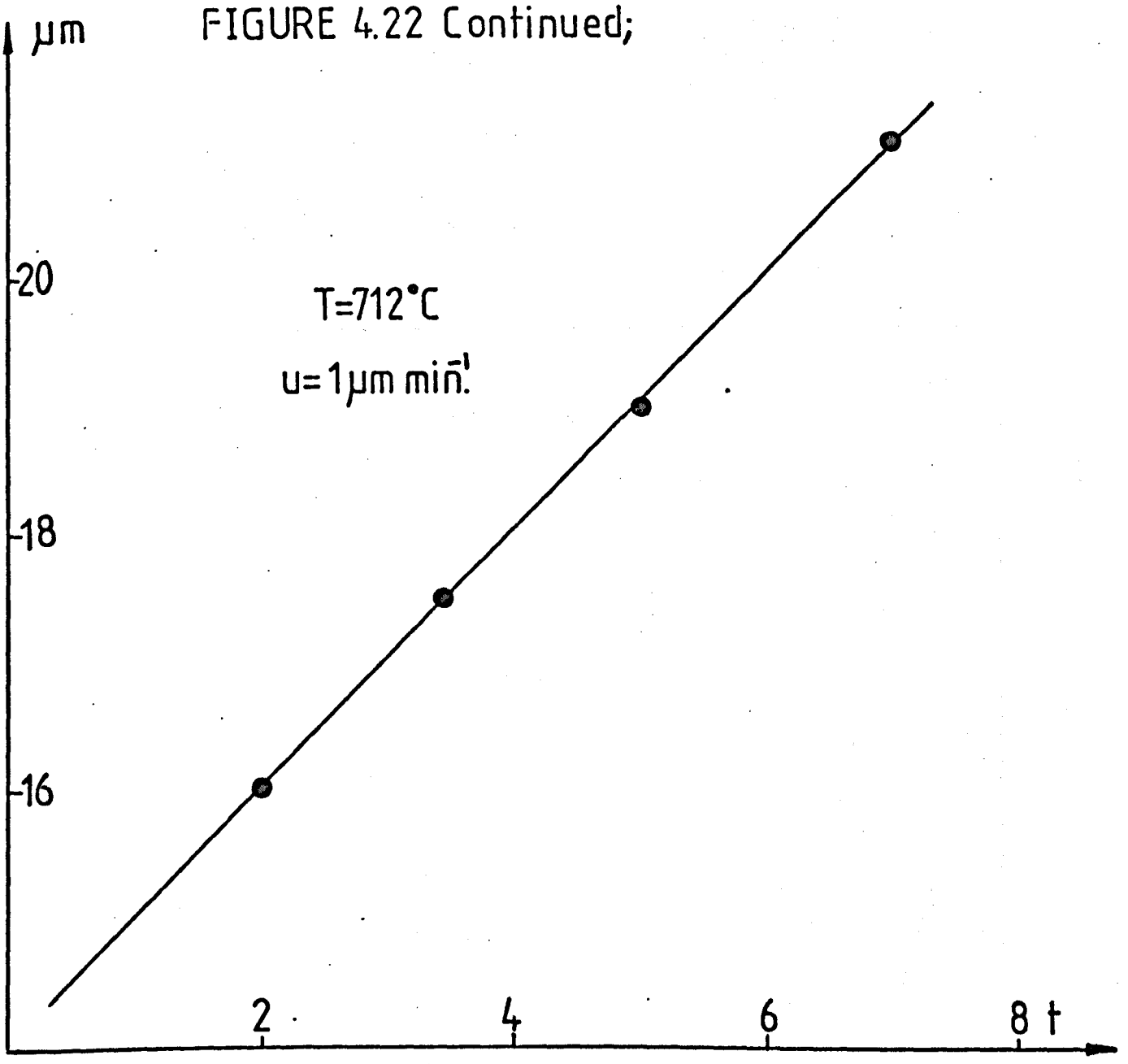

FIGURE 4.23 Growth rates as a function of temperature for glasses G13′ and G2.

(●) (○)

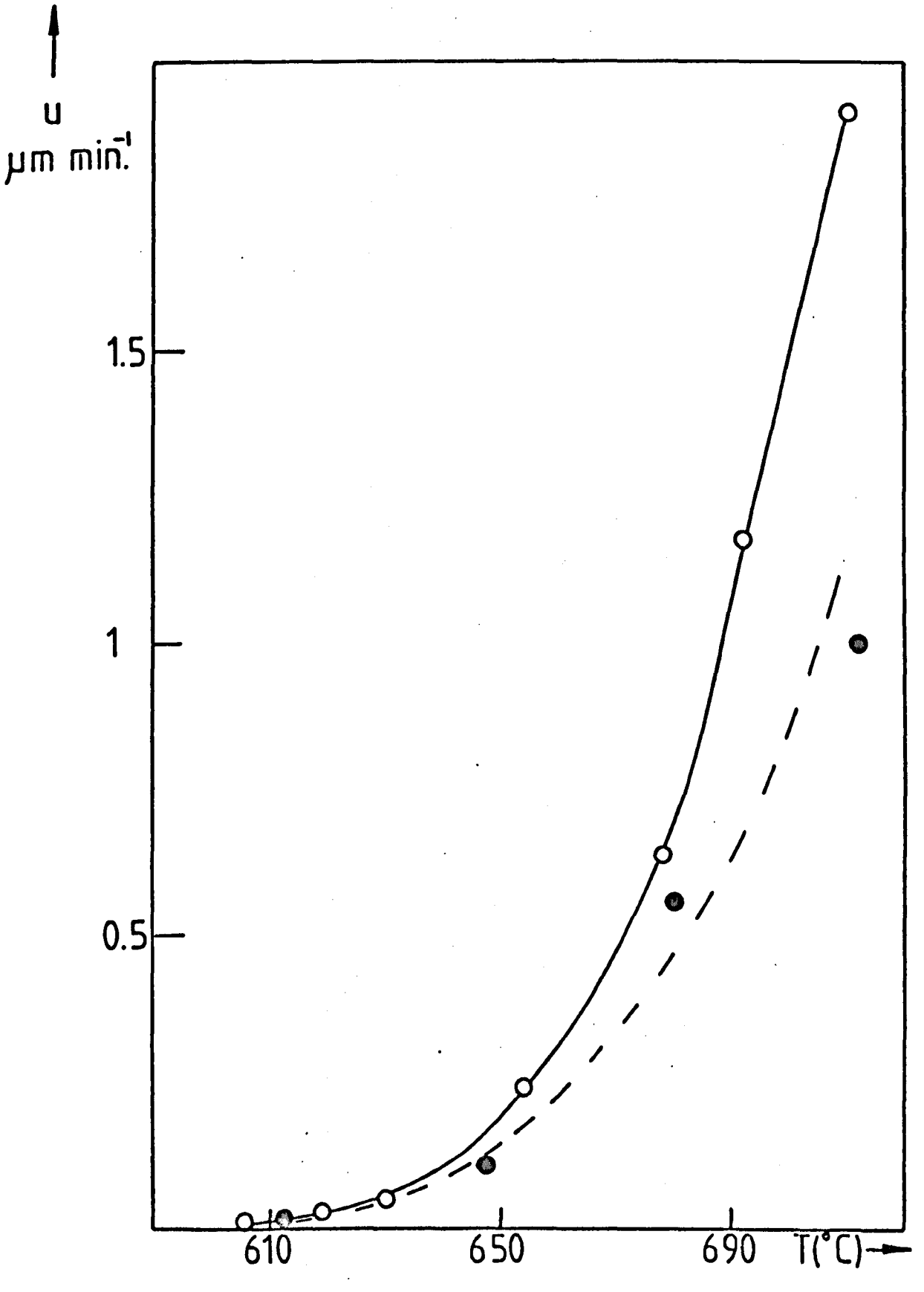

FIGURE 4.24 $Log_{10}\eta$ as a function of temperature for glasses G13′ (●) and G2 (○).

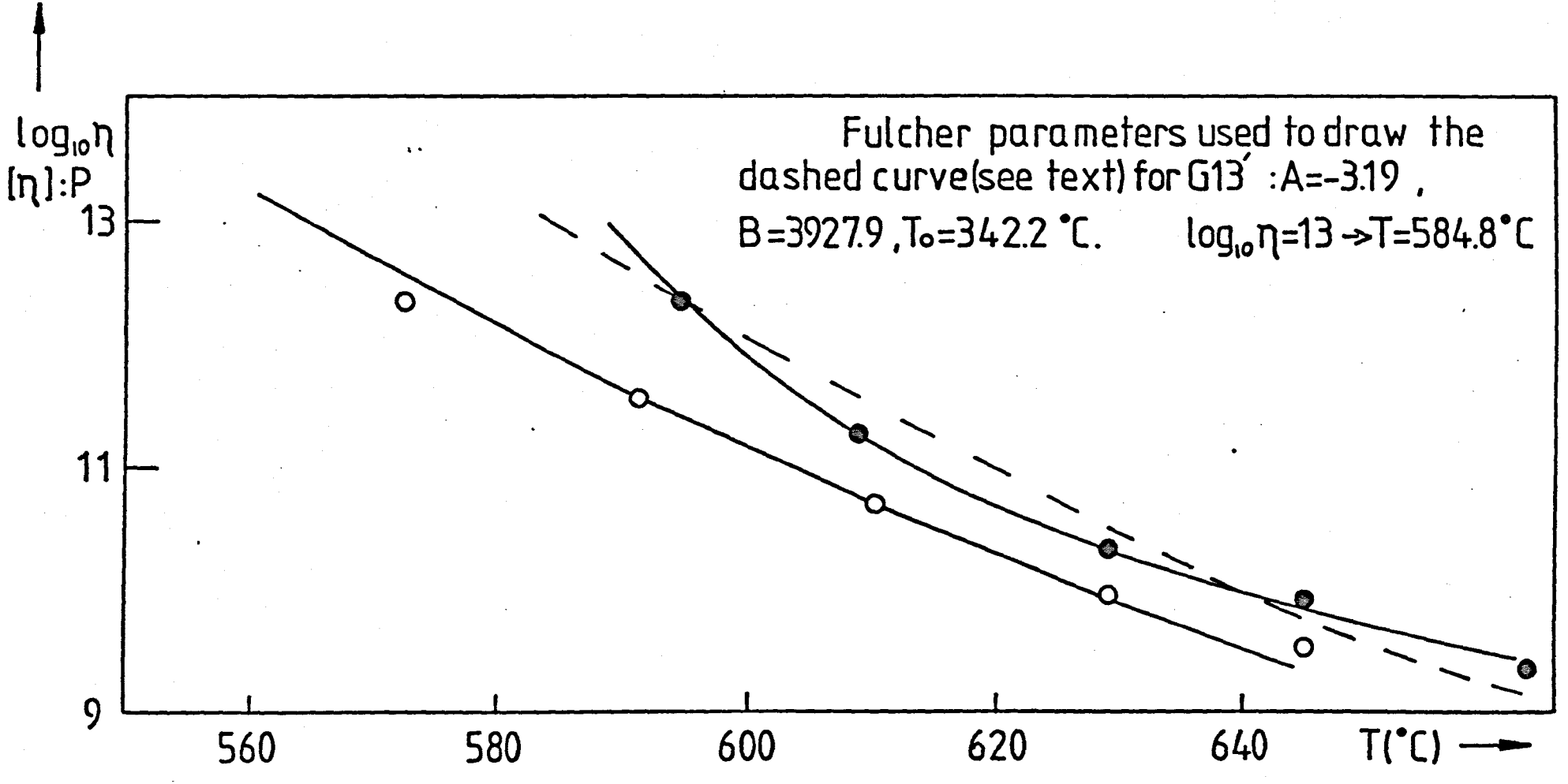

corresponds to 584.8°C, about 20°C higher than for G2. The Fulcher curve fitted to only the low temperature data for G13 is also shown (continuous curve).

The 'DTA Tg' values for G12 and G13′ were 586 and 592°C respectively, the greater value for G13′ being consistent with the increase in viscosity observed for ZrO_2 addition. For the heats of fusion the trend is not as clear. For G12 ΔH_f was 52.3 ±2.6 cal g^{-1} whereas for G13′ it was 61.9 ±3.1 cal g^{-1}. These values are close to ΔH_f for G2 (58.2 ±2.9 cal g^{-1}).

The liquidus temperature for G13′ was 1269°C, about 7°C lower than for G2.

Crystallization of both G12 and G13′ gave the low form of NC_2S_3. The only differences between the two glasses were in the relative intensities of the x-ray peaks.

4.4 P_2O_5, TiO_2 and MoO_3 Additions

The nominal glass compositions are listed in Table 2.1. The nucleation densities were determined from equation (2.2) using a fixed nucleation time of 40 min. The growth temperature ranged from 720 to 740°C and the growth time from 4 to 10 min. For each composition the growth temperature was fixed.

The nucleation results for G9 (3 mole% TiO_2) and G8 (3 mole% P_2O_5) are compared with the base glass G2 in Figure 4.25. It is clear that the addition of TiO_2 caused a significant decrease in nucleation for temperatures above the maximum in the nucleation curve for G2 but no significant change at lower temperatures.

FIGURE 4.25 $Log_{10}(Nv/t)$ vs. T(°C) FOR GLASSES

G8(3 mole% P_2O_5), G9(3 mole% TiO_2) and G2.

(o) (●) (×)

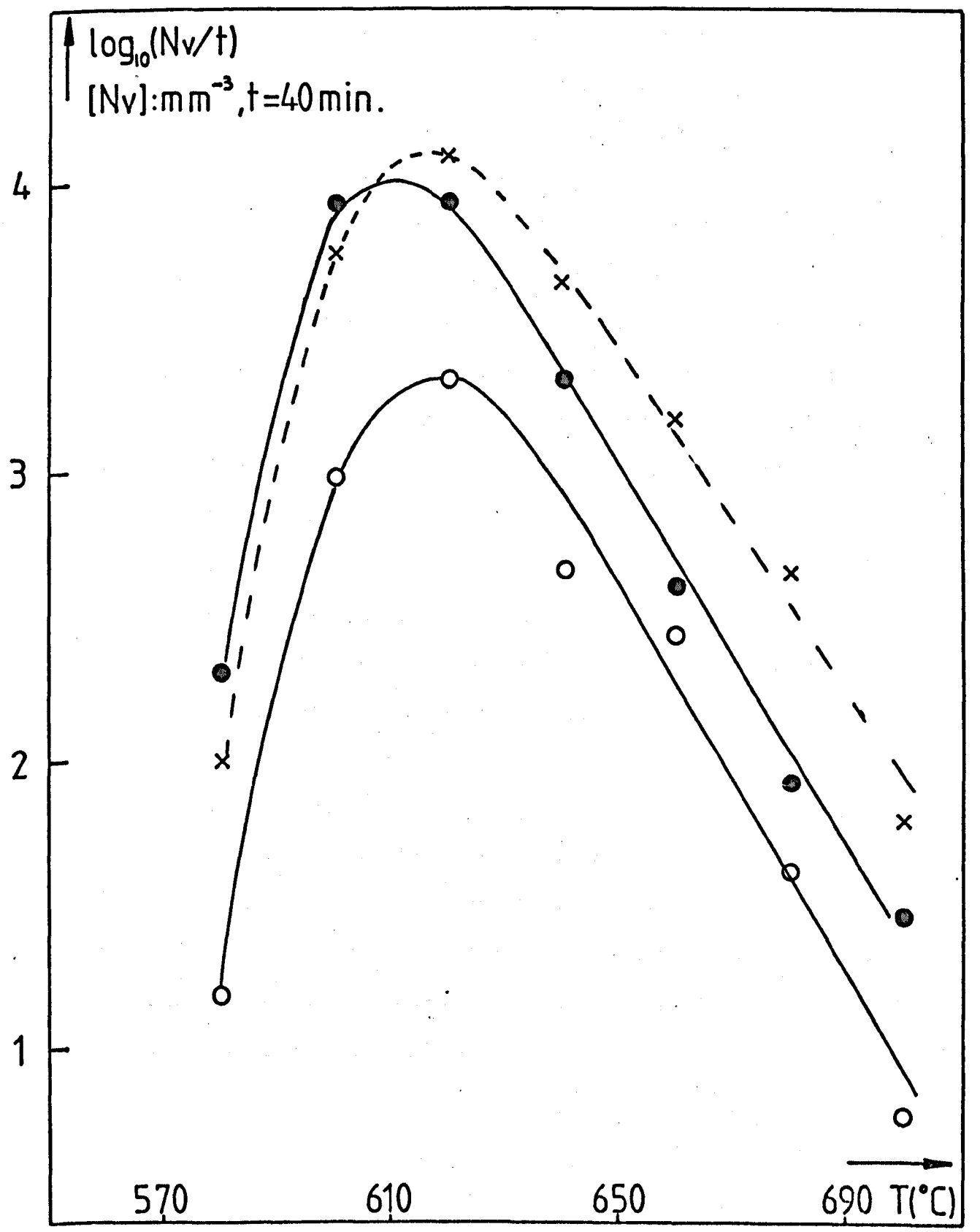

However, for addition of P_2O_5 the nucleation decreased significantly over the whole range. The maximum N_v/t of 10^4 mm^{-3} min^{-1} for G9 occurred at about 610°C compared with 2.1×10^3 mm^{-3} min^{-1} for G8 at about 618°C.

It is also interesting to compare the morphologies of the crystals in G8 and G9 with G2. Optical micrographs for G8 and G9 are shown in Figures 4.26 and 4.27. In G9 (3 mole% TiO_2) the spherulites have a smooth spherical cross section but in G8 they are more irregular in appearance.

The nucleation results for the glasses containing MoO_3 (G10 and G11) are shown in Figure 4.28. A decrease in the maximum nucleation rate with increasing MoO_3 content was observed. The temperature of the maximum for both glasses decreased to about 602 C. The maximum for G10 was 4.47×10^3 mm^{-3} min^{-1} and for G11 1.74×10^3 mm^{-3} min^{-1}. Also, MoO_3 additions caused a considerable decrease in the nucleation densities at higher temperatures but at lower temperature the densities remained close to those for G2.

Optical micrographs for G10 and G11 are shown in Figure 4.29 and 4.30. For the 3 mole% MoO_3 glass the spherulites had an irregular spherical shape whereas for G11 the crystals had an approximately cubic morphology.

No further work was carried out on these compositions except for the X-ray identification of the phases precipitated. Each glass was nucleated for 40 min at its maximum nucleation rate followed by growth for 20 min at 730°C to obtain complete crystallization. In both cases the crystalline phase present was identified as the low form of NC_2S_3.

Figure 4.26 (top left)

Optical micrograph of G8 nucleated at 600°C for 40 min and grown at 725°C. Mag X200.

Figure 4.27 (top right)

Optical micrograph of G9 nucleated at 620°C for 40 min and grown at 725°C. Mag X500

Figure 4.29 (bottom left)

Optical micrograph of G10 nucleated at 600°C for 40 min and grown at 730°C. Mag X200.

Figure 4.30 (bottom right)

Optical micrograph of G11 nucleated at 581°C for 40 min and grown at 730°C. Mag X100.

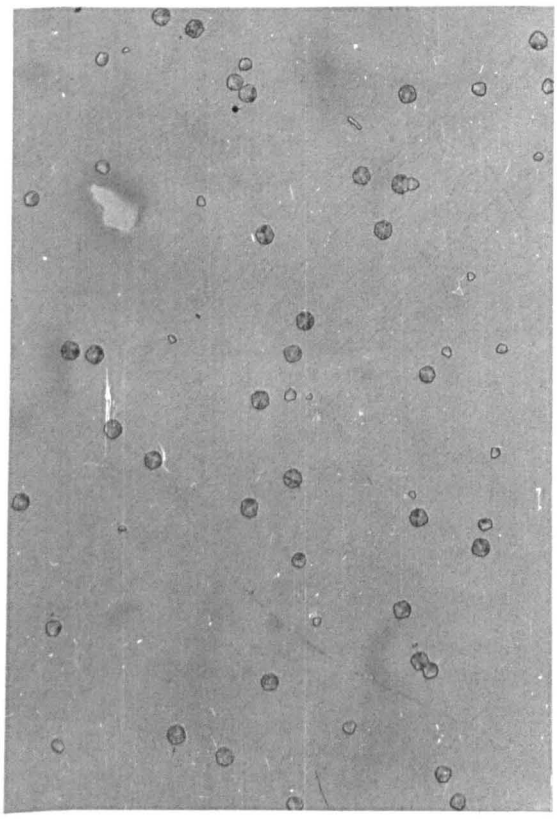

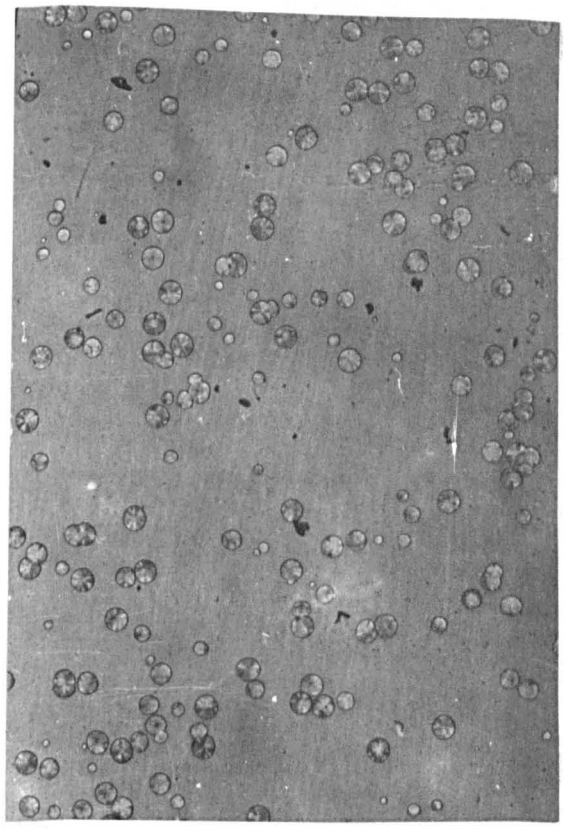

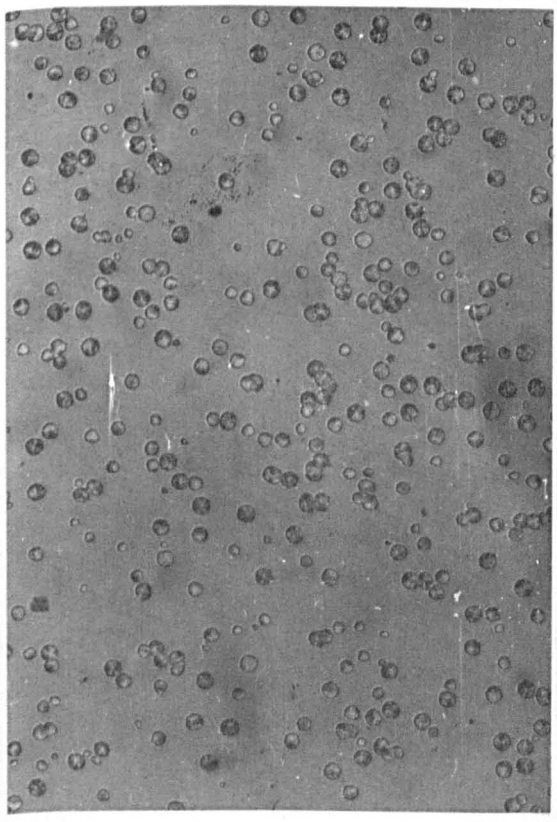

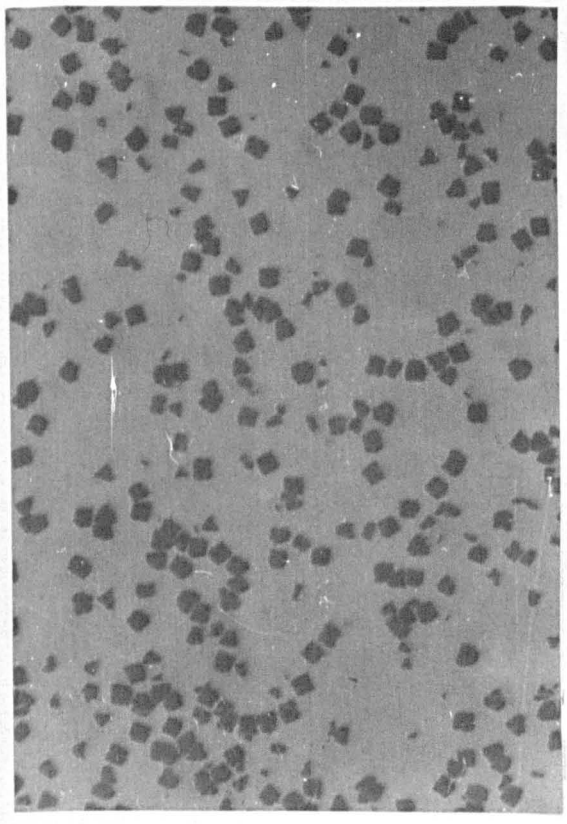

FIGURE 4.28 $Log_{10}(Nv/t)$ AS A FUNCTION OF T(°C)
FOR GLASSES G10(3mole%MoO_3),G11(6mole%MoO_3)and G2.
(o) (●) (×)

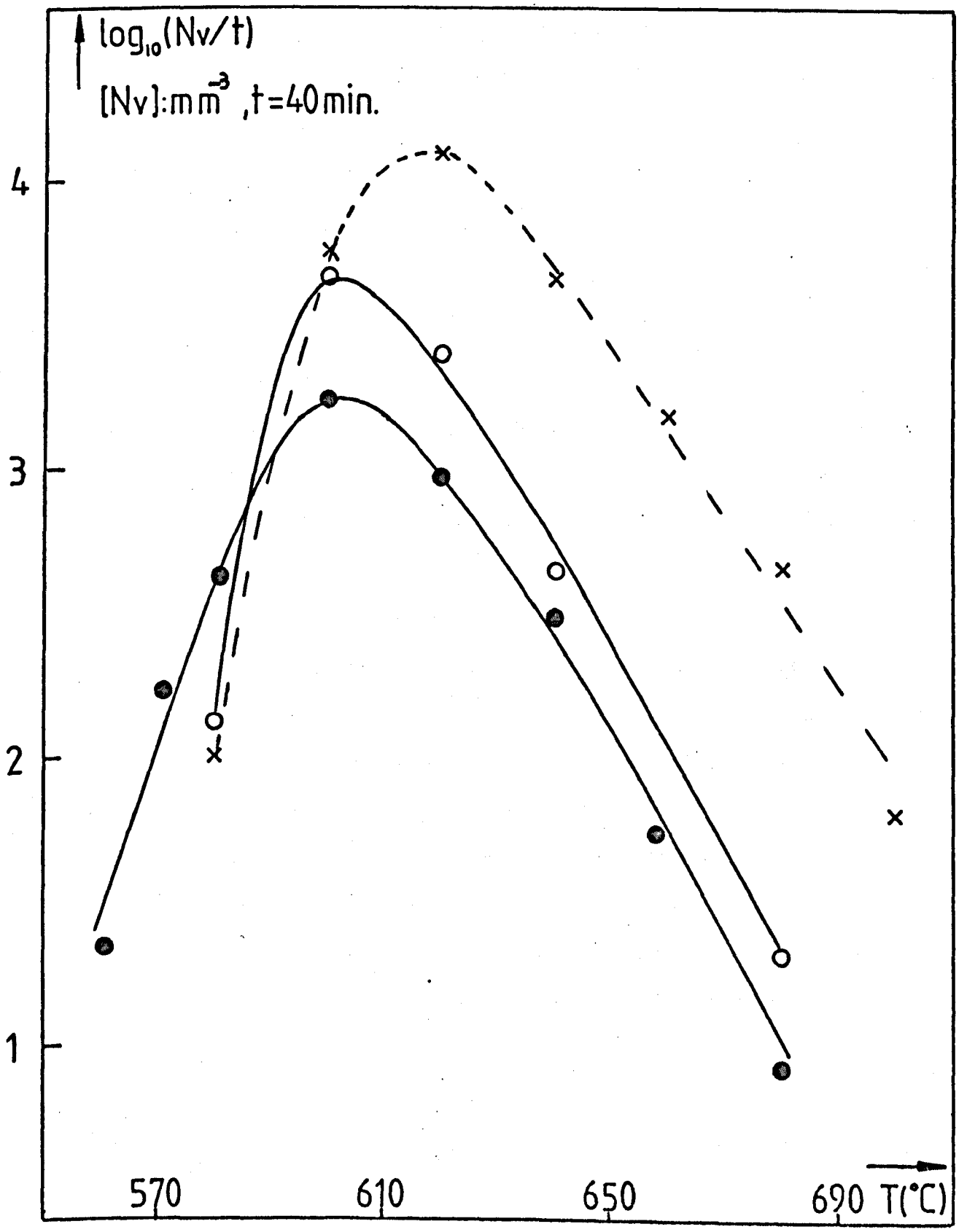

4.5 Pt ADDITIONS

The effects of the addition of platinum on nucleation in the NC_2S_3 composition were studied. Two glasses were melted with 0.2 wt.% Pt (G24) and 0.46 wt.% Pt (G25). Although no chemical analysis of these glasses was carried out their compositions were expected to be close to G2 (see section 2.1), since the batch quantities for soda, lime and silica were the same for all these glasses.

4.5.1 Nucleation, Viscosity, DTA and X-ray results

The nucleation vs time behaviour was investigated at 595, 621 and 641°C for G24 and G25 and compared with the base glass G2 (Figures 4.32, 4.33 and 4.34). The nucleation densities were calculated from the more accurate equation (2.1) since a large variation in particle size was expected, some particles having been nucleated heterogeneously and others homogeneously. Typical optical micrographs for G24 and G25 are shown in Figure 4.31. The steady nucleation rates (I_o) and the intercepts with the time axis (t_o), calculated by least squares, are given in Table 4.9. Let us first consider Figure 4.32. Addition of 0.2 wt.% Pt to G2 causes little change in nucleation at 595°C. Addition of 0.46 wt.% Pt gives a large increase in nucleation initially but for times longer than 50 min the nucleation is less than in the other glasses. The steady state nucleation rate I_o in G25 is also less than in G2. Similar behaviour is found at 621°C (Fig. 4.33). For times less than 20 min for G24 and 40 min for G25 the nucleation density is higher than in G2. Finally at 641°C (Figure 4.34)

FIGURE 4.32 Nucleation density (Nv) as a function of time at the given temperature for glasses G2, G24 and G25.

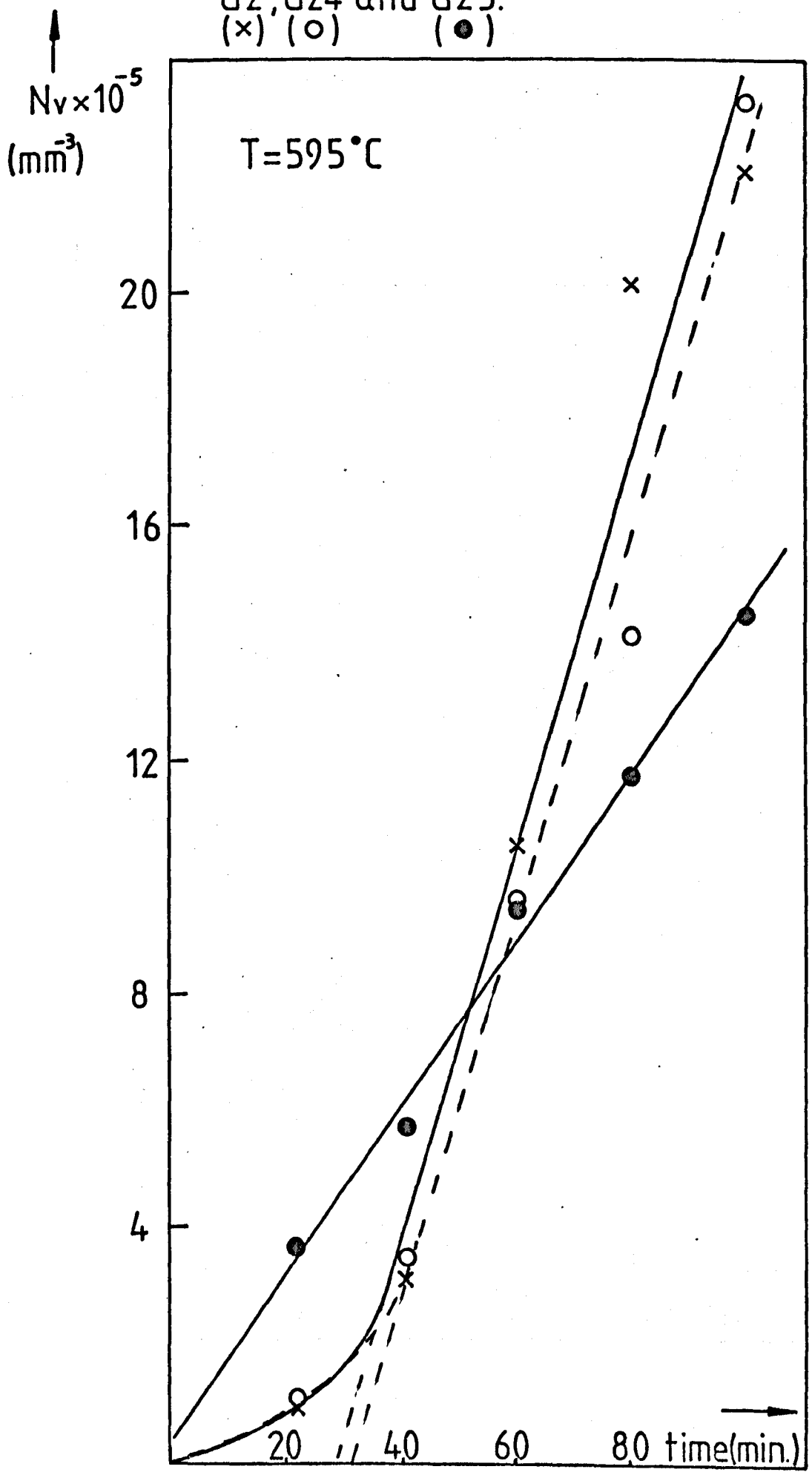

FIGURE 4.33 Nv vs. time, at the given temperature, for glasses G2, G24 and G25.
(×) (○) (●)

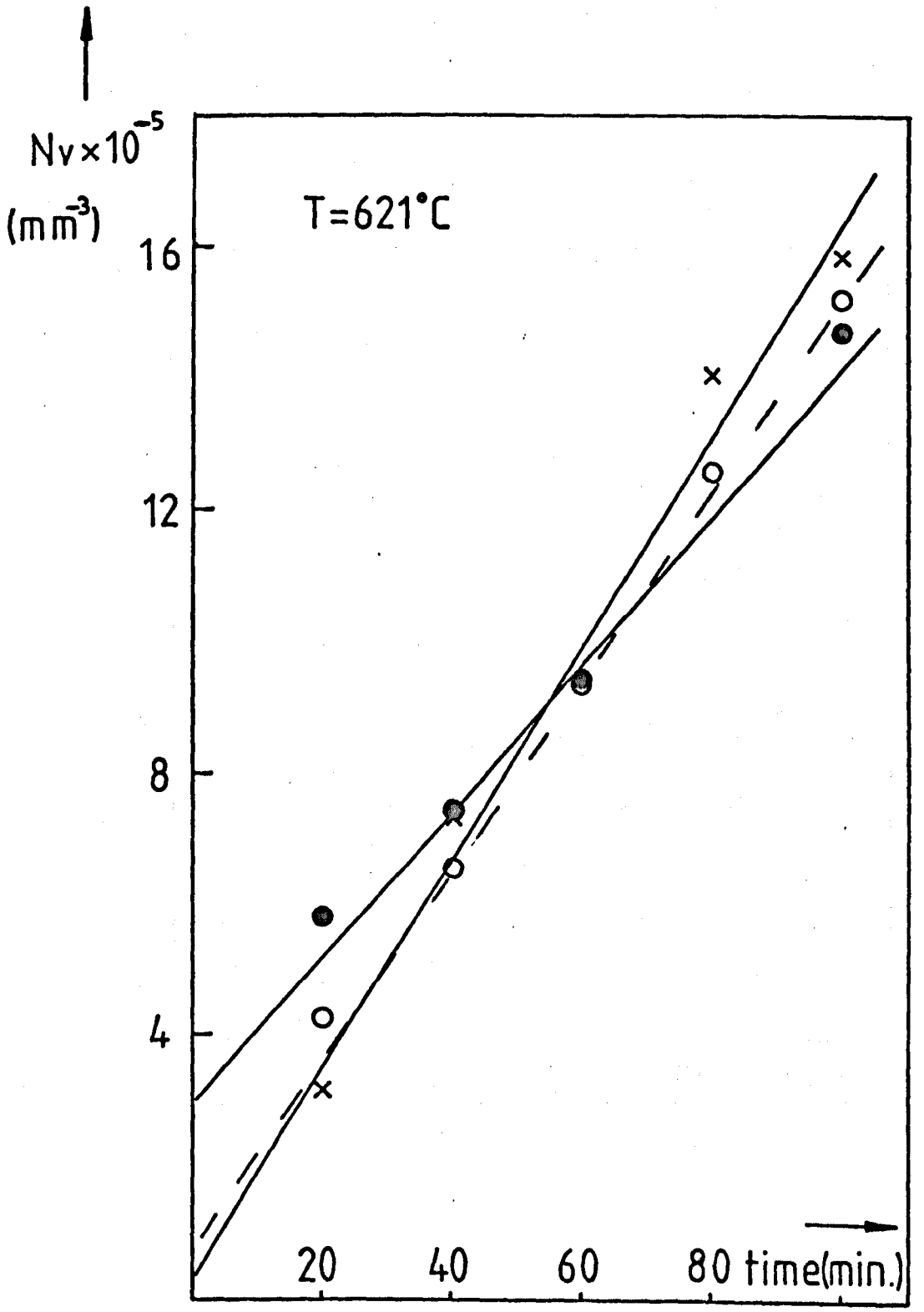

FIGURE 4.34 Nv vs.time,at the given temperature, for glasses G2,G24 and G25.
(×) (○) (●)

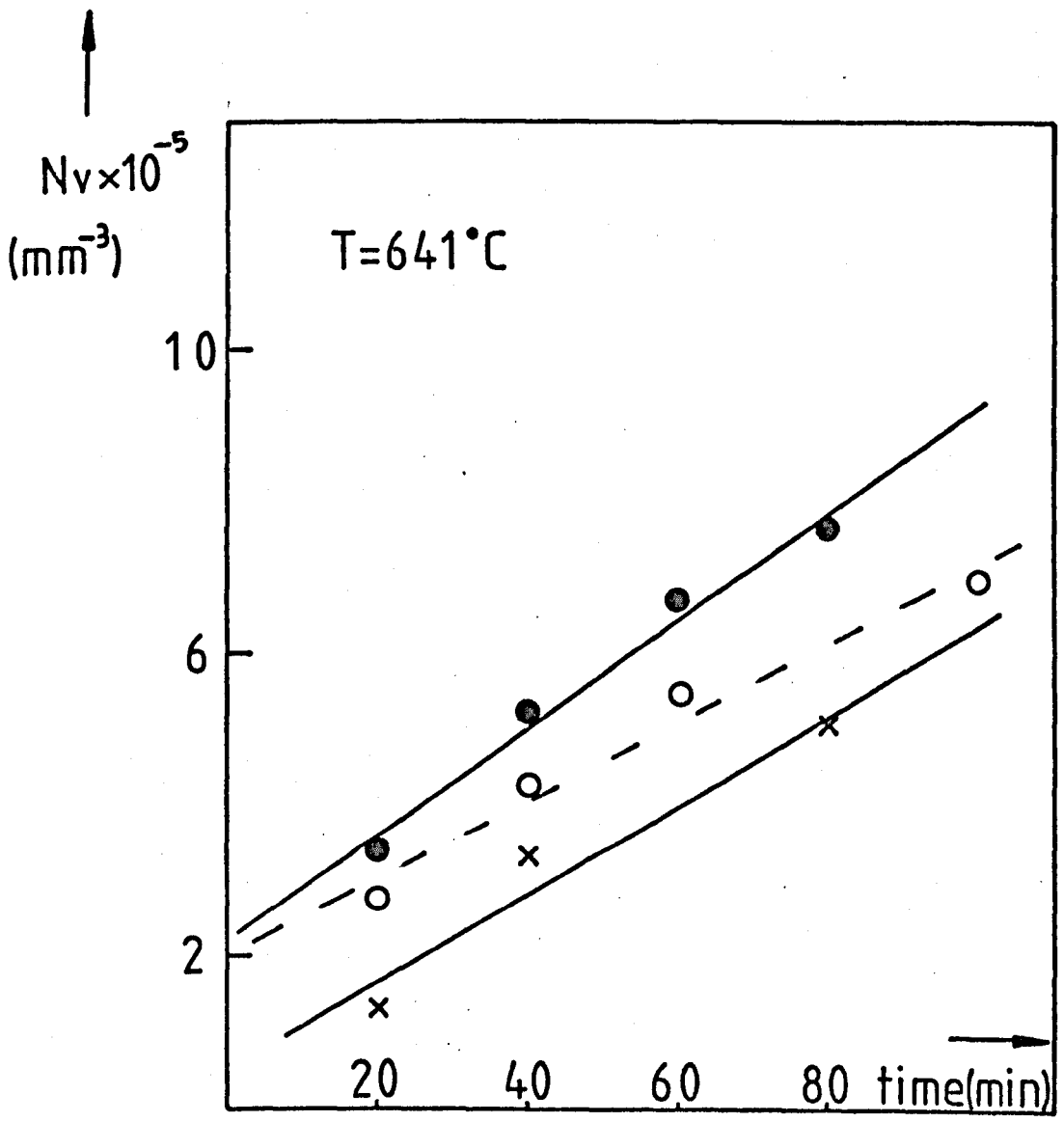

Figures 4.31a (top left), b(top right)

Optical micrographs for glasses G24 and G25

a. G24 nucleated at 642°C for 80 min and grown for a short time at 730°C. Mag X500.

b. G25 nucleated at 639°C for 20 min and grown for a short time at 730°C. Mag X500

Figure 4.31c

Stereoscan micrograph of G25 heated at 682°C for 40 min and etched. Mag X3,400.

Figure 4.38 (a.,b)

Electron micrographs at a 100 kV electron accelerating voltage, of G25 heated at 596°C for 6 hr 21 min. Mag X15,300.

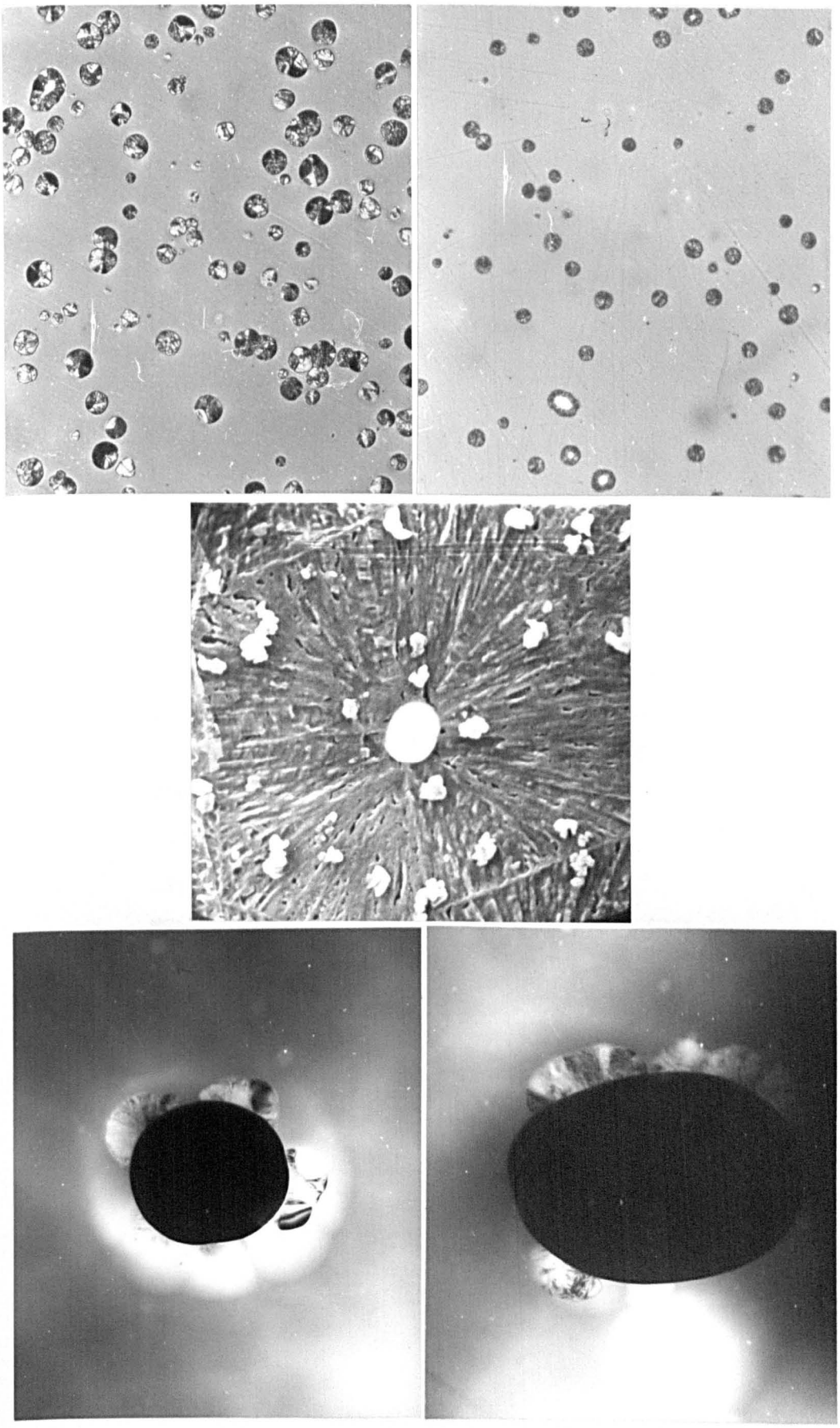

TABLE 4.9

STEADY STATE NUCLEATION AND INTERCEPTS FOR GLASSES G2, G24 AND G25

Glass Code	T(°C)	I_o (mm^{-3} min^{-1})	t_o (min)
G2	595	33608.5	28.7
G2	621	16060.7	-1.9
G2	641	5863.3	-8.8
G24	595	32576.1	31.5
G24	621	14434.5	-5.0
G24	641	5147.6	-39.8
G25	595	14218.8	-2.8
G25	621	11195.2	-26.2
G25	641	6995.0	-32.2

NOTE: The steady state nucleation rate value (I_o) and the intercept (t_o) were calculated by least squares method.

the nucleation densities in G24 and G25 are larger than in G2 independent of time. However there is no significant difference in the I_o values for the three glasses at this temperature. In Figure 4.35 $\log_{10}(N_v/t)$, where t = 40 min, is plotted versus temperature for G25. For t = 40 min the $\log_{10}(N_v/t)$ values are higher than in G2, the increase being the greatest at either below or above the maximum for G2.

The results for G2 are summarized in Fig. 4.36. They are in close agreement with the results for G16 (see Figures 3.14 and 3.15) although the compositions, both nominally NC_2S_3 were slightly different.

The viscosity results for G25 are compared with G2 in Figure 4.37. At the high temperatures the viscosities of G25 and G2 are nearly identical. However at the lower temperatures G25 is slightly more viscous than G2. The curve plotted for G25 corresponds to the Fulcher equation fitted to the low temperature data for G25 and the high temperature data for G2. Using the Fulcher extrapolation 10^{13} p occurs at 570.7°C for G25, 6°C higher than for G2.

The DTA trace for G25 was very similar to G2. The 'DTA Tg' was 581°C (579°C for G2). The ΔH_f value was 58.4 cal g^{-1}, very close to the value for G2 (58.2 cal g^{-1}). The ΔH_c value was 39.7 cal g^{-1} (35.8 cal g^{-1} for G2). The low form of NC_2S_3 was identified by X-ray diffraction in crystallised samples of G25. No Pt peaks were detected.

4.5.2 Electron microscopy and Electron microprobe results

After examination of a large number of foils of Pt containing glasses the early stages of growth of NC_2S_3 crystals on Pt

FIGURE 4.35 $Log_{10}(Nv/t)$ AS A FUNCTION OF TEMPERATURE(°C) FOR GLASSES G25 AND G2 .
(●) (×)
The values ◑ were obtained from figures 4.32,33and34.

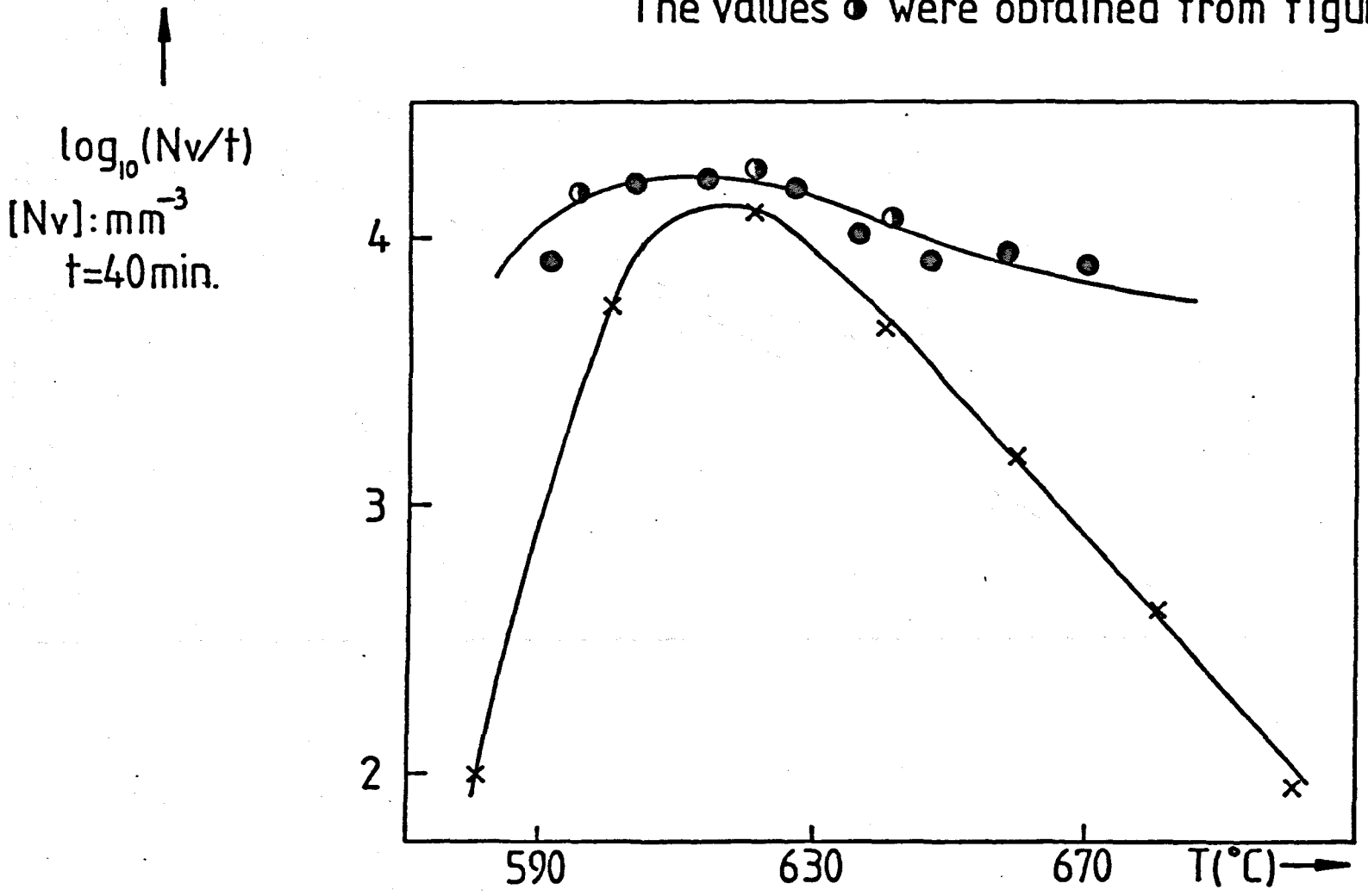

FIGURE 4.36 Nucleation density for glass G2 as a function of time at the given temperatures.

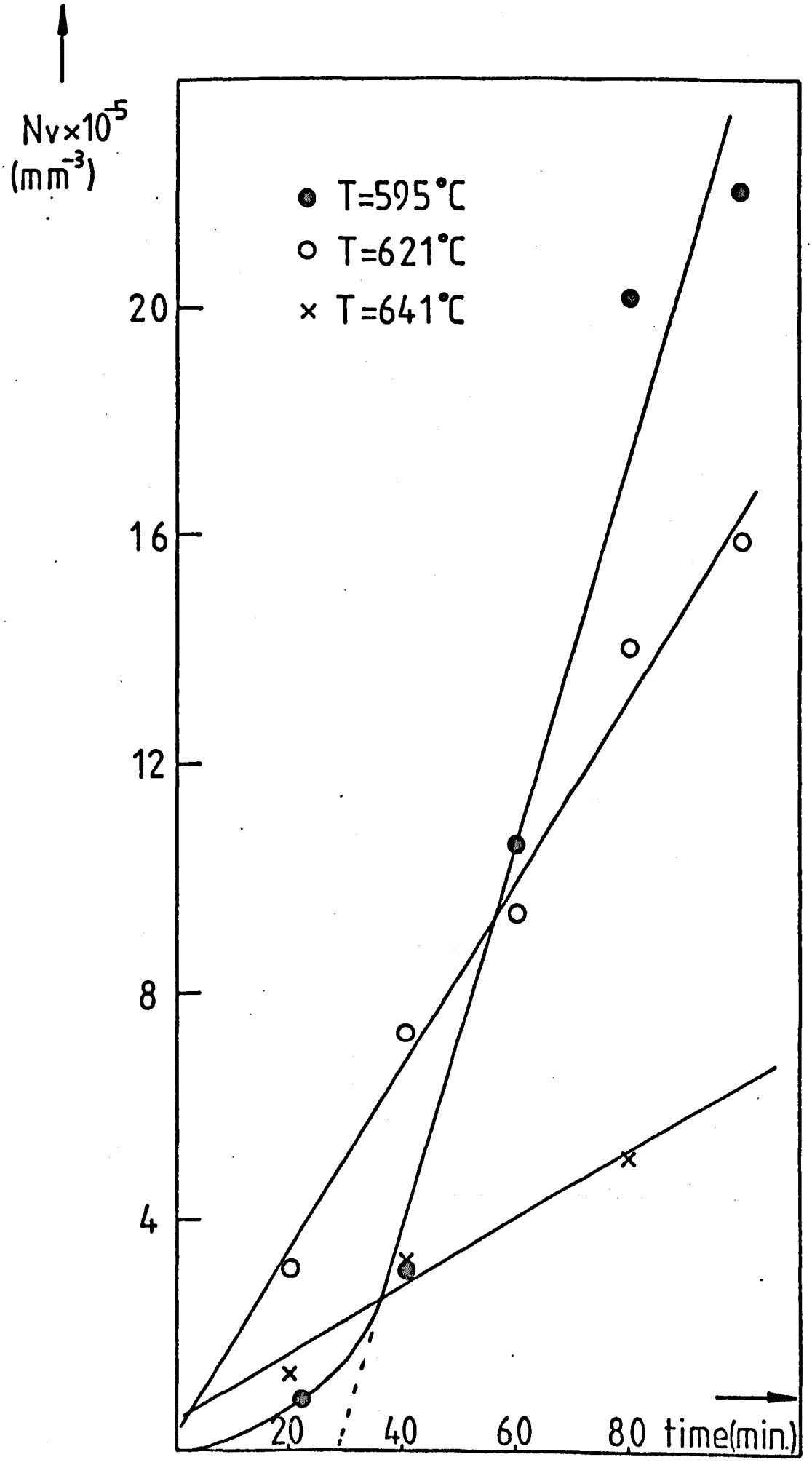

FIGURE 4.37 $Log_{10}\eta$ vs.T(°C) FOR GLASSES G25 AND G2.
(●) (×)

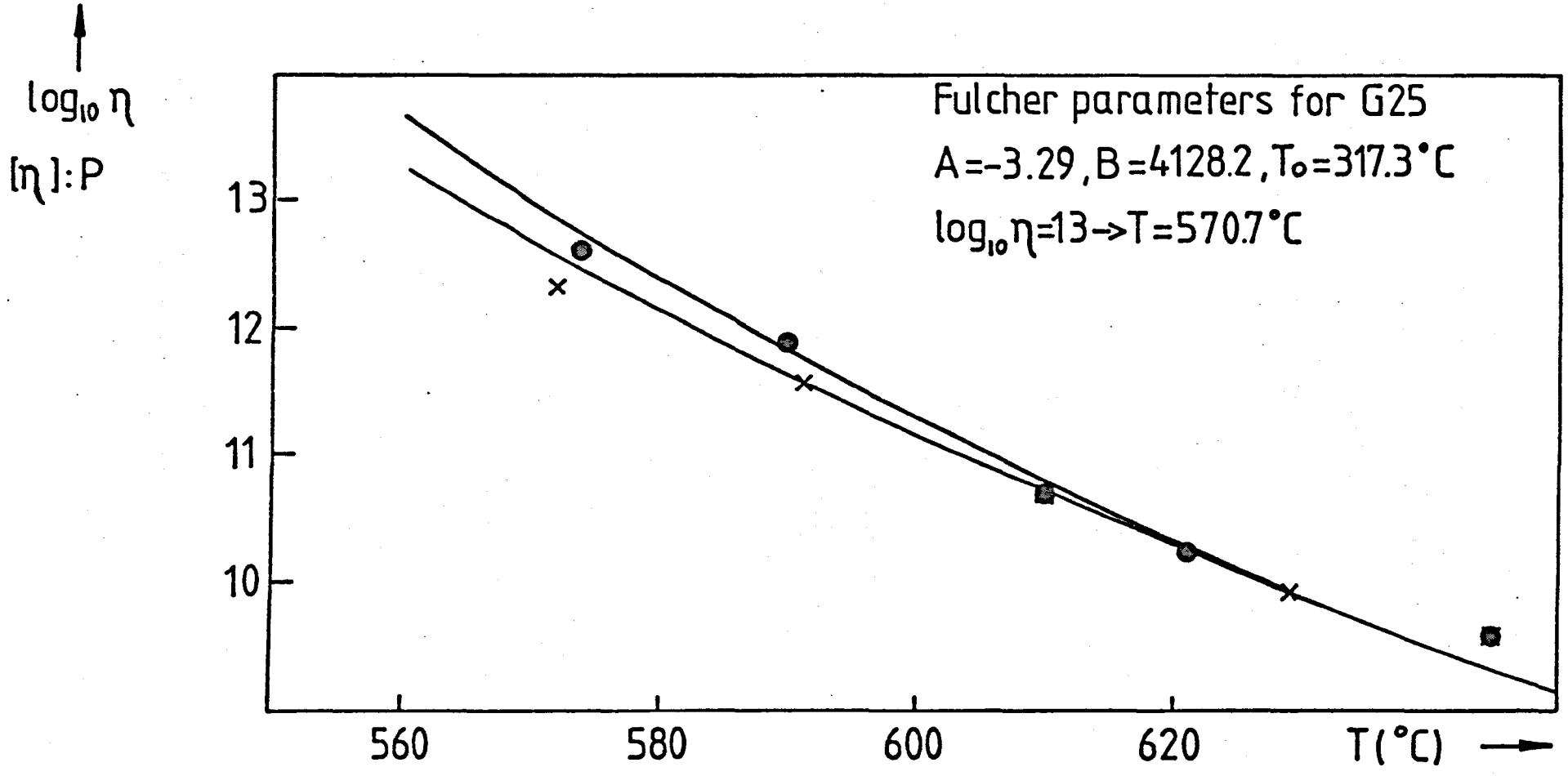

centres was detected. A series of electron micrographs taken at 100 kV are shown in Figure 4.38. The magnifications are constant, with the exception of the last two micrographs, allowing the sizes of the particles to be compared directly. It is clear that several individual NC_2S_3 crystals have nucleated heterogeneously on the larger Pt particles. A layer of crystals is clearly observed surrounding the smaller Pt particles. Also it appears that the crystals prefer to grow on more highly curved surfaces at the earlier stages. Very little structure can be observed inside the Pt particles. It was not possible to take electron diffraction patterns of the Pt centres in the 100 kV electron microscope.

In order to confirm that the particles were Pt crystals a high voltage electron microscope was used (900-1000 kV). The X-ray d spacings for pure Pt obtained by Swanson and Tatge (4.10) are given in Table 4.10, and compared with the values obtained from electron diffraction. A pattern taken at 900 kV is shown in Figure 4.39(a). A Pt particle showing a clear sector is shown in Figure 4.39(b). At least eight crystals are seen growing from the particle in Figure 4.40. Selected area diffraction patterns from two of the crystals are also shown. It is interesting to note that the main row of spots in both patterns corresponds to the (11.0) ($d = 5.34$ Å) reflection of NC_2S_3. The direction of these rows is tangential to the surface of the Pt particle. In the same patterns weak spots of the (311) ($d = 1.184$ Å) reflection of Pt can be observed. This may suggest that the crystals are growing with a definite orientation with respect to the Pt particle. Another pattern from a Pt particle is shown in Figure 4.41.

Figure 4.38 (c,d,e,f,g) (continued)

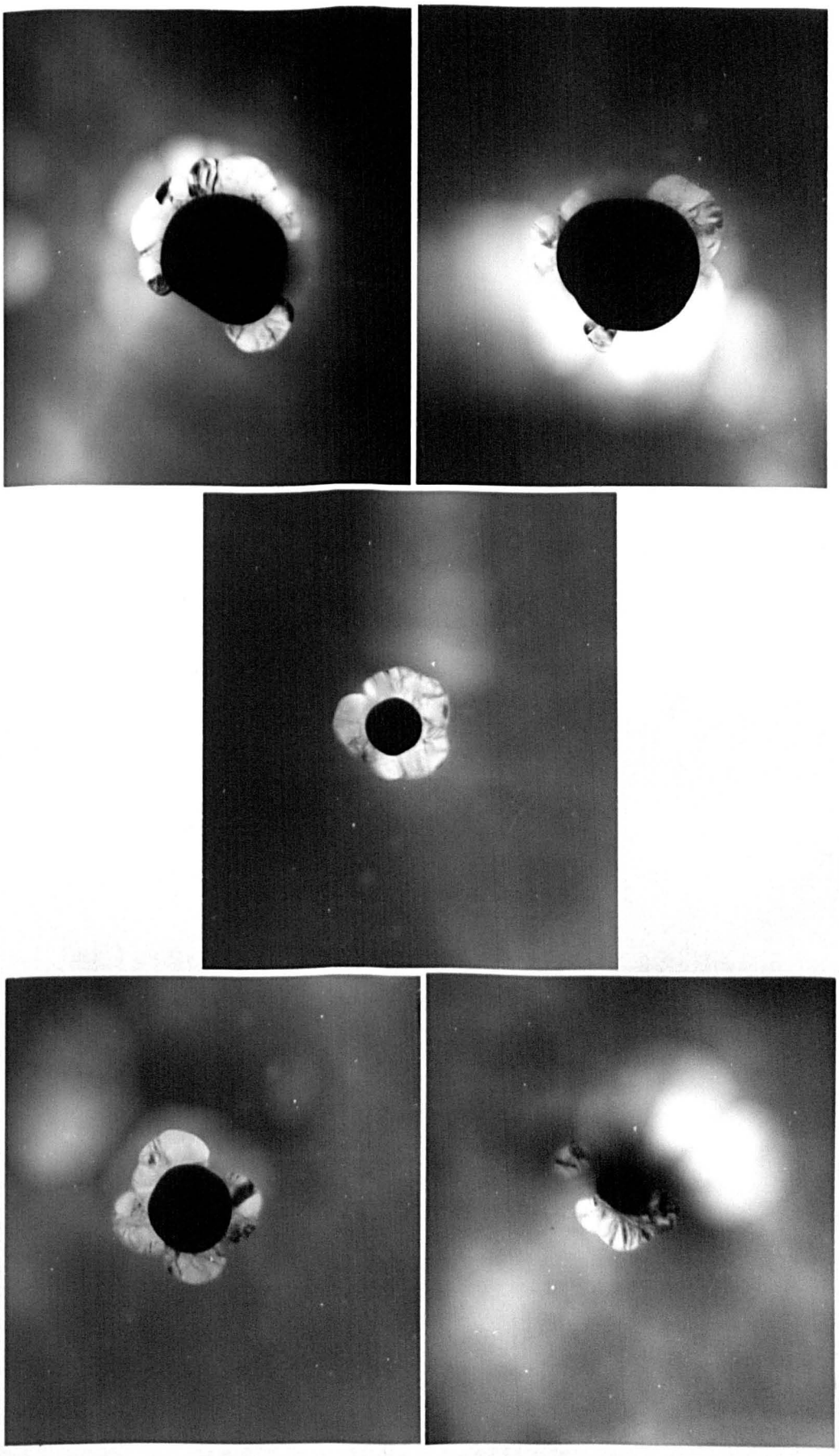

Figure 4.38 (h,i,j) (continued)

Figure 4.38 (k,1) (continued)

(k) Mag X22,000 ; (1) Mag X33,600

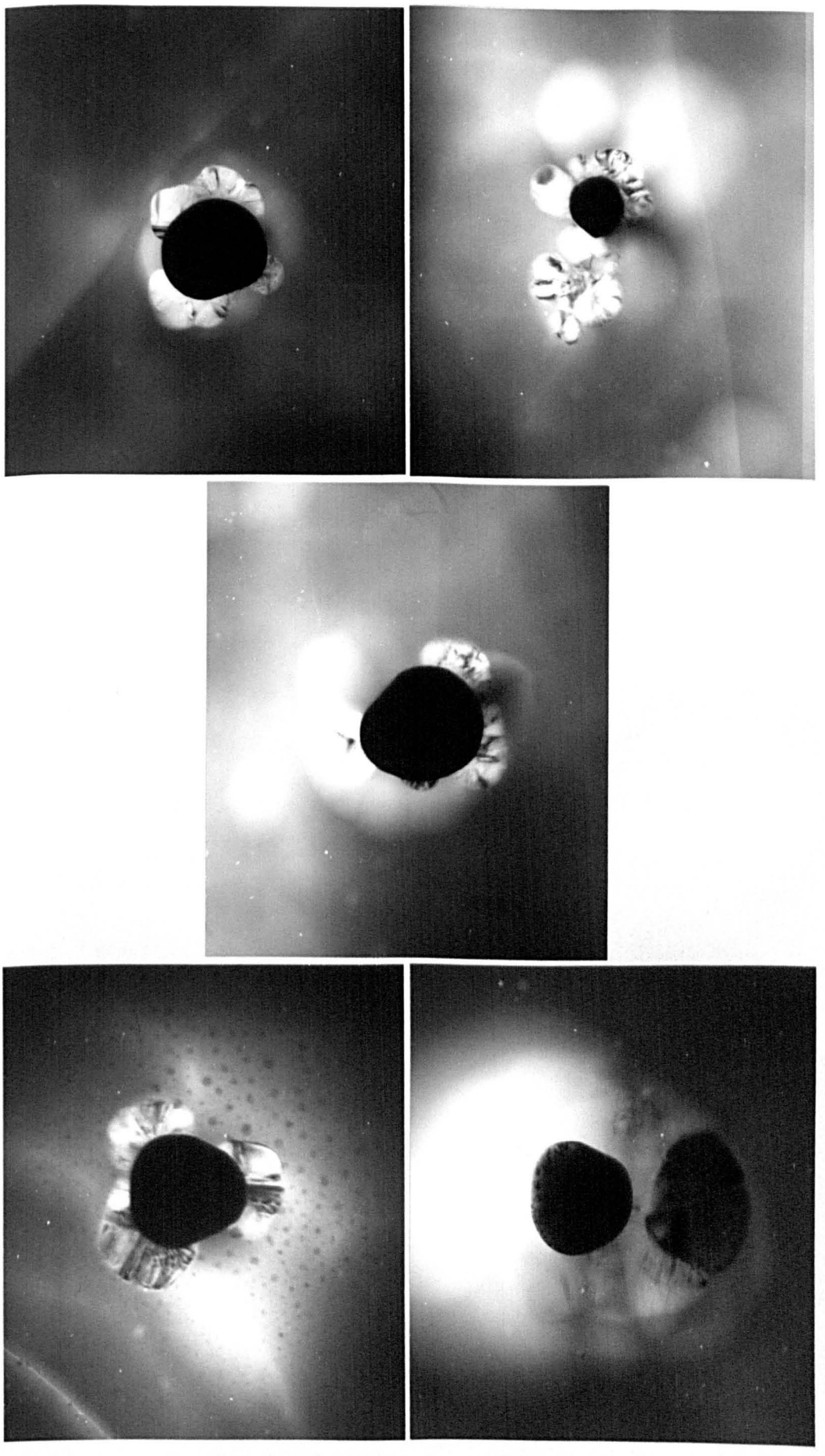

TABLE 4.10

X-RAY DATA FOR Pt FROM SWANSON AND TATGE (4.10) AND d SPACINGS OBTAINED FROM ELECTRON DIFFRACTION (Camera Length CL = 16.222 Å mm)

hkℓ	d(Å)	I	d(Å) From this work	Comments
111	2.265	100	2.809	Ring pattern - Unidentified
200	1.9616	53	1.961	Spot patterns
220	1.3873	31	1.387	"
311	1.1826	33	1.184	"
222	1.1325	12		
400	0.9808	6		
331	0.900	22		
420	0.8773	20		
422	0.8008	29		

Figures 4.39a,b

Electron diffraction pattern and micrograph of a Pt centre in glass G25 as quenched taken at 900 kV accelerating voltage. Mag X59,000.

Figures 4.40 a,b and c

Figure 4.40b Electron micrograph (900 kV) of G25 heated as explained in Figure 4.38. Mag X17,200.

Figure 4.40a Selected area diffraction pattern (SAD) of top left crystal in Figure 4.40b.

Figure 4.40c. SAD of top right crystal in Figure 4.40b.

Figure 4.41a,b

Same glass and conditions as in Figures 4.39a and b.

Figure 4.42

EPMA line scan through a Pt particle. (See text)

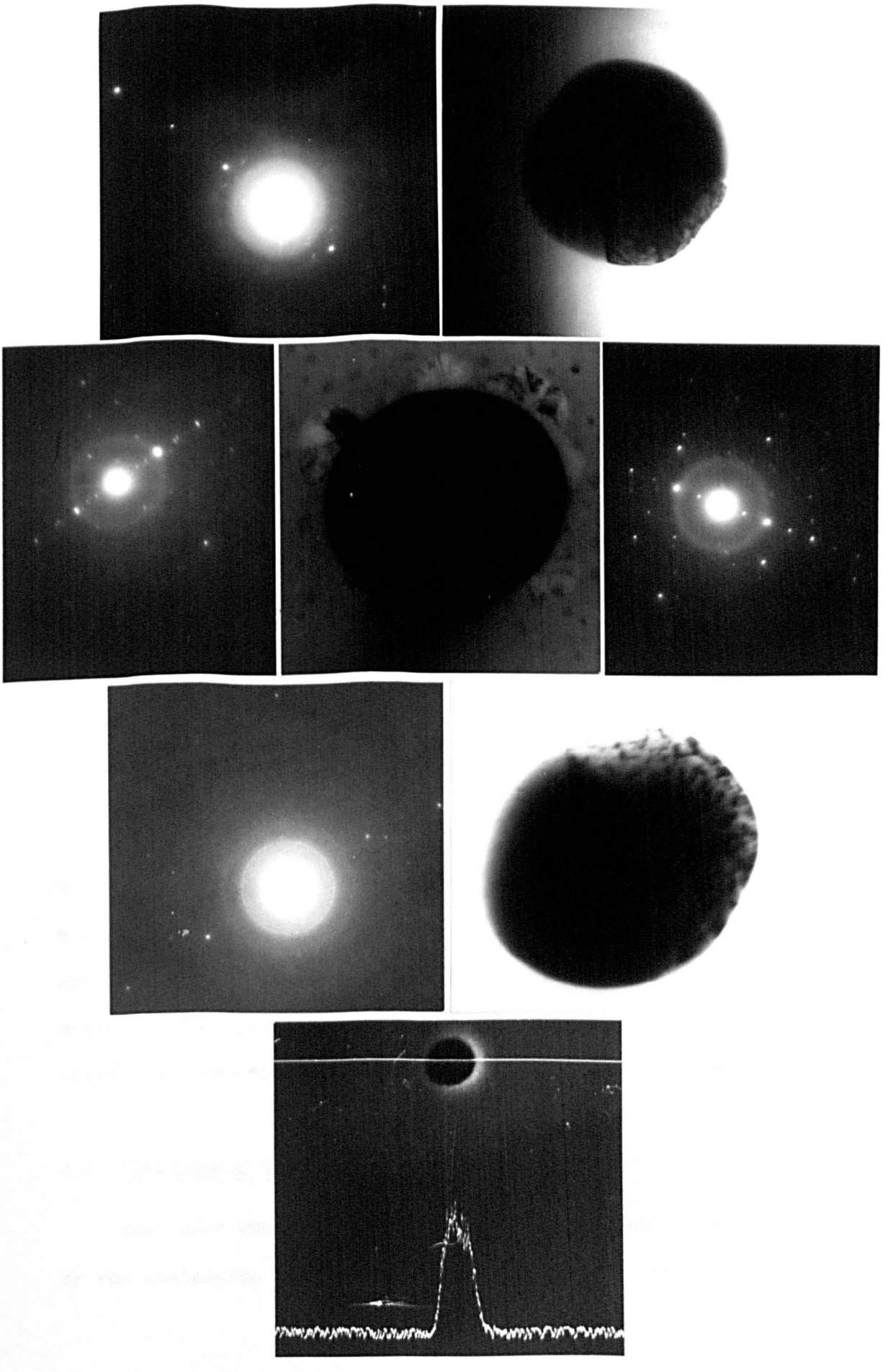

Two clear rings and two single spot patterns are observed. The 1.184 and 1.387 Å d spacings from this pattern (see Table 4.10) match very closely the (311) and (220) Pt d spacings. The 2.809 Å d spacing obtained from the ring pattern, however, remains unidentified. Another Pt particle exhibiting an unidentified microstructure is shown in Figure 4.41.

Samples of G25 were prepared for EPMA examination. The distribution of Pt between precipitated particles and the surrounding glass and Pt levels in crystals were of interest. The samples were coated with a thin layer of Al to prevent charge accumulation from the electron beam, and examination for Pt carried out at an electron accelerating potential of 20 kV using Pt Lα as the analysis line. The metallic particles in G25 were identified as Pt after a direct comparison had been made (using counts) of the intensity of the Pt Lα nucleation line from the particles in the sample and from a standard Pt wire of purity greater than 99.99%. A line scan through one of the particles is shown in Figure 4.42. No Pt was detected in the surrounding glass at distances 1.5 to 2 μm from the particles. At closer distances Pt was detected, but probably originated by X-ray excitation from the particles themselves. Also analysis of Pt particles indicated the presence of small amounts of silicon and calcium. Sodium was not detected in the particles.

4.6 'ULTRASONIC WAVES' EFFECT ON NUCLEATION

Some work was carried out on the effect of ultrasonic waves on the nucleation characteristics of glass G17. The apparatus

used is schematically shown in Figure 4.43. A heat resistant steel rod of the appropriate length (for maximum transmission of the sonic waves) was connected to the head of an ultrasonic drilling machine. The lower end of the rod was in direct contact (under pressure) with the sample. The cylindrical sample was held in position by a metallic bush. The specimen rested on a steel rod into which a T/C was inserted almost touching the sample. The temperature of the furnace (nichrome wound) was monitored with a Eurotherm controller. Only four runs were made, two with ultrasonics (US) and two without ultrasonics (NUS). In Table 4.11 the temperature-time schedules in the four runs are compared. The nucleation results, determined using equation (2.2), are given in Table 4.12. It would appear at first sight that the application of ultrasonic waves has slightly increased the nucleation. However it is very unlikely that the effect is significant due to uncertainties arising from difficulty in obtaining exactly the same heating schedules in the experimental runs.

There still exists the possibility that ultrasonic waves might change the nucleation incubation time. Thus it would be very interesting to use this technique at lower temperatures for much longer times (say at 570°C for 10 hours) since the effect of ultrasonics might be much larger than at the temperatures and times used in the present experiments.

GENERAL VIEW

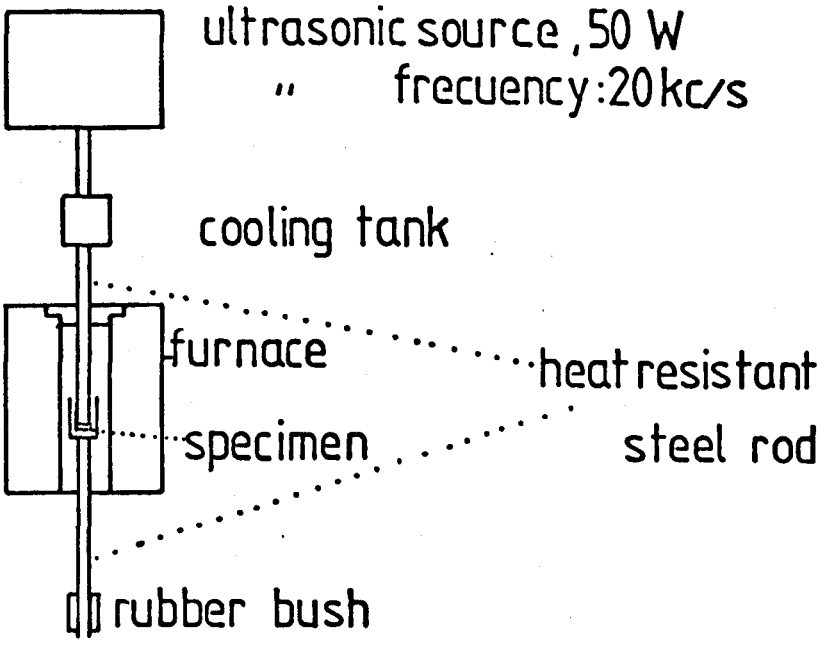

ENLARGED VIEW OF THE SAMPLE HOLDER

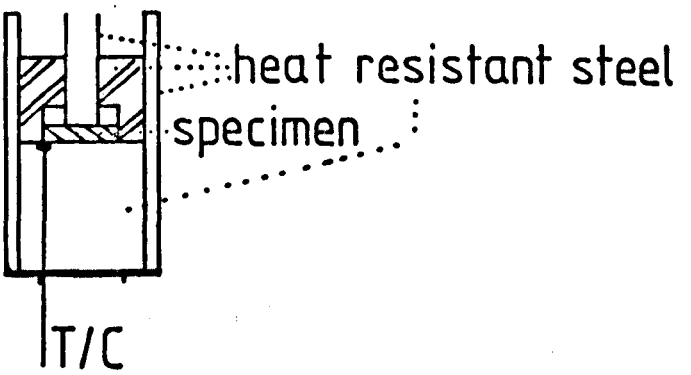

FIGURE 4.43 ULTRASONIC APPARATUS.

TABLE 4.11

DETAILED RUNS MADE

Run 1 (US)		Run 2 (NUS)		Run 3 (US)		Run 4 (NUS)	
T(°C)	time (min)	T(°C)	time (min)	T(°C)	time (min)	T(°C)	time (min)
580	6	588	4	605	7	620	8
601	12	602	10	624	10	630	16
612	20	610	13	630	19	630	36
614	27	619	35	635	25	630	41
614	40	620	40	632	32	Out	45
Out	45	Out	45	632	40		
				Out	45		

TABLE 4.12

NUCLEATION DATA FOR GLASS G17 (WITH AND WITHOUT ULTRASONIC WAVES)

Run	Mag.	A (mm^2)	N(No. particles)	b' (mm)	log N_v	log N_v/t
1 (614°C) US	800	2 x 20974.5	412	2.75	6.26	4.61
2 (619°C) NUS	800	"	380	3.55	6.12	4.46
3 (632°C) US	800	3 x 20974.5	282	2.56	5.95	4.30
4 (630°C) NUS	800	4 x 20974.5	321	2.46	5.90	4.25

CHAPTER 5

DISCUSSION AND ANALYSIS OF THE EXPERIMENTAL RESULTS. PROPERTIES OF SOME GLASS CERAMICS IN THE SODA-LIME-SILICA SYSTEM

5.1 Analysis of Experimental Results for Nucleation

5.1.1 Theoretical considerations

To a good approximation equation (1.46) can be written as $I = N_v \frac{kT}{h} \exp\left(-\frac{W^*}{kT}\right) \exp\left(-\frac{\Delta G_D}{RT}\right)$ where ΔG_D is the activation free energy for diffusion per mole. If the diffusion coefficient for nucleation $D = D_o \exp\left(-\frac{\Delta G_D}{RT}\right)$ and the viscosity are related through equation (1.43) we obtain

$$\exp\left(-\frac{\Delta G_D}{RT}\right) = \frac{D}{D_o} = \frac{kT}{3\pi\lambda D_o \eta} \tag{5.1}$$

Substituting back in the nucleation equation

$$\frac{I\eta}{T} = \frac{N_v k}{3\pi\lambda^3} \exp\left(-\frac{W^*}{kT}\right) = A_c \exp\left(-\frac{W^*}{kT}\right) \tag{5.2}$$

where $D_o = \nu\lambda^2 \simeq \frac{kT}{h}\lambda^2$ and A_c is given in terms of the pre-exponential factor $A \simeq N_v \frac{kT}{h}$ by

$$A_c = \frac{Ah}{3\pi\lambda^3 T} \tag{5.3}$$

From equations (5.2) and (1.2a) it follows that the plot $\ln(\frac{I\eta}{T})$ vs $\frac{1}{\Delta G^2 T}$ should be linear, the slope and appropriate intercept enabling the interfacial energy σ and the pre-exponential factor to be calculated.

Let us examine in more detail the meaning of equation (5.1). According to Oishi et al (5.1) for soda-lime glasses the apparent activation energy for diffusion (ΔH_D) of oxygen increases rapidly in the transformation range. From equation (5.1) the same trend should be observed for ΔH_η, the activation energy for viscosity. For many systems the viscosities as a function of temperature are better described by a Fulcher equation than an Arrhenius equation with a constant activation

energy. By comparing $\eta = \eta_0 \exp\left(\frac{\Delta G_\eta}{RT}\right)$ (where $\Delta G_\eta = \Delta H_\eta - T\Delta S_\eta$ and $\Delta H_\eta = [\partial(\Delta G_\eta/T)/\partial(1/T)]_P$ and also ΔG_η, ΔH_η and ΔS_η are now considered as functions of temperature) with the Fulcher expression $\eta = 10^A 10^{B/T-T_o}$ we obtain

$$\Delta H_\eta = \ln 10 \frac{BRT^2}{(T-T_o)^2} \qquad (5.4a)$$

$$\Delta S_\eta = \ln 10 \frac{BRT_o}{(T-T_o)^2} + R \ln\left(\frac{\eta_0}{10^A}\right) \qquad (5.4b)$$

$$\Delta G_\eta = \ln 10 \frac{BRT}{T-T_o} - RT \ln\left(\frac{\eta_0}{10^A}\right) \qquad (5.4c)$$

It can be noticed that ΔH_η <u>increases</u> with T decreasing. For example with $T_o = 300°C = 573°K$, for T = 873, 853, 833 and 803°K the values $\frac{\Delta H_\eta}{\ln 10\, BR} = \frac{T^2}{(T-T_o)^2}$ are 8.47, 9.28, 10.26 and 12.19 respectively.

Let us examine the variation of ΔG_η with T. From equation (5.4c) we obtain

$$\frac{d\Delta G_\eta}{dT} = - \ln 10 \frac{BRT_o}{(T-T_o)^2} - R \ln\left(\frac{\eta_0}{10^A}\right) \qquad (5.5)$$

Clearly, for T approaching T_o the derivative is <u>negative</u> showing that ΔG_η increases with decreasing temperature. However for the temperature range of interest, say from 750 to 950°K, the variation of ΔG_η is not obvious because now the $\ln\left(\frac{\eta_0}{10^A}\right)$ value could play an important role. Using typical values for the Fulcher constants (A = -4, B = 4×10^3 and To = 300°C = 573°K) at T = 850°K the first term in equation (5.5) is -172. A reasonable estimate of η_0 appears to be 10^{-6} on the basis of the analysis of Litovitz and Macedo (5.2) for B_2O_3 glass. The second term in

equation (5.5) then becomes +9.1. Therefore unless η_0 is smaller than approximately 10^{-44} the activation free energy for viscosity should increase with T decreasing. Then from equation (5.1) the activation free energies for diffusion and viscosity should follow a similar trend with falling temperature. Furthermore, the diffusion coefficients calculated from equation (5.1) agree with the measured values to within an order of magnitude (see (5.1)). Hence it appears that the approximations involved in the derivation of equation (5.2) are reasonable.

5.1.2 Glasses G2 and G16

In order to analyse the experimental nucleation rates for G2 with equation (5.2) ΔG is needed. Although it is reasonable to consider G2 as a single component glass, the simple equation (1.18) for ΔG, which assumes $\Delta C_p = 0$, may not be sufficiently accurate. We have already shown how to calculate ΔG if a reasonable average value for ΔC_p is known (see equation 1.19 and 1.20). There is considerable evidence that ΔC_p is different from zero for G2. In section 3.1.b it was shown that from DTA ΔH_c (35.9 cal g^{-1}) is lower than ΔH_f (58.2 cal g^{-1}). The relationship between ΔH_c and ΔH_f is

$$-\Delta H_c = \Delta H = -\Delta H_f - \int_{T_c}^{T_m} \Delta C_p \, dT' \qquad (5.6)$$

where $\Delta C_p < 0$ (as in equation (1.17)) and T_c is the crystallization temperature. Using the above ΔH_c and ΔH_f values, putting $T_m = 1564°K$ and $T_c = 973°K$ (see Figure 3.7), and assuming ΔC_p is independent of temperature we obtain $-\Delta C_p = (\Delta H_f - \Delta H_c)/(T_m - T_c) = 12.33$ cal $mole^{-1}$ $°K^{-1}$ = 0.035 cal g^{-1} $°K^{-1}$.

Before going further let us consider some results from the literature. Following a similar method to that described above Rita et al (5.3) obtained - ΔC_p = 21.4 cal mole^{-1} °K^{-1} for $2PbO.SiO_2$. Using calorimetry Takahashi and Yoshio (5.4) measured ΔH and ΔC_p for lithium, sodium and potassium disilicate glasses and hence determined ΔG values. For example, for the $K_2O.2SiO_2$ glass the ΔC_p was different from zero and the experimental ΔG was described fairly closely by Hoffmann's equation (equation (1.21)).

An independent measurement of ΔC_p for NC_2S_3 was attempted using Differential Scanning Calorimetry (DSC). A Perkin Elmer DSC-2 instrument was employed at a heating rate of 40°C min^{-1}. From the individual traces obtained for the glass, glass ceramic and a standard sapphire sample, the sample specific heats (cal g^{-1} °K^{-1}) were computed from

$$C_p^{\,i} = \frac{W_{sap.}}{W_i} \times \frac{D_i}{D_{sap.}} \times C_{p_{sap.}}$$

where W_i and D_i are the weights (g) and the relative displacements (mm) from the base line of specimen i. The suffix sap. refers to the sapphire. The C_p vs. T curves are shown in Figure 5.1. The following may be observed: (i) the almost constant specific heat for the glass ceramic, (ii) the increasing specific heat for the glass from about 530°C, and (iii) the short 'plateau' between the 'hump' and the onset of crystallization in the glass. The 'hump' observed for the glass may be related to the fictive temperature of the glass and to the heating rate. The ΔC_p at 667°C is -0.104 cal g^{-1}K^{-1} = -36.9 cal mole^{-1}K^{-1} which is three times greater than the previously calculated value from DTA of -0.035 cal g^{-1} °K^{-1}. Unfortunately we have no information on the effect of heating rate on

FIGURE 5.1 SPECIFIC HEAT CURVES FOR GLASS G2 AND G2 FULLY CRYSTALLIZED. (DSC)

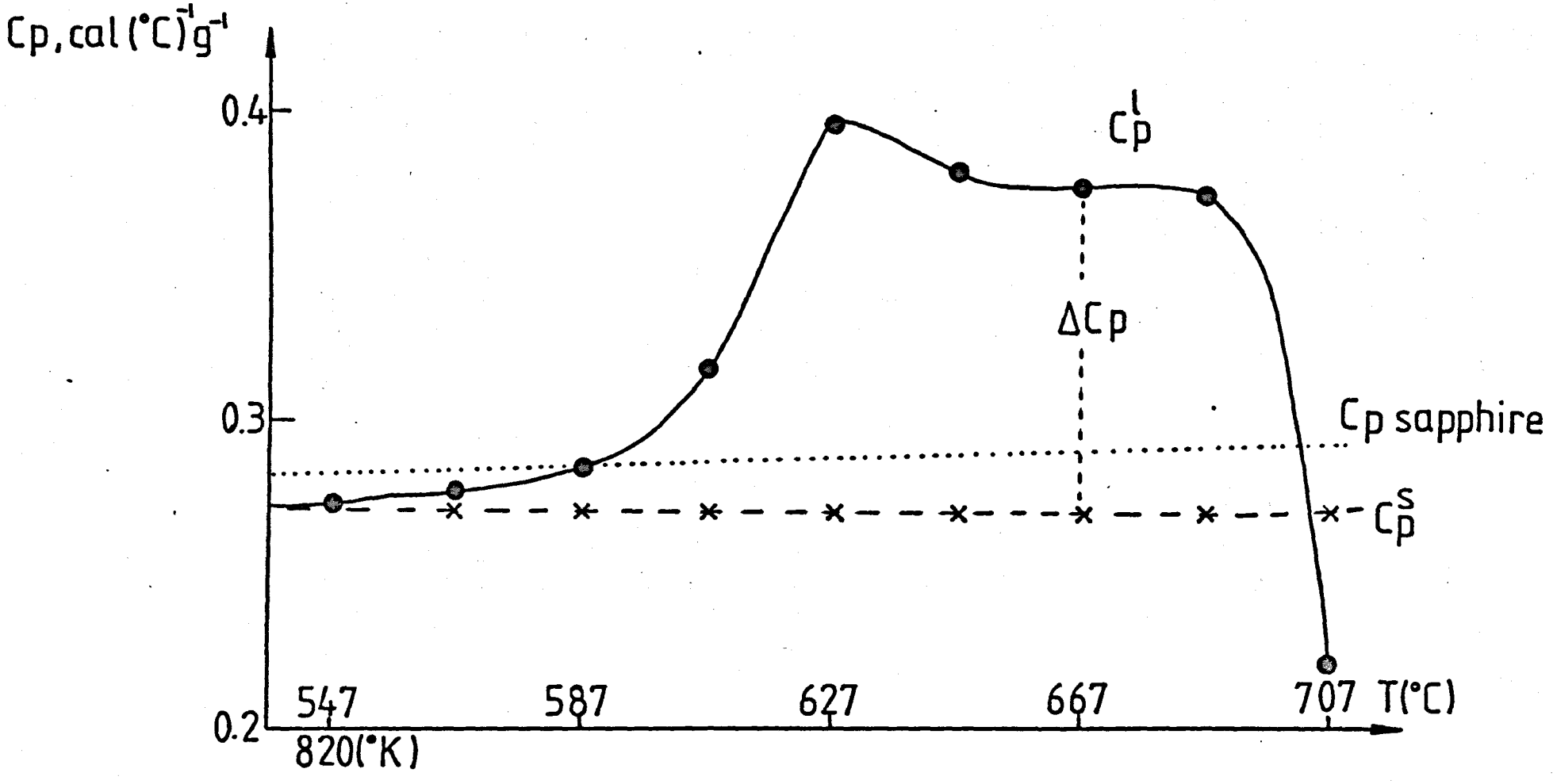

the position of the 'plateau'. It is possible that for slower heating rates, the earlier onset of crystallization may lower the 'plateau' (with respect to the C_p^s curve). Due to these uncertainties it was decided to adopt the value obtained from DTA as the average ΔC_p. However the DSC results showed clearly how the specific heat of the glass approached that of the crystalline NC_2S_3. The DSC also enabled the absolute specific heat for the crystalline NC_2S_3 to be determined. For example at 530°C C_p^s was 0.271 cal g^{-1} $°K^{-1}$.

It is interesting to calculate the specific heat of the glass from the Dulong and Petit law (5.5) where the maximum heat capacity at constant volume (C_v) is given by

$$C_v = 3R(g\ atom^{-1}) \tag{5.7}$$

From the chemical composition of NC_2S_3 in mole fractions (0.166 for Na_2O, 0.333 for CaO and 0.5 for SiO_2) we obtain C_v = 3R (g $atom^{-1}$) x 0.0451 (g atom/g glass) = 0.269 cal g^{-1} $°K^{-1}$. Haggerty et al. (5.6) used specific heat measurements to demonstrate structural differences between glass formers. For example for temperatures near the transformation range the B_2O_3 glass gave a C_v value which was 60% of the theoretical 3R whereas for SiO_2 glass the C_v was very close to the 3R value. In the present case the C_v for the NC_2S_3 glass (at T = 537°C, C_v = 0.266 cal g^{-1} $°K^{-1}$ where the $C_p - C_v$ value quoted below was used) is almost the theoretical 3R value indicating the three dimensional network structure of this particular glass. Now, C_v is related to C_p by

$$C_p - C_v = \frac{T\ V_m\ \alpha_v^2}{\beta} \tag{5.8}$$

where $\alpha_v = \frac{1}{V}\left(\frac{\partial V}{\partial T}\right)_p \simeq 3\ \alpha_L$ is the volume thermal expansion and α_L is the

linear thermal expansion. $\beta = -\frac{1}{V}\left(\frac{\partial V}{\partial P}\right)_T$ is the compressibility. Substituting T = 750°K, V_m = 128.88 $cm^3 mole^{-1}$, $\alpha_L \simeq 120 \times 10^{-7}$ $(°K)^{-1}$ and $\beta = 2.25 \times 10^{-12}$ cm^2 $dyne^{-1}$, the β value corresponding to a typical soda-lime glass (5.7), $C_p - C_v$ was estimated as 3.75×10^{-3} cal g^{-1} $°K^{-1}$ which gave C_p as 0.266 cal g^{-1} $°K^{-1}$. This is in close agreement with the measured value for both glass and glass ceramic at 530°C.

It is worth noting that from the DSC trace for the glass ceramic it was possible to obtain an independent measurement of the heat of the polymorphic transformation of NC_2S_3. The value of $\Delta H_r \simeq 1.6$ k cal $mole^{-1}$ compares well with the 1 k cal $mole^{-1}$ value found from the DTA traces.

The ΔG values can be calculated from equation (1.19) with ΔC_p = -0.035 cal g^{-1} $°K^{-1}$. The experimental $\ln\left(\frac{I\eta}{T}\right)$ values are plotted against $\frac{1}{\Delta G^2 T}$ in Figure 5.2, where the I values are now expressed in cm^{-3} s^{-1}. For temperatures higher than 610°C a good straight line can be drawn through the experimental points. Assuming a spherical shaped nucleus σ and A_c were calculated from the slope and appropriate intercept of the straight line, as explained previously. Using least squares analysis the results were σ = 173.6 erg cm^{-2} and $\log_{10} A_c$ = 68.5. The latter value gave $\log_{10} A$ = 77.2, using equation (5.3) with T = 873°K and $\lambda \simeq 7.4 \times 10^{-8}$ cm. This value is much greater than the theoretical value $\log_{10}\left(N_v \frac{kT}{\eta}\right)$ = 34.9.

For temperatures lower than 610°C the experimental points lay well below the straight line. This effect may be explained in terms of non steady state effects where the nucleation rates (for 40 min) tend to be underestimated.

FIGURE 5.2 Ln(Iη/T) AS A FUNCTION OF $1/\Delta G^2 T$ FOR G2

o Values for G2 where ΔG was calculated with ΔCp as $-0.035\ cal\,g^{-1}\,°C^{-1}$.

● " " " " " " " " " " as explained in the text.

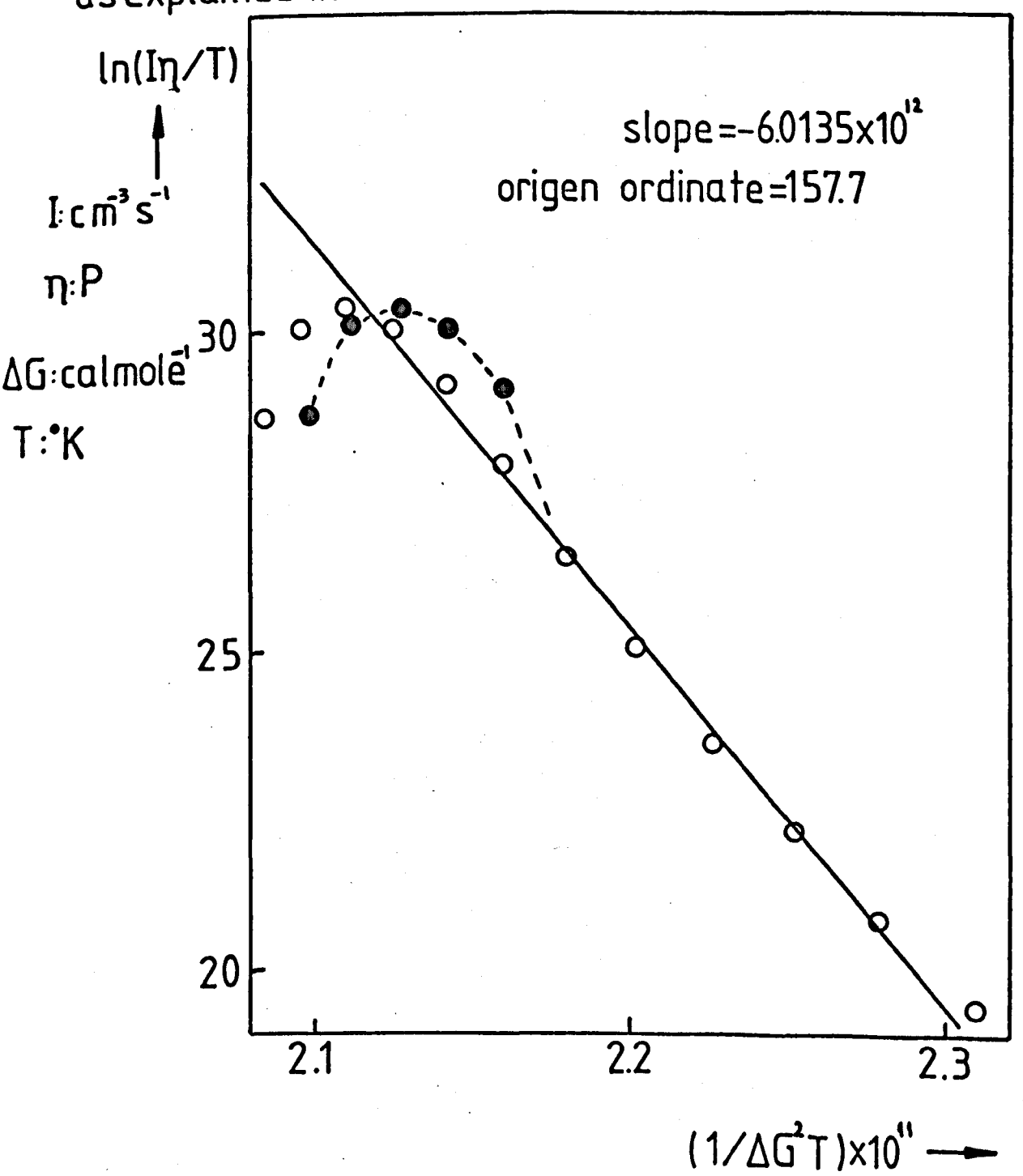

From the DSC observations (Figure 5.1) it appears that ΔC_p is approximately constant above 900°K but then decreases to approximately zero at 850°K. In order to investigate this effect ΔG was calculated using equation (1.19) where three temperature ranges were considered: $900 < T < 1562$, $\Delta C_p = -0.035$ cal g^{-1} K^{-1}, for $850 < T < 900$, $\Delta C_p = -\frac{0.035}{50}(T - 850)$ and for $T < 850$ $\Delta C_p = 0$. The results are shown in Figure 5.2 by the dotted line. Although there is a tendency to shift the experimental points with respect to the straight line, the overall fit appears poorer. We conclude that the variation in ΔC_p we have used is probably too abrupt and that a smoother variation in ΔC_p would be more appropriate.

For glass G16 the steady state I_o and 'approximated' nucleation rates (using N_v for 40 min, see Figure 3.16) were used together with the viscosity data (equation (3.8)) to test equation (5.2). The ΔG values calculated for G2 were used due to the very similar thermal properties for both glasses (see sections 3.1.4b and 3.2.4). The $\ln\left(\frac{I_n}{I}\right)$ vs. $\frac{1}{\Delta G^2 T}$ plots are shown in Figure 5.3. All the steady state values lay on a good straight line, which gave σ as 193.1 erg cm^{-2} and $\log_{10}A$ as 98.5. The straight line indicates good agreement with the theory over the temperature range considered assuming a constant σ is independent of temperature but allowing ΔG_D to increase with decreasing temperature in accordance with the viscosity. However, as for G2 the pre-exponential factor is again too large when compared with the theoretical value. It should be noticed that the values for σ and $\log_{10}A$ for G16 are somewhat higher than those obtained for G2. This is probably due to the small difference in composition between G16 and G2. (See

FIGURE 5.3 Ln(Iη/T)AS A FUNCTION OF $1/\Delta G^2 T$ FOR G16

● $I(cm^{-3} s^{-1}) = I_o$, steady state values

o I for 40 min. nucleation time

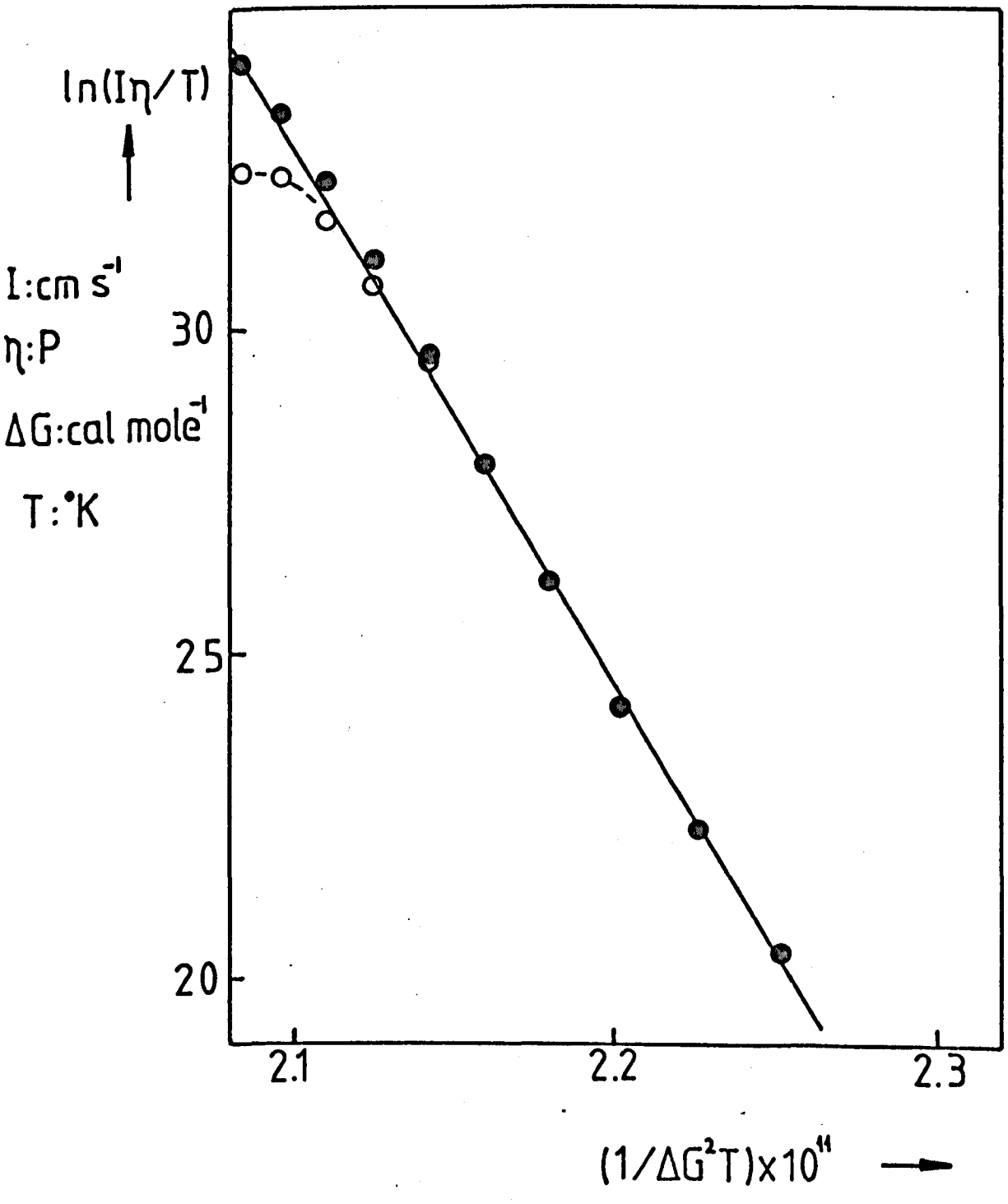

Sections 3.1 and 3.2). Figure 5.3 also shows that the 'approximate' nucleation rates (using the N_v for 40 min) only fall on the straight line above 605°C. This emphasizes the importance of using the steady state nucleation rates in these plots.

Using the above σ value the theoretical size of the critical nucleus can be made from equation (1.2b). For example at T = 873°K, r* is 16.1 Å. It is interesting to compare the present σ value with that given by the equation obtained by Matusita and Tashiro (5.8) in analysing alkali disilicate glasses:

$$\sigma = 0.45 \frac{\Delta H_f}{N_A^{1/3}} \left(\frac{\rho_s}{M}\right)^{2/3}$$

where N_A is the Avogadro's number, ρ_s is the solid density (2.80 g cm^{-3} for crystalline NC_2S_3) and M is the molecular weight (354.42 g for NC_2S_3). The value σ is 193 erg cm^{-2} which compares well with the value for G16 but is higher than that for G2.

The nucleation intercepts (t_o) in Table 3.10 for G16 will now be analysed in terms of $\tau = \frac{6}{\pi^2} t_o$ (see equation (1.8b)). James (5.9) has shown that the incubation time τ (see equation (1.7b)) can be expressed as

$$\tau = \frac{16}{\pi^2} \frac{h\lambda^2\sigma}{\left(\frac{V_m}{N_A}\right)^2 \Delta G_v^2} \exp\left(\frac{\Delta G_D}{RT}\right) \qquad (5.9)$$

Also he related τ to η using the Stokes-Einstein equation (1.43) as follows

$$\tau \simeq \frac{48}{\pi} \frac{\sigma\lambda^5\eta}{\left(\frac{V_m}{N_A}\right)^2 \Delta G_v^2} \qquad (5.10)$$

In Figure (5.4) four different plots are shown: $\ln(\tau\Delta G_v^2)$ vs $\frac{1}{T}$ according to equation (5.9), $\ln\tau$ vs $\frac{1}{T}$, $\ln\left(\frac{\tau\Delta G_v^2}{\eta}\right)$ vs $\frac{1}{T}$ according to equation (5.10), and $\ln\eta$ vs $\frac{1}{T}$. From the first plot the slope gave an apparent activation energy of 78.2 kcal mole^{-1}. From the intercept, by using equation (5.9) with $\sigma = 193$ erg cm^{-2}, λ was 0.2 Å which is an order of magnitude lower than the theoretical 7.4 Å value. So far the agreement between experiment and equation (5.9) appears reasonable. However from a similar analysis the apparent activation energy ΔH_η for viscosity was 196 kcal mole^{-1}. Nevertheless it is interesting to calculate the absolute τ value from equation (5.10). For example at 585°C using the measured viscosity ($\log_{10}\eta = 12.1$) and $\lambda \approx 7 \times 10^{-8}$ cm we obtained $\tau = 2.3 \times 10^4$ S which is 17 times greater than the measured τ (1.37×10^3 S). For theory and experiment to agree the viscosity at 585°C should be $\log_{10}\eta = 10.87$ which is outside the experimental error in the measurements. However it is known (see section (5.1)) that the Stokes-Einstein equation may be in error by about an order of magnitude at temperatures near the transformation range. On this basis and in view of the uncertainties in the estimation of the quantities in equation (5.10) the agreement between theory and experiment is reasonable.

5.1.3 Effect of composition. Glasses G18 to G23

Unfortunately for glasses G18 to G23 the $\Delta G(T)$ is not known. However from the DTA results for ΔH_c and ΔH_f some knowledge of ΔG can be acquired. For example (see Table 3.15) for glasses G19, G21 and G22 having approximately 49 mole% SiO_2 (i.e. less than 50 mole%)

FIGURE 5.4 $\ln(\tau\Delta G_v^2)$, $\ln\tau$, $\ln(\tau\Delta G_v^2/\eta)$ and $\ln\eta$ as a function of $1/T$ for G16

● $\ln(\tau\Delta G_v^2)$, o $\ln\tau$, + $\ln(\tau\Delta G_v^2/\eta)$, × $\ln\eta$

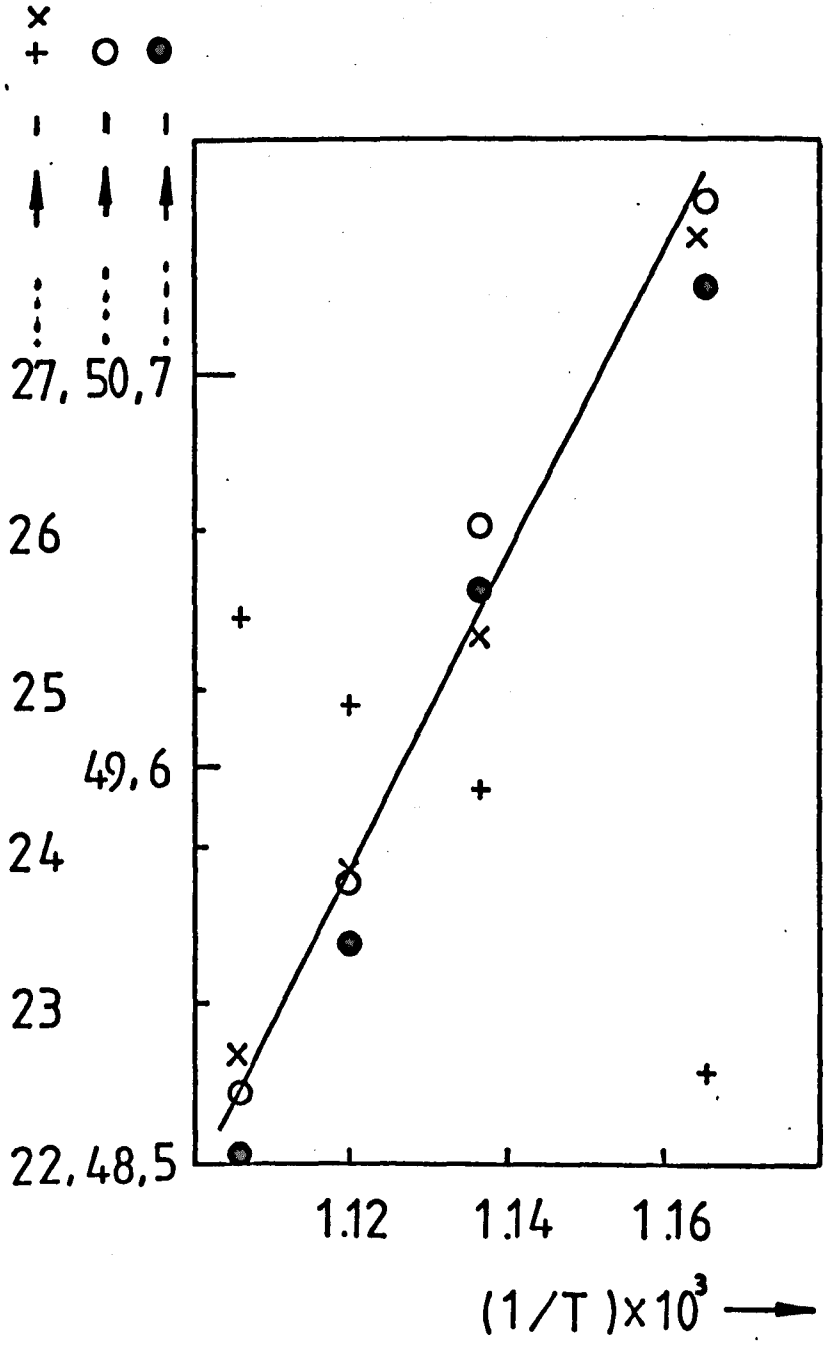

T :K

T :s

ΔGv :erg cm⁻³

the values of ΔH_c and ΔH_f are approximately constant. For glasses G18 and G20 with more than 50 mole% SiO_2 the ΔH_f and ΔH_c are also nearly constant. However the values for G23 are smaller than those for G18 and G20. These observations might suggest that the six glasses can be separated into two groups, one on either side of the NS-CS join of the ternary diagram. However other important information, for example the extent of solid solution, for NC_2S_3 crystals, for these compositions is not known. Consequently it was decided to use another approach in interpreting the observed nucleation for these glasses. This was based upon considerations of the viscosity changes, the relative position of the nucleation curves and the expected W_i^* (according to the theory of nucleation) for each glass. From equation (5.2) we obtain

$$\ln\left(\frac{I_i\,\eta_i}{T}\right) = \ln A_c - \frac{W_i^*}{kT}\,.$$

So by assuming the same A_c for every glass and relating to G2, for which $\Delta G(W^*G_2)$ is known, we obtain

$$kT\left[\ln\left(\frac{I_{G_2}\eta_{G_2}}{T}\right) - \ln\left(\frac{I_i\eta_i}{T}\right)\right] + W^*_{G_2} = W^*_i \qquad (5.11)$$

The plots W_i^* vs T for glasses G18 to G23 and for G2 are shown in Figure 5.5. For example if the W^* are the same the observed changes in nucleation (I) should correspond to the observed changes in viscosity (η). Also it is useful to plot the nucleation according to equation (1.4b) where σ and ΔG_D have been taken as constants independent of temperature

FIGURE 5.5 $\dot{W}_i^*$ AS A FUNCTION OF T(°C)

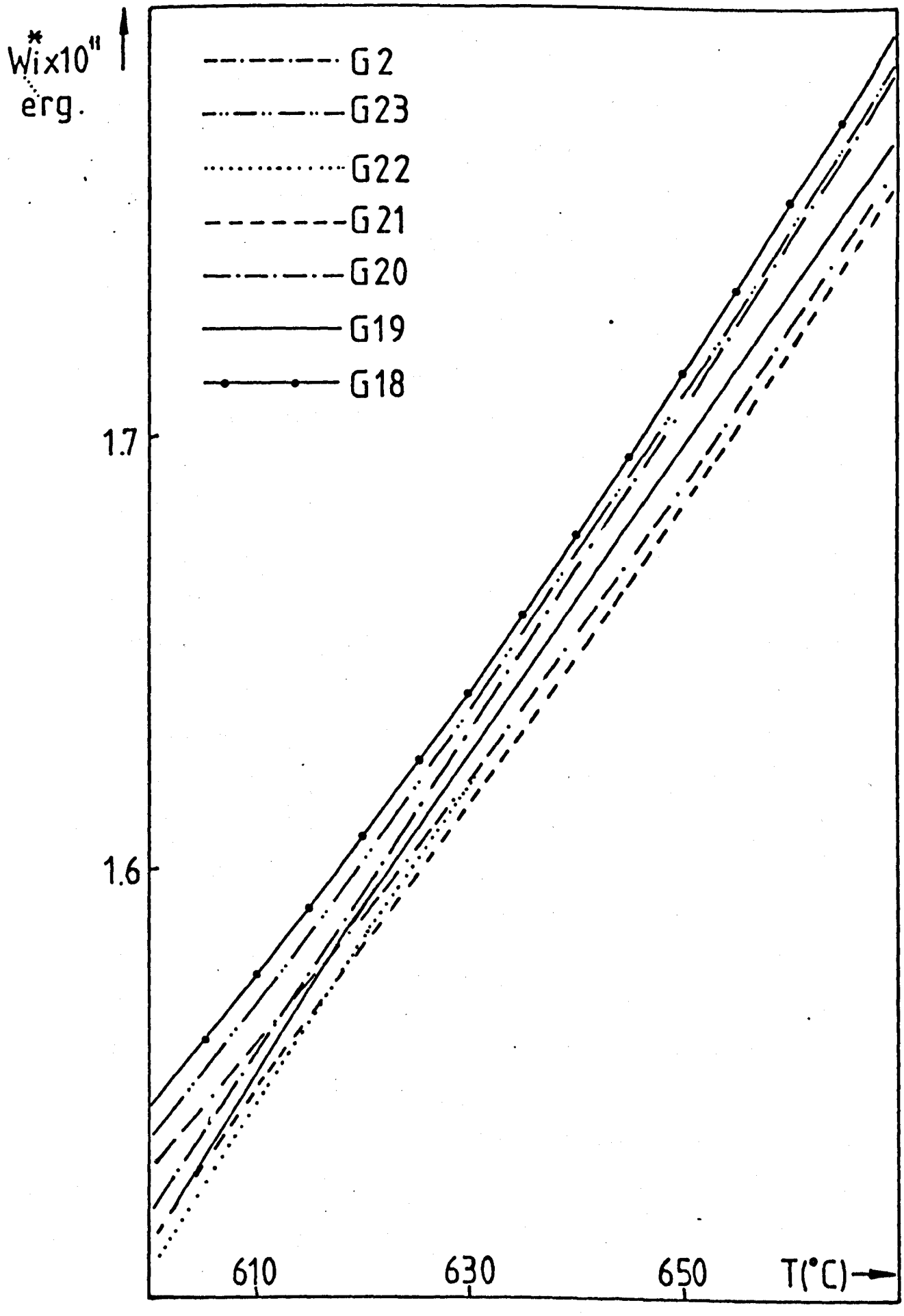

(Figure 5.6). From this figure the general effect, on nucleation, of different values of σ and ΔG_D can be observed.

From now on we will consider G2 and G17 as having the same viscosity (see section 3.1). Also we will use o.m. to signify ' order of magnitude'.

Due to possible non-steady state effects we will analyse the results for temperatures higher than the maximum in nucleation.

Glass G19 (increased Na_2O content as compared to G2) had a much greater nucleation than either G2 or G18 (decreased Na_2O content as compared to G2). From Figures 3.31 and 3.34 it is observed that at high T the changes in nucleation, for G19 compared to G2, approximately correspond to the changes in η. For example at 630°C the changes in nucleation and viscosity are both 1 o.m. From Figure 5.5, at high T, W^*_{G19} is slightly higher than W^*_{G2}. It is difficult to decide whether the changes in W^* are due to changes in σ or ΔG although the similar ΔH_c and ΔH_f values for G19 and G2 suggest that the ΔG values may be close. However it is clear that the lower η_{G19} as compared to η_{G2} suggests that $\Delta G_D^{G19} < \Delta G_D^{G2}$. Comparing G18 to G2, I_{G18} was lower than I_{G2} by about ½ o.m. for all T. Also W^*_{G18} is greater than W^*_{G2}. As the η are nearly the same it may be assumed that $\Delta G_D^{G18} \approx \Delta G_D^{G2}$. Then the lowering in nucleation is probably only due to changes in W^*. These changes could be due to a lower ΔG for G18 when compared with G2, since the ΔH_f for G18 is lower than G2. However it is impossible to draw conclusions about changes in σ.

For G21 (higher CaO content than G2) the increased I at high T(½ o.m.) corresponds approximately to the increase in η (½ o.m.). As the ΔH_f value for G21 was nearly the same as for G2, it may be assumed that

FIGURE5.6 Ln(I/A) AS A FUNCTION OF T(°C) Acc.TO EQUATION(1.4b) FOR DIFFERENT $\sigma, \Delta G_0$ CONBINATIONS AND THE SAME $\Delta G(T)$

$[\sigma]$: erg cm^{-2}

$[\Delta G_0]$: kcal $mole^{-1}$

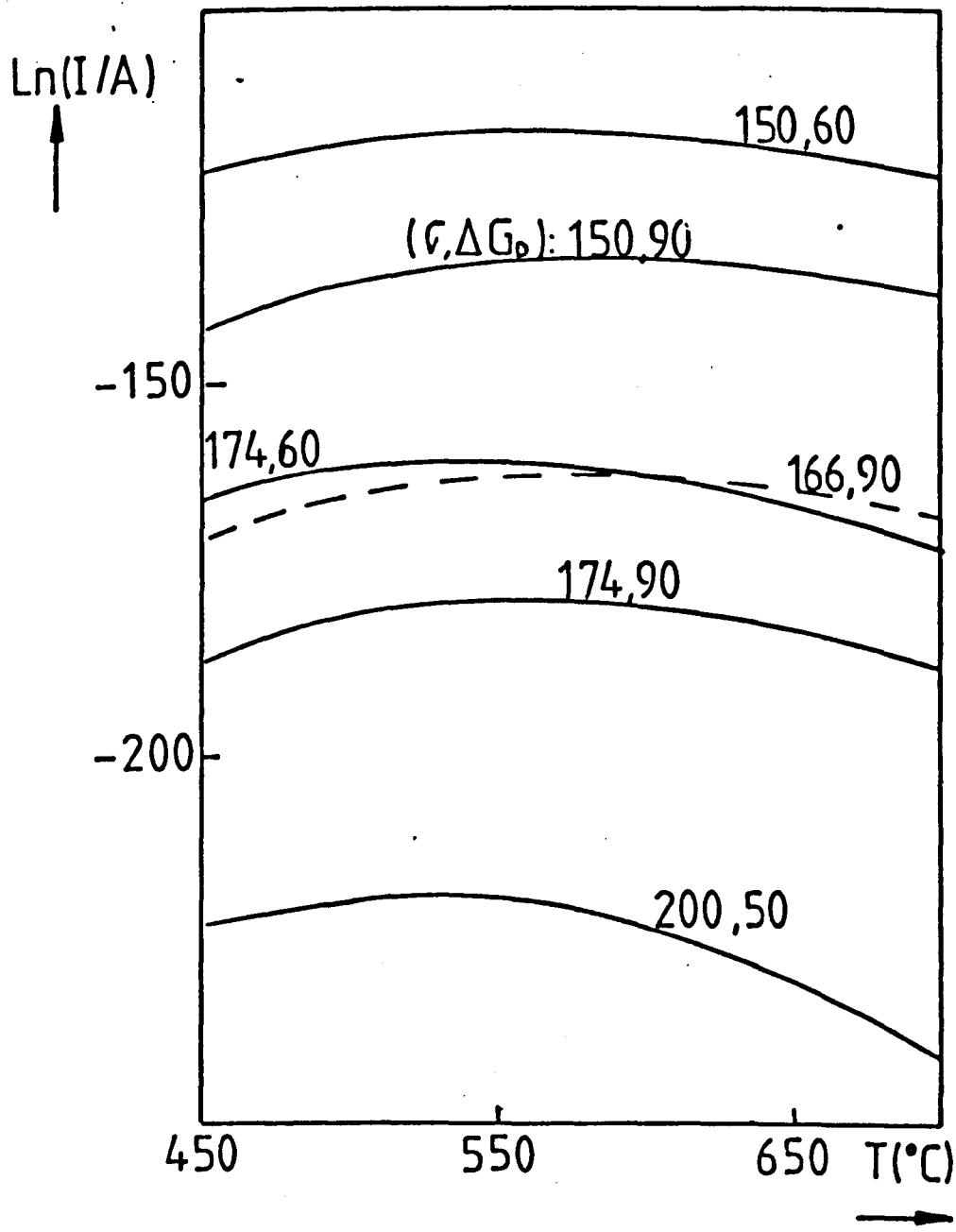

$\Delta G^{G21} \approx \Delta G^{G2}$. Then it may be concluded that σ has not changed appreciably (see Figures 5.5 and 5.6). Although the nucleation for G20 was very close to G2 at temperatures higher than 630°C the viscosity of G20 was ½ o.m. lower than for G2. As a result the W^*_{G20} is higher than G2 (Figure 5.5). This may be due to a lower ΔG for G20 (the ΔH_f was lower than G2).

For G22 the increase in I (¼ o.m.) as compared to G2 approximately corresponds to the decrease in η (0.60 o.m; see Figures 3.45 and 3.46). Hence the W* values were similar. Furthermore the ΔH_c and ΔH_f values for G22 were similar to G2, suggesting that the ΔG values are similar. Then it may be concluded that σ has not changed appreciably.

For G23 the η was close to that for G2. Also W^*_{G23} was much greater than W^*_{G2}. This change could be due to a much lower ΔG for G23 since the ΔH_f was lower than that for G2. Again no conclusions can be made about σ.

In conclusion we note that for the above glasses the changes in nucleation do not always correspond exactly with the changes in viscosity showing that other factors (σ, ΔG_v) are involved. However viscosity data are a useful aid in the interpretation of the observed nucleation for these soda-lime glasses. The decrease in internal nucleation of NC_2S_3 with increased SiO_2 content for glasses lying on the NC_2S_3 - S join (5.10) has been confirmed in this work. However the situation for other joins (for example NC_2S_3 - C) is not obvious. For example although for G20 (16.92 mole% Na_2O, 32.33 mole% CaO and 50.75 mole% SiO_2) the SiO_2 content is increased, the nucleation is also increased. This finding is of a practical interest because for G20 the higher SiO_2 content could mean a better chemical durability.

5.1.4 Effect of Water Addition on Nucleation

Let us briefly review the main effects of water in glass. By increasing the water content in vitreous silica the viscosity, density, acoustic velocity and refractive index decrease whereas the thermal expansion increases (5.11). Although the viscosity is also reduced in binary and ternary silicates (5.12), the density and refractive index are increased with water content increasing (5.13). These effects may be explained by the rupture of silicon oxygen bridges produced by the introduction of water and also by the different association states of the OH groups. For example in vitreous silica the OH groups occur mainly as unassociated states (shown by the single absorption peak at 2.75 μm in the infra-red spectrum). The free OH groups cause the SiO_2 glass structure to become more open, i.e. decreasing the density and refractive index. On the other hand in multicomponent glasses the presence of hydrogen bonding causes a shrinkage of the glass network resulting in an increase in density. Maklad and Kreidl (5.14) studied a number of properties in sodium silicate glasses for different water contents. For example the kinetics of phase separation was clearly enhanced with increasing water content. They suggested that the diffusivity and viscous flow were increased. Wagstaff et al (5.15) showed that the crystal growth rate in vitreous silica increased in a H_2O atmosphere. The water was considered to enhance crystallization in two ways: by acting as a source of oxygen and by weakening the glass

structure. Eagan and Bergeron (5.16) found that increasing the water content in a lead tetraborate glass by a factor of three caused an increase in the crystal growth rate, for a particular crystallographic direction, by 20%. However, the increase in growth rate did not correlate with the observed decrease (7%) in viscosity. They suggested that the water content at the crystal-liquid interface would be greater than in the bulk liquid giving a localized, greater reduction in viscosity. Mukherjee et al. (5.17) found that the crystallization rates in lanthanum silicate glasses prepared from 'gels' were much higher than in glasses prepared from the oxides. They considered that the OH groups not removed during the dehydration of the gels had a great influence on crystallization.

We have already shown the large effect of water content on the crystal nucleation and growth rates and viscosity of soda-lime-silica and lithia-silica glasses in section 4.1. An interpretation of the effect on nucleation rates follows. Let us consider first the lithia glasses L1 and L3 (bubbled with steam) for which the viscosity has been measured (see Figure 4.8). The results from Figure 4.2 are plotted, in terms of equation (5.2), in Figure 5.7, where the ΔG for L1 was taken from reference (5.18). Due to the similar compositions for L1 and L3 and similar liquidus temperatures (see Tables 4.1 and 4.4), as an approximation, the ΔG values for L1 and L3 were taken the same. The following can be observed:

(i) for L1 (almost the exact $Li_2O.2SiO_2$ or 'LS_2' composition) the theory fails in fitting the nucleation rates (calculated from the N_V for 4 hours heat treatment) at temperatures lower than

FIGURE 5.7 Ln(Iη/T) vs.1/ΔG²T FOR GLASSES L1 and L3

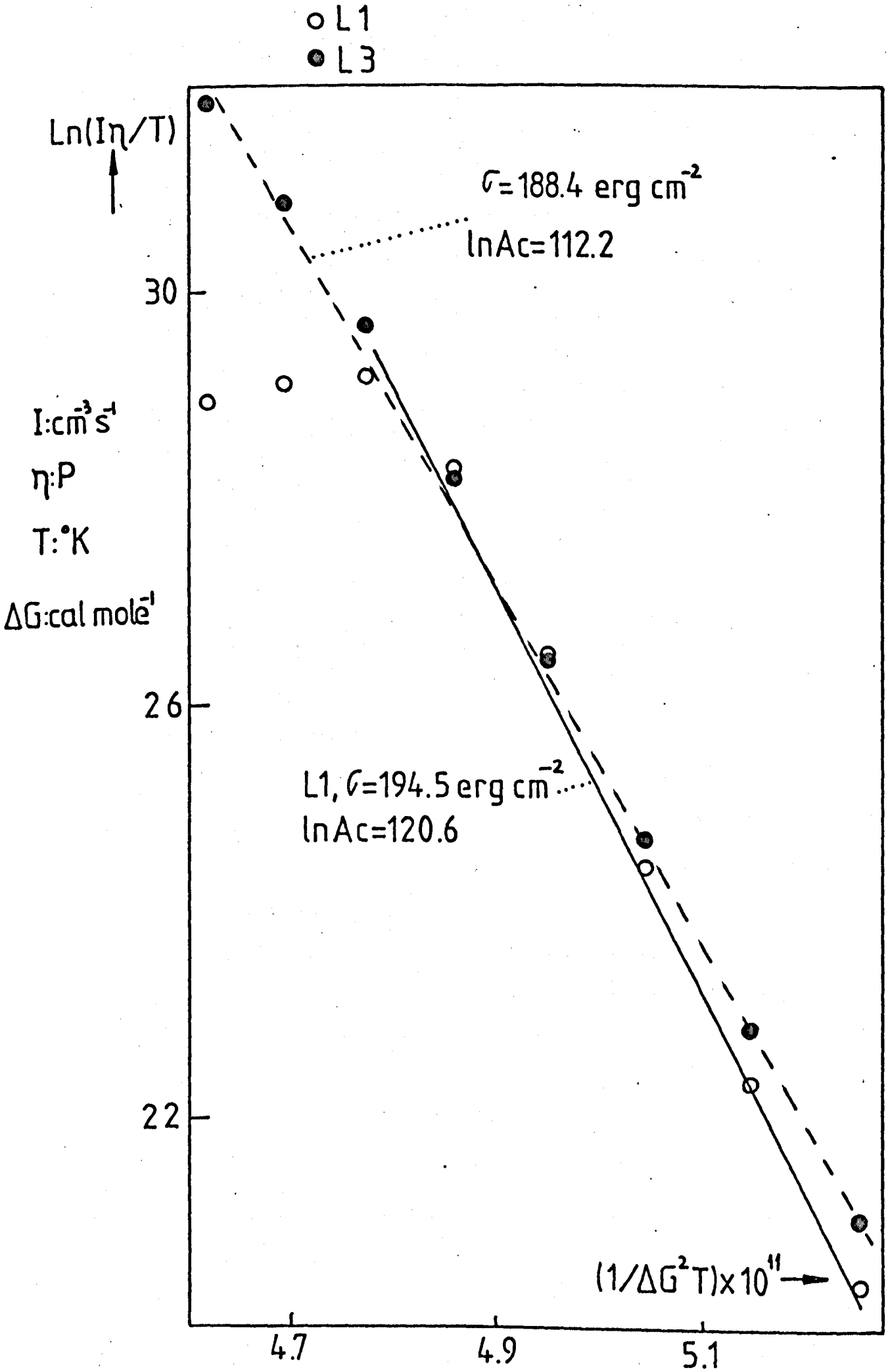

460°C. This is certainly due to non-steady state effects. For example at 465°C the τ value for L1 was 36.5 min (5.9). However, at higher temperatures a straight line can be drawn through the points in Figure 5.7. The σ and A_c values determined by least squares were 194.5 erg cm^{-2} and 120.6, respectively. These results are slightly higher than those obtained by Rowlands (5.18) using the steady state I_o values provided by James (5.9) and the viscosity data obtained by Matusita and Tashiro (5.19). Rowlands obtained σ = 185 erg cm^{-2} and ln A_c = 113.

(ii) For L3 a straight line could be fitted to <u>all</u> the experimental points indicating that for temperatures as low as 440°C the approximated nucleation rates (using N_v data for 4 hours) were probably very close to the steady state values. The σ and ln A_c values were 188.4 erg cm^{-2} and 112.3 respectively.

It should be mentioned that in the above calculation of σ a spherical shaped nucleus has been assumed. However, it is known (5.20) that in the early stages of growth of LS_2, the internally nucleated crystals are plate-shaped. From nucleation theory only a value proportional to $\bar{\sigma}^3$ is obtained. Rowlands (5.18) has shown that very different values of $\bar{\sigma}$ are obtained for different critical nucleus shapes. Although for L3 there is no information on the crystal morphology in the early stages of growth, it appears reasonable, based on the similar compositions of L1 and L3, to assume that the crystals precipitated in L3 are of similar shape to those precipitated in L1. Then, if the crystal morphology (at the early stages of growth) is unique, a direct

comparison between the σ values for L1 and L3 seems reasonable.

In Figure 5.8 the W^*_i values (see equation (5.11)) are plotted against temperature. It can be observed that at higher temperatures $W^*_{L1} \simeq W^*_{L3}$ suggesting small differences in the σ values (for similar ΔG). Also, the lower σ for L3, obtained above, accounts for W^*_{L3} being lower than W^*_{L1} at the lower temperatures. It may be concluded that for the lithia glasses the observed effect of water content on nucleation may be explained in terms of a reduction in viscosity (and ΔG_D) and a slight lowering of σ.

For the soda-lime glasses the situation is more complex due to the observed differences in compositions (see Table 4.1). However, there is no doubt that the increased nucleation of G14 (see Figure 4.2) is due to the higher water content. G14 has almost 3 mole% more SiO_2 than the base glass G2. Then on the basis of the effect of composition shown in the previous section it would be expected that for a glass of similar composition to G14, but lower in water content, the nucleation would be much lower than G2. This is confirmed by the results for G15. The lower nucleation for G15 is partly explained by the increase in viscosity caused by higher SiO_2 content (see Figure 4.8). Also the liquidus temperature of G15 was lower than G2. This implies that ΔG (G15)< ΔG (G2) which would also contribute to the lower nucleation in G15. Unfortunately ΔG for G14 and G15 cannot be calculated. However, it is instructive to consider the W^*_i values plotted in Figure 5.9. The curves for G15 and G2 are separated considerably indicating that viscosity changes alone are not enough to account for the lower nucleation of G15 compared to G2. Comparing G15 with G14, W^*_{G15}, at higher temperatures, is much closer

FIGURE 5.8 W_i^* vs.T(°C) FOR L1 AND L3

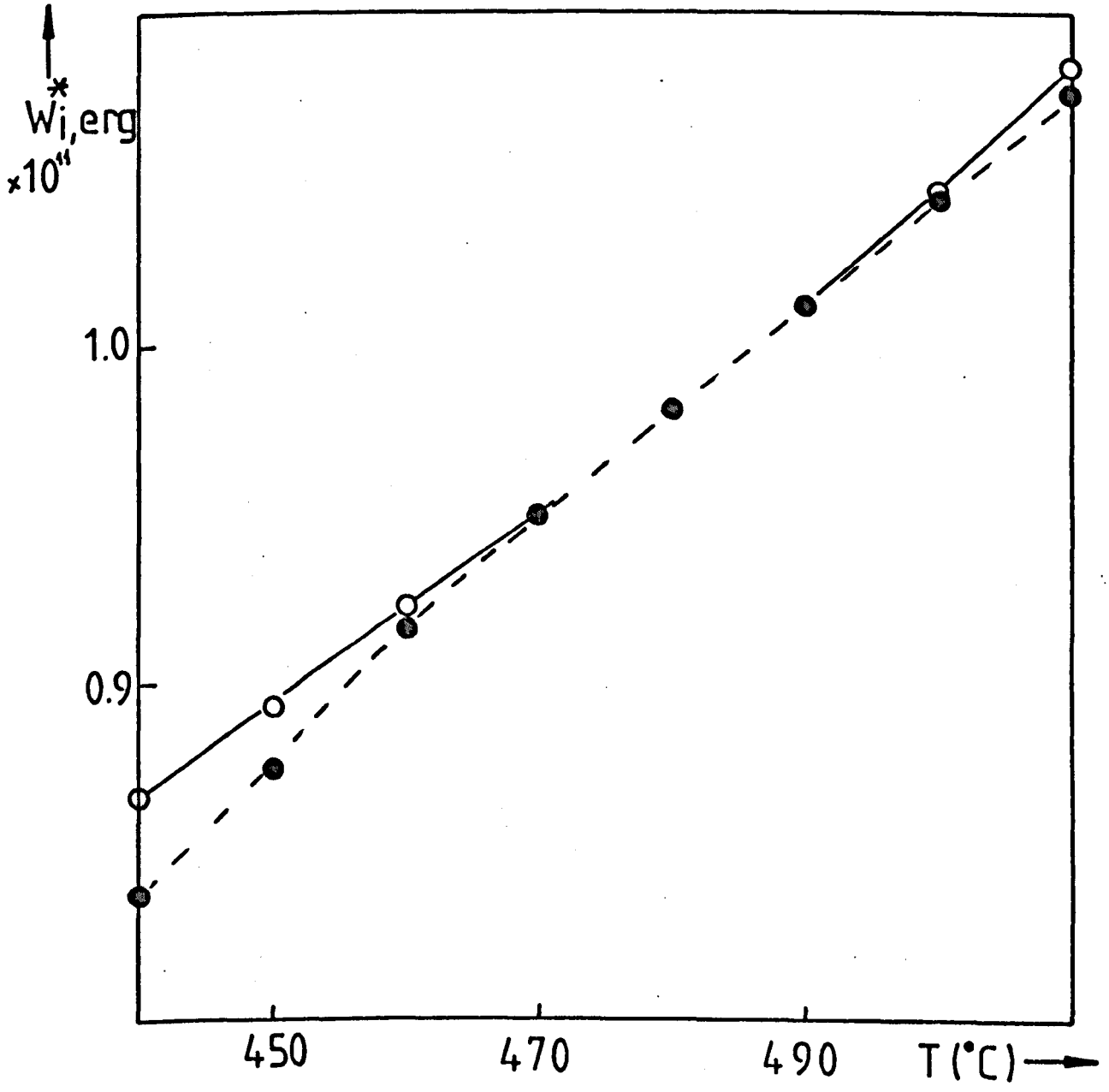

FIGURE 5.9 W_i^* vs. T(°C) FOR GLASSES G2, G14 and G15

× G2

● G14

○ G15

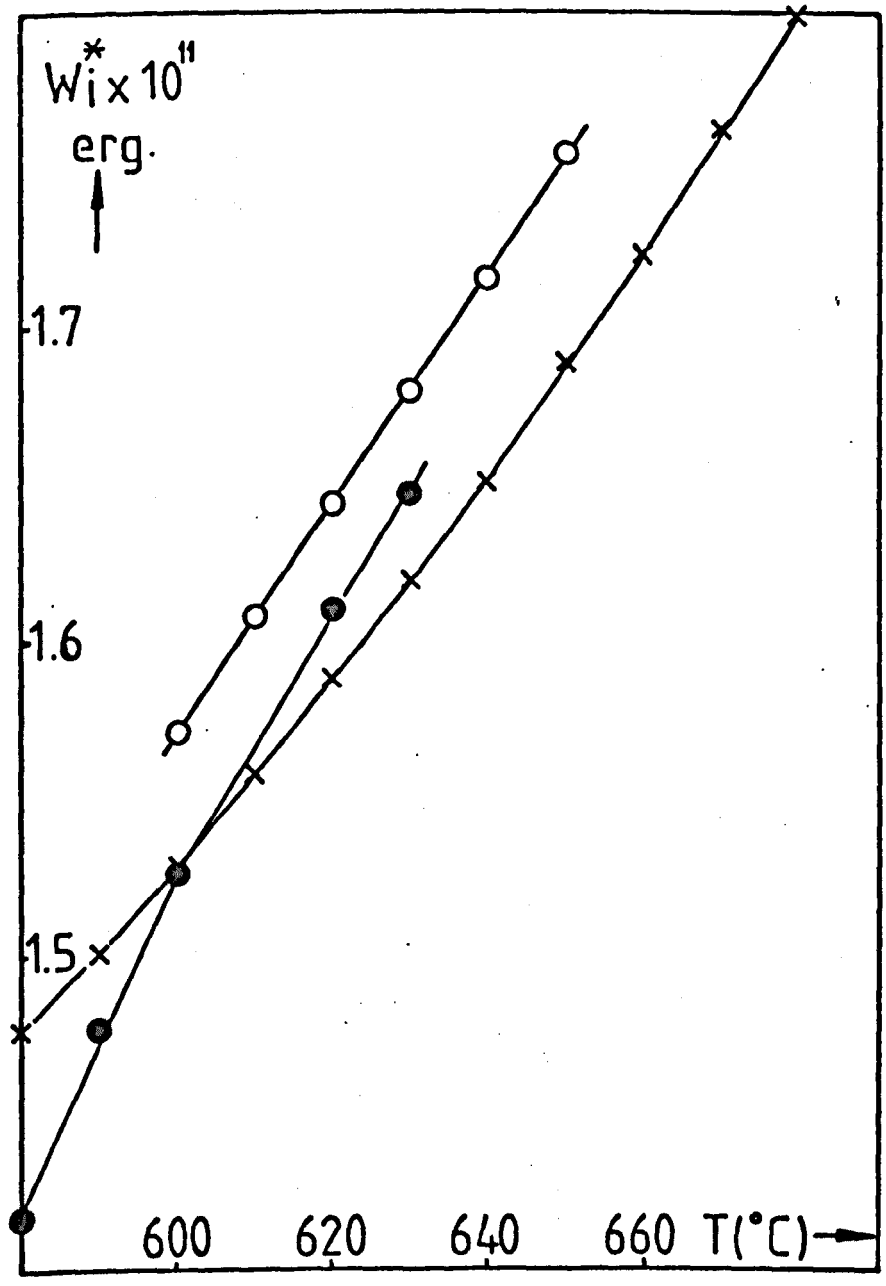

to W^*_{G14} than to W^*_{G2}. The ΔG values for G14 and G15 should be very close, since they have nearly the same compositions and liquidus temperatures. Hence the lower W^* for G14 compared with G15, is reasonably explained by $\sigma_{G14} < \sigma_{G15}$. A similar conclusion was obtained above when comparing the lithia-silica glasses L1 and L3. Thus the effect of water content on nucleation of soda-lime glasses may be explained in terms of a decrease in viscosity (and ΔG_D) and a lowering of σ.

The introduction of water into a multicomponent glass probably produces hydrogen bridging bonds as well as a direct rupture of Si-O bridges according to $\equiv Si\text{-}O\text{-}Si \equiv + H_2O \rightarrow \equiv Si\text{-}OH + HO\text{-}Si \equiv$. The observed lowering of viscosity, with water content, may suggest that the main result of water introduction is the rupture of Si-O bonds. If the Stokes-Einstein relationship between diffusivity and viscosity is accepted the lowering of viscosity with increasing water content implies an increase in the diffusion coefficient of the rate limiting species. As mentioned above (5.1) a close correlation has been found between the activation energies for self diffusion of oxygen and for viscous flow in soda-lime glasses. This may suggest that the effect of water is to increase the diffusion coefficient of oxygen in silicate glasses. Measurements of the self-diffusion coefficient of oxygen in water containing glasses may clarify this point.

To conclude this section let us consider the structure of the NC_2S_3 glass and the possible ways that water could be incorporated into it. According to Stevels' formula (5.21) $y = 6 - \frac{200}{p}$, where y is the number of non-bridging oxygens and p the mole % of SiO_2. For NC_2S_3 y is 2 indicating a 'broken' network structure and 'non-bridging

oxygens'. However the specific heat C_v is close to the theoretical value (3R) in the transformation range suggesting an essentially three dimensional network structure. Some of the possible atomic configurations in the glass may be represented schematically as follows:

(5.12a)

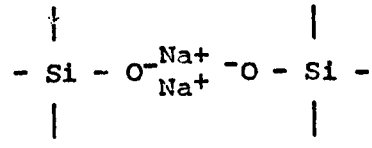

(5.12b)

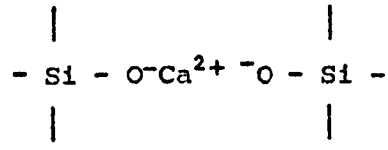

(5.12c)

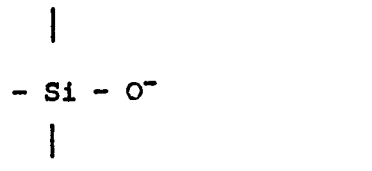

(5.12d)

The probability of the occurrence of the configuration (5.12d) alone (without any modifier cation near) may be low due to the high modifier content (50 mole%) in the glass.

It has long been known that water solubility ((5.22), (5.23)) in silicate and borate systems is proportional to the square root of the partial pressure of water in the atmosphere ($p_{H_2O}^{\frac{1}{2}}$). This indicates a reaction of water with high silica content glasses of the type:

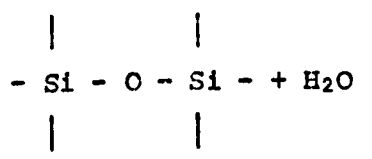

(5.13)

However in binary alkali silicate molten glasses (5.22) the solubility of water has a minimum at about 25 mole% alkali oxide, this value depending on both the temperature of measurement and the type of alkali present. This indicates the formation of hydrogen bonds according to

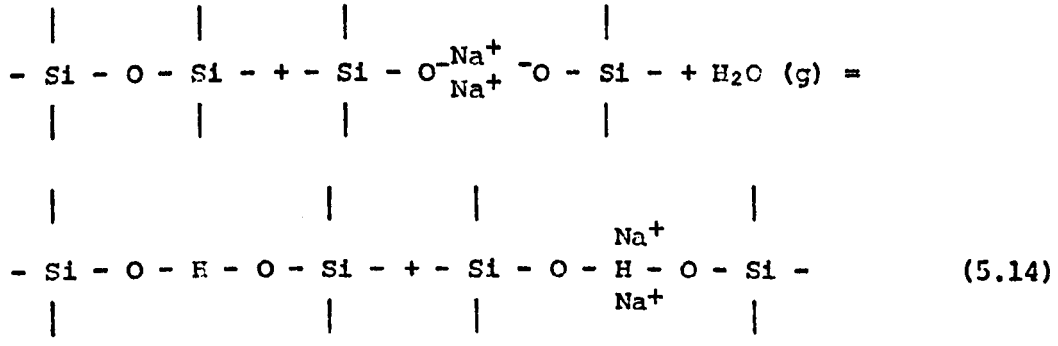

(5.14)

Thus the reaction of water with the NC_2S_3 glass structure is probably mainly represented by equations (5.13) and (5.14) plus, tentatively, a reaction of the kind

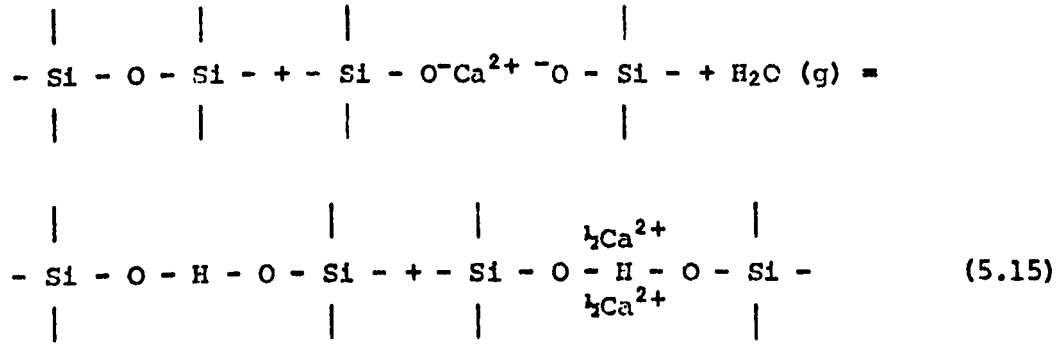

(5.15)

5.1.5 Effect of NaF content on nucleation

Let us first discuss how NaF may be incorporated into the glass structure. It is probable that NaF dissolves as Na^+ and F^- ions, these ions being accommodated in the structure in different ways (5.24). The Na^+ cation (radius 0.98 Å) probably acts as a network modifier,

disrupts the Si - O bonds and occupies 'holes' in the network. On the other hand the F^- ion may replace an O^{2-} ion due to their similar sizes. According to reference (5.25) the radii for F^- and O^{2-} are 1.33 and 1.32 Å respectively, assuming a coordination number of 6. According to reference (5.26) the values are 1.36 and 1.40 Å respectively.

For silicate glasses effects of NaF may be represented schematically as

$$\equiv Si - O - Si \equiv + NaF \rightarrow \equiv Si - ONa + \equiv Si - F$$

The F^- tends to replace oxygens and to "break up" the structure. This also causes a lowering of viscosity. Ravinovich (5.25) has discussed the incorporation of F^- into the network. He first considered a Si_2O_7 unit in the glass

$$\begin{array}{cccc} & O_4 & & O \\ O_3 & . Si_1 & O_1 & . Si_2 \; O \\ & O_2 & & O \end{array}$$

At high temperature there is an instant during the strong vibrations of the network atoms when O_1 is closer to Si_2 than to Si_1, thus Si_1 is shielded by O_2, O_3 and O_4 which have been polarized in such a way as to shield Si_1. Energetically the introduction of F^- as

$$\begin{array}{cccccc} & O_4 & & & O & \\ O_3 & . Si_1 & F^- & \ldots \; O & . Si_2 & O \\ & O_2 & & & O & \end{array}$$

is favoured because F^- can shield Si_1 better than O_1 (furthermore, the polarizations of O_2, O_3 and O_4 is reduced). This occurs at high temperature favouring the F^- inclusion in the structure and weakening it. The replacement of O_2, O_3 and O_4 for F^- is less probable because F^- has a

lower polarizability than O^{2-} (polarizability $\alpha_0:O^{2-} = 2.76 \times 10^{-24}$ cm^3, $\alpha_0:F^- = 0.96 \times 10^{-24}$ cm^3), so that SiF_4 is not likely to form. At low temperature (low vibrations) O^{2-} tends to shield Si_1 and Si_2 better than F^-, so that F^- leaves the silicate network and eventually combines with a modifier cation forming metallic fluorides.

On cooling to form a glass the F^- ion may remain in the same structural state as when in equilibrium at high temperature. If, however, the fluoride content is very high, even on very fast cooling the F^- ion may leave the silicate groups and precipitate as metallic fluorides. In conclusion, the introduction of NaF into the NC_2S_3 glass will tend to weaken the network structure due to the way Na^+ and F^- are incorporated.

The general effects of NaF content on nucleation have already been discussed in Chapter 4 (see Figure 4.9). In Figure 5.10 the W^*_i values for G2 and G5 are plotted against T using the measured viscosities for these glasses as explained previously. Tentative values of W^*_i are also given for G3 and G4 although the viscosities of these glasses were not measured directly. Viscosities of G3 and G4 were estimated from the data for G2 and G5 (Figure 4.17). The $\log_{10}\eta$ curves for G2 and G5 are almost parallel, and as a reasonable approximation the $\log_{10}\eta$ curves for 3 and 6 mole% NaF (G3 and G4) were linearly interpolated between the curves for G2 and G5 according to the following expression $\log_{10}\eta_{G1} = \log_{10}\eta_{G2} - 0.0823\ C$ where C is the concentration of NaF in mole% ($0 < C < 18$). The predicted $\log_{10}\eta$ values for G3 and G4 are consistent with the 'DTA Tg' values for these glasses (Table 4.7). The 'DTA Tg' was found previously to correspond approximately to a fixed η level

FIGURE 5.10 $\overset{*}{W}i$ vs. T(°C) FOR GLASSES G2, G3, G4 and G5

× G2, + G3, ● G4, ○ G5

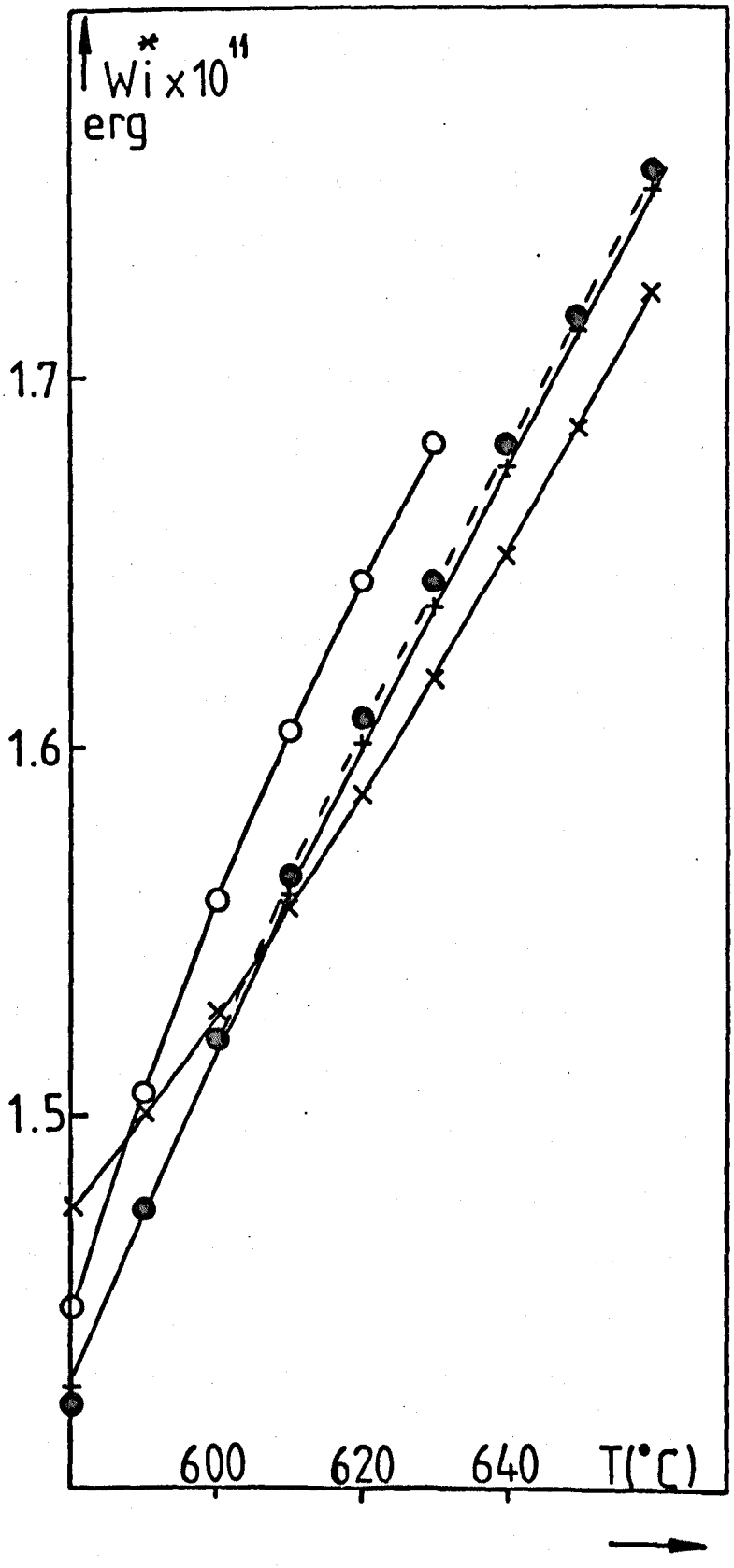

$\log_{10}\eta = 12.2$ (see section 3.1.4). It is likely that ΔG for G5 (18 mole% NaF) is significantly different from the ΔG for G2. On the other hand it may be assumed that the ΔG for G3, which nominally contained 3 mole% NaF, is close to that for G2. This assumption seems reasonable from both the DTA results (Table 4.7) and the closeness in the compositions of G3 and G2 (due to the high F^- losses mentioned in section section 4.2, G3 contained less than 3 mole% NaF). On the basis of these approximations σ for G3 can be estimated from the plot $\ln\left(\frac{I_{G3} \times \eta_{G3}}{T}\right)$ vs $\frac{1}{\Delta G^2 T}$. This is shown in Figure 5.11 together with the similar plot for G2. The σ value was 194 erg cm^{-2} which is larger than the value for G2. We may conclude that the effect of small additions of NaF on the nucleation of NC_2S_3 is reflected in a lowering in viscosity and an increase in σ. The increase in W* observed for larger additions of NaF (compare G5 and G2 in Figure 5.10) may be partly explained by an increase in σ but a decrease in ΔG may also be involved.

From a practical point of view addition of the 'nucleating agent NaF' is beneficial since it increases nucleation and lowers the temperature range where nucleation occurs. However we shall see later that NaF additions tend to decrease the chemical durability towards acids.

The effect of replacing oxygen ions by fluoride ions in the glass is shown by the results for G7 in Figure 4.9. This composition contained NaF but the sodium content was the same as in G2. No viscosity measurements were made for this glass. However, the increase in nucleation and the shift in the position of the maximum nucleation to lower temperature indicate that the effect of fluoride substitutions may be very similar to that of a straight addition of NaF.

FIGURE 5.11 Ln(Iη/T) vs. $1/\Delta G^2 T$ FOR GLASSES G2 and G3

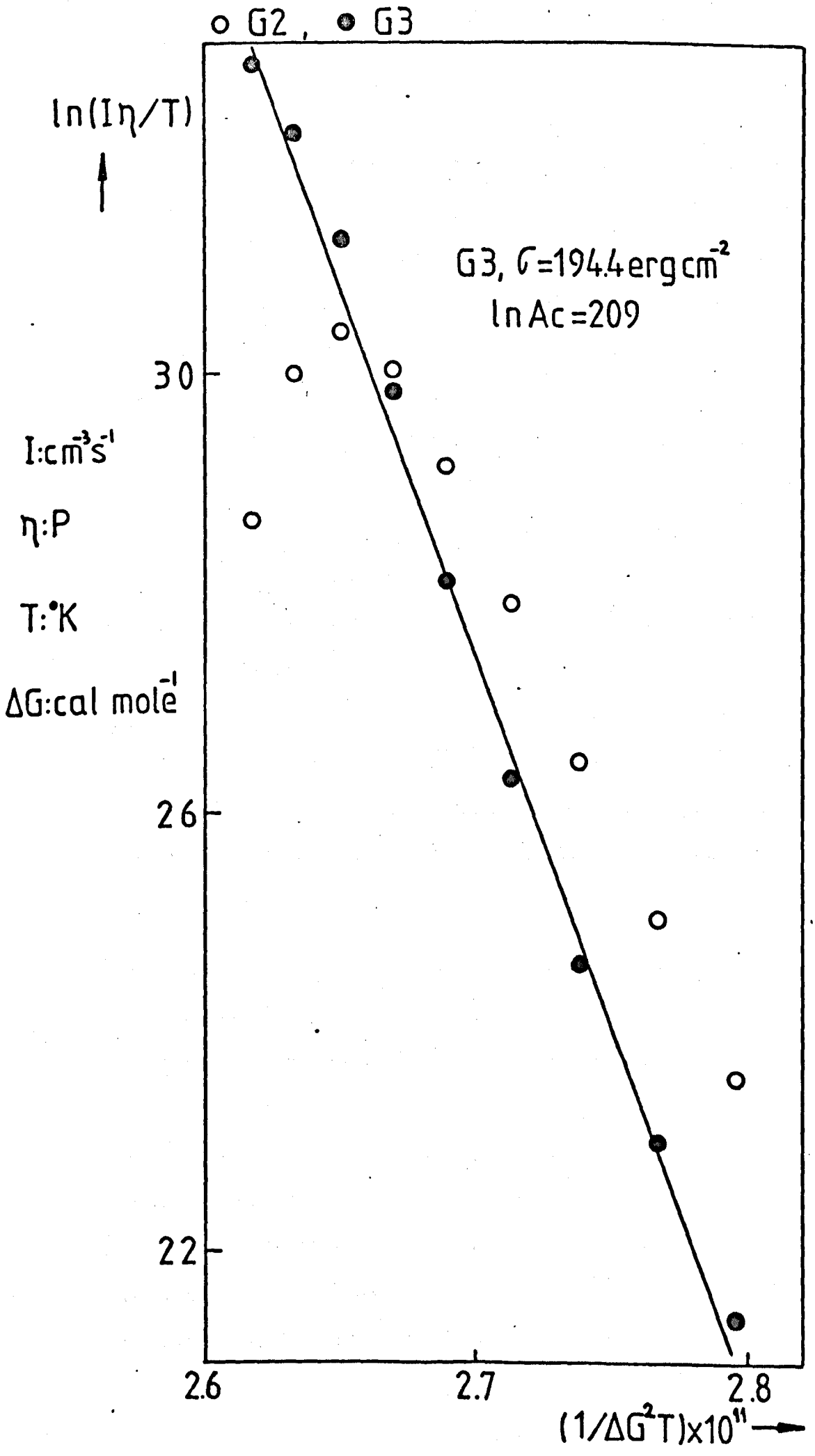

Glass G6 (55 mole% NaF) was melted to test the idea that if the NaF content was made large enough, the precipitation of NaF (and presumably CaF_2 in a soda-lime glass) might occur first and perhaps heterogeneously nucleate the main crystal phases. The temperature of the maximum in nucleation for G6 (Figure 4.9) was considerably lowered compared to G2 which is consistent with the lowering of viscosity. However the nucleation rates were also reduced. From the X-ray observations (see section 4.2.4) the NC_2S_3 phase precipitated first, and well before the NaF (and CaF_2) peaks could be detected. Furthermore the NaF (CaF_2) peaks appeared at the same time as the change in crystallization morphology occurred (Figure 4.13). Hence there was no evidence for heterogeneous nucleation of NC_2S_3 on metallic fluorides in this glass. A compositional analysis (with, for example, an electron microprobe) of the crystals at the initial stages and after the formation of the secondary growth (Figure 4.13) may help in the understanding of the crystallization process in G6.

5.1.6 Effect of ZrO_2, P_2O_5, TiO_2 and MoO_3 additions to the NC_2S_3 nucleation

The viscosity for G12 (3 mole% ZrO_2) was estimated by interpolating between the results for G2 and G13′ in the same manner as used for the NaF glasses. Assuming ΔG for G12 was identical to that for G2, σ was found to be 178 erg cm^{-2} from the plot in Figure 5.13. This value is very close to that for G2. It should be noted that the shape of the critical nucleus was taken as spherical, for comparison with G2. From Figure 5.12 it is clear that the V^* values for G12, G13′ and G2

FIGURE 5.12 $\overset{*}{W}i$ vs. T(°C) FOR G2, G12 and G13'

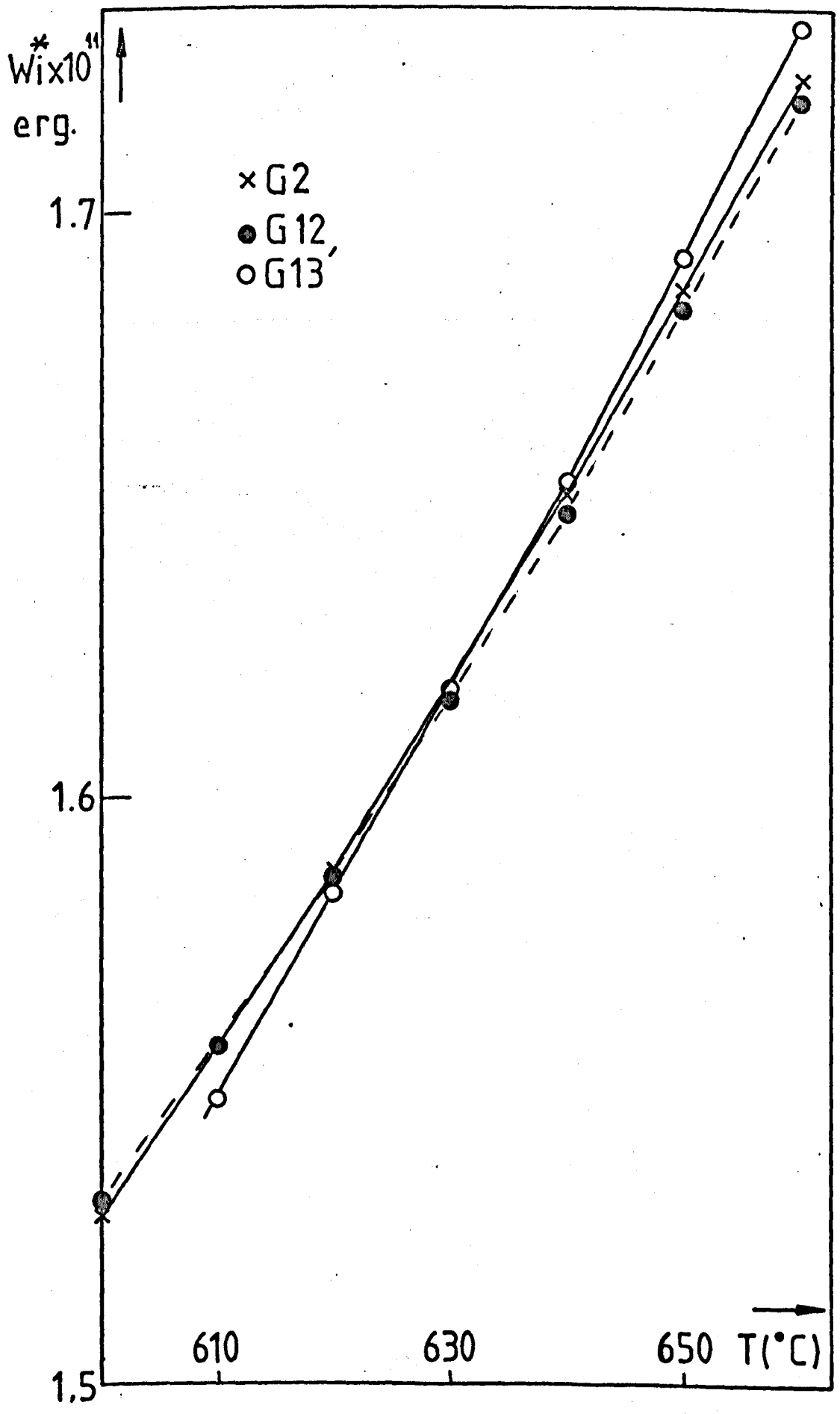

FIGURE 5.13 $Ln(I\eta/T)$ vs. $1/\Delta G^2 T$ FOR G2 and G12

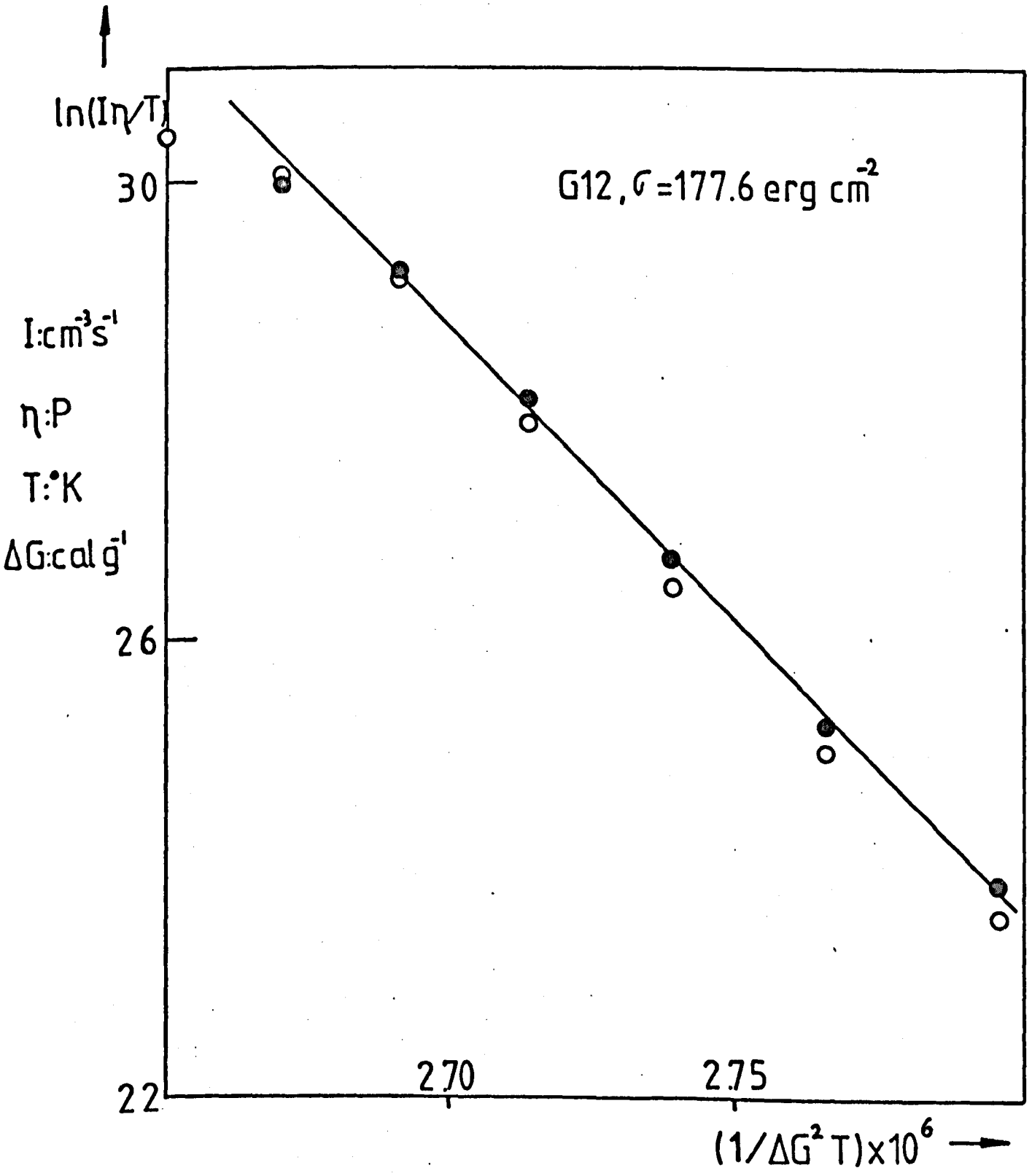

are close together. Also, at higher temperatures that the maximum in nucleation, G13′ has a lower nucleation rate than G2 by approximately 0.7 o.m. This corresponds fairly closely with the increase in η of G13′ relative to G2 (approximately 0.5 o.m.). It may be concluded that ZrO_2, rather than acting as a nucleating agent, is depressing nucleation by increasing η (and ΔG_D) and keeping σ approximately the same as for G2. However, as ZrO_2 addition also decreased the growth rates, this oxide could be useful practically as an additive to 'stabilise' the NC_2S_3 glass or the glasses containing water and fluoride. For all these glasses the production of large (5 cm x 5 cm x 10 cm) clear pieces was difficult owing to the high crystal growth rates and nucleation rates observed.

The phosphorous ion P^{5+} (5.24) can be accommodated into the silicate glass structure because it is normally tetrahedrically co-ordinated. However due to the higher positive charge the formation of one double bond per PO_4 unit is highly probable. According to McMillan (5.24) "the presence of this type of double-bonded oxygen within the silicate network creates conditions favouring separation of phosphate grouping from the silicate network". The effect of P_2O_5 on crystal nucleation in the present system was shown in Figure 4.25. The decrease in nucleation on adding P_2O_5 (glass G8) may be due to an increase in viscosity, an increase in σ or a decrease in ΔG or a combination of these possibilities. Unfortunately viscosity measurements were not carried out on G8.

Although only limited work has been carried out for glasses containing P_2O_5 the information obtained may have some practical interest.

Very recently considerable attention has been given to bio-glass ceramic materials. According to Hench (5.27) 'bio glass' considered as "a glass designed to elicit specific physiological responses" was designed to provide "surface reactive calcium and phosphate groups and an alkaline pH at an interface with bone, teeth and other hard tissues". A very useful glass had the following composition: 24.5 mole% Na_2O, 24.5 mole% CaO, 45 mole% SiO_2 and 6 mole% P_2O_5, which was very convenient (after crystallization) for segmental bone replacements. Another application was the coating of 316L surgical stainless steel (the thermal expansion coefficient of the bio glass closely matched the steel). Also it was found convenient to increase the viscous flow properties of the base glass by adding fluoride. The present work has shown that fluoride addition produces a considerable increase in nucleation as well as a reduction in viscosity. Now, it is possible that the effect of P_2O_5 in reducing nucleation of the NC_2S_3 phase might be utilised in making suitable bio-glass ceramics with high strength and fine microstructure in this area of the soda-lime-silica system. That is, as nucleation is increased with fluoride addition the glass should accept a larger quantity of P_2O_5 and still exhibit appreciable internal nucleation. Presumably the higher the P_2O_5 and CaO content (CaO content is already quite high for glasses near the NC_2S_3 composition) the better will be the bonding properties of these bio-glass ceramics.

TiO_2 and MoO_3 are similar to P_2O_5 in their effects on nucleation (Figures 4.25 and 4.28). Measurements of viscosity and growth rates may help in clarifying the role of TiO_2, MoO_3 and P_2O_5 additions in

the nucleation of the NC_2S_3 phase. It should be noted that 3 mole% addition of either P_2O_5 or MoO_3 produced a larger reduction in nucleation than 3 mole% addition of either ZrO_2 or TiO_2

5.1.7 Heterogeneous Nucleation

A number of investigations have contributed to the basic understanding of heterogeneous nucleation in glass forming systems. However let us first briefly consider the work of Rindone and Rhoads (5.28). When $PtCl_4.2HCl$ was added tp silicate melts the colours produced ranged from transparent grey to turbid grey. In phosphate glasses a low concentration of platinic chloride produced a grey colour whereas a higher concentration gave a yellow colour. Rindone and Rhoads concluded that in phosphate glasses Pt could exist in both atomic and ionic states. In the silicate glasses, the grey colour arose from precipitation of metallic Pt in a colloidal form. Rindone (5.29) has shown that Pt additions to a $Li_2O.4SiO_2$ glass considerably increased the crystallization rate of $Li_2O.2SiO_2$. In a later paper (5.30) Rindone found that the rate of crystallization was the highest for a Pt addition of 0.005 wt.%. However, Hench (5.31) in a similar investigation found that in order to reproduce Rindone's results it was necessary to add 100 times more Pt. Gutzow and Toschev (5.32) have shown that, for additions of 0.5 wt.%, the effectiveness of the catalysts Ir, Pt, Rh, Au and Ag in the crystallization of $NaPO_3$ and $Na_2B_4O_7$ glasses could be better explained in terms of the thermal expansion differences between the metals and the glasses rather than in terms of lattice mismatching. Maurer (5.33) found

that the precipitation of lithium metasilicate crystals on gold particles in a lithium potassium alumino silicate glass occurred only after the gold colloid size was of the order of 80 Å. He suggested that when the gold particles were less than 80 Å in size they were ineffective as heterogeneous nucleation sites since the high curvature of the particles would introduce strains in the lithium metasilicate crystal nuclei.

In this work Pt was added as $PtCl_4$ as explained in Chapter 2. The additions of 0.2 and 0.46 wt.% Pt for G24 and G25 respectively were chosen to produce reasonably large Pt centres and hence to minimize possible size effects in the heterogeneous nucleation process. The distribution of the maximum calliper diameter of the Pt particles in glass G25 (see Figure 4.38) ranged from 0.30 to 3.30 μm with an average diameter of 1.19 μm. Very occasionally 'large' (about 10 μm) Pt inclusions were observed on the optical cross sections. Such inclusions have also been observed in neodymium glasses melted in Pt crucibles (5.34). We were able to measure experimentally the average contact angle between the NC_2S_3 crystalline phase and the Pt particles precipitated in G25 heat treated at 596°C for 6 to 21 min. (Figure 4.38). The average contact angle, as defined in equation (1.9) was 90° ±10°. From equation (1.12) and the expression for $f(\theta)$ (see Chapter 1) the thermodynamic barrier for heterogeneous nucleation was found to be 0.50 times that for homogeneous nucleation.

The effect of $PtCl_4$ additions on nucleation in the base glass G2 was shown previously in Figures 4.32, 33, 34 and 35. It is clear from Figure 4.35 that the number of NC_2S_3 crystals present after 40 minutes was greater in G25 than in G2, particularly at higher tempera-

tures (> 630°C). This was due to the heterogeneous nucleation on Pt particles present in G25 in addition to the normal, homogeneous, nucleation which was also present, and would indicate a greater overall nucleation rate in G25 than in G2. However at temperatures lower than 620°C the situation was not as clear. For example, there was a 'cross over' for the nucleation curves for G25 and G2 (Figures 4.32 and 4.33). If the compositions for G25 and G2 were exactly the same and if Pt was effectively nucleating NC_2S_3 crystals (as clearly shown in the electron micrographs) the same increased nucleation observed at higher temperatures for all times (e.g. in Figure 4.34), would have been expected also at the lower temperatures for all times. The 'cross over' effect at lower temperatures strongly indicates that there were compositional differences between G2 and G25 (only G2 was chemically analysed). This explanation is further supported by the viscosity measurements. The viscosity for G25 was slightly greater than that for G2 at lower temperatures (< 600°C) whereas at higher temperatures there was little difference in the viscosities (Figure 4.37).

It is worth mentioning at this point that Firth et al. (5.35) found that in melting lead crystal glasses, to which KCl was added, considerable losses of alkali chlorides occurred. During melting fumes of KCl and HCl were evolved and the iron content was reduced by ferric chloride volatilization. It is possible that the chlorine produced by the $PtCl_4$ decomposition has enhanced Na and/or Ca volatilization giving a final glass slightly more viscous than the base glass G2. Naturally, this suggestion must be carefully checked by chemical analysis.

The nucleation results above 630°C were analysed as follows. From the average size 1.19 μm of the approximately spherical Pt particles, the nominal Pt content of G25, the density of metallic Pt and G2, the volumetric density M of Pt centres was estimated as 6.7 x 10^8 cm^{-3}. From the results in Figures 4.32 to 4.34 the difference between the number of crystals per unit volume for G25 and G2 was calculated for 20 and 40 min. for the three heat treatment temperatures. The mean value was 1.9 x 10^8 cm^{-3} which is of the same order (but less than) the number of Pt centres (M). This suggests that, for times up to 40 min., only a fraction of the Pt particles were acting as nucleation sites (i.e. they were not 'saturated').

Now from Figure 4.34 the intercept (t=0) for G25 was 2.25 x 10^5 mm^{-3}. Using the N_V/t (t=40 min) values shown in Figure 4.35, subtracting the N_V intercept (t=0) and dividing by 40 min., the steady state I_O values for G25 were obtained above 620°C. For G2 the intercept was 0.5 x 10^5 mm^{-3} at 621 and 641°C. Using the same procedure the I_O values for G2 were also obtained and are plotted in Figure 5.14. These results indicate that the steady state nucleation for G25 is higher than for G2. We will now apply heterogeneous nucleation theory. The steady state I_O values for G2 were subtracted from those for G25. Following a similar procedure to that for the homogeneous case (section 5.1) an expression for ${}^{v}I^{f}$, the total heterogeneous nucleation rate per unit volume of liquid (see equation (1.15)) can be obtained as follows:

$$\frac{{}^{v}I^{f} \times \eta}{T} = A_c{}^{f} \exp\left[- f(\theta) \frac{16}{3} \pi \frac{\sigma^3 v_m^2}{k\Delta G^2 T}\right] \qquad (5.16)$$

where $A_c{}^{f} = M \frac{n^f k}{3\pi\lambda^3}$

FIGURE 5.14 I_o VALUES AS A FUNCTION OF T(°C)
FOR G2(○) AND G25(●)

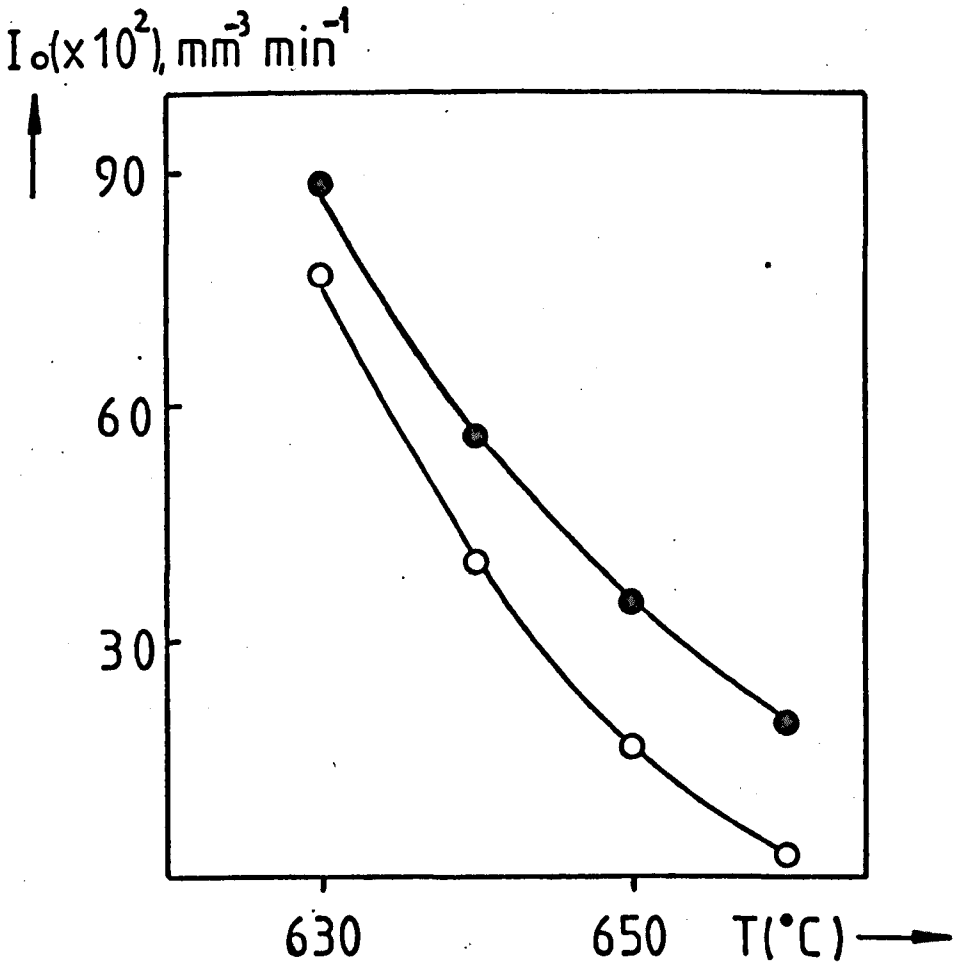

Thus from a plot of $\ln\left(\frac{v_I f \eta}{T}\right)$ vs $\frac{1}{\Delta G^2 T}$ it should be possible to obtain $f(\theta)\ \frac{16}{3}\frac{\pi\sigma^3 v_m^2}{k}$. Such a plot is given in Figure 5.15 using the values in Table 5.1. The ΔG for G2 was used in the calculation and the measured

TABLE 5.1 $v_I f$ DATA FOR G25 - ΔG IS SUCH AS $[\Delta G]$ IS IN cal mole^{-1}

T (°C)	T (°K)	$v_I f = I_{Pt} - I_{G2}$	ln I	ln I	$\ln\left(\frac{I\times\eta}{T}\right)$	$\frac{1}{\Delta G^2 \times T} \times 10^{11}$
630	903	1166.9	7.062	22.82	23.072	2.1604
640	913	1599.1	7.376	21.87	22.433	2.180
650	923	1861.1	7.529	20.99	21.690	2.202
660	933	1662.0	7.416	20.15	20.732	2.226

viscosities for G25. From the slope of the plot and the σ and V_m for G2 (section 5.2) $f(\theta)$ was found to be 0.60. This is in remarkably good agreement with the $f(\theta)$ value calculated from the θ measured on the electron micrographs. However this result must be regarded as tentative. Thus, it would be interesting to obtain further nucleation data for glasses G2 and G25, particularly at higher temperatures for a series of times at each temperature, in order to confirm the above determination of heterogeneous nucleation rates. Also chemical analysis of G25 might help to understand some of the observations at lower temperatures.

In the theory discussed previously nucleation on a flat substrate was assumed. The Pt particles, however, had both flat and curved surfaces. Fletcher (5.36) has solved exactly the case of heterogeneous nucleation on a spherical surface of radius R. The thermodynamic barrier W_f^* was given by

FIGURE 5.15 $Ln(^{v}I^{f}\eta/T)$ vs. $1/\Delta G^{2}T$ FOR GLASS G25

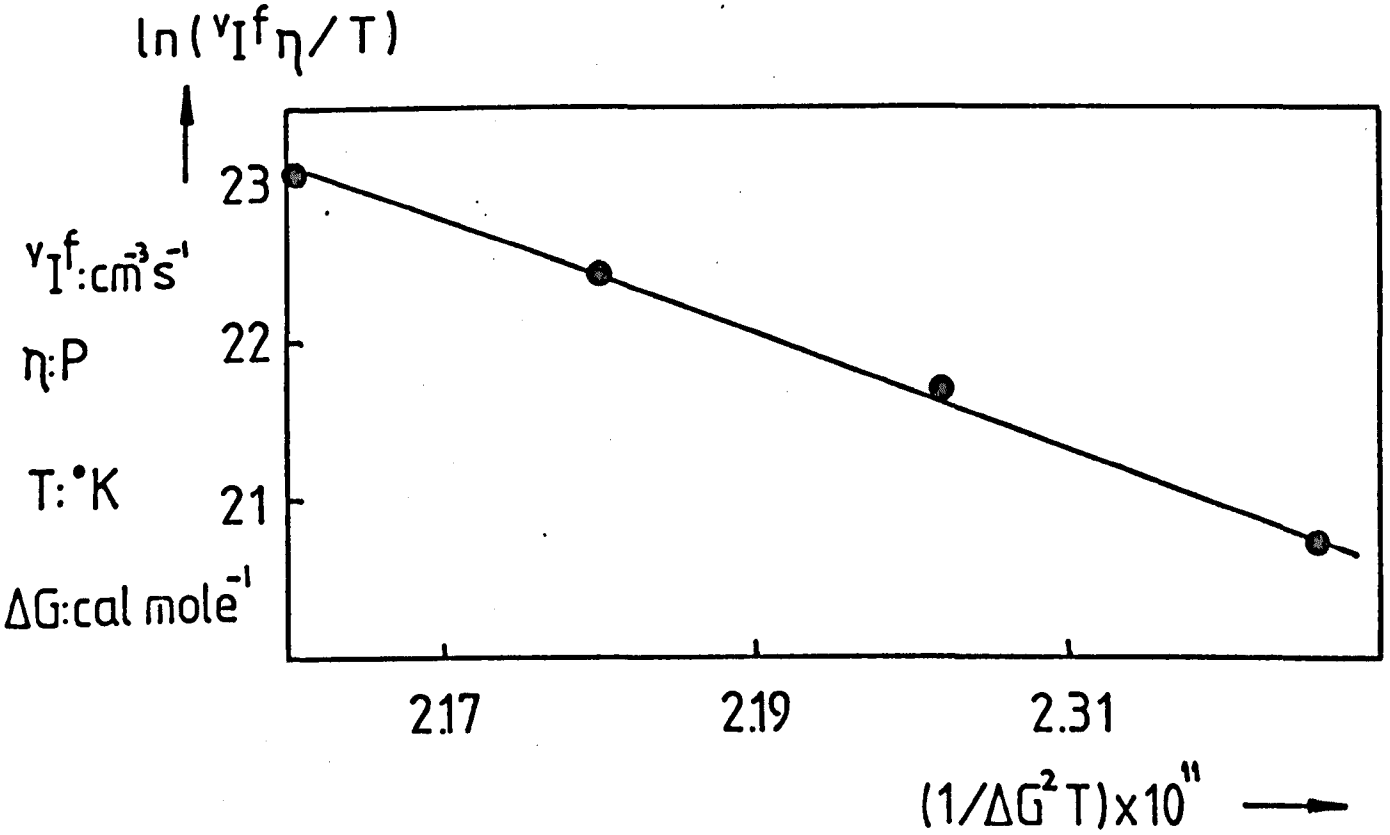

$$W_f^* = \frac{16}{3}\frac{\pi\sigma^3}{\Delta G^2} V_m^2 \frac{f(m,x)}{2}$$

where $f(m,x)$ is a complex function of $m(= \cos\theta)$ and $x(= R/r^*)$. Here r^* is the critical radius for homogeneous nucleation. In our case $m \cong 0$ and $x \sim 10^3$ and the factor $\frac{f(m,x)}{2}$ is very little different from the $f(\theta)$ factor for a flat substrate, and the assumption of a flat substrate is justified.

The fact that the NC_2S_3 crystals grow preferentially on the more curved surfaces of the Pt particles might be related to a crystallographic orientation relationship between the NC_2S_3 and the Pt during growth. Thus the flat surfaces could belong to specific crystallographic planes and the 'lattice mismatch' with the NC_2S_3 might be greater than on the curved surfaces. This point is difficult to check since the positions of the 'formula units' inside the unit cell of the NC_2S_3 phase are not known. Other effects such as differences in thermal expansion (mentioned above) are again difficult to estimate since there is no information on the thermal expansion for different crystal directions of the NC_2S_3 phase. The problem may be even more complex since small levels of silicon and calcium were detected inside the Pt particles. It is possible that different levels of these impurities may exist near the curved surfaces than near the flat surfaces thereby altering the chemical interaction between the NC_2S_3 crystals and the platinum.

5.2.1 Growth rates for G2 and G16

The steady state growth rates for G2 and G16 were shown in Figures 3.5 and 3.21 respectively. A plot $\frac{um}{1 - \exp(-\frac{\Delta G}{RT})}$ vs T (°C) for G2

is shown in Figure 5.16. This plot would be an horizontal straight line if the normal growth model applied (see section 1.3). The ordinate changes to 1.2 orders of magnitude for temperatures between 610 and 710°C which is too large to be explained in terms of systematic errors in either the growth rates or viscosity measurements. This observation may suggest that the active site fraction f (see equation (1.35)) is a function of temperature. An attempt was made to fit the function $\frac{u\eta}{1 - \exp(-\frac{\Delta G}{RT})}$ to the screw dislocation and surface nucleation growth models. No satisfactory fit could be obtained over the whole temperature range for either model. However a fit could be obtained to the surface nucleation model (see equation (1.39)) for high temperatures only, provided the edge interfacial free energy per unit area γ was about 300 erg cm^{-2} (taking a_0 as 10^{-7} cm) which appears a very reasonable value. Thus none of the three models are completely satisfactory in describing the growth rates, although the surface nucleation model is perhaps the best of the three. The real growth mechanism is probably more complex than any of the models.

It must be remembered that all these models depend on the validity of the Stokes-Einstein relationship. Meiling and Uhlmann (5.37) and Ainslie et al. (5.38) have pointed out that the diffusion coefficient for transport in the bulk liquid may exceed that calculated from the Stokes-Einstein relation by a factor of 10 or 100.

The intercepts with the time axis of the linear plots of the maximum crystal size vs time for G16 and G2 (Figures 3.19, 23 and 24) are difficult to explain. However, it may be significant that these "growth" intercepts for G16 are similar in magnitude to the intercept

FIGURE 5.16 Reduced growth rate as a function of temperature for glass G2

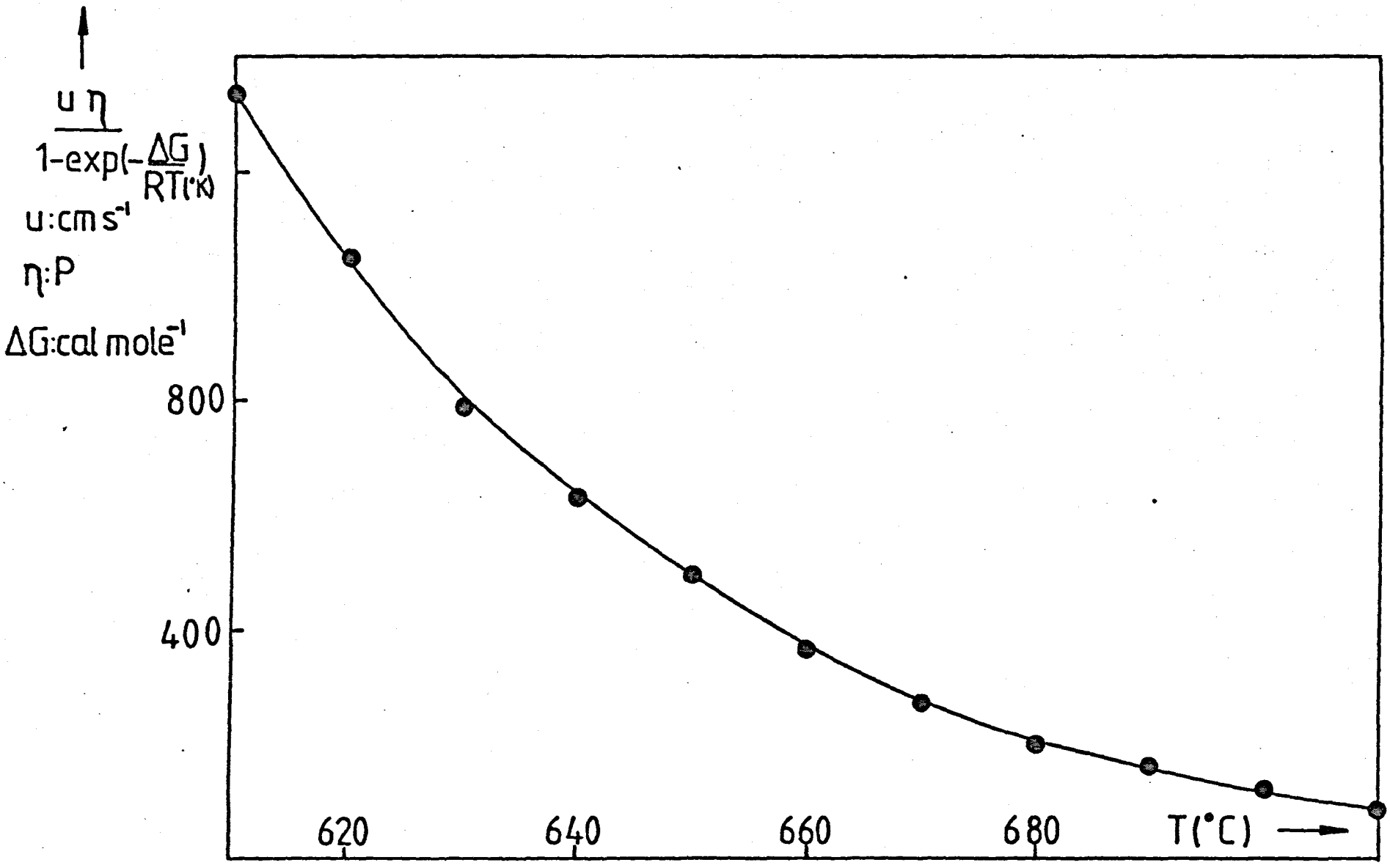

times on the nucleation (N_V vs time) plots, which suggests that they may be related to the nucleation incubation times. According to Filipovich and Kalinina (5.39) the growth intercept with the time axis can be taken as "the moment of nucleation of the first spherulites". Gutzow et al. (5.40) estimated this time as $\tau_1 \simeq \frac{1}{I_o} + \frac{\pi^2}{6}\tau$ where I_o and τ are calculated from the linear part of the N_V vs time curves as explained in Chapter 1.

Another possibility which must be considered is that the growth intercept times arise from variations in the crystal growth rates themselves with time, particularly for the early stages of growth. According to Schaeffer and Glicksman (5.41) "when considering the growth of a spherical crystal immediately following a nucleation event in a highly supercooled liquid the effects of interface curvature, kinetics and time dependent heat flow are all important". They computed theoretical curves of growth rate versus the dimensionless "time" parameter τ_o for various values of the parameters $\Delta\psi$ and ξ. τ_0 was defined as $4\alpha t/r^{*2}$ where α was the thermal diffusivity ($cm^2\ s^{-1}$), r^* the radius of the critical nucleus and t the time. The dimensionless supercooling $\Delta\psi$ was defined as $C\Delta T/\beta$ where C and β were the specific heat of the supercooled liquid and the latent heat of fusion per unit volume respectively. ξ was given by $\sigma\gamma_0 Tm/2\alpha\beta$ where σ was the interfacial energy per unit area, γ_0 a 'kinetic coefficient' ($cm\ s^{-1}\ °C^{-1}$) and Tm the melting temperature (°C). In our case a supercooling of 500°C produced a $\Delta\psi$ value of 3.4. Although in glassy systems γ_0 is a strong function of T we estimated γ_0 as about 3.4×10^{-9} $cm\ s^{-1}\ °C^{-1}$ using the growth data at 606.5 and 620°C for G16. Also ξ (using $\sigma = 150$ erg cm^{-2}) was 5×10^{-12}.

Schaeffer and Glicksman do not give growth rate vs time curves for these values of $\Delta\psi$ and ξ. However from their curve for $\Delta\psi = 1.5$ for very small ξ τ_0 is about 10^3. Taking α as 10^{-2} cm^2 s^{-1} and r* as 15 Å t was estimated as 5.6×10^{-10} s. Consequently, according to the analysis of Schaeffer and Glicksman, after the critical size has been reached the time intercept on the growth plots is negligible.

The effect of the increase in temperature at the crystal-liquid interface due to the latent heat evolved during crystal growth was analysed by Hopper and Uhlmann (5.42) for a sodium disilicate glass where the crystal size vs time plots were linear. After a theoretical analysis for a plane interface they concluded that for small samples (4 mm) the interface heating (estimated as 0.25°C above the furnace temperature) can be ignored.

Finally, let us consider the possible effects of time lags in the two dimensional (2D) nucleation model for growth. Gutzow et al. (5.43) studied the crystallization process in a $NaPO_3$ glass where appreciable time intercepts in both the crystal size vs time plots and in the N_V vs time plots were found. They were able to calculate an average incubation time from a combination of the incubation times for both internal and surface nucleation which was proportional to

$$\frac{\sigma}{\Delta G_v^{\,2}} \frac{T^3\eta}{\exp(-\frac{3K_2}{T\Delta T})}$$

where K_2 is a constant obtained from analysis of the growth rates according to the 2D nucleation model. Gutzow et al. claim that their experimental data are described by this relationship, but only tested the theory for four intercept values. In a later paper Gutzow and

Toschev (5.44) showed that an incubation time in surface nucleation would only reduce the growth rate and that the growth rates would not be dependent on time. Their analysis assumed that the propagation of monolayers was very rapid so that every nucleus formed on a fresh surface without steps (small crystal model). They concluded that "non steady effects should be invariably expected at high undercoolings and especially in the vicinity of the temperature of glass transition Tg". However recently Calvert and Uhlmann (5.45) have disagreed with these conclusions. First, they suggested that the "large crystal model", should have been applied. In this model the crystal is assumed to be sufficiently large that the time between nucleation events is much smaller than the time for the nucleating layer to spread across the interface. Secondly using this model they showed that the "transients can almost always be ignored in treating crystal growth from the melt".

We conclude tentatively that the origin of the intercepts in the size vs time plots is strongly related to the incubation time in the three dimensional nucleation and is probably not related to the mechism of crystal growth. It is clear, however, that further work is needed to confirm this conclusion. Finally, it is interesting to note that intercepts with the time axis in crystal size vs time plots have also been observed in metallic systems. Hull et al. (5.46) studied the rates of nucleation and growth of pearlite in austenitic commercial steels where appreciable intercepts for both nucleation and linear growth with the time axis were found (although these intercepts were much shorter than in glass systems). They also concluded that

the intercepts in the crystal size plots might be related to the transients in internal nucleation.

5.2.2 Growth rates for glasses with H_2O, NaF and ZrO_2 additions

Plots of $\log_{10}u$ vs $\frac{1}{T(^\circ K)}$ for G2 and G14 are shown in Figure 5.17. The increase in growth rates for G14 (bubbled with steam) ranges from 0.4 of an order of magnitude (o.m.) at 680°C to 0.7 o.m. at 620°C. On the other hand the viscosity of G14 at 620°C is about 0.4 o.m. lower than that for G2. Hence the changes in growth rates closely match the changes in viscosity, within experimental errors. This is the expected behaviour if the diffusion coefficient for growth is proportional to the reciprocal of the viscosity. In section 5.1 a similar relationship between the diffusion coefficient for nucleation and viscosity was assumed. These relationships, if correct, imply that the diffusion coefficients for growth and nucleation are the same, which appears reasonable in single component systems. It should be noticed that these plots for G2 and G14 exhibited slight curvature. The curvature for G2 cannot be explained by a variation in the factor $1 - \exp(-\frac{|\Delta G|}{RT})$ since this factor only ranges from 0.984 at 610°C to 0.968 at 700°C. It has already been explained that the results for G2 are not described satisfactorily by any of the growth models. However the slopes of the plots, which should be proportional to the activation enthalpies $\Delta H'_D$ according to the normal growth model, were very close for G2 and G14 at low temperatures (giving apparent $\Delta H'_D$ values of 108 and 107 kcal mole^{-1} for G2 and G14 respectively). At temperatures

FIGURE 5.17 $\log_{10}u$ as a function of $1/T(^{\circ}K)$ for glasses G 2 and G14 (○) (●)

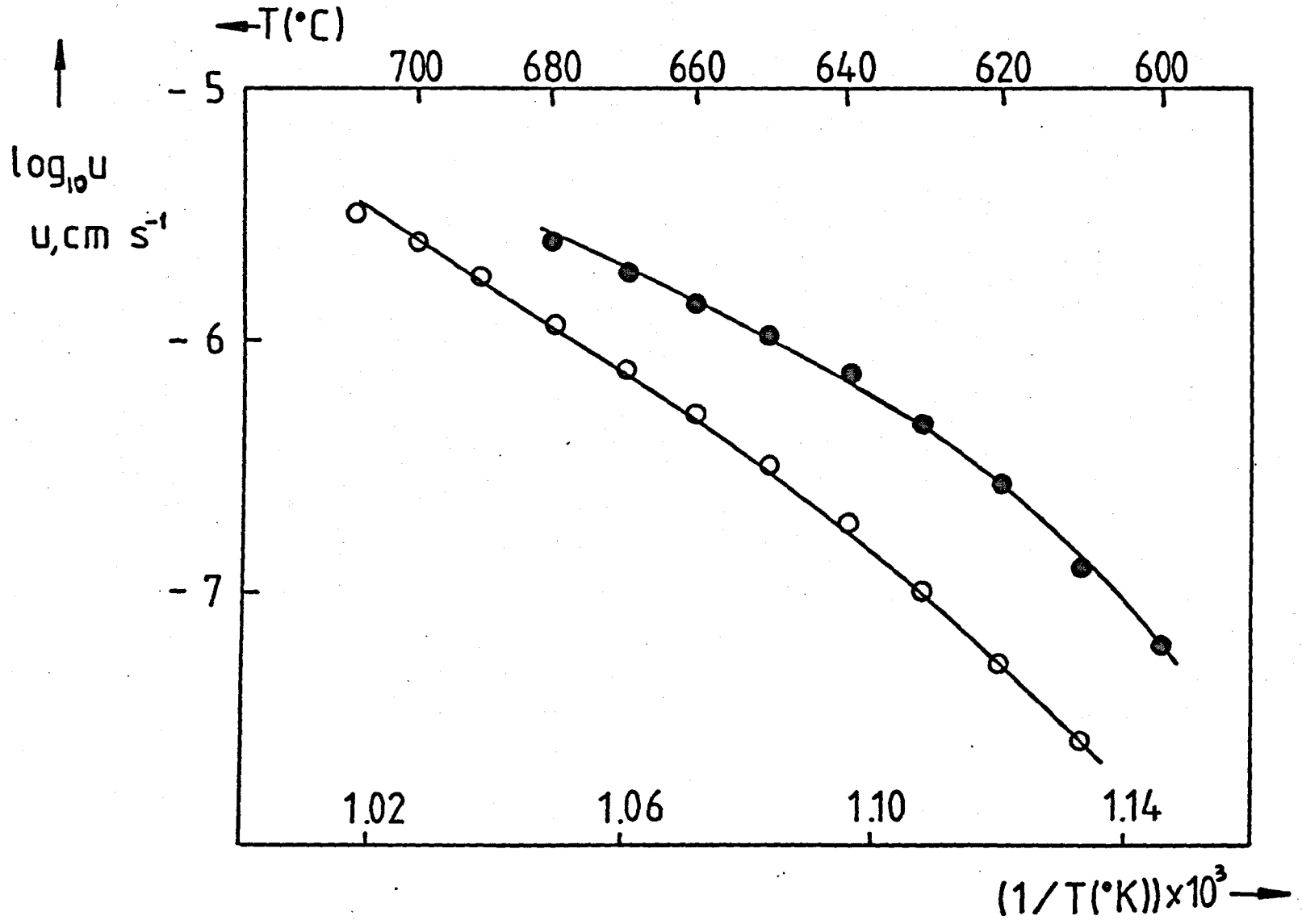

higher than 630°C the corresponding values were 72 and 60 kcal mole^{-1}. Hence, although the slopes vary with temperature there is no appreciable difference between them in the same temperature range.

The $\log_{10}u$ vs $1/T(^{\circ}K)$ plots for the lithia silica glasses L1 and L3, which are shown in Figure 5.18, are parallel straight lines. From the slopes $\Delta H'_D$ was 74 kcal mole^{-1} for both L1 and L3. The growth rates for L3 were 0.3 o.m. greater than for L1. The difference in growth rates corresponds closely with the difference in viscosities. For example, at 520°C the viscosity of L3 was 0.4 o.m. less than for L1. Hence, it may be concluded that water additions to soda-lime-silica glasses and lithia-silica glasses <u>increase</u> the crystal growth rates by decreasing the <u>kinetic</u> barriers to growth ($\Delta G'_D$).

The $\log_{10}u$ vs $1/T(^{\circ}K)$ plots for the fluoride glasses G3, G4 and G5 and for glass G13' (containing 6 mole% ZrO_2) are shown in Figure 5.19. The growth rate for G5 was 1.2 o.m. higher than that for G2 at 640°C. This change closely matches the decrease in viscosity of G5 relative to G2 (1.3 o.m. at 640°C as shown in Figure 4.17). It is interesting to note that in contrast to G2 and G13' the plots for the fluoride glasses exhibit no detectable curvature. There was also a gradual change in the slopes of the linear plots for the fluoride glasses. Thus $\Delta H'_D$ was 69.4, 65.8 and 49.3 kcal mole^{-1} for G3 (3 mole% NaF addition), G4 (6 mole% NaF) and G5 (18 mole% NaF) respectively. Although ΔG is not known for these fluoride glasses it is probable that at the higher undercoolings involved any changes in $1 - \exp(-\frac{|\Delta G|}{RT})$ are negligible. We conclude that the effect of NaF additions on growth, can be explained in terms of a reduction in the

FIGURE 5.18 $Log_{10}u$ as a function of 1/T (°K) for glasses L1 and L3 (o) (●)

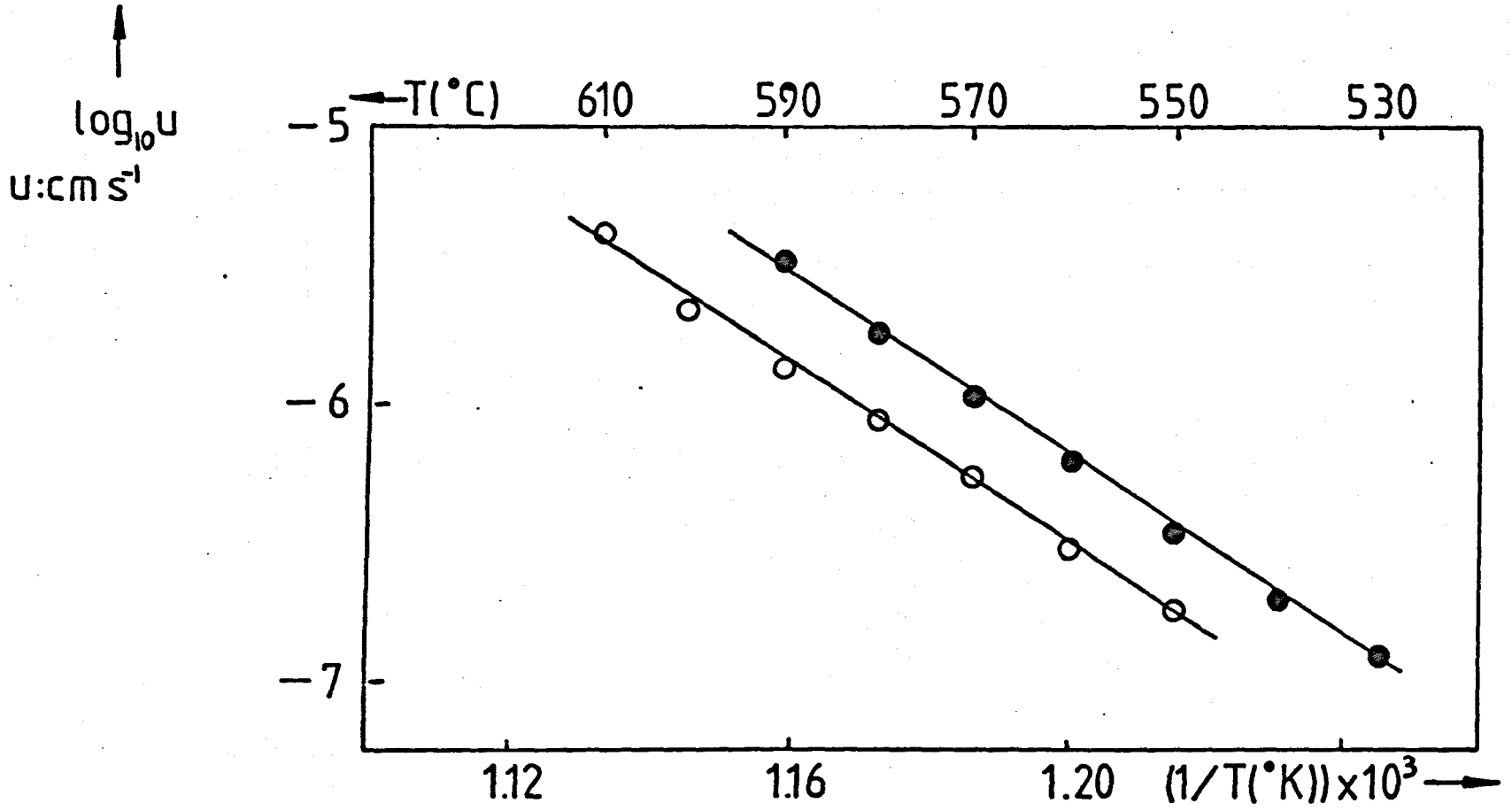

FIGURE 5.19 $Log_{10}u$ as a function of 1/T(°K) for glasses G2, G3, G4, G5 and G13'
(+) (×) (●) (○) (∘)

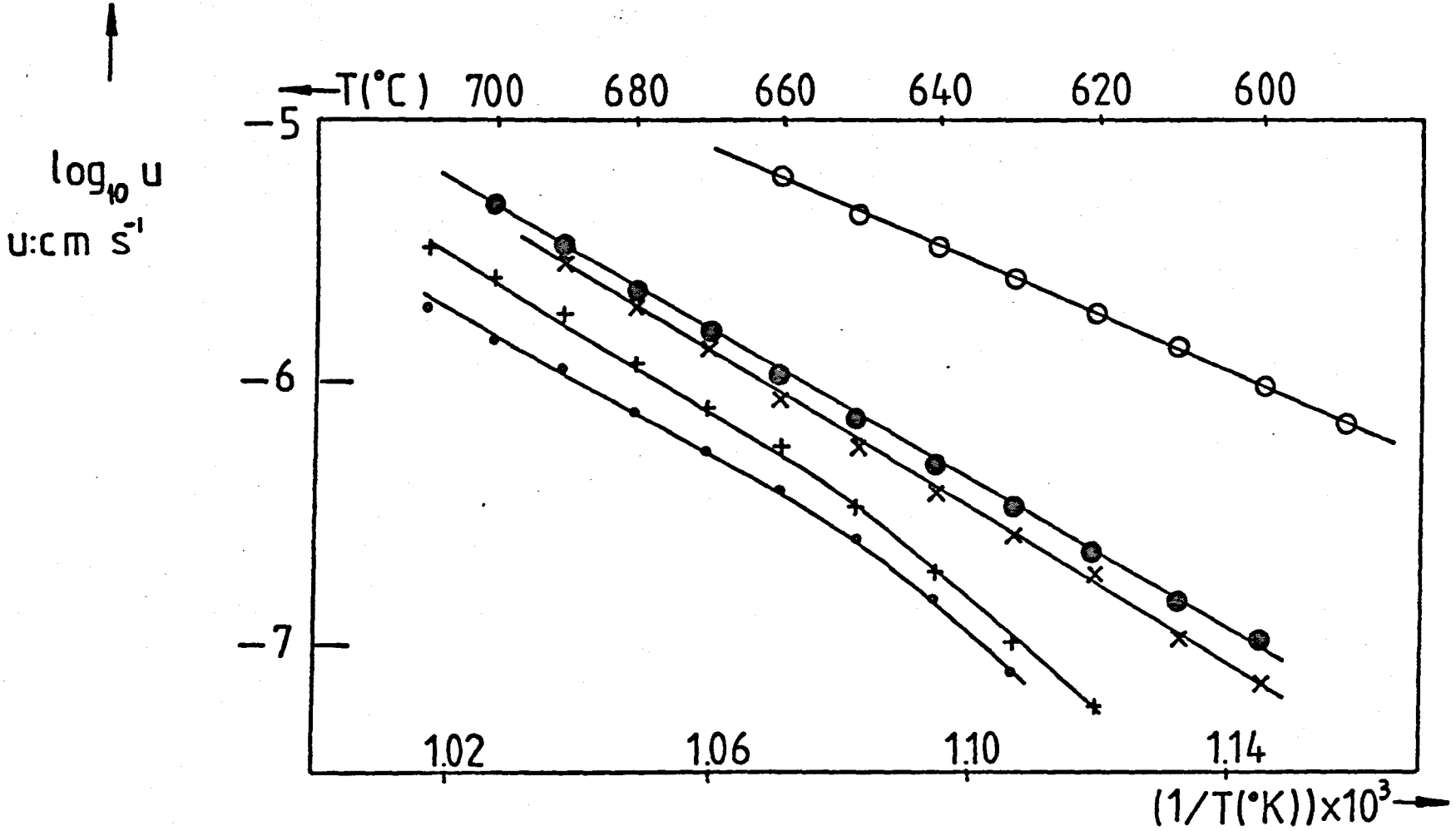

kinetic barrier to growth (i.e. $\Delta G'_D$) and also by a decrease in the activation enthalpy $\Delta H'_D$. This resembles the effect of H_2O additions, as discussed above.

For addition of ZrO_2 (Figure 5.19) the decrease in u relative to G2 (0.2 o.m.) is slightly smaller than the measured increase in η relative to G2 (0.4 o.m. at 620°C). The activation enthalpy is approximately the same as that for G2. Hence ZrO_2 addition appears to cause an increase in the kinetic barrier to growth ($\Delta G'_D$).

5.3 Properties of some glass ceramics in the N-C-S system

In this section some physical and chemical properties of the NC_2S_3 glass ceramics will be presented and briefly discussed. A limited investigation of the crystallization of compositions other than NC_2S_3 is also reported.

Large pieces of glass could be cast in special moulds without perceptible surface crystallization. For example, cylinders 2 cm in diameter and 5 cm long could be easily cast even for the glasses containing fluoride with quite high crystal growth rates. Annealed glass cylinders could then be converted to glass ceramics of nearly 100% crystallinity by a standard two stage heat treatment. As an example, cylinders of the G27 glass (NC_2S_3 + 1.12 wt.% Al_2O_3) and the corresponding glass ceramic are shown in Figure 5.20. The glass ceramic was obtained by heating the glass at 15°C min^{-1} from room temperature to the nucleation temperature (T_N = 610°C), maintained at T_N for 20.5 h, then heated at 5°C min^{-1} to the growth temperature (T_G = 736°C), held at T_G for 0.5 h and finally cooled to room temperature at 4°C min^{-1}.

Figure 5.20a,b (left)

Glass ceramic (top) and glass G27 (bottom). See text

Figure 5.21 (right)

Semi-transparent glass ceramics. (See text).

Figure 5.22 (left)

Transmission electron micrograph (TEM) of thin foil of glass ceramic A in Figure 5.21. Mag X24,800.

Figure 5.23 (middle)

TEM of sample D in Figure 5.21. Mag X20,500.

Figure 5.24 (right)

TEM of sample B in Table 5.2. Mag X 24,650.

Figures 5.25a,b (left and middle)

Stereoscan micrographs of fracture surfaces of glass B in Table 5.2. Mag X1,000. Left: non acid etched : Middle: acid etched.

Figure 5.27 (right)

TEM of ceramic used in thermal expansion measurements (heat treatment as explained in Figure 5.26). Mag X18,850.

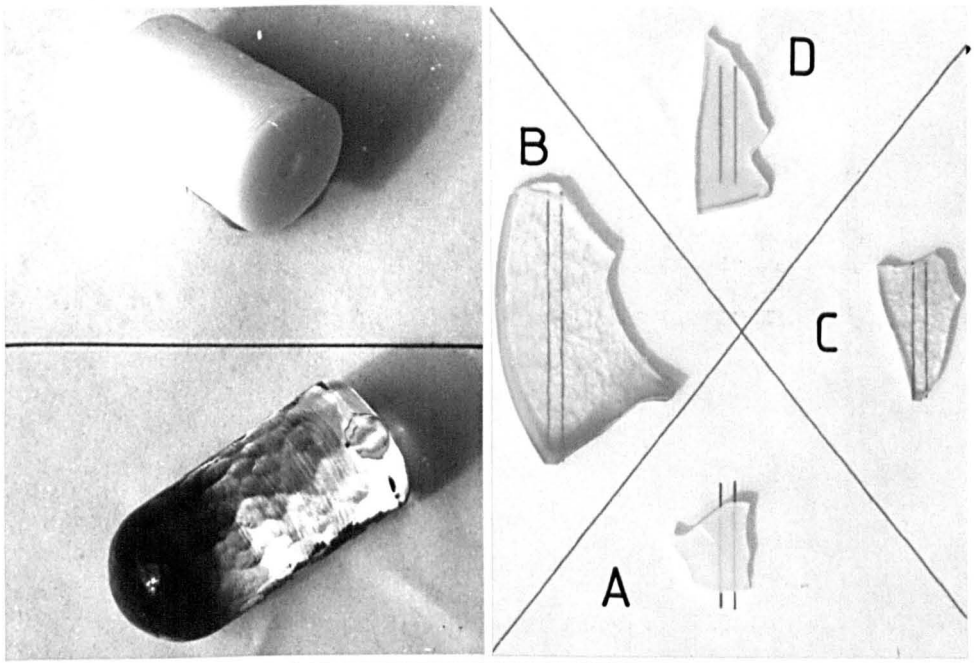
B
D
C
A

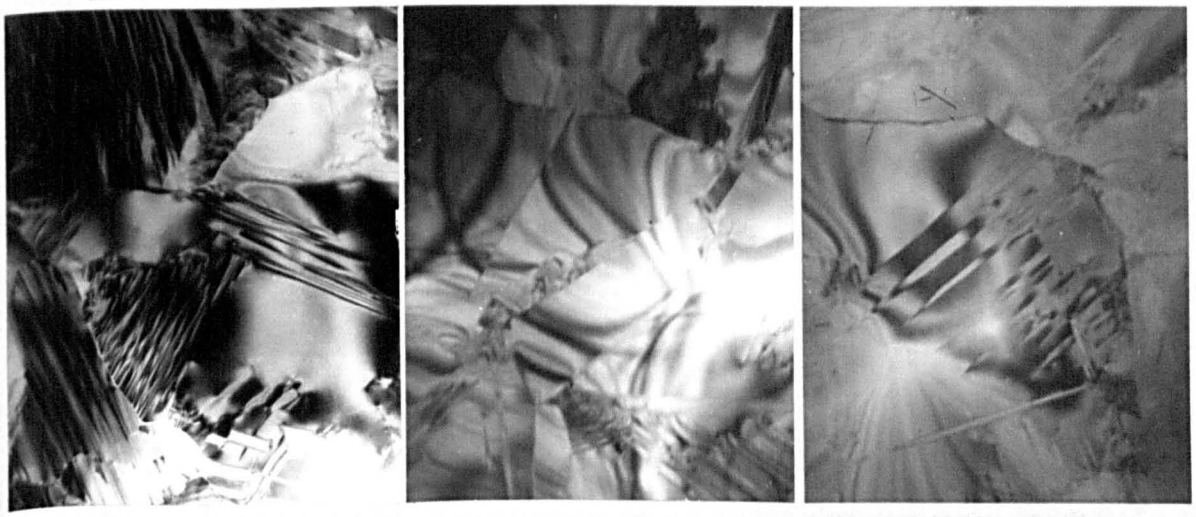

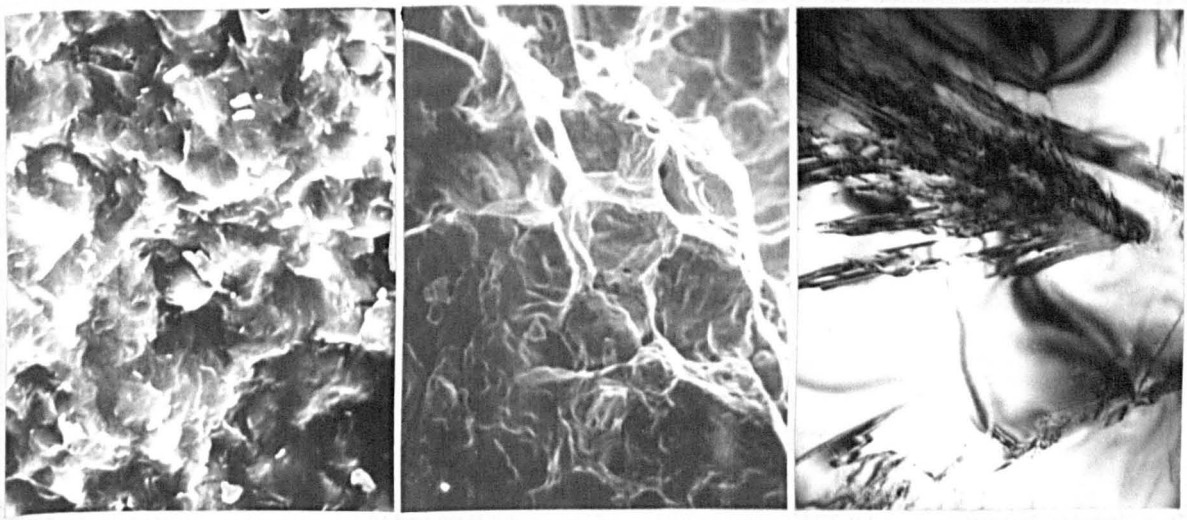

The densities of the glass and glass ceramic were 2.750 and 2.804 g cm^{-3} respectively.

For nucleation temperatures lower than 600°C it was possible to obtain fully crystalline semi-transparent bodies (Figure 5.21). Specimen A was obtained by heating glass G2 for 60 hr at 580°C followed by 3 hr at 660°C. A transmission electron micrograph from this specimen is shown in Figure 5.22. The crystal size was about 1 μm. The remaining specimens in Figure 5.21, which correspond to G17 heated for 66 h at 580°C followed by 20 min at 730°C, showed greater transparency. Specimens B and C were unpolished plates (2 mm in thickness) from different regions of the original heat treated sample. Specimen D was a polished plate which had been further heat treated for 49.5 h at 730°C. This showed that extended heat treatment at high temperatures produced negligible effect on the apparent transparency. An electron micrograph of this specimen is shown in Figure 5.23. Quantitative X-ray analysis showed that all of these specimens were nearly 100% crystalline. Although the transparency was not investigated in detail, its origin may be related to the close refractive indices for the glass (1.584, see ref.(5.7) and crystal ($1.596 \leq n \leq 1.599$, see ref.(5.47)) and the relatively small crystal sizes achieved.

5.3.1 Mechanical Properties

Breaking strength (σ_{max}) and Young's modulus (E) measurements were carried out on glass G17 after various heat treatments. The results are summarised in Table 5.2 with the heat treatments used and a t test analysis. (N refers to nucleation and G refers to growth). The σ_{max}

TABLE 5.2 RESULTS FOR MODULUS OF RUPTURE AND YOUNG'S MODULUS

Glass Code	Heat Treatment	σ_f (MN m^{-2})	E(10^4 MN m^{-2})	t test
A		72.2 ±9.5	1.1 ±0.1	t_{BC} = 1.123 Not Significant
B	T_N = 621°C, t_N = 6 h 30 min T_G = 720°C, t_G = 25 min	100.7 ±21.2	1.8 ±0.2	t_{BD} = 4.105 Significant
C	T_N = 624°C, t_N = 5 h 50 min t_N = 720°C, t_N = 30 min	88.2 ±14.4	1.7 ±0.1	t_{CD} = 3.177 Significant
D	T_N = 664°C, t_N = 4 h 23 min t_N = 721°C, t_G = 33 min	66.5 ± 8.3	1.1 ±0.2	t_{BA} = 2.418 Doubtful

TABLE 5.3 THERMAL EXPANSION FOR GLASS AND GLASS CERAMIC G17.

Glass	Heat Treatment	Temperature Range (°C)	Thermal Expansion x 10^{-7} $°C^{-1}$
G17	annealed	200-500	143.0
G17	"	200-600	153.1
G17	T_N = 627°C, t_N = 2 h T_G = 722°C, t_G = 30 min	200-400	122.0
G17	"	200-500	166.3
G17	"	500-800	113.4

value for the untreated glass (A) is approximate since only four samples were broken (for the glass ceramics on average 8 specimens were used). The glass ceramics B, C, D were all nearly 100% crystalline from X-ray analysis. For B and D the difference in σ_{max} was significant, indicating that crystal size may influence the strength. An electron micrograph of B is shown in Figure 5.24 where the size of the crystals is approximately 5 μm. Also D may be expected to have a larger crystal size since the nucleation rate at 664°C is much lower than at 621°C.

In conclusion, the mechanical strength of the composition G17 was probably increased by the crystallization heat treatment. However, the optimum crystallization heat treatment giving maximum strength may involve nucleation treatments at lower temperatures and for longer times than used in the present work. The actual breaking mechanism may be related to the existence of cracks with a size corresponding to the average crystal size (5.48). Two stereoscan pictures of a fracture surface of B are shown in Figure 5.25. The very rough surfaces are probably due to crack diversion. However it is not known whether the cracks may propagate preferentially through the crystal boundaries or through the crystals themselves.

5.3.2 Thermal expansion

A number of thermal expansion measurements were made for glasses close to the NC_2S_3 composition. The percentage linear expansion vs T(°C) plots for glass G17 and the corresponding glass ceramic are shown in Figure 5.26. The glass was annealed before the run. The

FIGURE 5.26 Percentage expansion vs. T(°C)
for glass and glass ceramic G17

o glass (l_o=8.34 cm)
glass ceramic (l_o=6.84 cm)

Heat treatment
T_N=627 °C, t_N=2 h
T_G=722 °C, t_G=30 min.

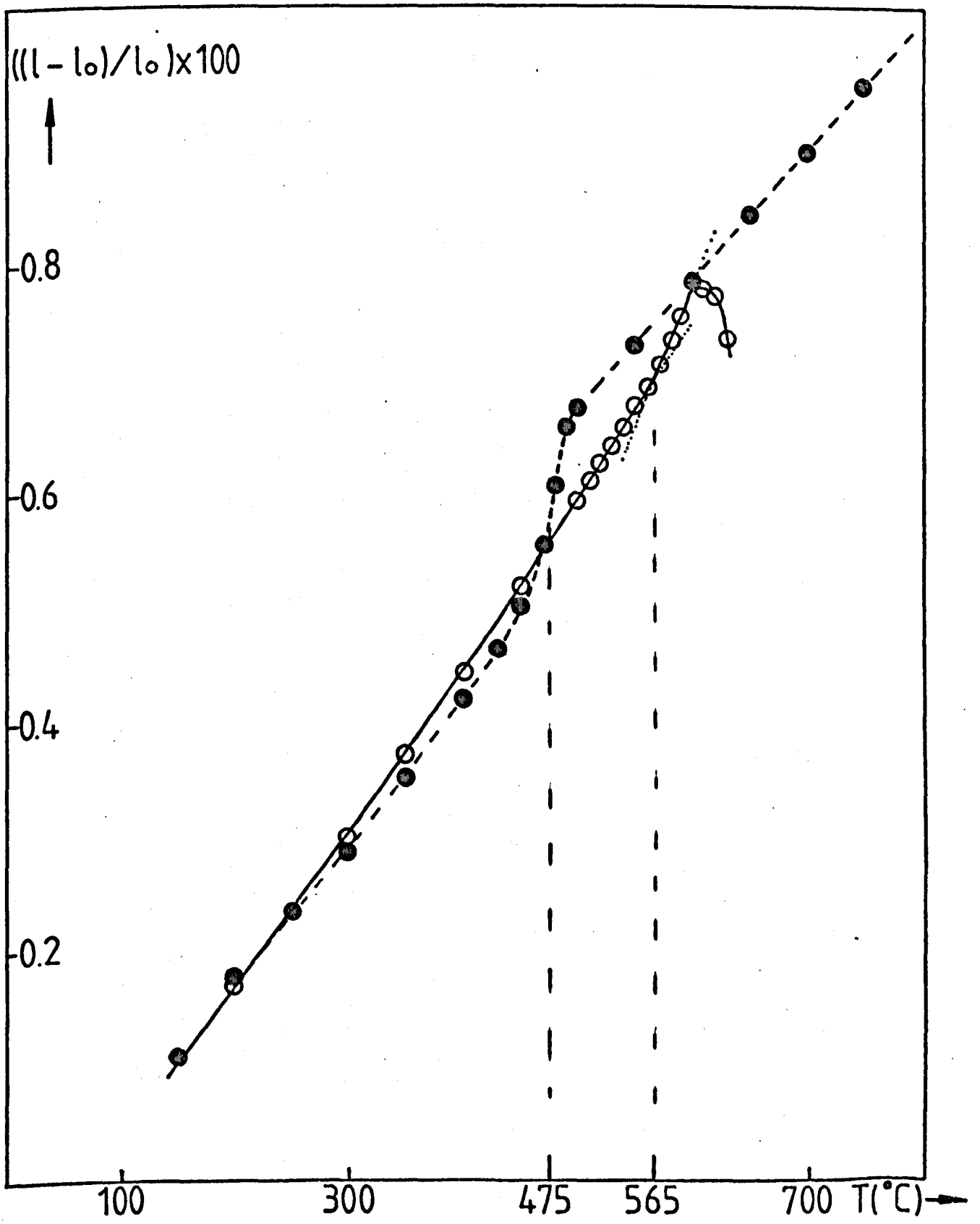

dilatometric softening point occurred at 610°C and the glass transformation temperature Tg at 565°C. The expansivities for two temperature ranges are given in Table 5.3. The crystallinity content of the glass ceramic, from X-ray analysis, was 95% and a typical transmission electron micrograph of the glass ceramic is shown in Figure 5.27. In the thermal expansion plot for the glass ceramic, the polymorphic transformation of the NC_2S_3 phase can be clearly observed in the temperature range 460-490°C. The overall change in the percentage expansion amounts to about 0.15 for this transition corresponding to a volume change of approximately 0.45%. As discussed in (5.2.4) stresses generated in such a transition might generate microcracks which could weaken the material. However the relatively small volume change for the NC_2S_3 glass ceramic may mean no significant effect on its strength after it is cooled through the transition temperature. The thermal expansion of the low form of the NC_2S_3 phase is higher than the expansion of the high form (Table 5.3).

An interesting point is the refractoriness of the glass ceramic as compared with the original glass. For example, with the axial load required in the expansion measurements, the ceramic did not show any softening up to the end of the run at 810°C. This is an increase of at least 200°C over the softening point of the glass. The similarity between the expansion coefficients of this glass ceramic and certain metals suggests its possible use in glass ceramic-metal seals. For certain applications of such seals the electrical properties of the glass ceramic are important. According to (5.49) the volume

resistivities of the NC_2S_3 glass and glass ceramic, at 400°C, are $10^{5.5}$ and $10^{7.5}$ Ω cm respectively. The value for the glass ceramic is quite close to the values quoted in (5.24) for glass ceramics considered as good insulators. As far as we are aware no data on other electrical properties, such as surface resistivity, are available for the present glass ceramic.

5.3.3 Chemical durability

The quantities of Na_2O and SiO_2 extracted from a number of glasses and corresponding glass ceramics attacked by either pure H_2O or a 0.024 M HCl water solution at 98°C were determined as mentioned in Chapter 2. The glass ceramics were prepared using the heat treatments given in Table 5.4.

The results are listed in Table 5.5. It is clear that for all the glasses water extracts more SiO_2 than the acid and that for all the glass ceramics water dissolves less SiO_2 than the acid. This may indicate that different corrosion mechanisms apply for the glasses and glass ceramics. For all the glasses and glass ceramics the acid dissolves more Na_2O than the pure water. For G16 (close to the exact NC_2S_3 composition) the extraction of Na_2O and SiO_2 is lower than that for the corresponding glass ceramic using both reagents.

Let us now examine the effect of varying the composition in more detail. In the following the results for the glasses are compared with the base glass G16; the results for the glass ceramics are compared with the base glass ceramic G16C.

NaF addition decreases the glass durability when compared to G16.

TABLE 5.4 DETAILED HEAT TREATMENT OF GLASSES G16, G13′, G5 G27, G28, G29 AND G30

Glass ceramic code	Heat treatment
G16C	T_N = 628°C, t_N = 47 min T_G = 740°C, t_G = 33 min
G13′C	"
G5C	"
G27C	T_N = 610°C, t_N = 20 h 30 min T_G = 736°C, t_G = 31 min
G28C	"
G29C	"
G30C	T_N = 626°C, t_N = 43 h T_G = 740°C, t_G = 23 min

TABLE 5.5 CHEMICAL DURABILITY RESULTS - C REFERS TO CERAMIC AND M_i IS THE $\frac{\text{Extracted mass of } Na_2O(SiO_2)}{\text{Initial mass}} \times 100$.

FOR 'N' SEE THE TEXT

	Reagent					
	H_2O				Acid	
Glass Code	N	M_{Na_2O}	N	M_{SiO_2}	M_{Na_2O}	M_{SiO_2}
G16	3.8	0.11	8.3	0.33	1.01	0.21
G16C	3.8	0.11	17.5	0.70	1.51	1.07
G13′	8.7	0.25	19.3	0.77	1.48	0.30
G13′C	3.1	0.09	16.3	0.65	1.50	0.96
G5	5.9	0.17	17.3	0.69	1.37	0.27
G5C	9.4	0.27	15.8	0.63	1.61	0.90
G27	9.7	0.28	25.3	1.01	1.07	0.22
G27C	3.6	0.105	12	0.48	1.63	0.96
G28	8.7	0.25	23.3	0.93	0.99	0.17
G28C			15.8	0.63	1.72	0.88
G29	9.7	0.28	26.6	1.06	1.26	0.16
G29C	2.8	0.08	10.8	0.43	1.56	0.69
G30	5.9	0.17	18.5	0.74	0.97	0.12
G30C	1.7	0.05	9.3	0.37	1.15	0.69

For the glass ceramic NaF addition increases the Na_2O extraction but decreases slightly the SiO_2 removal.

ZrO_2 addition also decreases the glass durability but increases slightly the durability of the glass ceramic towards acids and water.

For the glass Al_2O_3 addition increases the Na_2O and SiO_2 extraction by water. For acid attack the effects are more complicated. Whereas for 1.12 wt.% Al_2O_3 addition (G27) the Na_2O and SiO_2 extractions are very similar to those for G16, for G28 (2 wt.% Al_2O_3) and G30 (4 wt.% Al_2O_3) the extraction of both oxides is reduced. For G29 (3.5 wt.% Al_2O_3, 2 wt.% NaF) the SiO_2 removal is reduced but the Na_2O extraction is increased.

For the glass ceramics Al_2O_3 addition decreases the extraction of both Na_2O and SiO_2 under water attack. Also the removal of silica by acid is reduced. For Na_2O extraction by acid the situation is not as clear. Whereas for the greatest Al_2O_3 addition (4%) the removal of Na_2O is clearly reduced, for the smaller additions (1.12 and 2 wt.% Al_2O_3) the extraction is slightly increased.

According to El-Shamy and Ahmed (5.50) the extractions of Na_2O and SiO_2 for a commercial "soft soda glass" (72.3 SiO_2, 14 Na_2O, 9.3 CaO, 1.9 Al_2O_3, 1.5 MgO, 0.6 K_2O, 0.2 BaO and 0.2 SO_3 wt.%), attacked by deionised water at 100°C for one hour, were 0.0288 and 0.0399% respectively. First, it should be noticed that water extracted more SiO_2 than Na_2O, which is consistent with our results. Secondly, it is possible to compare the chemical durability of our glasses and glass ceramics with the results of El-Shamy and Ahmed. The ratio of the percentage extraction of Na_2O (SiO_2) obtained in this work to that

obtained in (5.50) for the soda-lime glass is listed in Table 5.5 under the letter 'N'. The N value for the Na_2O extraction from the glasses ranges from 3.8 for G16 to 9.7 for G27 and G29 whereas for the SiO_2 extraction it ranges from 8.3 for G16 to 26.6 for G29. For Na_2O extraction from the glass ceramics N ranges from 1.7 for G30C to 9.4 for G5C and for SiO_2 extraction N ranges from 9.3 for G30C to 17.5 for G16C. It is interesting to note that the extractions for one of the glass ceramics (G30C) were comparable with those for the commercial chemically durable glass. Also G29C (containing fluoride) behaved similarly to G30C. Although no quantitative microstructural data were obtained for these glass ceramics, the glass G29 was observed to have higher internal nucleation than G30.

5.3.4 Crystallization results for other compositions

The base glass compositions G47 and G53 belong to the αCS phase field of the ternary system (5.51) whereas G37 is on the boundary of the NC_2S_3 and βCS fields. To these glasses various amounts of ZrO_2, TiO_2, NaF, CaF_2, Na_2S, Cr_2O_3 and Fe_2O_3 were added. The DTA Tg and DTA peak crystallization temperature Tc for glasses G37 to G67 are listed in Table 5.6. For the three base glass compositions the DTA Tg was increased by Cr_2O_3, TiO_2 and ZrO_2 additions but decreased by Na_2S, Fe_2O_3, CaF_2 and NaF additions. The largest increase was obtained for the greatest ZrO_2 addition whereas the largest decrease was observed for the NaF additions. Several nucleation treatments at temperatures between the DTA Tg and Tc, and growth treatments at temperatures higher than Tc were given to a number of the glasses to investigate whether

TABLE 5.6 DTA RESULTS FOR GLASSES G37 TO G67.

THE BASE GLASS COMPOSITION IS AT THE TOP OF EACH GROUP.

THE MEANING OF THE SYMBOLS IN THE 2ND COLUMN ARE:

THE NUMBER PRECEDING THE LETTER CORRESPONDS TO THE wt% ADDITION TO THE BASE GLASS.

THE OXIDE OR COMPOUND ADDED IS REPRESENTED BY:

Z = ZrO_2; T = TiO_2; NF = NaF, CF = CaF_2; NSU = Na_2S; CR = Cr_2O_3 AND FE = Fe_2O_3

Glass Code		DTA Tg (°C)	T_c (°C)	
G37	(base glass)	547	768	
G38	6.5 Z	575	836	
G39	12.9 Z	633	878	
G40	6T	561	797	
G41	12.9T	577	793	
G42	9NF	464	725	
G43	9CF	506	730	
G44	9NSU	522	715	
G45	6CR	561	806	
G46	6FE	530	769	
G47	(base glass)	622	820	
G48	6Z	662	904	
G49	12Z	682	958	and 1031
G50	6T	629	841	
G51	12T	645	901	
G52	16.1T	646	909	
G53	9NF	519	746	and 800
G54	9CF	565	764	
G55	8.8NSU	-	-	
G56	6CR	630	832	
G57	6FE	605	810	
G58	(base glass)	627	804	
G59	6Z	661	850	
G60	12Z	685	903	
G61	6T	628	814	
G62	12T	641	832	
G63	9NF	520	674	
G64	9CF	562	750	
G65	9NSU	600	797	
G66	6CR	636	820	
G67	6FE	599	758	

they exhibited any internal nucleation. Also some glasses were heat treated from a temperature between the DTA Tg and Tc at a constant heating rate to a temperature higher than Tc. Various crystalline features observed in the heat treated glasses are shown in Figures 5.28 to 5.36. Only those glasses are mentioned specifically which exhibited internal nucleation or some other interesting characteristic. The glasses not mentioned did not show any internal nucleation for the heat treatments employed. For glasses G43 (9 wt.% CaF_2) and G44 (9 wt.% Na_2S) some internal nucleation was observed as shown in Figures 5.28 and 5.29 respectively. For the G47 series the considerable internal nucleation in G53 (9 wt.% NaF), was of particular interest (Figures 5.30, 5.31). A complex growth morphology of the crystals can be observed. For the G58 series, the base glass (Figure 5.32) gave some internal nucleation and again a complex growth morphology. The two crystals observed probably correspond to different orientations of the growth centres with respect to the cross section plane of the glass. For G62 (12 wt.% TiO_2 a very smooth crystalline surface layer was particularly noticeable (Figure 5.33). G67 (6 wt.% Fe_2O_3) showed surface crystallization and some internal nucleation (Figure 5.34). G66 (6 wt.% Cr_2O_3) showed precipitation of elongated centres resembling metallic particles in their high reflectance (Figure 5.35). Glass G64 (9 wt.% CaF_2) showed coarse internal nucleation (Figure 5.36). A number of X-ray diffractometer patterns were obtained for the G58 series. The d spacings of the strongest peaks matched quite closely those of the NC_2S_3 phase but not those of the αCS phase. For the glass containing NaF, the strongest NaF and CaF_2 peaks were detected. In conclusion it appears that other

Figure 5.28 (left)

Optical micrograph (OM) of G43 nucleated at T_N = 527°C for 10 h (t_N) and grown at T_G=762 C for 10 min (t_G). Mag X504

Figure 5.29 (right)

OM of G44 heat treated as follows: T_N = 581°C, t_N = 10 h. T_G = 740°C, t_G = 5 min. Mag X101

Figure 5.30 (top left); 5.31 (bottom left)

OM of G53 heat treated: T_N = 588°C; t_N = 14 h. T_G = 751°C; t_G = 10 min
Mag X101; Mag X504.

Figure 5.32a,b (right)

OM of G58 heated: T_N = 666°C, t_N = 12.5 h. T_G = 815°C, t_G = 25 min.
Mag X504.

Figure 5.33 (left)

OM of G62 heated at 1.1°C min^{-1} from 633°C to 875°C. Mag X32.

Figure 5.34a,b (middle and right)

OM of G67 heated as described in Figure 5.33. Mag X32; X504.

Figure 5.35 (left)

OM of G66 heated as described in Figure 5.33. Mag X504.

Figure 5.36 (right)

OM of G64 heated as follows: T_N = 583°C, t_N = 12 h 20 min
T_G = 782°C, t_G = 10 min
Mag X101.

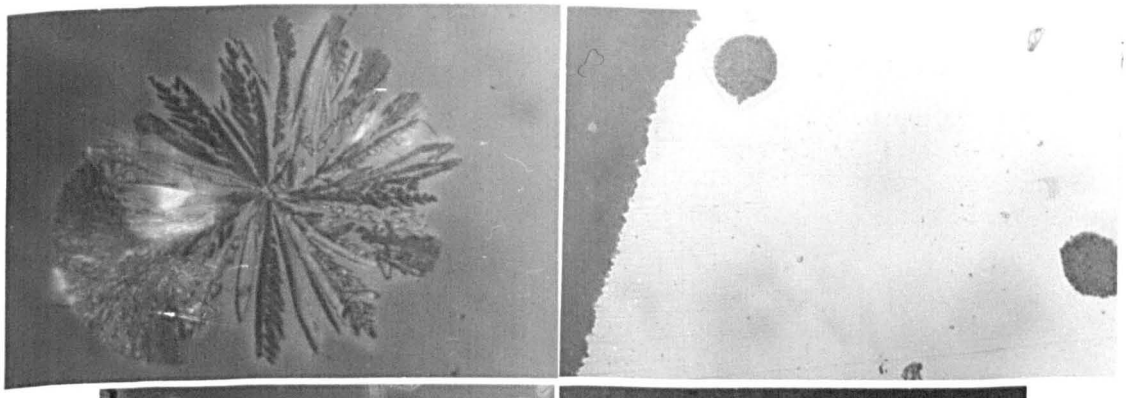
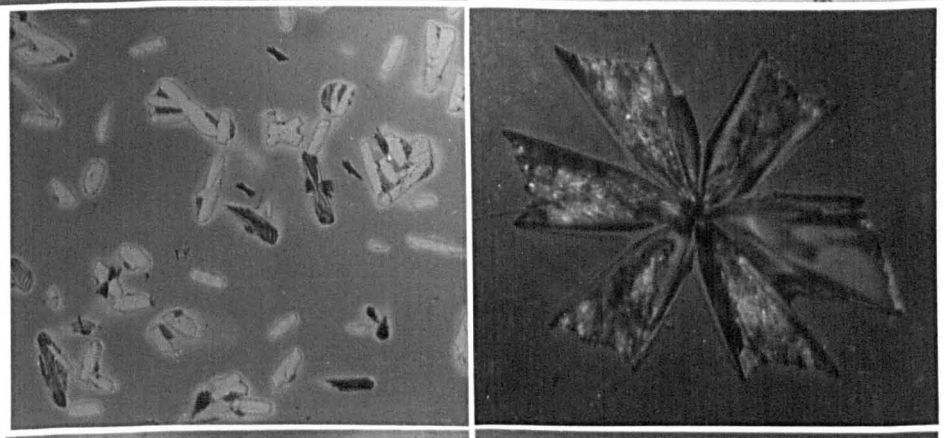
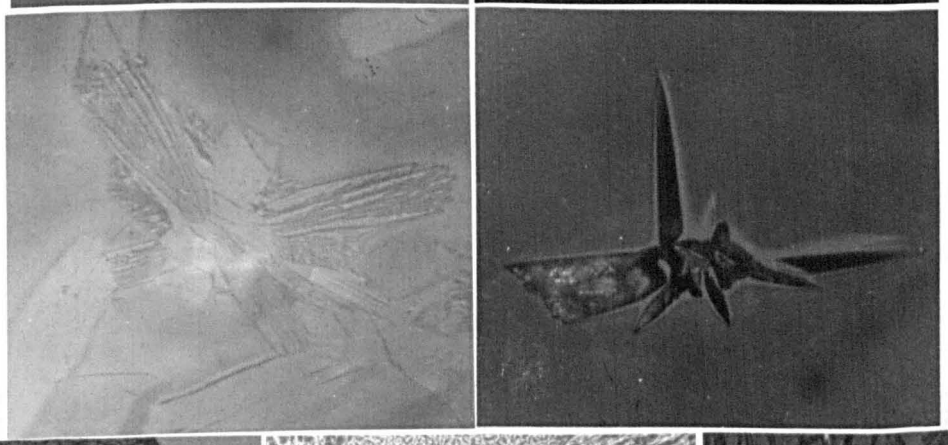
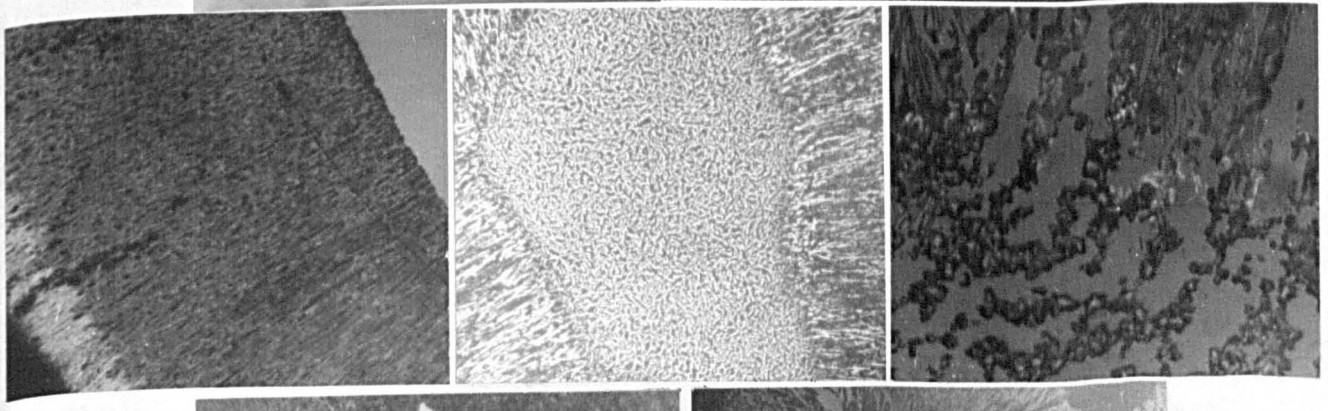
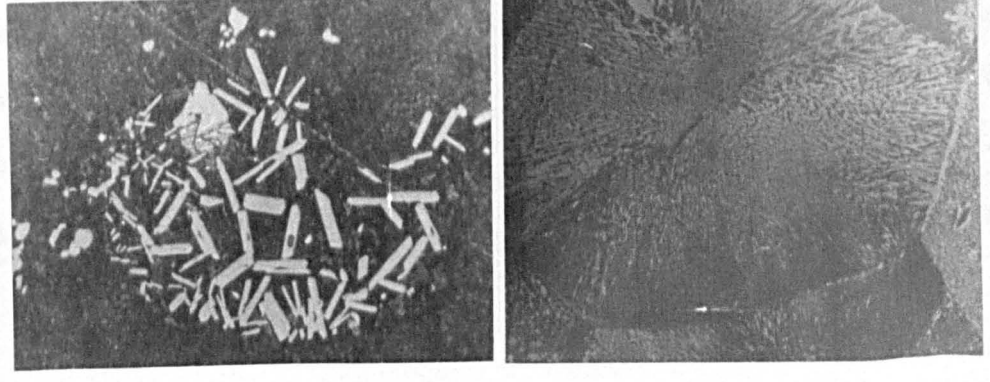

ternary compositions may be internally crystallized apart from those close to the NC_2S_3 and N_2CS_3 compositions,

In the present work we have concentrated attention on compositions exhibiting internal nucleation and capable of forming glass ceramics. However another possible method exists for forming a polycrystalline 'glass ceramic' material with a reasonable fine grain structure by sintering and crystallizing a glass powder. In this method the starting glass need not necessarily exhibit internal nucleation. Briefly, the glass powder is mixed with seeds of the main crystalline phase expected to precipitate from the glass composition (5.52). After forming, the preform is fired to achieve first sintering of the glass particles and then crystallization from the particle interfaces and/or the crystal seeds. It would be interesting to apply this technique to the soda-lime-silica system, particularly for glass compositions which do not internally nucleate i.e. for compositions other than those studied in the present work. A necessary requirement for the selection of such compositions is that they should form a glass but also have a reasonable high crystal growth rate. Of course the attraction of producing glass ceramics from soda-lime-silica glasses is their potential low cost.

Another possible application of glass ceramics in the soda-lime-silica system of low SiO_2 content is as hydraulic cements. According to Reference (5.53) a high compressive strength cement has been made by curing at room temperature a mixture of glass powder (10 wt.% Na_2O, 40 wt.% CaO and 50 wt.% SiO_2) and water. The NC_2S_3 glass ceramic might also be used for such an application. The improved mechanical

properties of the glass ceramic over the glass could mean a further improvement in the compressive strength of the cement.

5.3.5 Metallic precipitation

A number of photosensitive glasses containing Ag_2O were melted. These were prepared to investigate whether a high density of very fine metallic particles could be used to heterogeneously nucleate the main crystalline phases. The compositions of the glasses (G26 and G68 to G75) are listed in Table 2.1. CeO_2 and Sb_2O_3 were added as photosensitizing and thermoreducing agents respectively (5.54). It is thought that irradiation of the glass with ultra violet light (U.V.) produces metallic atoms. Upon heating more atoms are produced due to the action of the thermoreducing agent. These atoms diffuse onto the pre-existing nuclei and form metallic centres.

After casting, G26 (containing 0.5 wt.% Ag_2O) was slightly yellow indicating that probably the Ag_2O solubility limit for this glass had been exceeded. In contrast, G75 (containing 1.2 wt.% Ag_2O) had no perceptible coloration. A possible explanation may be found in the compositions of the base glasses (Table 2.1). A glass of, say, 80 mole% SiO_2 and 20 mole% modifier oxides may accept more modifier cations (Ag^+) than a glass of 50 mole% SiO_2 and 50 mole% modifier oxides where the interstitial sites are more fully occupied.

For the irradiation experiments a U.V.-HBO superpressure mercury lamp (WOTAN, 100W) was used at 5 cm from the specimen holder. An electron micrograph of G26, irradiated for 1 hr and heat treated is shown in Figure 5.37. A high density of very small (125 Å diameter)

Figure 5.37

TEM of G26 heated at 590°C for 1 hr and at 647°C for 54 min. (See text). Mag X29,600

Figure 5.38

(See text)

Figure 5.39

TEM of specimen No. 5 in Figure 5.38. Mag X60,300

Figure 5.40

TEM of G74. (See text). Mag X101,500.

Figure 5.41

TEM of G75 heated at 800°C for 55 min. Mag X30,800

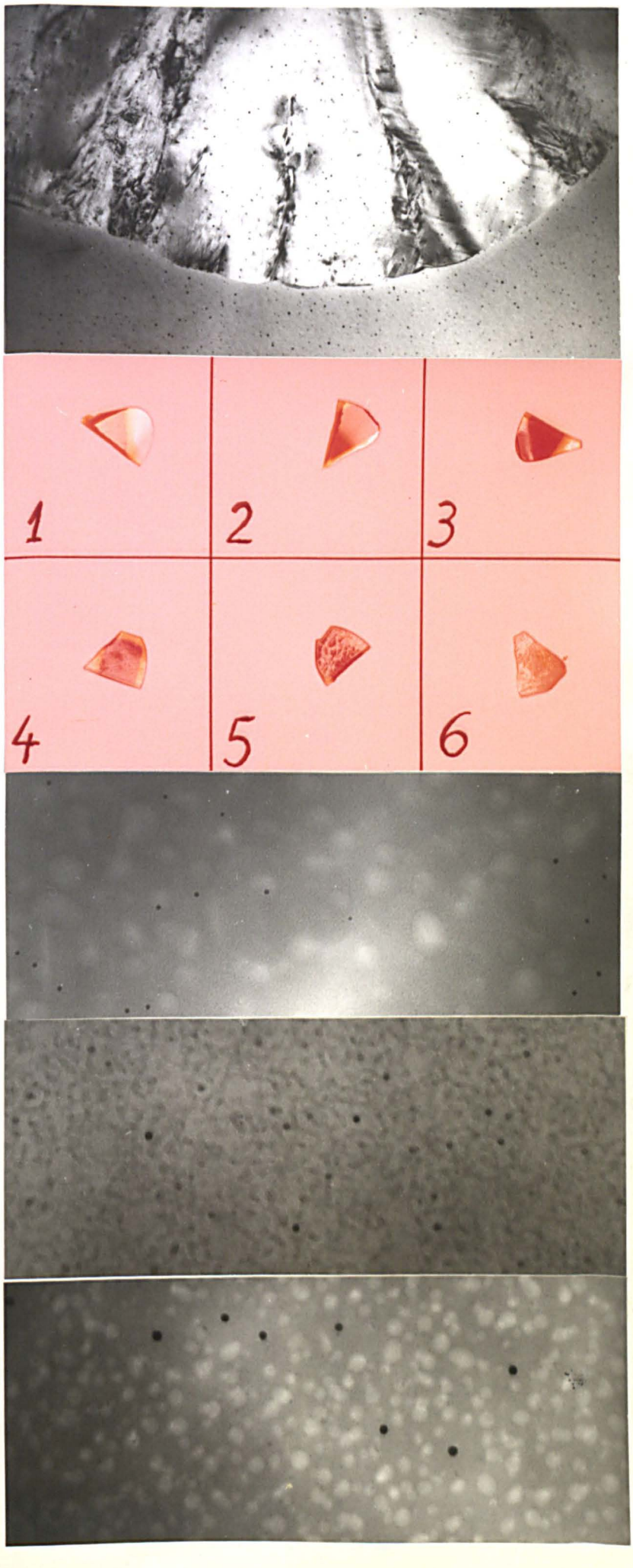
1
2
3
4
5
6

particles can be clearly observed. The diameter of the NC_2S_3 crystal is about 6 μm. No growth of NC_2S_3 crystals on the metallic particles was observed.

Six specimens of G74 (containing 0.5 wt.% Ag_2O) irradiated for 1 hr and heat treated for 1 hr at 640 (No. 1), 671 (No. 2), 704 (No. 3), 732 (No. 4), 764 (No. 5) and 782°C (No. 6) are shown in Figure 5.38. All the specimens were partially covered with metallic foils during the irradiation treatment to retain unexposed areas. Heat treatment produced the darker zones visible in the Figure and these corresponded exactly to the irradiated areas. Appreciable precipitation was also observed in the non-irradiated areas. Figure 5.39 is an electron micrograph of the darker area in specimen 5. The metallic particles have an average diameter of about 125 Å. Also present are droplets of liquid-liquid phase separation with a maximum diameter of 1200 Å. It should be noted that a glass of composition 10 Na_2O, 10 CaO and 80 SiO_2 (mole %) was extensively studied by Burnett and Douglas (5.55). They found that considerable liquid-liquid phase separation occurred at temperatures higher than about 600°C. The observed morphology was of the 'droplet' type at temperatures higher than about 680°C but a highly interconnected structure was found at lower temperatures. The immiscibility temperature was 895°C. Although the glass compositions are not exactly the same, our results compare well with the observations in reference (5.55). No internal crystallization could be found in any of the six specimens of G74. Only a thin crystalline surface layer was observed for specimens 4, 5 and 6. An electron micrograph of G74 irradiated for 46 min and heat treated at 645°C for 14 hr is shown in Figure 5.40. The

metallic particles have an average diameter of 126 Å. The phase separation structure is now of the interconnected type which is consistent with the findings of reference (5.55).

A DTA run for G75 showed the DTA Tg endothermic peak at 580°C and two exothermic peaks at 804 and 864°C. Considerable metallic precipitation was obtained without the U.V. treatment (Figure 5.41). Some internal crystallization was found in G75 heated at 686°C for one hour and then at 884°C for 10 min. Two electron micrographs are shown in Figure 5.42. It appears that the crystals grew from metallic particles. However the number of crystals was much lower than the number of metallic particles. The maximum dimension of the crystals was about 0.4 μm whereas the maximum diameter of the metallic precipitates was 360 Å. This glass had a relatively thick crystalline surface layer which became heavily cracked when cooled to room temperature. An X-ray powder pattern of the whole sample gave three peaks at d = 4.1, 2.4 and 1.4 Å which are close to the peak positions for the low form of cristobalite (5.56). Another electron micrograph of this glass is shown in Figure 5.43, together with a selected area diffraction pattern of one of the crystals. Two d spacings were obtained at d = 1.95 and 1.65 Å. The former value is very close to the 1.93 Å reflection of the low form of cristobalite (5.56). The 1.65 Å value could not be identified since only d spacings greater than 1.87 Å are reported in (5.56). It should be noticed that no phase separation was present in the glass (Figure 5.42).

To summarise, the photosensitive and thermal metallic precipitation processes worked well in the soda-lime-silica glasses investi-

Figure 5.42a,b

TEM of G75 (see text). Mag X35,500.

Figure 5.43a,b

5.43a TEM of G75 (see text). Mag X22,000.
5.43b SAD of marked crystal in 5.43a.

Figure 5.44

TEM of G76 (see text). Mag X20,300

Figure 5.45

TEM of G76 (see text). Mag X60,900.

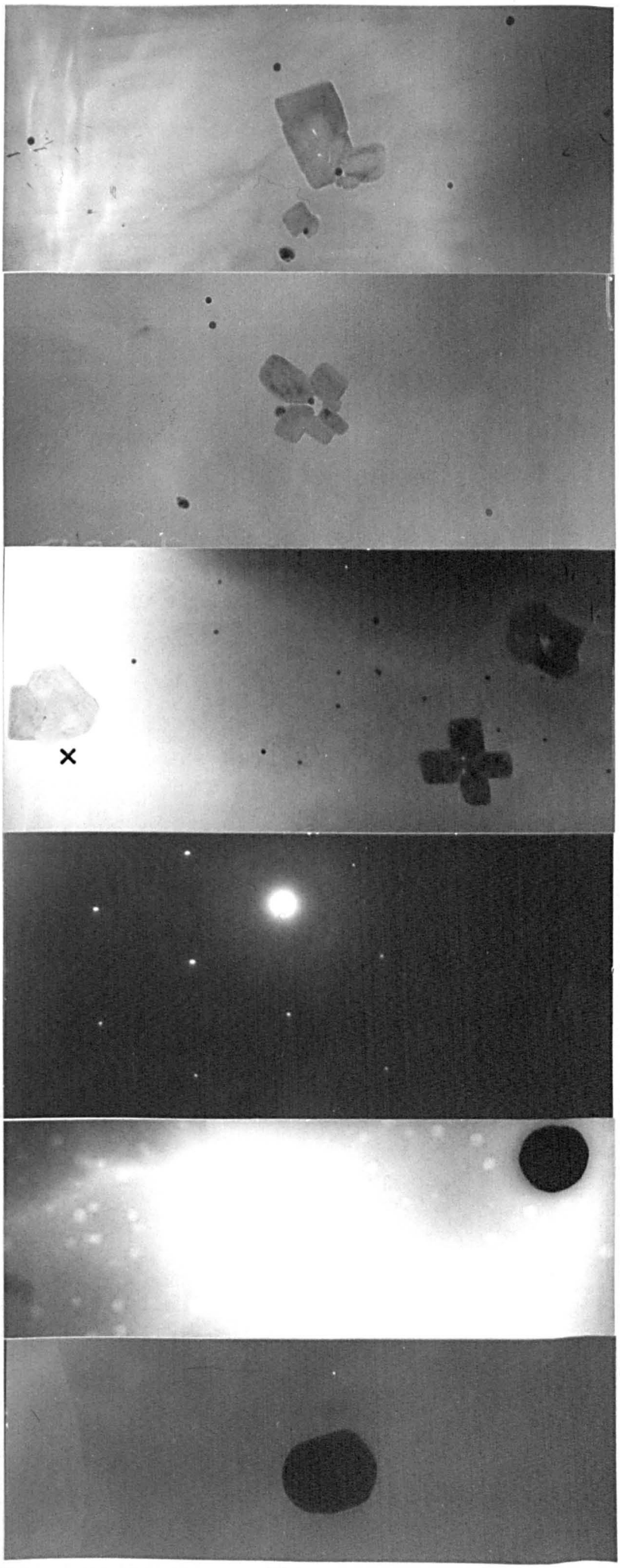

gated. Also there was evidence for heterogeneous nucleation on the metallic particles. However further work is needed to assess whether sufficient heterogeneous nucleation can be obtained to produce fine grain glass ceramics in this system.

Finally, a platinum containing glass (0.3 wt.% Pt) of high SiO_2 content (G76) was heat treated at various temperatures to determine whether internal crystallization could be obtained. An electron micrograph of G76 heated at 722°C for 1.5 hr and then at 880°C for 20 min is shown in Figure 5.44. A platinum particle and a fine scale liquid phase separation are clearly visible but no crystal growth can be observed. An electron micrograph of G76 heated at 722°C for 1.5 hr and then at 930°C for 20 min is shown in Figure 5.45. Again no crystal growth on the platinum particles can be observed. Also phase separation is no longer present.

CHAPTER 6

CONCLUSIONS AND SUGGESTIONS FOR FURTHER WORK

6.1 Conclusions

A number of experimental techniques were used in the present basic study of the homogeneous and heterogeneous crystal nucleation and growth processes in soda-lime-silica glasses. Optical microscopy and electron microscopy were particularly useful in the determination of nucleation densities and growth rates as well as in the studies of crystal morphology and metallic precipitation. Other data required to interpret the kinetics were heats of crystallization and fusion, which were obtained from DTA and DSC, liquidus temperatures and viscosities. The compositions of the glasses were determined by chemical analysis and the hydroxyl contents by infra-red spectroscopy. The products of crystallization were identified by X-ray diffraction. Various physico-chemical properties of the glasses and glass ceramics were studied including mechanical strength, chemical durability and thermal expansion. Scanning electron microscopy was also used to examine the microstructure of the materials produced.

The morphology of the internally nucleated NC_2S_3 crystals in the early stages of growth was studied by transmission electron microscopy. The crystal phase identified by selected area electron diffraction in the small crystals was the same as that identified by X-ray powder diffraction in fully crystallized specimens. Electron microscopy revealed many imperfections in the crystals. These were probably mainly stacking faults and/or twins.

In the studies of the kinetics of nucleation the double stage heat treatment method was used extensively, in conjunction with the optical microscopy to determine nucleation densities (N_v). The validity of

this method was analysed using measurements from scanning electron micrographs of specimens given only a single stage heat treatment. These measurements supported the use of the double stage method. For glass G16 the N_v/t values, where t was a constant heat treatment time (40 min), at a series of temperatures, were found to be a good measure of the steady state nucleation rates I_o, particularly at temperatures higher than the maximum in nucleation. At such temperatures 'steady state' conditions applied and the nucleation rate I was constant with time, whereas at much lower temperatures below the maximum non-steady state conditions increasingly applied with decrease in temperature, and N_v/t values underestimated the steady state nucleation rates I_o. The classical nucleation theory provided a good fit to the experimental nucleation rates for temperatures higher than the maximum in nucleation when the kinetic barrier ΔG_D was allowed to increase with decreasing temperature. The diffusion term involving ΔG_D was assumed to have the same temperature dependence as the viscosity. The thermodynamic driving force, ΔG, which was needed in the analysis was determined from measurements of the heat of fusion ΔH_f and the difference in specific heats of the crystal and liquid phases ΔC_p, using DTA and DSC. From the fit between theory and experiment the crystal-liquid interfacial free energy was found to be 174 erg cm^{-2} for G2.

The specific heat results themselves were of some interest. They indicated that the NC_2S_3 glass had essentially a three dimensional network structure despite its high content of modifier oxide (50 mole%).

The effect of varying the glass composition on the nucleation

kinetics of the NC_2S_3 phase was systematically studied. For glasses with a SiO_2 content lower than 50 mole% the nucleation was increased with respect to the base glass (G2). This was particularly interesting since on simple theoretical grounds the base glass, which was close to the NC_2S_3 stoichiometry composition, might be expected to show the highest nucleation rates. Thus the driving force ΔG should be greatest for the exact NC_2S_3 composition. It was concluded that decreasing the SiO_2 content caused a decrease in ΔG_D which overrided the effect on ΔG. This was supported by the observed decrease in viscosity. For SiO_2 contents higher than 50 mole% the nucleation was decreased for G18 (15.65 N, 33.74 C and 50.61 S (mole%)) and G23 (16.33 N, 32.7 C and 51 S (mole%)) but increased for G20 (16.92 N, 32.33 C and 50.75 S (mole%)). Viscosity data was again very useful as an aid in the interpetation of the results.

The effect of water additions on nucleation was clearly established. Existing data for lithium disilicate glass had showed that nucleation rates increased markedly with increase in the water content. Viscosity data on the same glasses obtained in the present study showed also that the viscosities decreased with water content. From analysis of the nucleation results it was found that ΔG_D was considerably reduced with increase in water content whereas the interfacial energy σ was only slightly lowered. For the soda-lime-silica glasses increase in the water content also gave a large increase in nucleation rates and a decrease in the viscosities. Although the interpretation was more difficult than in the case of the lithia glasses due to changes in the glass compositions, essentially the same conclusions were reached.

Small additions of NaF had very similar effects to the addition of water on the NC_2S_3 glass. The viscosity of the glass was decreased while the maximum nucleation rate of NC_2S_3 crystals was increased and the temperature of the maximum was shifted to lower temperatures. It was concluded that for small additions of NaF, ΔG_D was decreased and σ was increased. For large additions of NaF the maximum in nucleation was shifted to much lower temperatures but overall the nucleation rates were greatly reduced. The major (probably NC_2S_3) phase still precipitated first and this was followed by precipitation of metallic fluorides on the crystals of the major phase. There was no evidence for the fluorides precipitating first and these then acting as heterogeneous sites for crystal growth of the major phase.

Additions of P_2O_5, TiO_2 and MoO_3 to the NC_2S_3 composition reduced the crystal nucleation. For ZrO_2 addition, analysis indicated that ΔG_D was increased whereas σ was not significantly affected.

A detailed investigation of heterogeneous nucleation was carried out on platinum containing glasses. Due to possible changes in composition the theoretical analysis was confined to the results at the higher temperatures. The $f(\theta)$ value obtained from theoretical analysis of the nucleation data was in good agreement with a value derived from the measured contact angle between the platinum and the crystal phase.

Concerning the growth rate kinetics a good correlation was found between the changes in growth rates and the changes in viscosity for the glasses containing H_2O, NaF and ZrO_2. Also the apparent activation enthalpies ($\Delta H_D'$) did not change appreciably for the H_2O and ZrO_2 additions

NC_2S_3 glass ceramic, with P_2O_5 and NaF additions, could be in the field of biomaterials.

Finally, a limited investigation of other base glass compositions was reported. The high density of internal crystals found for NaF additions was of particular interest and also the evidence for internal crystal nucleation in compositions in which silver had been precipitated.

6.2 Suggestions for Further Work

It would be very useful to have accurate data of the self-diffusion coefficients of various species, for example, oxygen, in the NC_2S_3 glass at temperatures in the transformation range and above. Knowledge of the diffusion coefficient for the rate limiting species as a function of temperature could be used to critically analyse the nucleation rates in terms of the classical nucleation theory. This would avoid the necessity of employing the Stokes-Einstein relationship between the diffusion coefficient and viscosity, which may be in error as mentioned previously. Although diffusion data for oxygen exists for silicate glasses as discussed in Chapter 5 there is no information available for compositions such as NC_2S_3 which show internal nucleation.

Thermodynamic data were obtained in the present work in order to calculate the driving force ΔG for the NC_2S_3 composition. It would be worthwhile to obtain further data on this composition to check the present DTA and DSC results, for example high temperature calorimetry might be used to determine the enthalpies of the liquid (glass) and crystalline phases as a function of temperature. It would also be interesting from a fundamental point of view to determine ΔG accurately for the compositions close to NC_2S_3 used in the present study, since the nucleation kinetics could be analysed in greater detail. However accurate thermodynamic data would be much more difficult to determine for these compositions. Thus the activities of the Na_2O, CaO and SiO_2 components in solution would be required as a function of temperature, which would be a difficult experimental task.

It is clear that water content must be carefully considered in

any future fundamental studies of nucleation and growth in glasses. Thus different melting conditions, for example, the use of electric or gas furnaces, could produce small differences in water content and, as a result, significant changes in nucleation and growth rates. Such factors deserve further study since they could produce differences in the results for nominally the same glass compositions prepared in different laboratories. The effect of water is also of interest in the preparation of glass ceramics. For certain compositions a deliberate increase in water content could shorten the crystal nucleation and growth times or usefully lower the heat treatment temperatures required while maintaining the same fine grain microstructure, provided no deleterious effects on the properties of the resultant materials occurred and convenient methods of introducing the higher water contents during the melting could be devised. Further work on the effects of water content on the crystallization and properties of more complex compositions of greater technological interest would be of considerable interest. The results in this thesis are also relevant to crystallization studies of glasses prepared by the 'gel' process, which recently has attracted considerable interest (5.17). Such glasses may have different (often higher) water contents than glasses prepared conventionally by fusion of oxides.

Further work on platinum precipitation and its effect on heterogeneous nucleation would be of fundamental interest. As suggested in Chapter 5 further nucleation results could be obtained for the NC_2S_3 glass, particularly at higher temperatures. The effect of platinum precipitation on the nucleation kinetics could also be studied in

other systems. There is evidence (5.30) that platinum induces heterogeneous nucleation in lithia-silica glasses.

With regard to crystal growth results, clearly the origin of the intercepts with the time axis on the crystal size versus time plots is not well understood. Further work on the soda-lime-silica system and possibly other systems such as lithia-silica may help to decide whether these intercepts are closely related to the incubation times for internal nucleation, as has been suggested in Chapter 5.

Some possible uses of glass ceramics based on compositions close to NC_2S_3 have already been discussed above. In view of the potential application of P_2O_5 containing glass ceramics as biomaterials more detailed studies of the effect of P_2O_5 on crystallization and glass ceramic formation in the soda-lime-silica system would be useful. The bonding properties of the glass ceramics to hard tissues would be also of great importance.

The 'alternative' method of making glass ceramics by sintering and crystallizing fine glass powder into a solid material mentioned in Chapter 5 would also be an interesting field for study, since in principle the method could be applicable to a wide range of compositions in the soda-lime-silica and other systems.

Finally, further detailed work is required on the properties of the NC_2S_3 glass ceramics, particularly those with a fine grain microstructure produced by longer nucleation treatments at lower temperatures, before the possible practical applications of these materials can be assessed.

APPENDICES

APPENDIX AO

FREE ENERGY OF MIXING AND REGULAR SOLUTIONS

Consider Section 1.2b and Figure 1.6. From equation (1.23) we obtain:

$$\Delta Gm^{\ell}(A) = G_A^{\ell} - G_A^{0\ell} = RT \ln a_A^{\ell}$$
$$\Delta Gm^{\ell}(B) = G_B^{\ell} - G_B^{0\ell} = RT \ln a_B^{\ell} \qquad (AO.1)$$

where $\Delta Gm^{\ell}(A)$, $\Delta Gm^{\ell}(B)$ are the partial molar free energies differences of component A and B respectively (1.4). Now the free energy of mixing at composition X_A is defined as

$$\Delta Gm^{\ell} = X_A \Delta Gm^{\ell}(A) + X_B \Delta Gm^{\ell}(B) = \Delta Hm^{\ell} - T\Delta Sm^{\ell} \qquad (AO.2)$$

where ΔHm^{ℓ}, ΔSm^{ℓ} are the enthalpy and entropy of mixing respectively. Using equations (AO.1) and (AO.2) it is found

$$\Delta Gm^{\ell} = X_A RT \ln a_A^{\ell} + X_B RT \ln a_B^{\ell} \qquad (AO.3)$$

Now using $a_A^{\ell} = X_A \gamma_A^{\ell}$, equation (AO.3) gives:

$$\Delta Gm^{\ell} = X_A RT \ln \gamma_A^{\ell} + X_B RT \ln \gamma_B^{\ell} - T[-R(X_A \ln X_A + X_B \ln X_B)] \qquad (AO.4)$$

If the entropy of mixing is the ideal entropy of mixing

$$\Delta Sm^{\ell} = -R(X_A \ln X_A + X_B \ln X_B) \qquad (AO.5)$$

we identify ΔHm^{ℓ} as

$$\Delta Hm^{\ell} = \Delta Hm^{\ell}(A) + \Delta Hm^{\ell}(B) = X_A RT \ln \gamma_A^{\ell} + X_B RT \ln \gamma_B^{\ell}$$

Here $\Delta Hm^{\ell}(i) = H_i^{\ell} - H_i^{0}$ where H_i^{0} represents the standard state of component i.

Then
$$\Delta Hm^{\ell}(i) = RT \ln \gamma_i^{\ell} \qquad (AO.6)$$

The regular solution model in Hildebrand's sense [(1.21), see also (1.22)] supposes that $\Delta Hm^{\ell}(i)$ are <u>independent of temperature</u>. This means that $- RT \ln \gamma_A^{\ell}$ can be calculated from equation (1.25) at $T = T_L$

$$- R T_L \ln \gamma_A^{\ell} = \frac{\Delta H_f}{Tm} (Tm - T_L) + RT_L \ln X_A \equiv - RT \ln \gamma_A^{\ell} \qquad (AO.7)$$

Now using (AO.7) and equation (1.25) we obtain:

$$\Delta G = \frac{T_L - T}{Tm} \left[- \Delta H_f + RT_m \ln X_A \right] \qquad (AO.8)$$

It is also possible to define the activity of component A in solution as $G_A^{\ell} - G_A^{0s} = RT \ln a_s$, i.e. the activity is referred to the pure solid A. Thus from equation (AO.8)

$$\ln a_s = \frac{T_L - T}{T} \left(- \frac{\Delta H_f}{RT_m} + \ln X_A^{\ell} \right) \qquad (AO.9)$$

From equations (AO.6), (AO.7)

$$\ln X_A = - \frac{1}{RT_L} (\Delta Hm^{\ell}(A) + \Delta H_f) + \frac{\Delta H_f}{RT_m} \qquad (AO.10)$$

Now for the case

$$\Delta Hm^{\ell} = \Omega X_A X_B \qquad (AO.11a)$$

that is
$$\Delta Hm^{\ell}(i) = (1 - X_i)^2 \Omega \qquad (AO.11b)$$

where Ω (see (1.4)) is negative when the interaction between unlike

atoms is attractive and $\Omega > 0$ if the interaction is repulsive. From equation (AO.6) we find

$$\ln \gamma_A^{\ell} = (1 - X_A)^2 \frac{\Omega}{RT} \qquad \text{(AO.12)}$$

where now the constant in equation (AO.7) can be explicitly evaluated if Ω is known. This Regular model predicts inmiscibility for $\Omega > 0$ ($\Delta Hm^{\ell} > 0$) and the consolute temperature is given by $T_c = \frac{\Omega}{2R}$. It must be said that the stable and/or metastable phase diagrams are rarely symmetrical as may be deduced from equation (AO.11a). However, Hildebrand's regular solution concept is still valid if ΔHm^{ℓ} is written as a polynomial in X_A and X_B. It is also possible to symmetrize the gap by choosing the right end components. All these possibilities are extensively discussed in (1.19).

A1 ESTIMATION OF THE EXPERIMENTAL ERRORS IN N_V

From equation (2.1)

$$N_V = \frac{2}{\pi} \frac{\sum_{i=1}^{M_0} N_i d_i}{A} \tag{2.1}$$

where d_i is the particle cross section diameter in size class i and M_0 is the number of classes. It is convenient to define the following function

$$\frac{\pi}{2} N_V = \sum_{i=1}^{M_0} \frac{N_i/d_i}{A}$$

Let us consider the following function: $f(x_1, x_2, \ldots, x_{M_0}) = \sum_{i=1}^{M_0} x_i$

where $\{x_i\}$ are independent variables. By using the approximated value for the variance of f:

$$\mathrm{Var} f(x_1, x_2, \ldots, x_{M_0}) \simeq \sum_{i=1}^{M_0} \left(\frac{\partial f}{\partial x_i}\right)^2_{x_i = \bar{x}_i} \mathrm{Var} x_i$$

it is found that

$$\mathrm{Var} f \simeq \sum_{i=1}^{M_0} \mathrm{Var} x_i \leq M_0 \, \mathrm{Var} x \tag{A1.1}$$

The last approximation is always valid provided the largest $\mathrm{Var} x_i$ is chosen. By identifying $f(x_1, x_2, \ldots, x_{M_0})$ with $\sum_{i=1}^{M_0} N_i/d_i$ the characteristic x value can be chosen as $x = \frac{N}{d_{max}}$ where d_{max} is the maximum cross section diameter which is also the largest particle diameter. By using the experimental error Δd_{max} as an estimation for the variance of d i.e. $\mathrm{Var} d \simeq (\Delta d_{max})^2$ and the Poisson distri-

bution for N (VarN = N) it is found that:

$$\mathrm{Var}x = \frac{1}{d_{max}^2}\mathrm{Var}N + \frac{N^2}{d_{max}^2}\frac{\mathrm{Var}d}{d_{max}^2} = \frac{N}{d_{max}^2} + \frac{N^2}{d_{max}^2}\left(\frac{\Delta d_{max}}{d_{max}}\right)^2 \qquad (A1.2)$$

$$\text{As } N_v = \frac{f}{A},\ \mathrm{Var}N_v = \frac{\mathrm{Var}f}{A^2} + \frac{f^2}{A^2}\frac{\mathrm{Var}A}{A^2} \qquad (A1.3)$$

By putting $\mathrm{Var}A \simeq (\Delta A)^2$ where ΔA is the error in the measurement of the print area we obtain:

$$\mathrm{Var}N_v = \frac{\mathrm{Var}f}{A^2} + \frac{f^2}{A^2}\left(\frac{\Delta A}{A}\right)^2$$

$\frac{\Delta A}{A}$ can be estimated from: $\frac{\Delta A}{A} \simeq \frac{\Delta u}{u} + \frac{\Delta v}{v}$ where $A = uv$, and u and v are linear dimensions, so that

$$\frac{\Delta A}{A} \simeq 2\frac{\Delta u}{u} = 10^{-2} \qquad (A1.4)$$

Hence:

$$\frac{\mathrm{Var}N_v}{N_v^2} = \frac{1}{N_v^2 A^2}\mathrm{Var}f + 10^{-4} \simeq \frac{\mathrm{Var}f}{N_v^2 A^2},$$

that is:

$$\mathrm{Var}N_v \simeq \frac{\mathrm{Var}f}{A^2} \qquad (A1.5)$$

Now, using equations (A1.5), (A1.1) and (A1.2)

$$\mathrm{Var}N_v \simeq \frac{M_0 \mathrm{Var}x}{A^2} = \frac{M_0 N}{A^2 d_{max}^2}\left(1 + N\left(\frac{\Delta d_{max}}{d_{max}}\right)^2\right) \qquad (A1.6)$$

Taking $N = 382$, $\frac{\Delta d_{max}}{d_{max}} \simeq 0.05$, $M_0 = 8$, $A_{print} = 17120\ mm^2$, $d_{max(\text{in print})} = 4.23$ mm and print magnification 148.8 we obtain

for the standard deviation $\sigma N_V = (\mathrm{Var}N_V)^{\frac{1}{2}} = 3516$.

So $\frac{\sigma N_V}{N_V} \times 100 \simeq 18\%$ where $N_V = 19130\ mm^{-3}$,

$$N_V \pm \sigma N_V = 19130 \pm 3516$$

Again it is stressed that this approach only gives an upper estimate of the actual error in N_V.

CHEMICAL METHODS AND RESULTS

The chemical analyses for five glasses are listed in Table A2.1 below. The method of analysis is shown in brackets where TA = Triple Acetate, FP = Flame Photometry.

TABLE A2.1

Glass	wt.% Na_2O	wt.% CaO	wt.% SiO_2	wt.% F
Nominal NC_2S_3	17.49	31.65	50.88	-
G2	17.07 (TA)	31.40 (EDTA)	51.53	-
G16	16.85 (TA)	31.54 (EDTA)	51.61	-
G5	16.28 (FP)	29.65 (EDTA)	51.30	0.77
G14	15.44 (TA)	30.10 (EDTA)	54.46	-
G15	14.50 (FP)	30.00 (EDTA)	55.00	-

The losses found for G2 were 0.42 wt.% Na_2O and 0.25 wt.% CaO.

The glass (1 g) was dissolved in approximately 15 ml of AR HF (40%) and 4 ml of AR perchloric acid. During heating, evaporation of silica occurred as silicon tetrafluoride and also the excess of perchloric acid. The remaining solution was transferred to a 250 ml volumetric flask, which was filled to the mark with distilled water.

Na_2O was determined by the Triple Acetate Method (TA). The sodium in the solution (from the glass) was precipitated as $Na\ C_2H_3O_2.Zn(C_2H_3O_2)_2.3UO_2(C_2H_3O_2)_2.6H_2O$. Knowing the weight of precipitate the following conversion formula gives the wt.% of Na_2O:

$$\text{wt.\% } Na_2O = \frac{\text{weight } Na_2O}{\text{weight glass}} \times 100 = \frac{\text{weight ppt} \times 0.020158}{\text{weight glass}} \times 100.$$

For example a typical calculation for G2 is:

$$\frac{0.84765 \times 0.020158}{0.10001} \times 100 = 17.07 \text{ wt.\% } Na_2O .$$

CaO was determined by the EDTA titration technique. A 0.025 N, EDTA solution was prepared from disodium ethylene dimitrilotetroacetate and checked with a 0.0099 N solution of zinc in HCl. For example for glass G14 the mass dissolved was 1.0102 g and the volume to be titrated was 20 ml (from the initial 250 ml solution); the EDTA volume was 17.35 ml so, CaO content (ppm) in 20 ml was:-

$$\frac{17.35 \text{ (vol. titrated)} \times 0.025 \times 10^{-3} \text{ (EDTA strength)} \quad 56.08 \text{ (mol CaO)}}{20 \text{ (vol. of solution)}}$$

= 1216.24 ppm,

so:

$$\frac{1216.24 \times 10^{-6} \times 250}{1.0102} \times 100 = 30.10 \text{ wt.\% CaO}$$

Although the Na_2O content, from flame photometry (FP), was always lower than compared with the triple acetate method, measurements were carried out for glasses G2 and G5 for comparison purposes. The results were G2: 15 wt.% Na_2O and G5: 16.06 wt.% Na_2O meaning a relative increase in Na_2O content of 7.1% for glass G5 compared to G2. Hence by assuming the true level of Na_2O as 17.07 wt.% Na_2O for G2 (Table A2.1) the true Na_2O content of G5 should be approximately 1.21 + 17.07 = 18.28 wt.% Na_2O which in turn implies a loss of 18.94 - 18.28 = 0.66% in Na_2O, where the value of 18.94 was calculated for G5 on the assumption that the Na^+ coming from NaF would combine with the atmospheric O_2 to give Na_2O.

The Li_2O content in glasses melted by P.S. Johnson (2.16) nominally of the $Li_2O.2SiO_2$ composition were also measured by flame photometry.

The levels of fluoride in the glasses were measured by the following technique: the fluoride was put into solution by fusing the glass with NaOH (in a silver crucible) followed by treatment with hydrochloric acid. The F^- concentration was measured from the potential difference developed between two electrodes placed in the solution - one a reference electrode and the other a lanthanum fluoride electrode permeable to F^-. By measuring the voltage for known fluoride solutions a calibration curve was constructed. This curve, which was not linear, was used to estimate the fluoride content of the glasses. The calibration curve was obtained from the following data:

Potential Difference (mV)	Strength x 10^4 (g F/100 ml)
-59	250
-53.5	200
-46	150
-36	100
-25	62.5
-19	50
- 0.8	25
-22.5	12.5
. 45.5	5

For G5 the reading was 12.5 mV corresponding to 0.00155 g F^- and the amount of glass was 0.2004 g, giving 0.77 wt.% F. This corresponds to a 33% loss of Fluoride since the nominal fluoride content was 1.15 wt.%.

If was found that the higher the nominal fluoride content of the glasses the higher the loss. For example, for glass G6 the loss amounted to almost 43%, i.e.

$$\frac{\text{(nominal) } 5.73 \text{ wt.\% F} - \text{(measured) } 3.28}{5.73} \times 100 = 42.8\%$$

The level of losses found in this work are similar to the values obtained by R. Amos (2.17) using this technique.

A3 Chemical Durability

Both for Na_2O and SiO_2 determination the calibration curves were obtained from data produced after taking at least five measurements for each strength of the standard solutions.

A3.1 Procedure for Na_2O determination

Make up a standard solution of sodium ions (from either AR Na_2CO_3 or Na_2SO_4) containing 1000 ppm and by diluting appropriate aliquots to 100 ml obtain solutions containing 0, 1, 2, 3, 4 and 5 ppm Na^+ in 1 vol.% HCl. Calibrate the flame photometer with the 5 ppm solution (for full scale deflection) and with the 0 ppm solution (for zero deflection). Measure the intermediate solutions (always checking the 0 and 100 deflections) after five independent readings have been obtained. Plot scale readings vs. ppm Na^+. Determine Na^+ content in the given solution by carrying out the appropriate dilution.

A3.2 Colorimetric determination of SiO_2

Reagents

1. Standard 50 ppm SiO_2 solution (by fusing pure SiO_2 with Na_2CO_3)
2. Ammonium Molybdate solution: Dissolve 4.0g of ammonium molybdate crystals in about 40 ml of H_2O. Add 5 ml of concentrated H_2SO_3, while stirring. Make up to 50 ml in a volumetric flask.
3. Tartaric Acid solution 20% w/v (by diluting the right amount of tartaric acid in H_2O).

4. Reducing agent: (i) Dissolve 10 g of sodium meta-bisulphite in 80 ml of H_2O. (ii) Dissolve 1.6 g of sodium sulphite (hydrated) and 0.16 g of 1-amino-2-naphthol-4-sulphonic acid in about 15 ml of water. Mix solutions (i) and (ii) and make up to 100 ml with water.

Procedure

Take a given volume of unknown solution in a 100 ml volumetric flask. Prepare five volumetric flasks of 100 ml to which 0, 1, 2, 5 and 10 ml of the standard 50 ppm silica solution have been added. Make up to about 50 ml with distilled water and add 2 ml of the prepared ammonium molybdate solution. Shake the flasks and leave them for 15 minutes. Add 2 ml of the tartaric acid solution and 2 ml of the reducing solution and make up to 100 ml with distilled water. Leave for a further 20 minutes before measuring. Measure the absorbance at 650 nm using 1 cm cells. Plot desorbance against concentration of silica and read off the silica content of the unknown solution.

A4 FORTRAN PROGRAM TO CALCULATE THE A, B AND TO CONSTANTS FROM EQUATION (2.8) BY A LEAST SQUARES FIT

```
      MASTER FULCHER EQUATION BY LEAST SQUARE
      DIMENSION X(50), Y(50), F(50)
      READ (1, 100) N
100   FORMAT (I2)
      S1 = 0.0
      S2 = 0.0
      S3 = 0.0
      S4 = 0.0
      S5 = 0.0
      S6 = 0.0
      S7 = 0.0
      S8 = 0.0
      DO 1 I = 1,N
      READ (1, 101) X(I), Y(I)
101   FORMAT (2F 10.4)
      X(I) = X(I)
      F(I) = X(I)*Y(I)
      S1 = S1 + (X(I)**2.0)
      S2 = S2 + (X(I)*Y(I))
      S3 = S3 + X(I)
      S4 = S4 + (X(I)*F(I))
      S5 = S5 + (Y(I)**2.0)
      S6 = S6 + Y(I)
      S7 = S7 + (Y(I)*F(I))
      S8 = S8 + F(I)
    1 CONTINUE
      E = N
      D = (S1*(E*S5-S6**2.0))-
     1(S2*(E*S2-S3*S6 )) +
     2(S3*(S2*S6-S3*S5))
      A = ((S4*(E*S5-S6**2.0))-
     1(S2*(E*S7-S6*S8))+
     2(S3*(S6*S7-S8*S5)))/D.
      TO = ((S1*(E*S7-S6*S8))-
     1(S4*(E*S2-S3*S6))+
     2(S3*(S2*S8-S3*S7)))/D.
      C = ((S1*(S5*S8-S6*S7))-
     1(S2*(S2*S8-S3*S7))+
     2(S4*(S2*S6-S3*S5)))/D
      B = C + A*TO
      WRITE (2, 102) D, A, TO, C, B
102   FORMAT (1H, 5HDET =, E14.8/1H, 2HA =, E14.8/1H,
     13HTO=, E14.8/1H, 2HC=, E14.8/1H, 2HB=, E.14.8)
      STOP OK
      END
      FINISH
```

Typical chart of measurements for the rotating cylinder apparatus. The $\langle\theta\rangle$ deflection was calculated as $\langle\theta\rangle = \frac{(\theta_R-\theta_{OR})+(\theta_{OL}-\theta_L)}{2}$ as explained in the text.

Stabiliz. time	T(°C) Before	T(°C) After	Zero (cm) Deflection,	Left (cm) Deflection	Right (cm) Deflection	3 Wires	2 Wires	1 Wire	Glass and Comments	$\frac{(\theta''_R-\theta_{OR})+(\theta_{OL}-\theta_L)}{2}$
30	1524		42.35		63.5	x			NBS710, ρ = 2.522 g/cm^{-3}	
			42.40	19.8		x				<θ> = 0.3739
			40.1		51.6		x		Total weight 21.60 g	
			40.1	28.3			x		23 cm level for furnace	0.1992
			40.5		44.3			x		
		1515	40.5	36.8				x	58.5 cm mirror-scale distance.	0.0641
60	1493		42.4		61.6	x				
			42.4	21.9		x			Always used maximum rotating speed.	0.3393
			37.0		48.6		x			
			37.0	24.4			x			0.2054
			37.25		41.2			x		
		1488	37.25	33.2				x		0.0634
30	1457		41.70		66.4	x				
			41.80	14.5		x				0.4415
			39.6		54.3		x			
			39.6	24.3			x			0.2514
			40.4		45.3			x		
		1455	40.4	35.3				x		0.0855
30	1436		42.0		71.8	x				
			42.0	9.0		x				0.5365
			38.3		55.1		x			
			38.3	20.0			x			0.3000
			35.0		40.7			x		
		1437	35.0	28.9				x		0.1099
30	1398		42.1		81.5	x				0.6735
			41.1		63.3		x			
			41.1	16.5-17.2			x			0.3970
			40.6		48.1			x		
		1398	40.6	33.2				x		0.1274
30	1372		40.7		50.0			x		
			40.6	31.2				x		0.1539
			41.1		69.3		x			
		1369	41.2	9.2			x			0.5146
30	1356		41.1		73.7		x			
			41.1	4.0			x			0.5953
			41.7		52.3			x		
		1352	41.7	31.0				x		0.1821

A5b DETERMINATION OF K VALUES (SEE TEXT)

Mass and Radius	No. of wires	Average period of oscillation in sec	I (g cm^2)	K (g cm^2 s^{-2})	K2	K3
800 g; 5.7 cm	3	11.65	13004.1			
	2	9.00	"			
	1	5.23	"	18953.4	6449.3	3851.3
343 g; 3.75 cm	3	5.21	2411.7			
	2	4.02	"			
	1	2.30	"			

A5c VISCOSITY MEASUREMENTS FOR THE NBS 710 STANDARD GLASS

T(°C)	<θ>3	<θ>2	<θ>1	Calculated Log_{10} η	Measured from NBS 710 Calibration	Data for NBS 710 according to Ref. (2.7)
1490.5	0.3393			1.53	1.69	1.70
		0.2064		2.11		
			0.0684	2.10		
1456	0.4445			1.64	1.80	1.80
		0.2564		2.20		
			0.0855	2.14		
1436.5	0.5368			1.73	1.89	1.87
		0.3000		2.27		
			0.1009	2.27		
1398	0.6735			1.83	1.98	1.995
		0.3970		2.39		
			0.1274	2.37		
1354		0.5958		2.57		
			0.1821	2.52		

NOTE: $\langle\theta\rangle_i$ i = 1,2,3 means the mean value of the deflection angle for the condition of i wires connected.

A5d

In this section it is shown that equation (2.6) approaches equation (2.5) when $y \ll \phi$ (see section 2.8.1). By using $\sin 2\theta_y = \sin(\pi - 2\theta_y)$ equation (2.6) transforms to

$$\frac{9}{32}\frac{Pt}{\eta\phi^{1/2}} \simeq \frac{3}{32}\phi^{3/2}\left[(\pi-2\theta_y) - \sin(\pi-2\theta_y)\right] \qquad \text{(A5d.1)}$$

If $\pi - 2\theta_y = u \to 0$ $\sin u \simeq u - \frac{u^3}{3!}$ so $u - \sin u \simeq \frac{u^3}{3!}$. So equation (2.8) gives

$$\frac{9}{32}\frac{Pt}{\eta\phi^{1/2}} \simeq \frac{3}{32}\phi^{3/2}\frac{(\pi-2\theta_y)^3}{6} \qquad \text{(A5d.1)}$$

Also $(\pi-2\theta_y) \simeq \sin 2\theta_y = 2\sin\theta_y \cos\theta_y = 2\left(1 - \frac{2y}{\phi}\right)\frac{2}{\phi}(\phi_y - y^2)^{1/2} \to$

$(y \ll \phi) \to \frac{4y^{1/2}}{\phi^{1/2}}$. Then equation (A5d.1) approaches:

$\frac{9}{32}\frac{Pt}{\eta\phi^{1/2}} \simeq \frac{3}{32} \times \phi^{3/2} \times \frac{1}{6} \times 64 \times \frac{y^{3/2}}{\phi^{3/2}} = y^{3/2}$, which is the same as equation (2.5).

In this Appendix the errors in the viscosities measured with the penetration viscometer are estimated (see section 2.8.1).

Let us calculate the error in $C = \frac{9}{32}\frac{P}{\phi^{1/2}}$ from the individual errors: $\frac{\Delta c}{c} \simeq \frac{\Delta P}{P} + \frac{1}{2}\frac{\Delta\phi}{\phi} \simeq \frac{5}{2256} + \frac{1}{2}\frac{0.001}{0.3175} \simeq 0.004$. From Equation (2.5)

$$\eta = \frac{c}{(y^{3/2}/t)} \quad \text{so} \quad \frac{\Delta\eta}{\eta} \simeq \frac{\Delta c}{c} + \frac{\Delta(y^{3/2}/t)}{< y^{3/2}/t >} \simeq 4 \times 10^{-3} + 4 \times 10^{-2} = 0.044$$

where $< y^{3/2}/t >$ is the mean value of $y^{3/2}/t$ and $\Delta(y^{3/2}/t) \sim \sigma_{n-1}$

Putting $v = \log_{10}\eta$ $\quad \frac{\Delta v}{v} = \frac{\Delta\eta}{\eta}\frac{1}{\log_{10}\eta} = \frac{0.044}{\log_{10}\eta}$. For example

for a viscosity level of $\eta = 10^{10}$ Poise : $\frac{\Delta v}{v} \simeq 0.0044$.

REFERENCES

CHAPTER 1

1.1 Levin, E.M. (1970), 'Phase Diagrams', Vol. 3, p. 143, edited by Alper, A.M., Academic Press, London.

1.2 Stookey, S.D. (1956), Brit. Patent No. 752,243.

1.3 McMillan, P.W. (1964), 'Glass Ceramics', Academic Press, London and New York.

1.4 Swalin, R.A. (1962), 'Thermodynamics of Solids', John Wiley & Sons, Inc., New York, London.

1.5 Ed. Zettlemoyer, A.C. (1969), 'Nucleation', Marcel Dekker, New York.

1.6 Christian, J.W. (1975), 'The Theory of Transformations in Metal and Alloys', Second Edition, Part 1, Pergamon Press, Oxford.

1.7 Rowlands, E.G. (1976), 'Nucleation and Crystal Growth in the Lithia-Baria-Silica System', Ph.D, Thesis, University of Sheffield.

1.8 Billig, W.B. (1962), 'Symposium on Nucleation and Crystallization in Glasses and Melts', edited by Reser, M.K., Smith, G. and Insley, H., p. 77, American Ceramic Society, Columbus, Ohio.

1.9 Kashchiev, D. (1969), Surf. Sci., 14, 209.

1.10 James, P.F. (1974), Physics Chem. Glasses, 15(4), 95.

1.11 Fine, M.E. (1964), 'Introduction to Phase Transformations in Condensed Systems', McMillan, London.

1.12 Jones, G.O. (1971), 'Glass', Second Edition, Chapman and Hall Ltd., and Science Paperbacks.

1.13 Hoffman, J.D. (1958), J. Chem. Phys., 29, 1192.

1.14 Takahashi, K. and Yoshio, T. (1973), Yogyo-Kyokai-Shi., 81(12), 524.

1.15 Cahn, J.W. and Charles, R.J. (1965), Physics Chem. Glasses, 6(5), 181.

1.16 Cahn, J.W. (1969), J. Am. Ceram. Soc., 52(3), 118.

1.17 Seward III, T.P. (1970), 'Phase Diagrams' Vol. 1, p. 295, edited by Alper, A.M., Academic Press, London.

1.18 Zarzycki, J. (1970), Discuss. Faraday Soc., 50. 122.

1.19 James, P.F. (1975), J. Mater. Sci., 10, 1802.

1.20 Uhlmann, D.R. and Kolbeck, A.G. (1976), Physics Chem. Glasses, 17(5), 146.

1.21 Hildebrand, J.H., Prausnitz, J.M., and Scott, R.L. (1970), 'Regular and Related Solutions', Van Nostrand Reinhold Company.

1.22 Rey, M. (1948), Discuss. Faraday Soc., 4, 259.

1.23 Uhlmann, D.R. (1971), 'Advanced in Nucleation and Crystallization in Glasses', edited by Hench, L.L. and Freiman, S.W., p. 91, American Ceramic Society, Columbus, Ohio.

1.24 Jackson, K.A. (1975), 'Treatise on Solid State Chemistry', edited by Hannay, N.B., p. 233, Plenum Press, New York, London.

1.25 Bergeron, C.G. (1972), 'Introduction to Glass Science', edited by Pye, L.D., Stevens, H.J. and La Course, W.C., p. 173, Plenum Press, New York.

1.26 Morey, G.W. (1960), 'The Properties of Glass' Reinhold Publishing Corporation, New York.

1.27 Shahid, K.A. and Glasser, F.P. (1971), Physics Chem. Glasses, 12(2), 50.

1.28 Segnit, E.F. (1953), Am. J. Sci., 251, 586.

1.29 Moir, G.K. and Glasser, F.P. (1974), Physics Chem, Glasses, 15(1),6.

1.30 Idem, ibid, (1976), 17(3), 45.

1.31 Dent Glasser,L.S. and Mileson, J.S. (1968), J. Am. Ceram. Soc., 51(1), 55.

1.32 Maki, I. and Sugimura, T. (1968), J. Ceram. Assoc. Japan, 76(5), 144.

1.33 Kröger, C. and Kreitlow, G. (1956), Glastech. Ber., 29, 393.

1.34 Taylor, H.E. and Hill, D.K. (1952) 'The Identification of Stones in Glass by Physical Methods', The Glass Delegacy of the University of Sheffield.

1.35a Frischat, G.H. and Oel, H.J. (1966), Glastech. Ber., 39, 50.

1.35b Idem, ibid, (1966), 39, 524.

1.36 Hammel, J.J. (1967), J. Chem. Phys., 46, 2234.

1.37 Russell, K.C., to appear in 'Nucleation III', edited by Zettlemoyer, A.C., Marcel Dekker, New York.

1.38 Burnett, D.G. and Douglas, R.W. (1970), Physics Chem. Glasses, 11(5), 125.

1.39 Strnad, Z. and Douglas, R.W. (1973), Physics Chem. Glasses, 14(2), 33.

1.40 Mukherjee, S.P. and Rogers, P.S. (1967), Physics Chem. Glasses, 8(3), 81.

1.41 Kalinina, A.M. and Filipovich, V.N. (1974), 10th International Congress on Glass, 14, 56, Kyoto, Japan.

1.42a Dietzel, A. (1937), Glass, 14(2), 60.

1.42b Swift, H.R. (1947), J. Am. Ceram. Soc., 30(6), 170.

1.43 Sadeghi, M.R. (1975) 'Homogeneous Nucleation and Crystal Growth in Soda-Lime-Silica Glasses', M.Sc., University of Sheffield.

1.44 Maurer, R.D. (1959), J. Chem. Phys., 31(2), 444.

1.45 Maurer, R.D. (1962), as reference 1.8, p. 5

1.46 Gutzow, J. and Toshev (1971), as reference 1.23, p. 10.

1.47 Rindone, G.E. (1958), J. Am. Ceram. Soc., 41(1), 41.

1.48 Ohlberg, S.M., Golob, H.R. and Strickler, D.W. (1962), as reference 1.8, p. 55.

1.49 Neilson, G.F. (1971), as reference 1.23, p. 73.

1.50 McMillan, P.W. (1971), as reference 1.23, p. 224.

1.51 Harper, H., James, P.F. and McMillan, P.W. (1970), Discuss. Faraday Soc., 50, 206.

1.52 Matusita, K. and Tashiro, M. (1973), Physics Chem. Glasses, 14(4), 77.

1.53 Ito, M., Sakaino, T. and Moriya, T. (1968), Bull. Tokyo Inst. Technol., 88, 127.

1.54 Filipovich, V.N. and Kalinina, A.M. (1968), Neorg. Mater., 4(9), 1532.

CHAPTER 2

2.1 As 1.10.

2.2 De Hoff, R.T. and Rhines, F.N. (1961), Trans. Metall. Soc., A.I.M.E., 221, 975.

2.3 De Hoff, R.T. and Rhines, F.N. (1968), 'Quantitative Microscopy', McGraw-Hill, New York.

2.4 J.A.N.A.F. Thermochemical Tables, 2nd Edition, issued June 1971, U.S. Department of Commerce, National Bureau of Standards, Washington.

2.5 Maghrabi, C.E. (1970), 'Studies of Glasses in the Germanium-Arsenic-Selenium System', Ph.D. Thesis, University of Sheffield.

2.6 Douglas, R.W., Armstrong, W.L., Edward, J.P. and Hall, D. (1965), Glass Technol., 6(2), 52.

2.7 Napolitano, A. and Hawkins, E.G. (1964), Journal of Research of the National Bureau of Standards, A. Physics and Chemistry, 68A(5), 439.

2.8 Douglas, R.W. (1956), J. Soc. Glass Technol., XL, 83P.

2.9 Lillie, H.R. (1939), J. Am. Ceram. Soc., 22(11), 367.

2.10 Dietzel, A. and Brückner, R. (1955), Glastech. Ber., 28, 455.

2.11 Hagy, H.E. (1968), J. Canadian Ceram. Soc., 37, LXV.

2.12 Lillie, H.R. (1933), J. Am. Ceram. Soc., 16(12), 619.

2.13 Scholze, H. (1959), Glastech. Ber., 32(3), 81.

2.14 Timoshenko, S.P. and Gere, J.M. (1974), 'Mechanics of Materials', Van Nostrand Reinhold Company.

2.15 Turner, W.E.S. and Winks, F. (1928), J. Soc. Glass Technol., 12, 57.

2.16 Johnson, P.S. (1976), Undergraduate Third Year Project, University of Sheffield.

2.17 Amos, R., Ph.D. Thesis in preparation, University of Sheffield.

CHAPTER 3

3.1 As 1.39.

3.2 As 1.43.

3.3 As 1.10.

3.4 As 2.3

3.5 Raghvan,. V. and Cohen, M. (1975), as reference 1.24, p. 67.

3.6 Frischat, G.H. (1975), 'Mass Transport Phenomena in Ceramics Materials', Scientific Research Vol. 9, p. 285, Ed. Cooper, A.R. and Heuer, A.H., Plenum Press, New York, London.

3.7 Blazek, A. (1973), 'Thermal Analysis', Chapter 3, Van Nostrand Reinhold Company, London.

3.8 As 2.4

3.9 As 1.33.

3.10 As 1.29.

3.11 As 1.32.

3.12 As 1.31.

3.13 Cullity, B.D. (1967), 'Elements of X-ray Diffraction' Addison-Wesley Publishing Company, Inc.

3.14 James, P.F. and Keown, S.R. (1974), Phil. Mag., 30(4), 789.

3.15 As 1.26.

CHAPTER 4

4.1 As 1.10.

4.2 As 2.16.

4.3 Shartsis, L., Spinner, S. and Capps, W. (1952), J. Am. Ceram. Soc., 35, 155.

4.4 Merker, L. and Scholze, H. (1962), Glastech. Ber., 35, 37.

4.5 Swanson, H.E. and Tatge, E. (1953), 'Standard X-ray Diffraction Powder Patterns', Nat. Bureau of Standards Circ., 539, 1, 31.

CHAPTER 5

5.1 Oishi, Y., Terai, R. and Ueda, H. (1975), as reference 3.6, p. 297.

5.2 Litovitz, T.A. and Macedo, P.C. (1965), J. Chem. Phys., 42(1) 245.

5.3 Rita, R.A., Bergeron, C.G. and Lukacs, J.M. (1973), J. Am. Ceram. Soc., 56(1), 47.

5.4 As 1.14.

5.5 Zemansky, M.W. (1968), 'Heat and Thermodynamics', McGraw-Hill.

5.6 Haggerty, J.S., Cooper, A.R. and Heasley, J.H. (1968), Physics Chem. Glasses, 9(2), 47.

5.7 As 1.26.

5.8 Matusita, K. and Tashiro, M. (1973), J. Non-Cryst. Solids, 11, 471.

5.9 As 1.10.

5.10 As 1.39.

5.11 Hetherington, G. and Jack, K.H. (1962), Physics Chem. Glasses, 3(4), 129.

5.12 As 4.4.

5.13 Scholze, H., Franz, H. and Merker, L. (1959), Glastech. Ber., 32(10), 421.

5.14 Maklad, M.S. and Kreidl, N.J. (1971), Proc. IXth International Congress on Glass, Versailles, France, Vol. 1, p. 75.

5.15 Wagstaff, F.E., Brown, S.D. and Cutler, I.B. (1964), Physics Chem. Glasses, 5(3), 76.

5.16 Eagan, R.J. and Bergeron, C.G., as reference 1.23, p. 202.

5.17 Mukherjee, S.P., Zarzycki, J. and Traverse, J.P. (1976), J. Mater. Sci., 11, 341.

5.18 As 1.7.

5.19 Matusita, K. and Tashiro, M. (1973), J. Ceram. Soc. Japan, 81(11), 500.

5.20 As 3.14.

5.21 Trap, H.L. and Stevels, J.M. (1960), Physics Chem. Glasses, 1(4), 107.

5.22 Kurkjian, C.R. and Russel, L.E. (1958), J. Soc. Glass Tech., 42, 130T.

5.23 Franz, H. (1978) 'Borate Glasses', Mat. Sci. Research, Vol. 12, Edited by Pye, L.D., Fréchette, W.D. and Kreidl, N.J., Plenum Press, N.Y. and London.

5.24 As 1.3.

5.25 Ravinovich, É.M. (1967), Neorg. Mater., 3(5), 855.

5.26 Banerjee, B.K. (1959), Proc. Nat. Inst. Sci. India, A25, 155.

5.27 Hench, L.L. (1976), 'The processing of Bioceramics'.III CIMTEC-RIMINI, May 27-31.

5.28 Rindone, G.E. and Rhoads, J.L. (1956), J. Am. Ceram. Soc., 39(5), 173.

5.29 As 1.47.

5.30 Rindone, G.E. (1962), J. Am. Ceram. Soc., 45(1), 7.

5.31 (1974), Proc. Xth International Congress on Glass, Kyoto, Japan. Discussion between Hench, L.L. and Rindone, G.E. No.15, 114, Part II.

5.32 As 1.46.

5.33 As 1.44

5.34 Doladugina, V.S. and Korolev, N.V. (1967), Soviet. J. Optical Technol., 716, 109.

5.35 Firth, E.M., Hodkin, F.W., Muirhead, C.M., Parkin, M. and Turner, W.E.S., (1926), J. Soc. Glass Technol., 10, p. 176.

5.36 Fletcher, N.H. (1958), J. Chem. Phys., 29(3), 572.

5.37 Meiling, G.S. and Uhlmann, D.R. (1967), Physics Chem. Glasses, 8(2), 62.

5.38 Ainslie, N.G., Morelock, C.R. and Turnbull, D, as reference 1.8, p. 97.

5.39 As 1.44.

5.40 Gutzow, I., Zlateva, E., Alyakov, S. and Kovatscheva, T. (1977), J. Mater. Sci., 12, 1190.

5.41 Schaefer, R.J. and Glicksman, M.E. (1969), J. Crystal Growth, 5, 44.

5.42 Hopper, R.W. and Uhlmann, D.R. (1973), J. Crystal Growth, 19, 177.

5.43 Gutzow, I., Toschev, S., Marinov, M. and Popov, E. (1968), Kristall. und Technik., 3(3), 337.

5.44 Gutzow, I. and Toschev, S. (1970), J. Crystal Growth, 7, 215.

5.45 Calvert, P.D. and Uhlmann, D.R. (1972), J. Crystal Growth, 12. 291.

5.46 Hull, F.C, Colton, R.A. and Mehl, R.F. (1942), Trans. Met. Soc. of A.I.M.E., 150, 185.

5.47 As 1.34.

5.48 McMillan, P.W. (1974), Proc. Xth International Congress on Glass, Kyoto, Japan, No. 14,1, Part II.

5.49 As 1.35a.

5.50 El-Shamy, T.M. and Ahmed, A.A. (1977), Proc. XIth International Congress on Glass, Prague, 3(A9), 181.

5.51 As 1.27.

5.52 Helgesson, C.I. (1975), VIIIth Int. Conference on 'Science of Ceramics', Cambridge, Sept. 22-25.

5.53 Forrauto, R.J. and Haynes, W.L. (1973), U.S. Patent 3,743,525.Jul.

5.54 Smithard, M.A. and Dupree, R. (1972), Phys. stat. sol.(a), 11, 695.

5.55 As 1.38.

5.56 1977 Powder Diffraction File - Alphabetical Index - Inorganic Compounds JCPDS International Centre for Diffraction Data.